Experimental and Numerical Study of Calcium Treatment of Steel

Harsh Priyadarshi

UNIVERSITE BRETAGNE SCIENCES LOIRE POUR L'INGENIEUR

CENTRALE NANTES

THESE DE DOCTORAT DE

L'ÉCOLE CENTRALE DE NANTES
COMUE UNIVERSITE BRETAGNE LOIRE

ECOLE DOCTORALE N° 602
Sciences pour l'Ingénieur
Spécialité : « *Mécanique des milieux fluides* »

Par

« Harsh PRIYADARSHI »

« Experimental and Numerical Study of Calcium Treatment of Steel »

Thèse présentée et soutenue à « Ecole Centrale de Nantes », le « 10/07/2019 »
Unité de recherche : Institut de Calcul Intensif (ICI)

Rapporteurs avant soutenance :

Cédric LE BOT	Maitre de conférences	INP Bordeaux
Stéphane ZALESKI	Professeur	Sorbonne Université, Paris

Composition du Jury :

Président :	Julien BRUCHON	Professeur, Ecole Nationale Supérieure des Mines de Saint-Etienne
Examinateur :	Thierry COUPEZ	Professeur, Mines-Paris Tech, Sophia-Antipolis
Examinateur :	Pascal GARDIN	Ingénieur de Recherche (H.D.R), ArcelorMittal R&D, Maizières lès Metz
Dir. de thèse :	Luisa SILVA	H.D.R, Ecole Centrale de Nantes
Co-Encadrant :	Benjamin BOISSIERE	Ingénieur de Recherche, ArcelorMittal R&D, Maizières lès Metz

Contents

List of Figures

List of Tables

Nomenclature

A_s	Interfacial area per melt volume between melt and atmosphere (m^{-1})
a_o	Activity of oxygen
a_{cao}	Activity of Cao in inclusions
A_c	Total surface area of capsule (m^2)
Bo	Bond number
Ca	Calcium
C_{ca}	Average concentration at calcium droplet / liquid steel interface (liquid steel side, ppm)
C_{ca}^{bath}	Average concentration of calcium in liquid steel (ppm)
C_l^Z	Equivalent liquid concentration (ppm)
C_D	Drag coefficient
C_{pw}	Specific heat of water (J/kg.K)
C_{pcad}	Specific heat of calcium droplet, Ca liquid (J/kg.K)
D_{ca}	Diffusion coefficient of liquid calcium in liquid calcium (m^2/s)
D_{ls}	Diffusion coefficient of calcium in liquid steel (m^2/s)
D_G	Diffusion coefficient of liquid calcium in argon (m^2/s)
d	Diameter of droplet (cm)
D_l	Diffusion coefficient in liquid medium (m^2/s)
$D_l \int (\nabla C.n) dA$	Mass flux at the interface ($ppm.m^3/s$)
d_{cad}	Diameter of calcium droplet (cm)
d_{cab}	Diameter of calcium bubble (cm)
d_p	Wire penetration depth (m)
d_w	Diameter of wire (m)
d_E	Equivalent bubble diameter (m)
D_O	Diffusivity of oxygen in liquid steel (m^2/s)
D_S	Diffusivity of Sulfur in liquid steel (m^2/s)
E_{ca}	Enhancement factor
E_{mix}	Mixing zone in the interface (m)
f_{ca}	Activity coefficient of Ca
Fr	Froude number
f_{st}	Surface tension force (N)
g	Acceleration due to gravity (m/s^2)

h_{min}	Minimum mesh size at the interface (m)
h	Height from interface (m)
$H(\alpha)$	Heavy side function
$H_{\varepsilon}(\alpha)$	Smooth heavy side function
$H_{\varepsilon i}^{c}$	Color function
H_{vw}	Enthalpy of vaporization of water (J/kg)
H_{vca}	Enthalpy of vaporization of Ca liquid (J/kg)
J	Rate of formation of bubbles per unit time per unit volume $(s.m^3)^{-1}$
Ja	Jacob number
K_{cad}	Average mass transfer coefficient of calcium droplet in liquid steel (m/s)
K_1	μ_{bd}/μ_l
K_{cadexp}	Average mass transfer coefficient of calcium droplet in liquid steel calculated experimentally (m/s)
K_l	Liquid side mass transfer coefficient at steady state (m/s)
K_G	Gas side mass transfer coefficient at steady state (m/s)
K_{ovl}	Mixed transfer coefficient (m/s)
K_{cao}	Equilibrium constant of Ca + O = Cao
K_{evp}	Mass transfer coefficient for calcium vaporization (m/s)
K_H	Henry's equilibrium constant for calcium dissolution reaction
K_1	Curvature per phase
k_{12}	Curvature of the interface
K_{cadnum}	Average mass transfer coefficient of calcium droplet in liquid steel obtained numerically (m/s)
K_{cabnum}	Average mass transfer coefficient of calcium bubble in liquid steel obtained numerically (m/s)
L_{max}	Interface thickness, ε (m)
Mo	Morton number
m_c	Mass of capsule (kg)
N	Absorption rate at the interface(kg/s)
N'	Average rate of transfer of gas per unit area $(Kg/s.m^2)$
n_1	Normal per phase

n_{12}	Normal to the interface
P_{Ca}	Vapor Pressure of calcium (atm)
P_{∞}	Ambient pressure (atm)
P_0	Initial gas pressure (atm)
Pe	Peclet number
P_l	Pressure inside the liquid phase (atm)
P_G	Pressure inside the gas phase (atm)
Re	Reynolds number
R_0	Initial radius of bubble (m)
R_c	Continuity residual
R_m	Moment residual
r_c	Critical radius (m)
Sh	Sherwood number
Sc	Schmidt number
SH	Super heat of molten steel (k)
S	Surface area of calcium droplet or calcium bubble (m^2)
St	Stokes number
T	Temperature (K)
Δt	Time step (s)
Δt^{cap}	Capillary time step (s)
T_c	Critical temperature (K)
v_t	Terminal velocity of droplet/bubble (m/s)
V_w	Wire feeding rate (m/s)
V_{cap}	Volume of capsule (m^3)
v	Velocity field (m/s)
$We_{critical}$	Critical Weber number
We	Weber number
W	Minimum work needed to form a bubble (J)

Greek letters

μ_{ls}	Viscosity of liquid steel (Pa.s)
μ_l	Viscosity of liquid medium (Pa.s)
μ_d	Viscosity of droplet (Pa.s)
μ_b	Viscosity of bubble (Pa.s)
μ_{cad}	Viscosity of calcium droplet (Pa.s)
μ_w	Viscosity of water (Pa.s)
μ_{air}	Viscosity of air (Pa.s)

μ_{cab}	Viscosity of calcium bubble (Pa.s)
σ	Surface tension (N/m)
$\sigma_{cad.ls}$	Surface tension between calcium droplet and liquid steel (N/m)
$\sigma_{cab.ls}$	Surface tension between calcium bubble and liquid steel (N/m)
σ_{cad}	Surface tension of calcium droplet w.r.t air (N/m)
$\sigma_{cad.cab}$	Surface tension between calcium droplet and calcium bubble (N/m)
σ_{wb}	Surface tension of water w.r.t to air (N/m)
σ_{12}	Surface tension of phase 1 w.r.t to phase 2 (N/m)
ρ_{ls}	Density of liquid steel (kg/m^3)
ρ_{cad}	Density of calcium droplet (kg/m^3)
ρ_l	Density of liquid medium (kg/m^3)
ρ_{air}	Density of air (kg/m^3)
ρ_{cab}	Density of calcium bubble (kg/m^3)
ρ_w	Density of water (kg/m^3)
ρ_b	Density of bubble (kg/m^3)
δ_r	Effective thickness (m)
$\delta_{\Gamma 12}$	Dirac function
α_w	Thermal diffusivity of water (m^2/s)
$\alpha(x)$	Distance function
α_{cad}	Thermal diffusivity of calcium droplet, Ca liquid (m^2/s)
λ_l	Thermal conductivity of liquid (W.m^{-1}K^{-1})
λ	Distance parameter
Ω_l	Liquid steel domain
Ω_c	Calcium domain
ζ	Strength parameter
Γi	Calcium liquid steel interface
$\mathcal{T}_h$	Triangular unstructured mesh
τ_{ls}	Shear stress at calcium liquid steel interface (liquid steel side, Pa)
u_ε	Smooth phase function
ε	Interface thickness (m)
$\emptyset$	Flux (kg/s)

Chapter 1:

Introduction

1 Introduction

Crude steel can be produced by blowing oxygen through molten pig iron, but the resulting product could fail to meet the required engineering material specifications. As a consequence, the produced material would be largely inferior to the steel produced through versatile modern technologies. Production of high-quality steel, suitable for modern day consumption demands numerous intermediate steps. One of these steps, to develop steel free of nonmetallic inclusions (mainly alumina inclusions), is the "*calcium treatment of liquid steel*." Before going further into the details of the calcium treatment of liquid steel, it is essential to overview the basic operations in the steel making process briefly.

1.1 Steelmaking Process

Steelmaking operations can be divided into three main steps:

a) Reduction: Ironmaking

The first and foremost step is to produce hot metal from iron ore. Mined iron ore, consists of iron oxides and various unwanted substances generally known as "gangue." Iron ore is reduced to metallic iron in "blast furnace" in the presence of coke as a reducing agent. During the blast furnace operations, iron-bearing material, coke and limestone are supplied through the top of the furnace, and they travel in the downward direction. At the same time, the hot air (at ~1200°C) is blown from the sideways at the bottom of the furnace. Furnace operation is an intricate process that includes numerous physicochemical processes, e.g., combustion, reduction, heat and mass transfer, fusion, etc. Throughout this process, various phases interact with each other in a complex manner. Once these processes are balanced, a steady state operating regime is established. Molten iron and slag are then taken out periodically from the bottom of the furnace. The metallic iron produced by this process contains a high percentage of carbon (~4%) and is passed to the steel making process in liquid form at approximately 1500°C.

b) Refining: Steelmaking

The refining of iron is the intermediate process where the carbon content of the hot metal is lowered by the oxidation process. At the same time, alloying materials are added to the furnace to achieve the desired chemical composition of the final product. Refining is comprised of two processes, namely: primary steelmaking and secondary steelmaking.

I. **Primary steelmaking**: Hot metal contains C ~ 4%, Si ~ 0.6 to 1%, Mn ~ 0.6 to 0.8% and P ~ 0.1 to 0.2%. In primary steel making, the oxygen is blown through the hot metal to lower the carbon content of the alloy and convert it into steel. The following reactions occur when oxygen is blown from the top:

$$[Fe] + [O] = (FeO) \quad \text{(i)}$$

$$[C] + [O] = \{CO\} \quad \text{(ii)}$$

$$[Si] + 2[O] = (SiO_2) \quad \text{(iii)}$$

$$[Mn] + [O] = (MnO) \quad \text{(iv)}$$

$$2[P] + 5[O] = (P_2O_5) \quad \text{(v)}$$

$$[C] + (FeO) = \{CO\} + [Fe] \quad \text{(vi)}$$

$$(Fe) + (MnO) = (FeO) + [Mn] \quad \text{(vii)}$$

In the above equations, square bracket denotes the element dissolved in steel melt, the round brackets denote the component dissolved in liquid slag and curly bracket denotes the gas phase.

Carbon is removed as a gaseous phase, and the other elements are removed as slag. Slag formation of desired chemistry is vital for the successful operation of converter steelmaking technology.

II. **Secondary steelmaking:** Secondary steelmaking is defined as any post steelmaking process performed before casting and hot metal depressurization. The objectives of this secondary refining are temperature homogenization, chemical adjustments for carbon, sulfur, phosphorous, oxygen, inclusion control, and degassing.

c) Continuous casting and finishing operations:

Molten steel can be cast continuously into billets, blooms, and slabs depending on the desired product (e.g., whether long or flat products). In continuous casting, tundish is the important refractory lined vessel that is used to feed the molten steel into the molds through a submerged nozzle. The cast steel can be forged or rolled in successive steps to produce the steel of the desired shape. Rolling is the most common method of shaping. The amount of work to which the steel is subjected and the schedule on which the work is carried out, significantly affect the properties of the end steel.

Overall, the objective of the abovementioned processes is to minimize the adverse effects on the structural integrity of the steel. One of the intermediate steps to attain this objective is the calcium treatment of liquid steel during secondary refining, which is explained in the following section.

1.2 Calcium treatment

The Steel coming out of the primary steelmaking process possesses high oxygen content. This oxygen must be removed before the steel is cast. Otherwise, carbon monoxide gas is formed during solidification, causing excessive porosity in the steel. Therefore, aluminum is used for metal de-oxidation during the secondary refining of steel. However, the presence of aluminum can lead to the formation of alumina inclusions (Al_2O_3), which are solid at the steelmaking temperature. This might further disrupt the flow in the mold cavity, which can ultimately deteriorate the machinability of the steel and can also lead to the surface defects. Therefore, one of the prime objectives in the steel making process is to control the alumina inclusions: their amount, composition, size, and other properties. To prevent the formation of solid

alumina inclusions, calcium treatment (addition of calcium in liquid steel) is widely used to transform solid Al_2O_3 into low melting point calcium-aluminates. However, it gives very irregular results in terms of calcium recovery. Even with many efforts done to understand the behavior of calcium in liquid steel, it is not yet accurately predicted.

On the one hand, excess addition of calcium in the melt may result in the formation of solid calcium sulfide, which could lead to the early clogging of the nozzle. On the other hand, too low amount of calcium transferred to the steel can worsen the steel castability. Therefore, the mechanism by which the calcium dissolves into the melt and transforms the solid inclusions must be understood to optimize the process conditions such as injection speed, injection depth, injection wire diameter, stirring time, etc.

1.3 Industrial Context

The process of calcium treatment of steel involves the injection of cored wire pure calcium or in the form of a mixture (SiCa, FeCa, etc.) as shown in Figure 1-1.

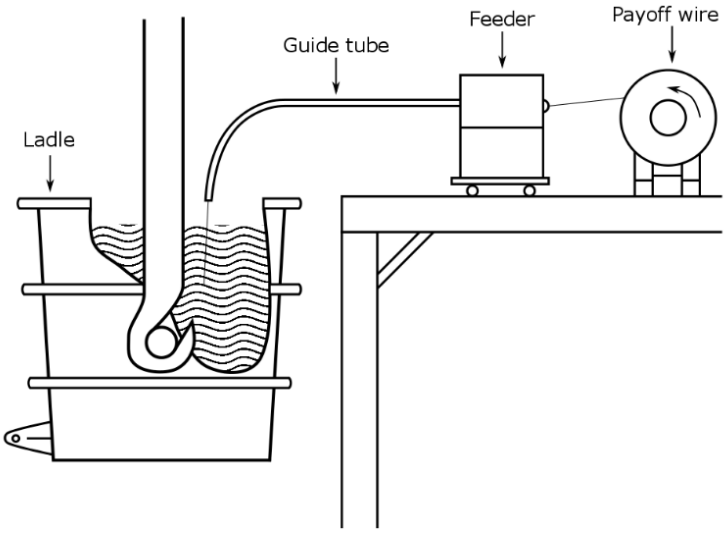

Figure 1-1 Calcium wire feeding process.

If the wire melts deeply enough so that the local Ferro-static pressure at the calcium release location is higher than the corresponding calcium vapor pressure, then the calcium is released under its liquid form. Otherwise, the calcium may be released under its gaseous form. Even dispersion of liquid calcium and prolonged contact of calcium with the steel melt ensures a maximum calcium-steel interaction. A much better yield is achieved if the calcium wire melting takes place deep inside the steel melt.

The addition of calcium transforms, solid inclusions of alumina (Al_2O_3) into liquid inclusions of calcium aluminates (C_xA_Y). Among the different calcium aluminates, those which are composed of approximately 50% of CaO and 50% of Al_2O_3 have a melting point below the steelmaking temperature (Figure 1-2). Those inclusions are liquid at operating temperature. Therefore, the objective is to provide enough calcium into the steel in order to form such inclusions ($12CaO7Al_2O_3$, for instance).

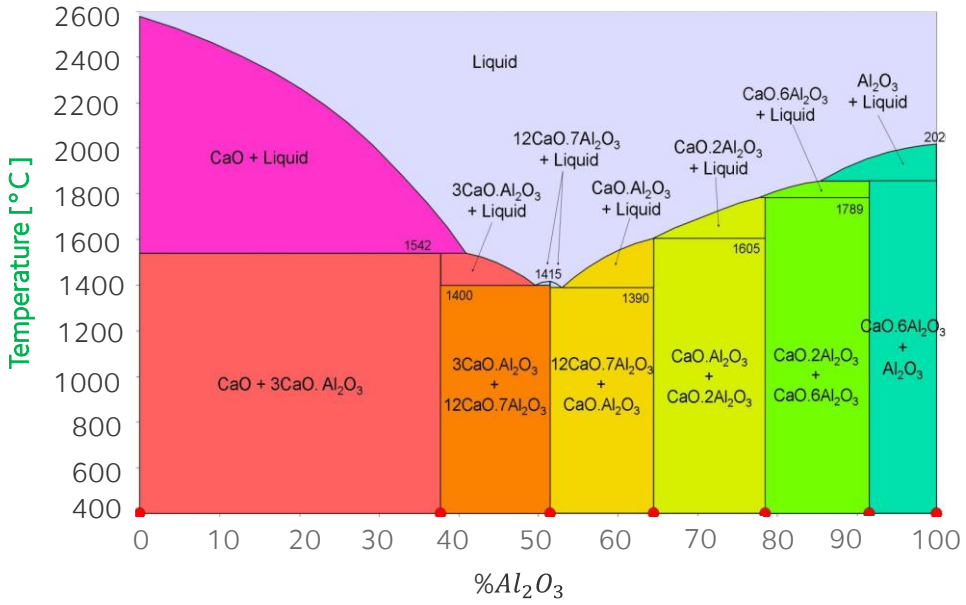

Figure 1-2 Phase diagram of Cao.Al_2O_3.

Figure 1-3 shows the nature of the modification and the morphology of the inclusions before and after calcium treatment schematically. It can be seen that the solid inclusions of alumina are transformed into liquid inclusions of spherical shape. The calcium aluminate particles are globular in nature due to the surface tension effect, which tends to retain their globular shape during hot rolling.

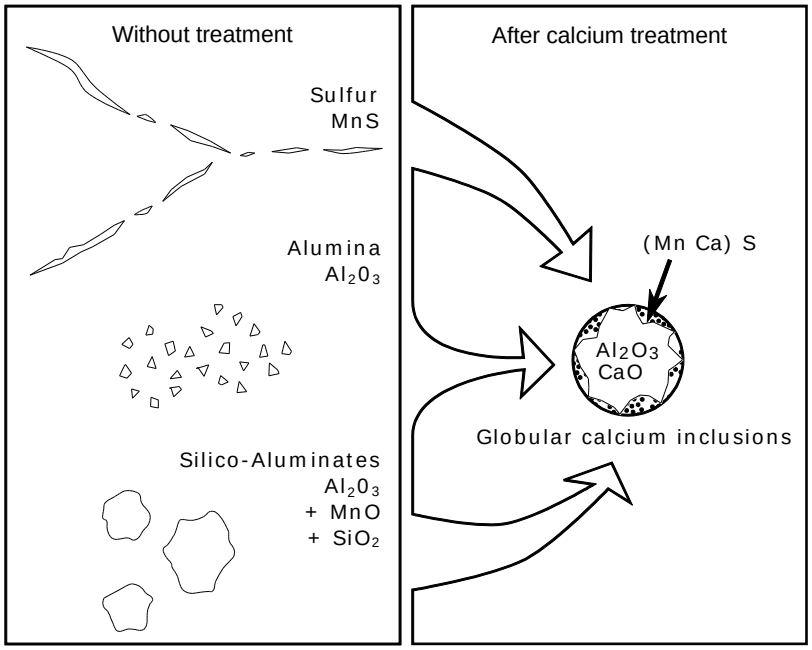

Figure 1-3 Transformation of solid inclusions by addition of calcium.

In the steelmaking process, mainly alumina and manganese sulfide (MnS) inclusions are formed and need to be modified. Alumina inclusions are brittle and break on deformation. Similarly, MnS inclusions become of the stringer type when submitted to deformation.

Different shapes are encountered for inclusions: globular, platelet, dendritic, polyhedral, etc. Globular-shaped inclusions include MnS, oxysulphides, iron aluminates, and some silicates. An excessive amount of strong de-oxidizer (mainly aluminum) results in the formation of dendrite shaped oxides and sulfide inclusions that tend to remain separate but in the aggregated state. Sharp edges and corners of the dendrite shaped inclusions may cause a local concentration of internal stress. This can considerably decrease ductility, toughness, and fatigue strength of steel. It is for such reasons that globular shaped inclusions are preferred.

Several metallurgical advantages are brought about with the modification of composition and morphology of oxide and sulfide inclusions via calcium treatment of liquid steel. The effect of calcium treatment on inclusion modifications are summarized below:

- manganese sulfides are reduced in number and size, as well as they are transformed to Ca-Mn sulfides with varying properties;
- aluminum oxides, which are generally hard, angular and often appear in clusters are reduced in number and replaced with complex $CaO\text{-}Al_2O_3$ or $CaO\text{-}Al_2O_3$ or $CaO\text{-}Al_2O_3\text{-}SiO_2$ inclusions;
- silicates are eliminated and replaced by $CaO\text{-}Al_2O_3\text{-}SiO_2$ inclusions;
- complex globular $CaO\text{-}Al_2O_3\text{-}SiO_2$ inclusions are formed, often surrounded by sulfide rim.

Different steps involved in the calcium treatment of liquid steel are explained in the section below.

1.3.1 Calcium treatment steps

Processing of calcium treatment in the steel can be divided into the following different steps:

- dissolution of the envelope of the metal cored wire;
- release of calcium in the form of liquid or gas;
- vaporization of the calcium in liquid steel;
- dissolution and transport of calcium in liquid steel;
- modification of the inclusions presents in the liquid.

The description of each step of the calcium treatment is described below (Figure 1-4).

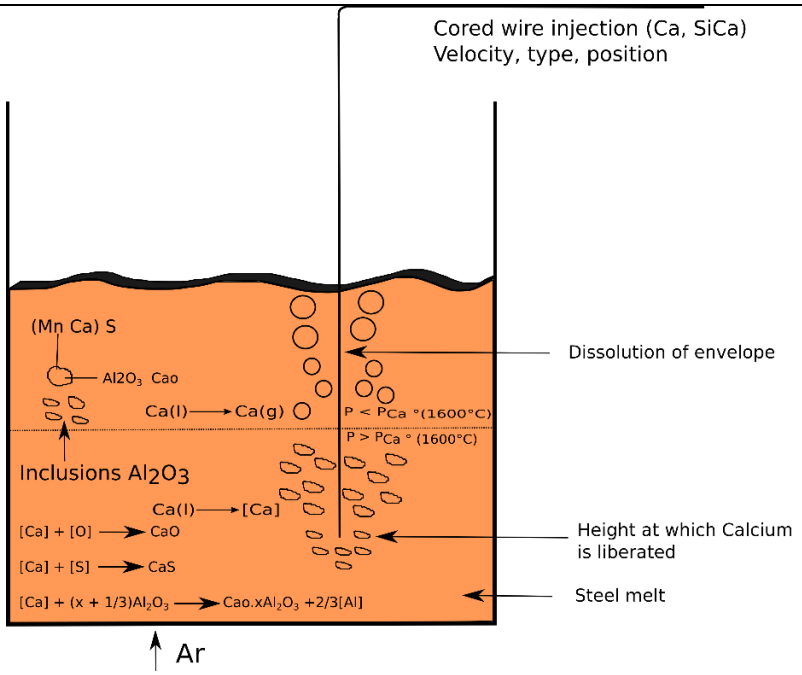

Figure 1-4 Calcium treatment of steel.

1) *Dissolution of the sheath:* During the introduction of the wire in the liquid metal (steel), liquid metal solidifies on the surface of the wire initially, and it forms the steel sheath. Formed steel sheath liquefies as it enters the bath encountering the rise in temperature. The dissolution model of the cored wire developed by Lee et al. [1] showed that its dissolution depends on three primary parameters: the rate of injection of the wire, the diameter of the sheath and the degree of overheating of the liquid metal. Sanyal et al. [2] have proposed a more precise description of the sub-layers present during the dissolution of the cored wire from the mechanism similar to the one proposed by Lee et al. [1]. The depth of penetration of the cored wire can, therefore, be estimated from existing models and operating parameters of the process. Multiple recent studies aim to optimize the cost and efficiency of calcium treatment of steel by developing innovative technologies for flux cored wires [3].
2) *Release of calcium in the form of liquid droplets or gas:* The underlying mechanism governing the calcium release in the form of liquid droplets or gas during the complete dissolution of the protective sheath is unknown. It should be noted that the calcium release can be directly in the gaseous form if the penetration depth of the wire is low or in other words where the Ferro-static pressure is lower than the calcium vapor pressure at 1600°C. However, it is preferable to release the calcium in the form of droplets to increase the residence time and improve the performance of calcium in liquid steel bath. The size and distribution of these droplets have been the subject of study for many researchers. The size of the droplets and the formed bubbles impose a specific exchange area and strongly determine the efficiency of the mass transfer between calcium and liquid steel. Therefore, it is essential to characterize their size to estimate the kinetics of calcium dissolution in the bath.

3) *Vaporization of the calcium in the bath*: The vaporization kinetics of the liquid calcium depends on the difference between the saturation vapor pressure (at operating temperature) and the local pressure in the bath. However, the phase transition cannot take place without the presence of nucleation sites. The solid inclusions present in the liquid steel bath act as a nucleation site for a phase transition. The correct description of the vaporization of calcium is essential for estimating the mixing phenomenon inside liquid steel. In brief, it can be said that the modeling of phase change is a complex subject that needs the attention of the researchers.
4) *Dissolution of calcium in the bath:* The dissolution of calcium in liquid steel is done in several stages. Initially, calcium reacts with oxygen and sulfur present in liquid steel bath to form calcium oxide and calcium sulfide, respectively. Lu et al. [4] [5] have shown that the kinetics of calcium transfer in bath strongly depends on the initial activities of oxygen and sulfur in steel. The formed species (CaO, CaS) are transported by diffusion and convection in liquid steel. The transfer of calcium in solution is limited by the renewal of the boundary layer at the interface (diffusion-convection of species) because calcium has very high reactivity with sulfur as well as with dissolved oxygen. The specific area of exchange imposed by the size of the droplets/bubbles of calcium is also a determining factor of transfer efficiency. This is explained further in the next chapter.
5) *Modifications of the inclusions present in the steel:* The transformation of the solid inclusions into liquid calcium aluminates have been widely studied. The equilibrium state of these inclusions depends mainly on the concentration of the oxygen, sulfur, and calcium content in the steel bath [6] [7] [8]. From the literature, it has been found that the kinetics of the transformation of inclusions mainly depend on their initial size. The mobility of the inclusions is also a function of their size. The larger ones experience the buoyancy force and quickly reach the slag while the smaller ones tend to follow the flow of the steel. The presence of slag and refractories also change the composition of the inclusions. It seems that the treatment of steel by calcium depends on the following parameters:
   - the initial composition of liquid steel;
   - the kinetics of calcium dissolution and transport of dissolved calcium in forms of oxide or sulfide;
   - the phase change of the calcium in the bath;
   - the kinetics of the transformation of inclusions.

If the calcium treatment is done properly, it can lead to the following advantages:

- it limits the plugging of the nozzle of ingot molds;
- it reduces the surface defects;
- improves machinability;
- makes the steel less vulnerable to crack.

Industrial complications concerning calcium treatment are explained in the following section.

1.4 Industrial problem

As explained earlier, calcium treatment has the benefit of modifying the composition, shape, and size of inclusions. However, it gives very irregular results in terms of calcium recovery. Figure 1-5 shows the different yields obtained for the same operating conditions (yield is the ratio between the amount of calcium effectively recovered in liquid steel and the amount of calcium introduced inside liquid steel).

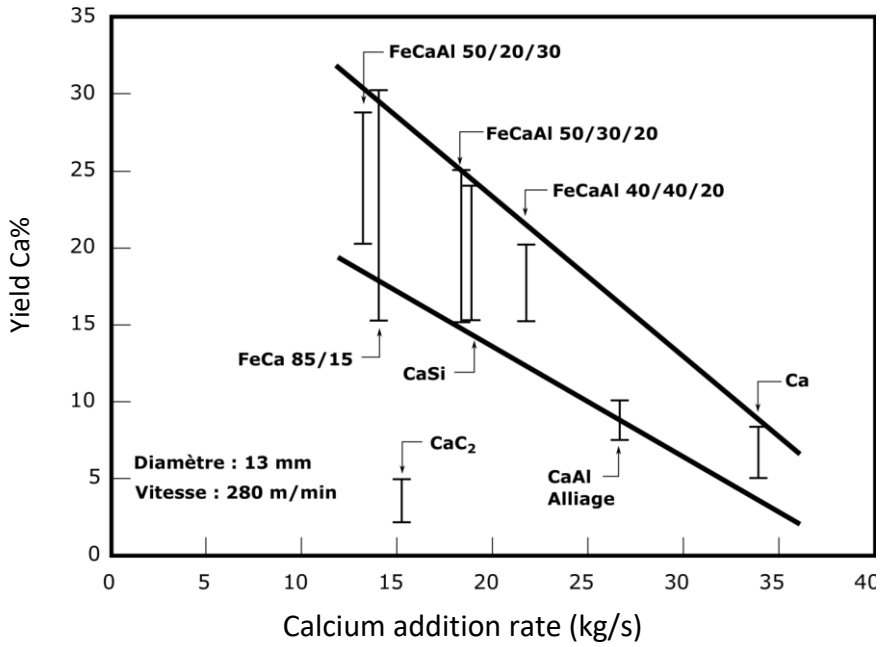

Figure 1-5 Calcium yield, dependent on the calcium addition rate for different cored wire fillings [9]

The above figure shows the achieved results in terms of calcium yield, depending on its addition rate. According to what is illustrated in Figure 1-5, an increase in the rate of calcium addition leads to a distinct reduction in the calcium yield, i.e., reduced calcium consumption. Results of the use of calcium, CaC_2, and CaSi under comparable conditions are shown for comparison purposes. The addition of CaC_2 cored wire does not match with the other results. The reason is an entirely different solution behavior of CaC_2 in a steel melt, compared to that of the other calcium-containing fillings. Therefore, it is difficult to predict the dissolution of calcium in liquid steel.

Even excess addition of the calcium in the melt with high sulfur results in the formation of solid calcium sulfide, which precipitates, and clogs the nozzle during the continuous casting. It can be seen in Figure 1-6 that there is a window for calcium addition in liquid steel so that it can form liquid oxides. Otherwise, there is a possibility of formation of CaS if excess addition is done and the formation of solid or partly solid oxides if insufficient calcium addition is done.

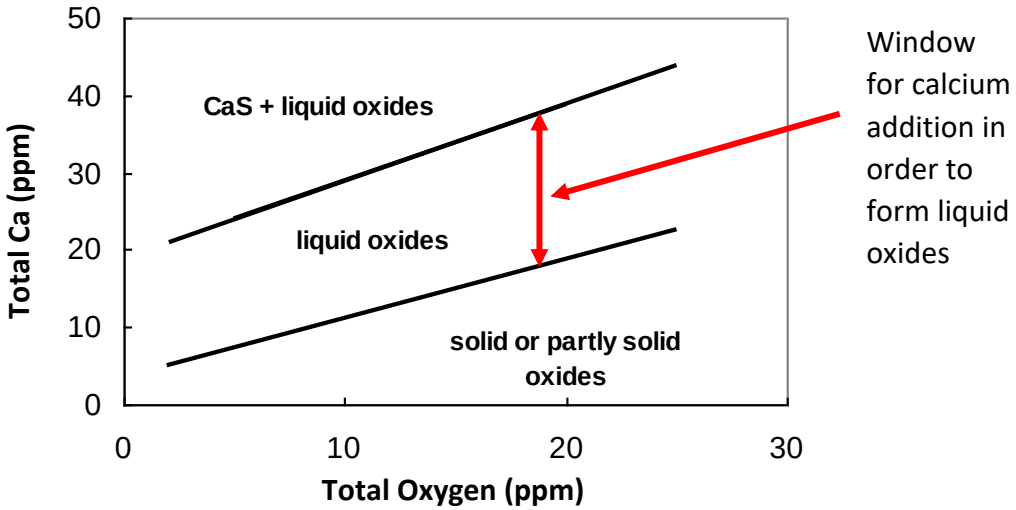

Figure 1-6 Formation of liquid oxides are delimited by the range shown in red

The consequences of uncontrolled calcium treatment are of different natures:

- CaS clogging for the steels with high residual Sulfur: Tiekink et al. [10] showed that the deposit responsible for the blockage of steel consists of a matrix of monocalcium hexa-aluminate ($CaO.6Al_2O_3$), which is in the form of solid at 1600°C.
- Calcium reacts with refractory elements, such as dolomite, to produce solid inclusions of $CaO\text{-}Mgo\text{-}Al_2O_3$. It's negative effect on the casting of steel is similar to those of solid alumina inclusions. This reduction is the result of the higher affinity of calcium with oxygen than most of the other elements used in steelmaking.
- Re-oxidation of the steel to the metal-slag interface: The re-oxidation of the steel results in the formation of monocalcium hexa-aluminate ($CaO\text{-}MgO\text{-}Al_2O_3$) solid inclusions. These inclusions tend to clog the nozzle more easily than the solid clusters of pure alumina.

Uncontrolled calcium treatment in the steel can pose severe problems in the steel as explained above. Therefore, there is a need to understand the dissolution mechanism of calcium in liquid steel finally.

The phenomenon of calcium treatment of steel remains a challenge in the steel making industry. Due to this very reason, all worldwide players of the steelmaking industry are looking forward to figuring out and investigate this well-known problem. The investigation demands research both based on experiments and if possible, with the help of numerical methods. Computational fluid dynamics (CFD) could be one way of exploring this complex physical problem. In fact, in certain cases, CFD can be used as a substitute for costly experimental setups. It can provide deep insights into the phenomena which are difficult to be monitored by the experiments. Therefore, the present study of calcium treatment of steel will cover two aspects: first is the experimental study, and the second one concerns the numerical modeling. Experiments are performed to estimate the mass transfer of calcium in liquid steel. A comparison of the experimental results with the numerical results (e.g., calcium retention in liquid steel) will help us to validate the numerical model developed and subsequently will

allow us to propose new measures to control the process parameters. In the numerical model developed, we will only deal with the dissolution of calcium in liquid steel without taking into account the formation of inclusions.
The next chapter illustrates the literature survey on calcium treatment and the description of the experimental and numerical approach is explained in the later chapters.

1.5 Résumé Français

Ce chapitre constitue l'introduction de cette thèse effectuée entre le centre de recherche ArcelorMittal de Maizières-les-Metz et l'Ecole Centrale de Nantes (ICI lab). Le sujet de thèse est l'étude expérimentale et numérique du traitement inclusionnaire de l'acier par injection de calcium. Un résumé des différentes étapes du processus de fabrication de l'acier est présenté. De nombreuses étapes intermédiaires pour le traitement de l'acier brut sont nécessaires pour produire un produit final de haute qualité, adapté à l'utilisation moderne. Afin de développer un acier avec une faible teneur en inclusions non métalliques (principalement de type alumine), une étape primordiale est étudiée : celle du traitement inclusionnaire de l'acier par injection de calcium. A la température du bain, le calcium est stable à l'état gazeux, ce qui rend la maîtrise de la quantité de calcium absorbée par la poche difficile. Le contexte industriel de traitement calcium est expliqué ci-dessous.

En sortie de convertisseur, l'acier possède une teneur importante en oxygène. L'activité de l'oxygène est généralement réduite par addition d'aluminium. Cette addition, à la température du bain, est responsable de la formation d'inclusions solides d'alumine. Ces inclusions s'ajoutent aux inclusions solides d'oxydes (SiO_2, MnO) déjà présentes. L'addition de calcium permet de transformer ces inclusions solides en inclusions liquides à la température du bain ce qui présente de nombreux intérêts :

- Limitation du bouchage des busettes de lingotières.
- Réduction de l'occurrence de défauts de surface liés à la propreté inclusionnaire.
- Amélioration de l'usinabilité.
- Réduction de la vulnérabilité à la fissure.

Cependant, l'addition de calcium donne des résultats très irréguliers en termes de rendement du calcium. Même si de nombreux efforts ont été déployés pour comprendre le comportement du calcium dans l'acier liquide, ce comportement n'a pas encore été prédit avec précision. Une addition excessive de calcium dans la masse fondue peut entraîner la formation de sulfure de calcium solide, ce qui pourrait entraîner un colmatage précoce de la buse. Au contraire, une faible quantité de calcium transférée à l'acier peut encore accentuée la coulabilité. Par conséquent, le mécanisme par lequel le calcium se dissout dans la masse fondue et transforme les inclusions solides doit être compris pour optimiser les conditions de traitement telles que la vitesse d'injection, la profondeur d'injection, le diamètre du fil d'injection, le temps d'agitation, etc.

Afin de comprendre le mécanisme de dissolution du calcium dans l'acier liquide, la thèse est divisée en deux parties, une expérimentale et une autre numérique. L'objectif est de confronter les résultats expérimentaux avec les résultats numériques. La comparaison des données numériques avec les résultats expérimentaux aidera à valider le modèle numérique développé et permettra ensuite de proposer de nouvelles mesures pour contrôler les paramètres du processus.

Chapter 2:

Literature Survey on Calcium Treatment

2 Literature Survey on Calcium Treatment

The present chapter provides deep insights into the calcium treatment at the experimental as well as at the industry levels. As explained in chapter 1, the major objective of calcium treatment in steelmaking is to improve product performance through inclusions modification. In order to do so, solid alumina inclusions are transformed to liquid calcium aluminates, so that they do not clog the nozzle. Thus, calcium addition has several positive effects:

- it transforms the shape and nature of the remaining inclusions which are less detrimental to the mechanical properties of the final product;
- the transformed inclusions are easier to remove by floatation thus reducing the total number of inclusions remaining in the steel;
- calcium breaks up interdendritic Al_2O_3 galaxies into fine type-III inclusions [11]. These particles remain in the steel through solidification, but they do not tend to clog the continuous nozzles. In addition, their globular shape is retained even during hot rolling, and the resulting absence of stringer or pancake inclusions give steel more uniform properties in all directions.

Calcium is injected in the steel at a temperature around 1550°C or 1600°C depending upon the type of steel to be produced. Since the boiling point of calcium is 1480°C (2716°F) at the atmospheric pressure, it exists as a vapor state at the steelmaking temperatures. Therefore, special measures are taken during the addition of calcium in liquid steels to ensure their proper recovery in the steel bath.

When calcium is injected at a certain depth, it is under a high external pressure, which increases its boiling point. The calcium vapor pressure and its dependence on temperature can be calculated from the equation (2.1):

$$\log P_{Ca}(atm) = -\frac{8082}{T} + 4.579 \quad (1000 - 2000K) \tag{2.1}$$

The vapor pressure of calcium [12] at three different temperatures can be seen in the table below.

Temp °C	Vapor pressure (atm)
1550	1.4
1600	1.846
1650	2.31

Table 2-1 Variation of the vapor pressure of calcium with temperature.

Ferro-static pressure at different ladle heights is shown in Figure 2-1 (density of liquid steel is supposed to be 7200 kg/m^3):

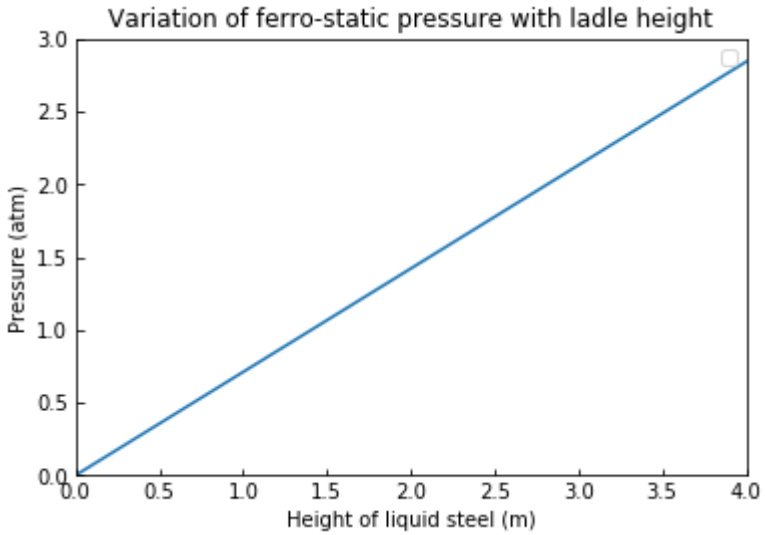

Figure 2-1 Ferro-static pressure variation with ladle height.

From Figure 2-1, it can be inferred that the vapor pressure of calcium, at the calcium treatment temperatures of 1550°C and 1600°C, is 1.4 atm and 1.8 atm respectively. If the calcium is released at a depth of more than 2 meters for the operating temperature of 1550°C then the loss of the burning of calcium can be minimized as the Ferro-static pressure will be higher than the vapor pressure of calcium. The same is true if the calcium is released at a depth of more than 3 meters for the operating temperature of 1600°C.

Wire penetration depth for aluminum wire injection can be obtained from an equation given by Mucciardi et al. [13] as follows:

$$d_p = \frac{145.4 \times d_w^{0.86} \times V_w^{0.52}}{SH^{0.34}} \quad (2.2)$$

Where d_p is wire penetration depth in the melt, d_w is the diameter of the wire, V_w is the wire feeding velocity, and SH is the superheat of the molten steel. Once the calcium is injected in liquid steel, subsequent chemical reactions take place which is explained further below.

According to Cicutti et al. [14], the added calcium reacts with solid Al_2O_3 inclusions generating calcium aluminates of lower melting point. Some of the calcium may also react with the dissolved sulfur resulting in the formation of CaS or Ca-MnS inclusions. Aluminates with high Al_2O_3 content or CaS inclusions are solid at steelmaking temperatures promoting nozzle blockage. Moreover, with the addition of calcium, the fraction of CaO content in the inclusions increases and the liquidus of the inclusions decreases until the composition percentage alters to approximately 50% CaO and 50% Al_2O_3 (Figure 1-2). To summarize, mainly two types of inclusions are formed after the calcium addition: calcium aluminates and sulfides of calcium and manganese. Between CaS and MnS inclusions, CaS is soluble in calcium aluminate liquid and therefore it is preferred over MnS inclusions.

Calcium, when introduced in steel, can be represented by the following series of reactions [15] [16]:

$$Ca(l) \rightarrow \{Ca(g)\} \quad \text{(i)}$$

$$\{Ca(g)\} \rightarrow [Ca] \quad \text{(ii)}$$

$$[Ca] + [O] \rightarrow (CaO)_{inc} \quad \text{(iii)}$$

$$[Ca] + [S] \rightarrow (CaS)_{inc} \quad \text{(iv)}$$

$$[Ca] + \left(x + \frac{1}{3}\right)(Al_2O_3)_{inc} \rightarrow (CaO.Al_2O_3)_{inc} + \frac{2}{3}[Al] \quad \text{(v)}$$

$$(CaO)_{inc} + \frac{2}{3}[Al] + [S] = (CaS)_{inc} + \frac{1}{3}(Al_2O_3)_{inc} \quad \text{(vi)}$$

$$[MnS] + 2[O] + [CaSi] \rightarrow (CaS)_{inc} + (SiO_2)_{inc} + [Mn] \quad \text{(vii)}$$

In the above equations, the square brackets denote the elements dissolved in steel melt, the curly bracket denotes the Ca in the gas phase and the round brackets denote the components dissolved in liquid slag inclusions.

One of the critical concerns is whether or not, added calcium will react with sulfur, like in reaction (iv) and form CaS or will modify Al_2O_3 to liquid calcium aluminate inclusions as described by reaction (v). The formation of CaS can occur if calcium and sulfur contents are sufficiently high. Since calcium has a higher affinity for oxygen than sulfur, the addition of calcium initially results in the conversion of alumina into calcium aluminates until the addition of calcium continues which results in the formation of calcium sulfides. For steel with low sulfur content, reaction (v) will first take place, followed by reaction (vi). At low calcium contents, calcium aluminates contain a high percentage of Al_2O_3 and exist in solid or partially solid form. As calcium content is increased, the percentage of CaO is also increased, and the aluminates become liquid.

During calcium treatment, dissolved calcium may react with sulfur, as explained above, to form solid CaS, which may also cause nozzle blockage. It seems that the condition to avoid CaS precipitation before the formation of liquid Ca-aluminates largely depends on the composition of Ca-aluminates, rather than the temperature for given steel. It is not a very effective way to inject calcium for sulfide modification at high sulfur levels. A significant amount of calcium is required to lower the sulfur level. Such a reaction cannot proceed because excessive calcium injection could generate a high vapor pressure, and given calcium has a high affinity to oxygen. The reaction of calcium with oxygen is favored over a reaction with sulfur. It will lead to poor steel cleanliness due to the formation of CaO and precipitation of sulfur as MnS inclusions during solidification. Therefore, for the steel products, where MnS inclusions need to be avoided, it is important to first reduce the sulfur level to a low value before calcium treatment. It is important to note that before calcium treatment, the activity of oxygen in the melt should also be reduced to a low level. This is done to avoid unnecessary formation of CaO inclusions and to utilize the injected calcium effectively to modify alumina and sulfide inclusions.

The transformation kinetics of inclusions are very fast and are not the limiting step in the calcium treatment. Instead, the mass transfer of calcium in liquid steel is the rate determining step. Therefore, different mechanisms concerning the mass transfer of calcium in liquid steel are studied and are explained further below.

2.1 Physical absorption

The dissolution of calcium in liquid steel can be explained by physical absorption or by chemical absorption. In physical absorption, a negligible chemical reaction takes place in the gas-liquid film (calcium gas-liquid steel interface) while chemical absorption is accompanied by the chemical reaction in the gas-liquid film. Chemical absorption results in the enhancement of absorption of gas in the liquid medium.

Dennis Lu [17] in his thesis, explained the physical absorption of calcium gas in liquid steel (gas-liquid mass transfer). If we consider the transport through the gas-liquid film boundary, two resistances are experienced at the interface. The first is the gas phase resistance, and the second is the liquid phase resistance. The absorption rate at the interface is expressed as [17]:

$$N = N'Z = \frac{K_G Z}{RT}(p - p_i) = K_l Z(C_A^z - C_A) \quad \textbf{(2.3)}$$

Where Z is the interfacial area between gas and the liquid per unit volume of the system, N' is the average rate of transfer of gas per unit area, p and p_i are the partial pressure of soluble gas in the gas bulk and at the interface, C_A^z is the concentration of dissolved gas corresponding to equilibrium with p_i, and C_A is the average concentration of dissolved gas in the liquid bulk. K_G is the gas side mass transfer coefficient, and K_l is the physical liquid side mass transfer coefficient. In the following subsections, the mass transfer rate through respective phases (liquid and gas phase) are discussed.

2.1.1 Liquid phase control

The following relation gives the mass transfer rate through the liquid boundary layer:

$$N = K_l Z(C_A^z - C_A) \quad \textbf{(2.4)}$$

The mass transfer coefficient K_l depends on the type of gas formed, including its geometry and velocity.

For a spherical bubble, Higbie's penetration theory can be applied to obtain the approximate liquid side mass transfer coefficient [18]:

$$K_l = 2\left(\frac{D_L}{\pi\theta}\right)^{\frac{1}{2}} \quad \textbf{(2.5)}$$

where D_l is the diffusivity in the liquid and the "lifetime" θ is the time of exposure for a part of liquid to gas bubble. It is given by the ratio of length of bubble spherical surface to mean velocity of bubble.

The theoretical value of the mass transfer coefficient obtained by different authors, by assuming potential flow over the upper surface (front part) of the bubble is [19] [20] [21]:

$$K_{lf} = 0.951 g^{0.25} D_L^{0.5} d_E^{-0.25} \quad (2.6)$$

In the above equation, K_{lf} represents the front side mass transfer coefficient, g represents the acceleration due to gravity and d_E being the equivalent bubble diameter. Webber [21] used penetration theory to relate the mean mass transfer rate from the rear part of bubble:

$$K_{lr} = 0.29 g^{0.25} D_L^{0.5} d_E^{-0.25} \quad (2.7)$$

K_{lr} represents the rear side mass transfer coefficient of the bubble.

2.1.2 Gas phase control

The mass transfer rate through the gas phase boundary is given by [16]:

$$N' = K_G (C - C_G^z) \quad (2.8)$$

Where C and C_G^z represent the concentration in the gas phase and on the surface of the gas, respectively. K_G is the gas side mass transfer coefficient.

2.1.3 Mixed control

In the case, where we have gas and liquid phase mixed control, the overall transfer rate is given by [16]:

$$N' = K_l \left(1 + \frac{K_H K_l}{K_G}\right)(C_l^G - C_l) \quad (2.9)$$

$$= K_{ovl}(C_l^G - C_l) \quad (2.10)$$

Where K_{ovl} is the overall or the mixed mass transfer coefficient, K_H is Henry's equilibrium constant for calcium dissolution reaction, K_G is gas-side mass transfer coefficient, and K_l is the liquid side mass transfer coefficient. The concentration in the gas phase (C_G) is converted to the equivalent liquid concentration C_l^G by:

$$K_H = \frac{C_l}{C_g^l} \quad (2.11)$$

Previous studies showed that calcium solubility, 0.024% (C_l= 21.6 mol/m^3) in liquid steel is in the equilibrium with 1 atm of pure Calcium gas. The value of C_l^G is obtained as 6.5 mole/m^3 [17]. Therefore, by putting the value of C_l^G and C_G in equation (2.11), K_H is calculated to be 3.32 [17].

No experimental investigations have been performed to determine the gas phase mass transfer coefficient. However, the coefficient can be estimated by assuming that the circulation within the bubble is the same as the liquid phase circulation [22], which leads to:

$$\frac{K_l}{K_G} = \left(\frac{D_l}{D_G}\right)^{0.5} \quad (2.12)$$

Using the estimates of $1*10^{-4}$ m^2/s for the diffusivity of calcium in argon from Chapman Enskog theory (D_G) and $3*10^{-9}$ m^2/s for the diffusivity of calcium in liquid steel (D_l,), the ratio of the mass transfer coefficient is estimated as:

$$\frac{K_G}{K_l} = 547.33 \tag{2.13}$$

Putting the obtained value in equation (2.9), one finds,

$$K_{ovl} \approx K_l \tag{2.14}$$

Hence, it can be concluded that the overall mass transfer step is mainly controlled in the liquid phase. As of now, we have studied the mass transfer associated with the physical absorption, and now we move towards the mass transfer associated with the chemical absorption mechanism.

2.2 Chemical absorption of calcium

Lu et al. [23] observed that calcium absorption in liquid steel is enhanced by high sulfur and oxygen contents in liquid steel. When calcium is injected in liquid steel, most of it gets vaporized into the argon atmosphere. The remaining dissolves in liquid steel through gas-liquid boundary where it is met by oxygen and sulfur which accounts for most of the de-sulfurization and de-oxidation.

2.2.1 Calcium dissolution

It is well known that the mass transfer of calcium in liquid steel depends on the interfacial area however it was found that it depends on the sum of sulfur and the oxygen content in the melt too [23]. During calcium injection, calcium dissolves through the gas-liquid boundary and interacts with the oxygen and sulfur diffusing towards the gas-liquid interface. The concentration profiles are shown schematically in Figure 2-2. C_S, C_O, C_{ca} represents the sulfur, oxygen, and calcium concentration, respectively. It is in the liquid film (δ_L) that these fluxes meet and the reaction between calcium, sulfur, and oxygen takes place. Strong calcium de-oxidation and de-sulfurization reaction in the liquid film result in the elevated slope and faster mass transfer rate. This explains the enhancement of calcium absorption by higher initial sulfur and oxygen contents in the melt. The effective thickness, δ_r for the reaction plane is determined by the equity of fluxes, which can be described by equation (2.15).

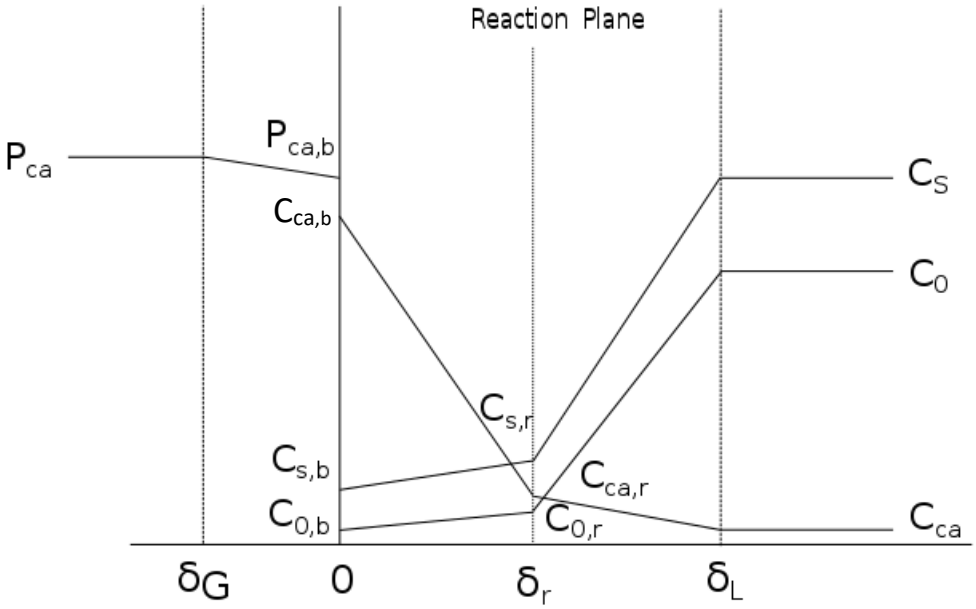

Figure 2-2 The instantaneous reaction mechanism for calcium dissolution with its chemical reactions with oxygen and sulfur at a reaction plane in the liquid plane **[23]**

$$\frac{\boldsymbol{D_o(C_o - C_{o,r})}}{\boldsymbol{(\delta_L - \delta_r)}} + \frac{\boldsymbol{D_s(C_s - C_{s,r})}}{\boldsymbol{(\delta_L - \delta_r)}} = \frac{\boldsymbol{D_{ls}(C_{ca,b} - C_{ca,r})}}{\boldsymbol{\delta_r}} \qquad \textbf{(2.15)}$$

Flux of oxygen Flux of Sulfur Flux of calcium

In the above equation, D_O is the diffusivity of oxygen, D_S is the diffusivity of sulfur, and D_{ls} is the diffusivity of calcium in liquid steel, respectively.

2.3 Calcium vaporization kinetics

Y.Higuchi et al. [24] found that the calcium dissolved in the melt reacts rapidly with alumina inclusions to form calcium aluminate or calcium sulfide. The content of CaO and CaS in the inclusions decreases gradually as the dissolved calcium vaporizes and decreases with time. A mathematical model of the kinetics is developed, which takes into account the evaporation rate of calcium and the reaction rate between inclusions and melt. The evaporation rate of calcium from the melt to the atmosphere is written as:

$$-\frac{dC_a}{dt} = K_s A_s C_{ca} \quad (2.16)$$

Where C_{ca} is the concentration of calcium in the melt (%), K_s is the mass transfer coefficient (m/s), and A_s is the interfacial area per melt volume between melt and atmosphere (m^{-1}) respectively. The mass transfer coefficient (K_s) is determined as 0.0075m/s based on the previous work [25].

The reaction rate between calcium in the melt and inclusions is written as:

$$-\frac{dC_{ai}}{dt} = K_i\left(C_{ai} - C_{a,e}\right) \quad (2.17)$$

Where, C_{ai} is the concentration of calcium in inclusions (%), $C_{a,e}$ is the equilibrium concentration of calcium in inclusions, and K_i is the apparent rate constant (s^{-1}).

Machlin [26] applied Higbie's penetration theory [18] to study the calcium vaporization kinetics, and they found that the overall vaporization process for calcium is mainly controlled in the liquid metal phase. More details can be found in the thesis of Dennis Lu [17].

2.4 Conclusion

Different aspects of calcium treatment of steel are presented in this chapter. A correlation between the vapor pressure of calcium with the temperature inside liquid steel is shown. The demonstrated correlation could be useful in calculating the appropriate depth of calcium injection at various operating temperatures to minimize the loss due to the burning of calcium.

A Literature survey showed that the quantity of calcium injected in liquid steel plays a pivotal role in inclusion modification. A too little calcium addition can lead to CA_6 or CA_2 solid inclusions, and too high calcium addition can lead to CaS formation. Both these conditions are not acceptable for the steel castability. Hence, choosing an optimal quantity of calcium injection has vital importance. Also, it is found that the melting point of calcium aluminate inclusions is at a minimum when the composition percentage becomes approximately 50% CaO and 50% Al_2O_3.

Several steps concerning the physical absorption of calcium is explained and it is found that the dissolution of calcium in liquid steel is mainly controlled in the liquid phase.

It is found that the dissolution of calcium in liquid steel not only depends on the interfacial area of calcium in liquid steel but also on the total sulfur and oxygen content in the melt. Sulfur and oxygen present in liquid steel can enhance the dissolution of calcium in liquid steel. Calcium vaporization kinetics has been presented also and it is found that, it is the liquid steel phase which controls the vaporization process too.

Based on this literature survey, we planned our experiments. The experimental apparatus used, methodology, and the experimental results obtained are described in the next chapter.

2.5 Résumé Français

Ce chapitre constitue l'étude bibliographique concernant le traitement de l'acier par addition de calcium. La relation entre la pression de vapeur du calcium et la température dans l'acier liquide est présentée. Cette relation permet de calculer la profondeur du bain au-dessus de laquelle le calcium devient thermodynamiquement stable à l'état gazeux.

Il a également été découvert que la quantité de calcium injectée dans l'acier liquide joue un rôle essentiel dans la modification des inclusions. Une très faible addition de calcium peut conduire à la formation d'inclusions solides de CA6 ou CA2, par contre, une addition très élevée de calcium peut conduire à la formation de CaS. Ces deux conditions ne sont pas acceptables pour la coulabilité. On constate que le point de fusion des inclusions d'aluminate de calcium est minimum lorsque la composition devient approximativement 50% de CaO et 50% de Al_2O3. Comme le calcium et l'oxygène présentent une forte affinité, il faut éviter toute introduction d'oxygène dans l'acier liquide lors du traitement au calcium, car le calcium formerait des inclusions de CaO.

Plusieurs étapes concernant l'absorption physique du calcium sont expliquées. Il est aussi montré que la dissolution du calcium dans l'acier liquide est principalement contrôlée en phase liquide.

L'examen de la littérature a révélé un point important : la dissolution du calcium dans l'acier liquide ne dépend pas seulement de l'aire interfaciale entre le calcium et l'acier liquide, mais aussi des teneurs en soufre et en oxygène du métal. Le soufre et l'oxygène présents dans l'acier liquide peuvent améliorer la dissolution du calcium dans l'acier liquide par la consommation rapide du calcium présent dans la sous-couche visqueuse.

La cinétique de vaporisation du calcium dissout dans le métal a également été présentée et il s'est avéré que c'est la phase de l'acier liquide qui contrôle également le processus de vaporisation.

Chapter 3:

Experimental Methods

3 Experimental Methods

As discussed earlier, calcium treatment due to its necessity is widely performed in the steel-making process. However, there are still disparities in the calcium treatment practices due to the lack of certitudes on the process parameters effect. This chapter presents the experiments carried out to assess the dissolution of both liquid and gaseous calcium in liquid steel. The experimental methodology composes of discharging a given quantity of pure calcium at the bottom of the crucible filled with quiescent liquid steel. The principal aim of the following work is to identify the mass transfer kinetics of calcium in liquid steel to be confronted with the numerical results obtained using the software ICI-tech presented in chapter 4.

As discussed in chapter 1, the dissolution mechanism of calcium in liquid steel isn't well-understood. Therefore studies have been conducted to gain a deeper understanding of the dissolution mechanism of calcium in liquid steel. This study of dissolution mechanism has profound importance as it governs the calcium mass transfer rate in liquid steel. The mass transfer rate of calcium in liquid steel is given by the equation below:

$$\emptyset = K_{ca.ls} S \rho_{ls} (C_{ca} - C_{ca}^{bath}) \quad (3.1)$$

In equation (3.1), $\emptyset$ represents the flux (kg/s), $K_{ca.ls}$ is the mass transfer coefficient between calcium and liquid steel (m/s), S is the surface area of calcium droplet or bubble (m^2), ρ_{ls} is the density of liquid steel (kg/m^3) and $(C_{ca} - C_{ca}^{bath})$ is the concentration difference (ppm) between calcium and liquid steel, respectively. In the quest for a better understanding of the dissolution mechanism, we need to determine the mass transfer coefficient between calcium droplets or bubbles and liquid steel. In order to determine this mass transfer coefficient, the size of the calcium droplets or bubbles, and the total calcium absorbed inside liquid steel needs to be determined. To achieve this objective, experiments are performed at the lab scale where calcium is injected in the induction furnace. The main objectives of these experiments are to:

- determine the total number of calcium droplets or bubbles formed;
- determine the size of the droplets or bubble;
- detect the total calcium absorbed inside liquid steel;
- calculate the average mass transfer coefficient.

In the next section, a description of the experimental approach is explained.

3.1 Experimental set-up

Our experimental device (Figure 3-1) is an induction furnace equipped with:

- crucible of 2.5 kg metal capacity;
- induction coil heater;
- an inert gas injector;
- a sampling device;

- a high-speed camera;
- a dispatcher;
- a capsule release cane.

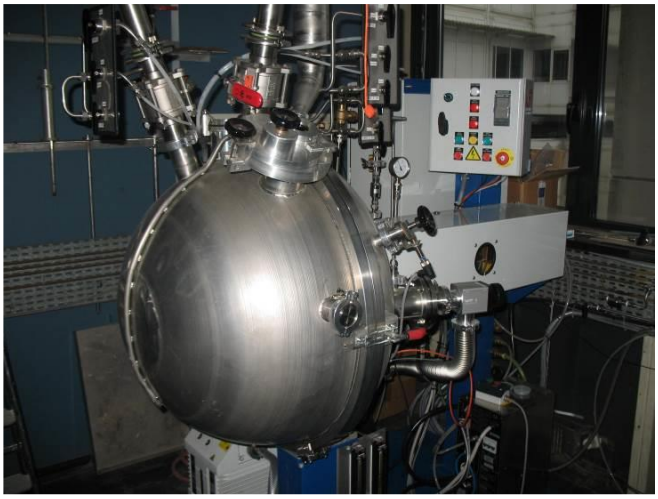

Figure 3-1 Induction furnace equipped with an injection device, sampling, and visualization.

The high-speed camera at the top of the furnace (not visible in Figure 3-1) gives access to the size of the calcium droplets or bubbles arriving at the surface of liquid steel. The sample analysis before and after injecting calcium helps to determine the total calcium absorbed in liquid steel (schematic illustration of the experimental set-up is presented in section 3.2). Inside the furnace, a crucible of 2.5 metal kg capacity (Figure 3-3) is present, which is surrounded by the induction coil heater. It is inside this crucible where stainless steel is melted. Temperature measurement is done either from the top of liquid steel bath with an immersed thermocouple, or it can be done by inserting the thermocouple from the bottom of the crucible. Calcium is injected at a temperature lower than 1484°C if the objective is to observe the calcium droplets at the surface of the liquid, and is injected at a temperature higher than 1484°C if the objective is to observe the calcium bubble. (1484°C is the boiling point of the calcium at atmospheric pressure).

The inside view of the furnace is shown in the figures below (Figure 3-2 & Figure 3-3). Description of the different parts of this experimental set up is detailed further in the text below.

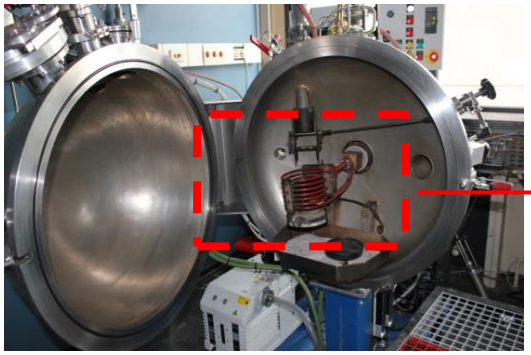

Figure 3-2 Inside view of the furnace.

Figure 3-3 Crucible inside the furnace.

3.2 Experimental scheme

Before going into the details of each part of the experimental setup, let us provide a global overview of the different actions taking place during the experiment. Figure 3-4 shows a schematic illustration of the experimental set-up in which the crucible which has a capacity of 2.5 kg of liquid steel, is surrounded by the induction coils. Temperature measurement is done from the top of the liquid metal bath with an immersed thermocouple. It is essential to have an exact idea about the temperature before injecting calcium, mainly because of safety concerns. Even a small quantity of calcium (~500 mg) above the boiling point of calcium (1484°C) can lead to splashing at the surface of the liquid metal. At the top of the crucible, there is a “camera” to capture the deformation at the liquid metal (steel melt) interface.

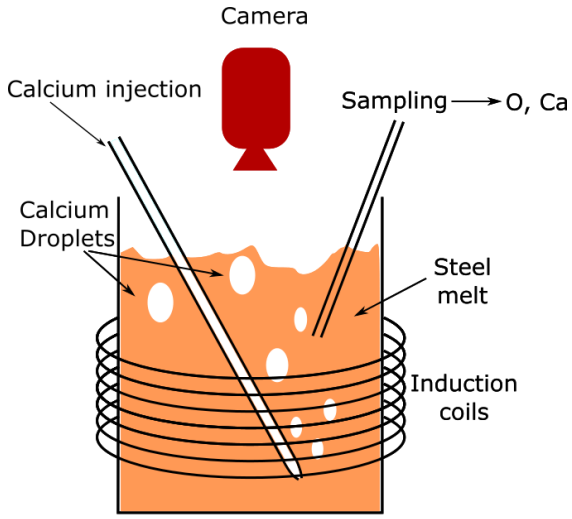

Figure 3-4 Schematic representation of the experimental setup.

Calcium can be injected with the help of a tube inside the liquid metal, as illustrated in Figure 3-4. Another method for injecting the calcium is to drop it in the form of a capsule, as shown in Figure 3-5. In this method, calcium is placed inside a capsule made up of stainless steel (weighted with tungsten), and then it is dropped from the top of the crucible into the molten stainless-steel. Tungsten, due to its high density, allows the capsule to sink deep inside the

liquid metal. Once the capsule reaches the bottom of the crucible, it melts down and henceforth the calcium is liberated in liquid-steel from the capsule. The liberated calcium could be under the form of droplets or bubbles depending on the temperature of liquid steel. Induction coils across the crucible are turned off when the calcium is injected to avoid mixing inside liquid steel while the calcium droplets or bubbles are rising. This method of injecting calcium inside the capsule allows the liberation of calcium from the center of the crucible, and it makes the operation more reproducible. Therefore, this approach is adopted in our experiments. The operation protocols are further explained in the section below.

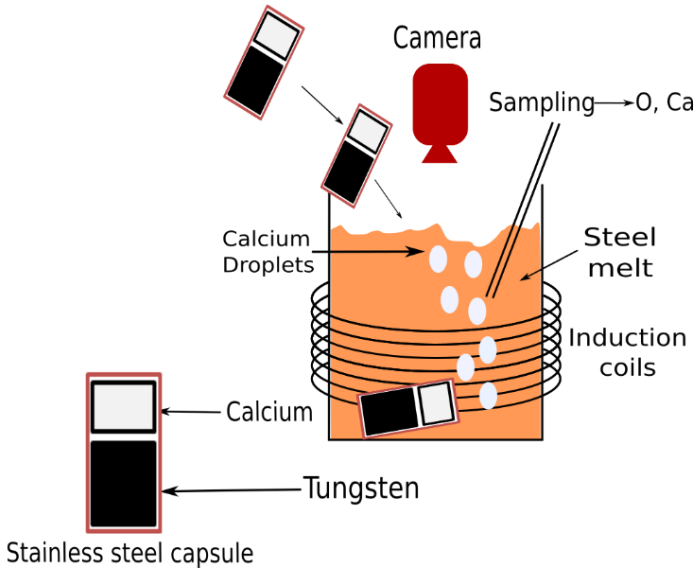

Figure 3-5 Schematic representation of the calcium injection and calcium release procedure.

3.3 Operating protocol

1) *Initial preparation:* Crucible (Figure 3-3) is surrounded by the induction coils, which are used to regulate the temperature of the crucible. To avoid the deterioration of the induction coils through the radiation of the crucible, a coated fibrous sheet of mica (not shown in the figure) is placed around the crucible. The crucible and its protections are brought to 400°C in a heating oven for degassing adhesives. The crucible is placed at the center of the induction coils, on a refractory base allowing vertical positioning, which can be seen in Figure 3-3. Dimension of the crucible used in our experiments is: height of 12cm, the outer diameter of a 10.2cm and inner diameter of 8.2 cm.
2) *Addition of Iron, alloying elements:* Iron and the other alloying metals are added according to the required composition. Carbon is added for the first de-oxidation of the liquid metal bath. 1.5g of carbon is added for 2.5kg of liquid steel (0.5g of carbon is added for each kg of liquid steel). Other elements are added according to the requirements. The addition of the materials is done through a dispatcher that can be

seen in Figure 3-6. 250g of material is allowed to pass through each compartment having a size between 3 to 10 mm.

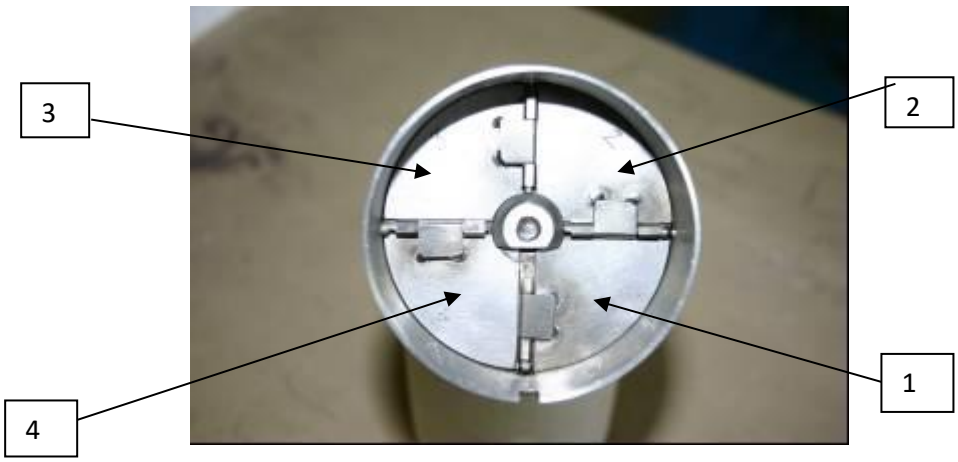

Figure 3-6 Top view of the dispatcher used for materials addition.

Figure 3-7 Assembly of the spillway.

Assembly of the spillway in the dispatcher can be seen in Figure 3-7. The assembly is put into the housing, and then the claws are tightened. The door of the enclosure is closed, and fasteners are put to prohibit the opening of the door.

To have a proper liquid steel bath, solidified stainless steel of required composition can also be considered for experiments. In our experiment, solidified stainless steel is placed inside the crucible and is then melted. This method allowed us to obtain a clear liquid steel bath surface. Solidified stainless steel of type 304 used in our experiments can be seen in Figure 3-8.

Figure 3-8 Solidified Stainless steel (type 304) used for experiments.

The weight of the solidified stainless steel is around 2.6 kg. It has a cylindrical shape with a height of around 6.6 cm. The diameter of the stainless-steel cylinder is taken such that it fits just inside the crucible (diameter = 8cm). The composition of the stainless steel (weight%) used in our experiments is given in Table 3-1.

Si	Mn	Cr	Ni	Al	P	S
0.358	1.87	18.03	8.07	0.008	0.042	0.036

Table 3-1 Composition of the stainless steel.

3.4 Experimental steps

Following are the experimental steps followed:

- Stainless steel (INOX) is put inside the crucible.
- The main switch of the control box, which can be seen in Figure 3-11 (b) is turned on.
- Cooling water, which is circulated across the walls of the furnace, is opened. Then, the water flow meter present at the back side of the furnace is monitored.
- The primary pump (vacuum pump), which can be seen in Figure 3-10 is turned on.
- It is verified that the gas valve is closed when the primary pump is turned on.
- When the primary pump is ON, the system is set under vacuum to decrease the pressure inside the furnace. Manometer, shown in Figure 3-11 (a) shows the pressure inside the furnace. When the pressure is below 0.1 mbar, heating is turned ON, and the power is increased to 15% (power is displayed on the Eurotherm, see Figure 3-11 (b). After about 20 minutes, power is increased to 20%. The power supply is gradually increased to prevent the crucible from getting sudden temperature shock. Sudden temperature shock could be hazardous as it can lead to crucible leakage.
- After about 25 min, the vacuum pump is stopped, the argon valve is opened such that the argon goes into the furnace and slowly the pressure is raised. Argon is injected through the gas valve shown in Figure 3-9. Argon increases the pressure above the liquid/solid metal as well as it helps in maintaining an inert atmosphere. The pressure is increased until it reaches 550 m bar and then the power is increased to 35%.

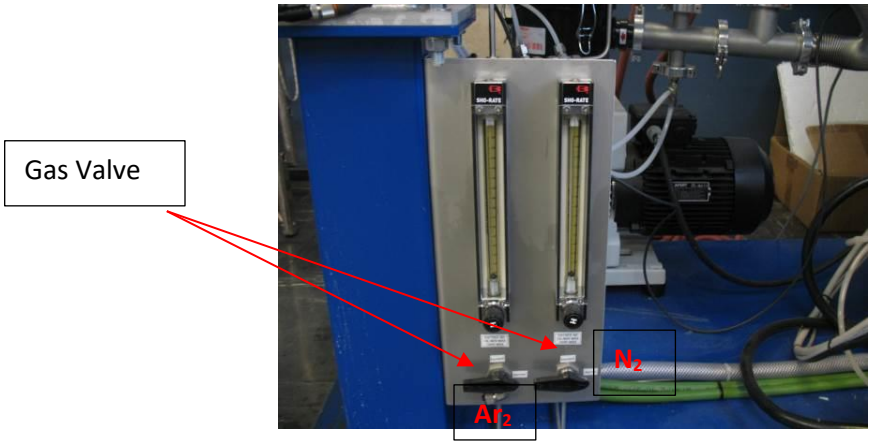

Figure 3-9 Arrivals of argon and nitrogen through the gas valve.

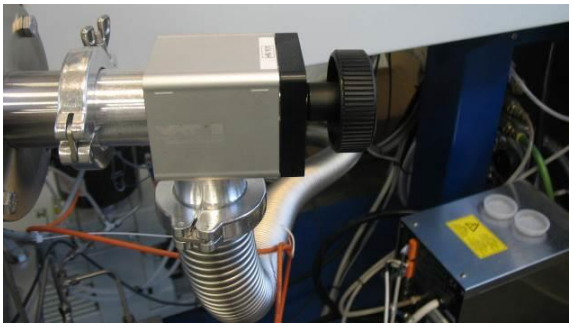

Figure 3-10: Vacuum pump.

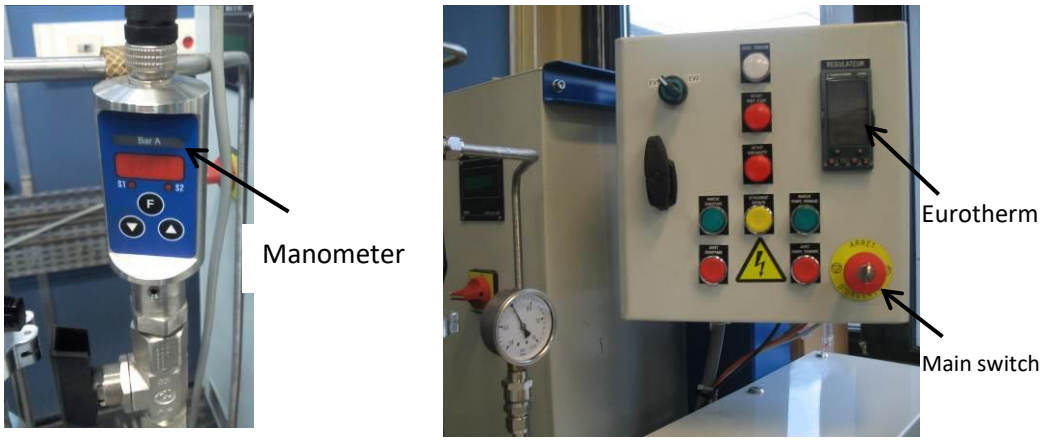

Figure 3-11. (a, b) a shows Manometer and b is the electric box with different controls and temperature display.

- Crucible is allowed to rotate at a certain time interval. It accelerates the melting of the solid stainless steel inside the crucible.
- Once the solid steel is converted into liquid, other desired elements are added step by step with the help of the dispatcher as explained earlier.

- The flow of argon is increased to maintain pressure close to 1 bar (close to atmospheric pressure).
- Sampling is done to analyze the O, N, S, C, and Ca content in the melt. Oxygen content in the liquid metal is controlled because if there is excess oxygen, we might have precipitation of CaO inclusions. It is necessary to do all the sampling above 850 mbar since it facilitates the suction of samples in the tube.
- Sampling is done with the tube, which can be seen in Figure 3-12. At the bottom, there is a quartz tube, and inside this quartz tube, liquid steel is imbibed to be analyzed. Once liquid steel is imbibed, the tube is taken out, and the sampling rod is dismounted to recover the samples in the quartz tube.
- Recovered samples in the quartz tube are then sent for chemical analysis.
- Depending upon the requirement of the oxygen level in liquid steel, de-oxidation is further done. Generally, for de-oxidation, carbon is introduced inside liquid steel. The amount of carbon needed to remove the oxygen in the form of CO_2 is calculated. It is then added in the crucible with the help of the dispatcher. It is advised to introduce the materials at a pressure above 900 mbar. Some time (approximately 10-15 mins) is given for carbon to dissolve in liquid steel before decreasing the pressure to 20 mbar. To increase the de-oxidation, the pressure is further reduced below 20 mbar. Reducing pressure also favors the de-oxidation process.

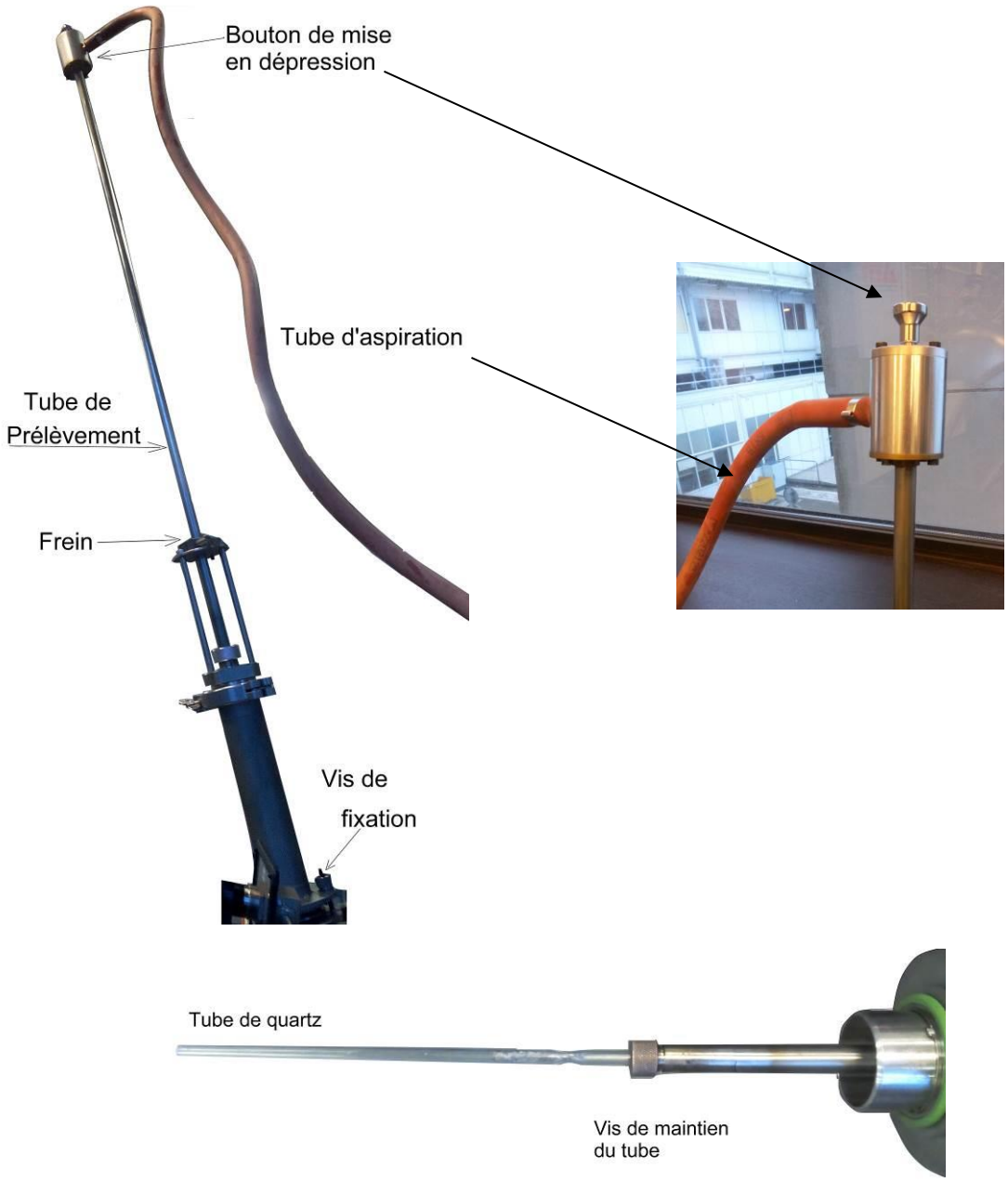

Figure 3-12 Description of the sampling tube used in the experiments.

- Once again, sampling is done to analyze the total oxygen content in liquid steel. If the desired level of oxygen is reached (generally less than 25 ppm in our experiments) then the power on the Eurotherm is adjusted to have the required temperature. For the temperature measurement, there is a thermocouple rod (not shown in figures) by which temperature is measured. Temperature measurement is done at different depth in liquid steel to ensure the thermal homogeneity.
- If the desired temperature is achieved, then calcium is injected.
- One important thing which should be noted is that, during the injection of calcium in liquid steel, the induction coils (inductors) surrounding the crucible should be turned off. By turning off the inductors, we want to get rid of the mixing caused by them. We

want to ensure that liquid steel is stagnant and thermally homogeneous. We are assuming these conditions to simplify the complexity of our numerical model developed.

- Schematic of the calcium injection procedure can be seen in Figure 3-13:

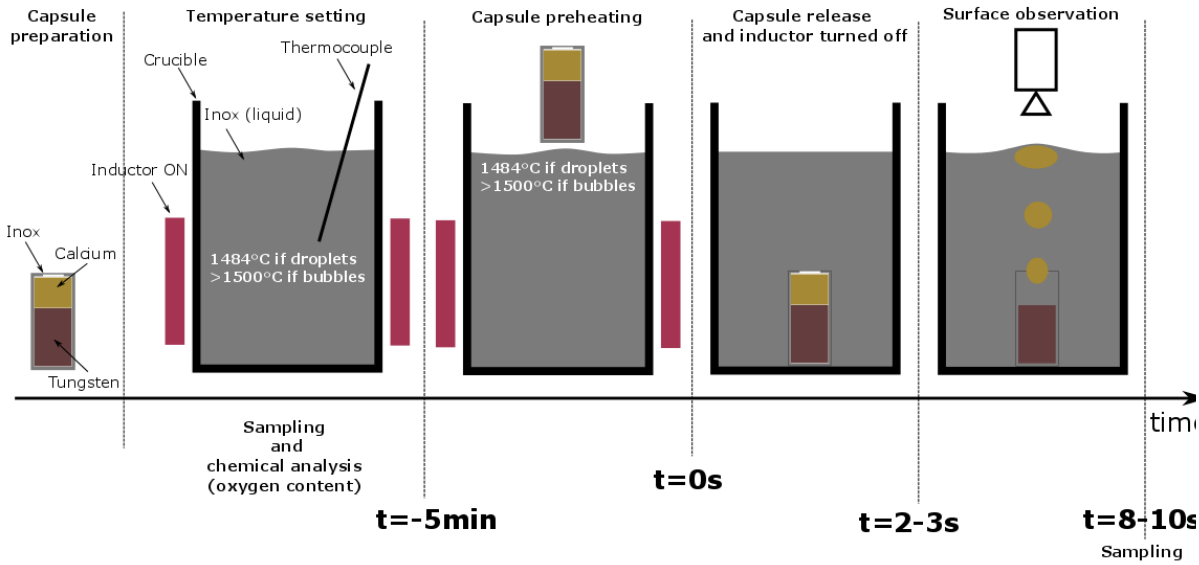

Figure 3-13 Schematic representation of the calcium addition in our lab-scale experimental set-up.

Steps followed during calcium injection can be seen from left to right in Figure 3-13. In the beginning, tungsten is put inside the capsule made up of stainless steel, then calcium is placed above the tungsten, and finally, the capsule is firmly sealed. The capsule used in our experiments is presented in Figure 3-14.

Figure 3-14 Capsule used in the experiments.

In our experiments, capsules of two different dimensions are used depending upon the quantity of calcium to be injected. The dimensions of the two-capsule used are illustrated in Figure 3-15 and Figure 3-16, respectively. The values shown are in millimeters.

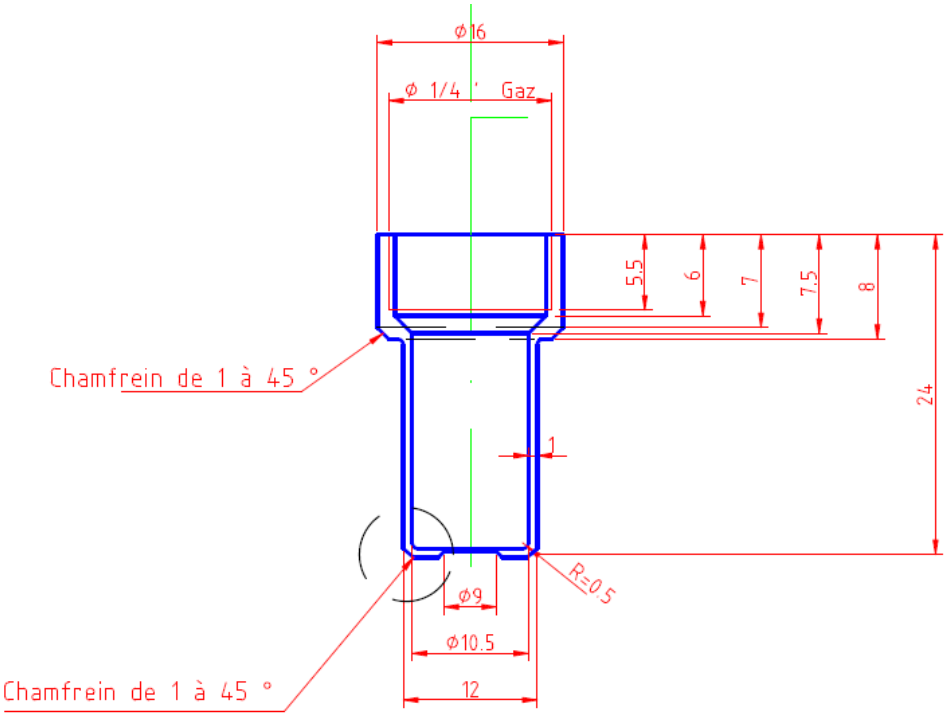

Figure 3-15 Dimension of the capsule used for less than 5g of calcium injection.

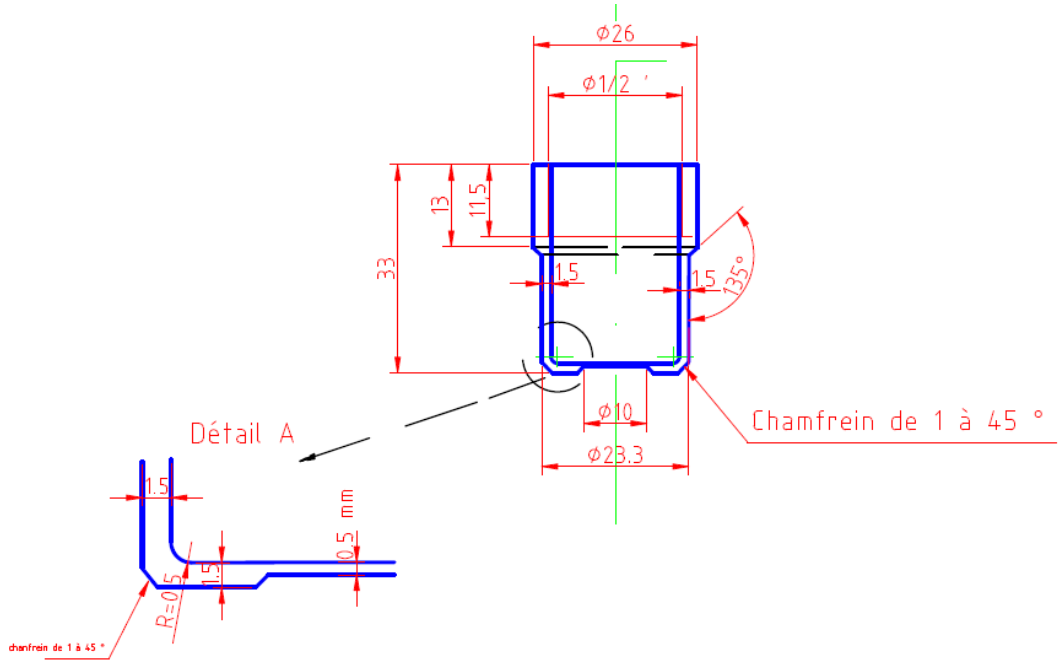

Figure 3-16 Capsule used for 5g and 6g of calcium injection.

The capsule is preheated before being finally dropped inside liquid steel. During preheating, the capsule is allowed to stay above the heated liquid steel for 2 to 3 minutes with the capsule being tied at the beneath of the tube. The objective is to heat the calcium before it is being dropped inside liquid steel so that the phase transformation time from calcium solid to calcium liquid can be reduced. Just before the capsule is dropped inside liquid steel, the inductors are turned off. Once the capsule is dropped, it goes at the bottom of the crucible because of the high density of tungsten inside the capsule. As the temperature of liquid steel is higher than 1450°C, the stainless-steel capsule melts, and calcium gets liberated from the capsule. At the temperature higher than 1450°C, calcium gets transformed into liquid calcium, and calcium droplets are formed because of the interfacial surface tension between liquid calcium and liquid steel. Once being liberated from the capsule, calcium droplet rises at the surface of liquid steel because of the density difference between calcium and liquid steel. As mentioned earlier, at the top of liquid steel, there is a camera (specification: 2000 image/s) that captures the surface deformation. Camera at the top of liquid steel provides two crucial information:

- the approximate size of the calcium droplets or bubbles arriving at the surface of liquid steel;
- the number of calcium droplets or bubbles arriving at the surface of liquid steel.

Another point that must be noted is that the final temperature of liquid steel is adjusted depending on the objective of the experiments. If the objective is to observe the calcium droplets, the experiments are performed at 1480°C. On the other hand, if the objective is to observe the calcium bubbles, then the experiments are performed at a temperature higher than 1484°C. In our experiments, to observe the calcium bubbles, the experiments are conducted at a temperature of 1550°C. Performing experiments at different temperatures helped us to understand the dissolution phenomenon of calcium droplets as well as of calcium bubbles and have encouraged us to validate our numerical model at different operating temperatures. Once the calcium bubbles arrive at the surface of the bath, samples are taken for analysis to know the chemical composition of liquid steel. Sample analysis methods are further explained in the section below.

3.5 Sample analysis

The foremost objective of doing the experiments was to calculate the total absorbed calcium inside liquid steel. Total absorbed calcium is the sum of calcium dissolved and the calcium trapped in the inclusions. Just after the calcium arrival at the surface of the bath, samples are taken in the quartz tube, which is later analyzed chemically. Images of the quartz tube taken for chemical analysis can be seen in Figure 3-17.

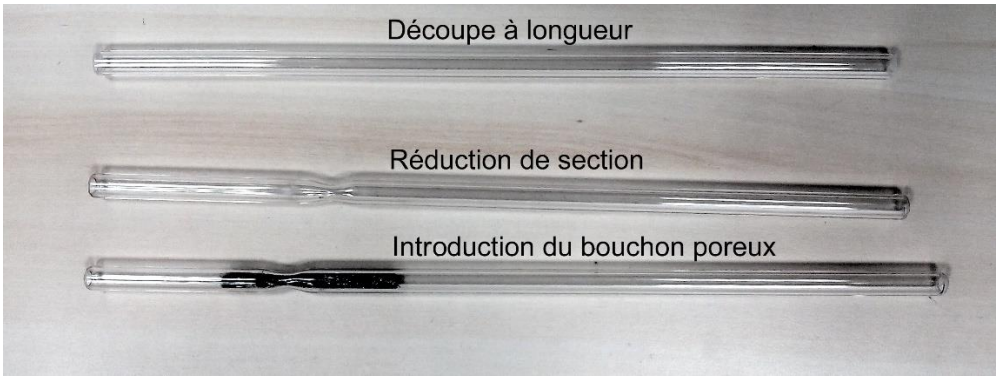

Figure 3-17 Quartz tube used for sampling.

One other way in which the samples are analyzed is that, just after all the calcium arrives at the surface of liquid steel, liquid steel is allowed to get solidified. Then, the ingot is vertically sliced and analyzed by spectrography to determine the total absorbed calcium content. The solidified ingot analyzed by spectrographic analysis can be seen in Figure 3-18.

Figure 3-18 Sample analysis of solidified metal ingots

For analyzing the metal ingots, sparks are given at various points of the plane of ingot and compositions are obtained at these different points. There are several methods to analyze the samples which are explained in the section below.

3.5.1 Spectrographic analysis

The spectrographic analysis is a process in sensor technology in which the chemical elements are determined by measuring the wavelengths or spectral line intensity of a sample of matter. The wavelength or spectral line is obtained in the form of excitation such as infrared. A schematic of the spectrographic analysis is illustrated in Figure 3-19. Spectroscopy is used in physical and analytical chemistry because atoms and molecules have unique spectra. As a result, these spectra can be used to detect, identify, and quantify information about the atoms

and molecules. The measured spectra are then used to determine the chemical composition and physical properties of the substance.

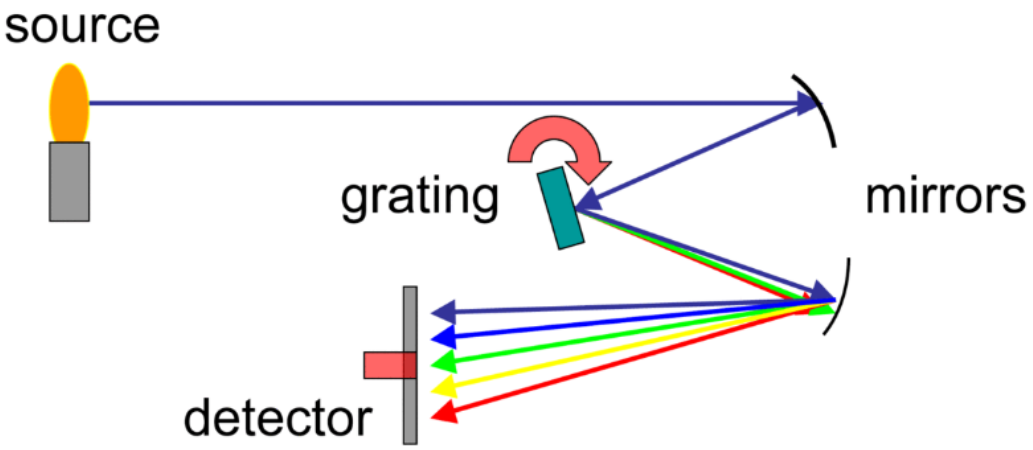

Figure 3-19 Schematic of Spectrographic analysis [27].

Types of spectroscopy are distinguished by the type of radiative energy involved in the interaction. In many applications, the spectrum is determined by measuring changes in the intensity or frequency of this energy. In our case, the source is an electrode with spark, and there is a fiber optic which recovers the emitted rays. An error of around 20% is obtained, which means that, if we get 20 ppm of total calcium absorbed in the steel, there can be an error of ± 4 ppm.

3.5.2 Scan electron microscope

A scanning electron microscope (SEM) is a type of electron microscope that produces images of a sample by scanning the surface with a focused beam of electrons. Generally, it gives information about the calcium inclusions, their size, shape, and topology. The electrons interact with atoms in the sample, producing various signals that contain information about the sample's surface topography and composition. The electron beam is scanned in a raster scan pattern, and the beam's position is combined with the detected signal to produce an image. SEM can achieve resolutions up to 1 nanometer. The schematic representation of SEM analysis can be seen in Figure 3-20.

The most common SEM mode is the detection of secondary electrons emitted by atoms excited by the electron beam. The number of secondary electrons that can be detected depends on specimen topography. By scanning the sample and collecting the secondary electrons that are emitted using a special detector, an image displaying the topography of the surface is created. Since in our study, we were not much interested in the inclusion formations; the scan electron microscope of the samples is not studied in detail.

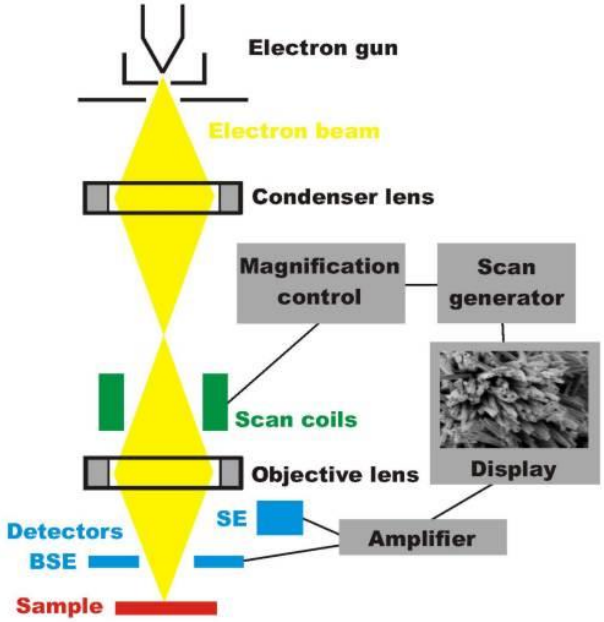

Figure 3-20 Schematic illustration of Scanning Electron Microscope [28].

3.5.3 Atomic emission spectroscopy

Atomic emission spectroscopy (AES) is a method of chemical analysis that uses the intensity of light emitted from a flame, plasma, arc, or spark at a particular wavelength to determine the quantity of an element in a sample. The wavelength of the atomic spectral line gives the identity of the element while the intensity of the emitted light is proportional to the number of the atoms of the element [29]. In our case, the solid samples to be analyzed are first put in acid solution, (HCl (10 ml), HNO_3 (5 ml) and HF (hydrofluoric acid)). The acid solution is soaked up, and then this acidic solution is excited with plasma. The wavelength and intensity of the emitted spectral lines give information about the quantity of the element. The error in atomic emission spectroscopy results varies between ±8 % ppm.

As mentioned earlier, we were interested in studying the mass transfer of calcium in liquid steel, and the mass transfer mainly depends upon the shape of the rising droplet or bubble and their terminal velocity. Therefore, it is important to know the shape of the calcium droplet or bubble and their terminal velocity at a steady state. The next section explains the expected shape regime and the terminal velocity of the rising calcium droplet or bubble in liquid steel.

3.6 Shape regime for calcium droplets and calcium bubbles

Before going into details of what has been observed in the experiments, it is important to have an idea about the regime in which the calcium droplet or bubble lies in the Grace diagram [30]. Grace diagram gives an idea about the shape regime as well as the terminal velocity of the droplet or bubble rising in the liquid medium. In order to place the droplet or bubble in the Grace diagram, Bond number (Bo) and Morton number (Mo) needs to be calculated. Bond number is a dimensionless number used to analyze the cases where two fluids of different densities are in contact and subject to gravity only. It represents the ratio of gravitational force

to the surface tension force. A high value of the Bond number (Bo) indicates that the system is relatively unaffected by the surface tension effects and a low value (less than 1) indicates that the surface tension dominates. Whereas, the Morton number (Mo) is a dimensionless number used together with the Bond number (Bo) to characterize the bubbles or drops moving in a surrounding fluid.

$$Bo = \frac{(\rho_l - \rho_d) g d^2}{\sigma} \tag{3.2}$$

$$Mo = \frac{\mu_l^4 (\rho_l - \rho_d) g}{\rho_l^2 \sigma^3} \tag{3.3}$$

In the above formula, ρ_l is the density of the continuous medium which is liquid steel in our case (ρ_{ls}), ρ_d is the density of the droplet which can be calcium droplet (ρ_{cad}) or calcium bubble (ρ_{cab}), σ is the interfacial surface tension between calcium droplet and liquid steel ($\sigma_{cad.ls}$), in the case of a calcium bubble, it is the interfacial surface tension between the calcium bubble and liquid steel ($\sigma_{cab.ls}$). μ_l is the viscosity of the continuous medium, which is liquid steel (μ_{ls}) in our case, d is the diameter of the calcium droplet (d_{cad}) or calcium bubble (d_{cad}). The properties of liquid steel, calcium droplet, and calcium bubble used for calculating the Bond number (Bo) and the Morton number (Mo) can be seen in Table 3-1.

ρ_{ls}	7200 (kg/m^3)
μ_{ls}	0.005 (Pa.s)
ρ_{cad}	1200 (kg/m^3)
μ_{cad}	0.001 (Pa.s)
$\sigma_{cad.ls}$	1.4 (N/m)
ρ_{cab}	0.5 (kg/m^3)
μ_{cab}	1e-05 (Pa.s)
$\sigma_{cab.ls}$	1.7 (N/m)
g	10 (m/s^2)

Table 3-1 Physical properties of the calcium droplet, calcium bubble, and liquid steel [31] [32].

Antonoff's [33] rule has been applied to calculate the interfacial surface tension between calcium droplet/liquid steel ($\sigma_{ca.ls}$) and between calcium bubble/liquid steel ($\sigma_{cab.ls}$) which predicts that the surface tension between two liquids is equal to the difference between the surface tension of the respective liquids. σ_{ls} (surface tension of liquid steel) and σ_{cad} (surface tension of calcium droplet) is found to be 1.7 N/m and 0.3 N/m at 1480°C [34]. Bond number and the Morton number for different calcium droplet/calcium bubble diameter can be seen in Table 3-2.

d (cm)	Bo (Calcium droplet)	Mo (Calcium droplet)	Bo (Calcium bubble)	Mo (Calcium bubble)
0.1	0.04	2.63e-13	0.04	1.76e-13
0.4	0.68	2.63e-13	0.67	1.76e-13
0.7	2.10	2.63e-13	2.07	1.76e-13
1	4.28	2.63e-13	4.23	1.76e-13
1.3	7.24	2.63e-13	7.15	1.76e-13
1.6	10.97	2.63e-13	10.84	1.76e-13
1.9	15.47	2.63e-13	15.28	1.76e-13

Table 3-2 Bond number and Morton numbers for calcium droplet and calcium bubble.

According to Bond and Morton numbers obtained, we can place the calcium droplet (in red) and calcium bubble (in blue) in the Grace diagram (Figure 3-21), then the dynamics can be predicted like terminal velocity and shape of the rising droplet or bubble.

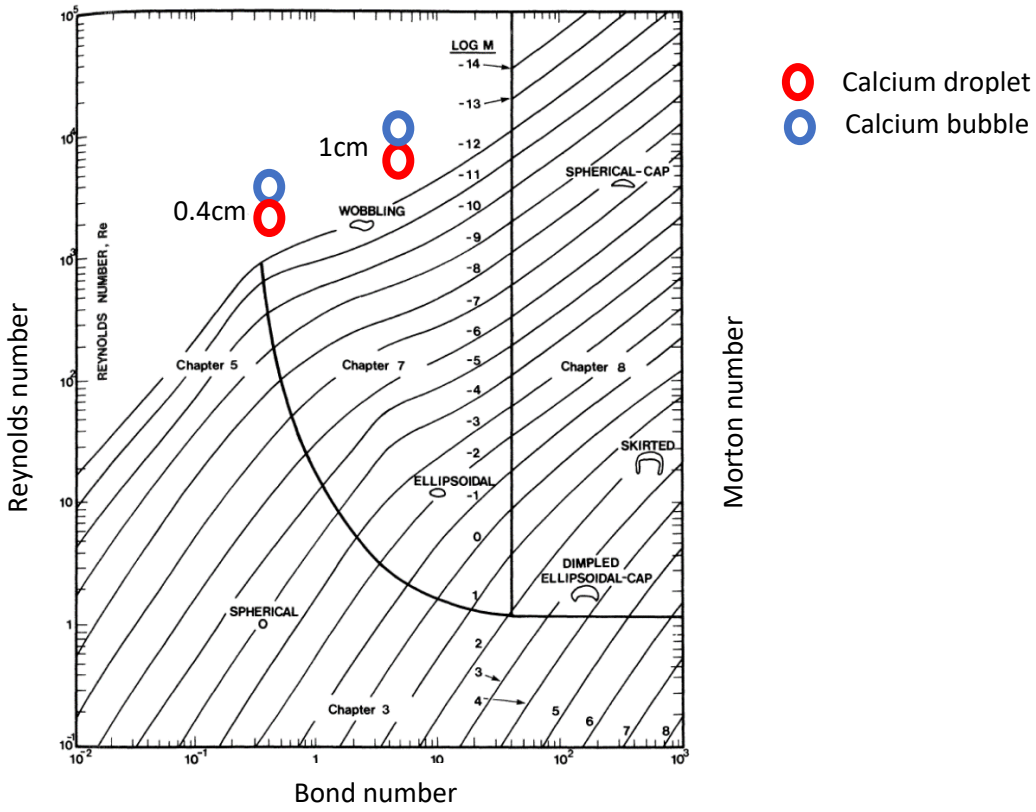

Figure 3-21 Shape regime for bubbles from Clift et al. [30]. Our typical Ca droplets are shown in red and typical Ca bubbles in blue.

3.7 Calcium droplet, bubble terminal velocity

Rising of a droplet or bubble in a viscous fluid under the influence of gravitational forces can [30] be grouped into three regimes (Figure 3-21): spherical, ellipsoidal and spherical cap as described in [30]. However, the transition from different regimes is not clearly defined. L.

Bower et al. [35] presented a brief description of the transition between different regimes. Different regimes and their respective terminal velocity are presented below:

Spherical regime: The size of the bubble is usually small, less than 1.5mm in this regime, and it is dominated by the surface tension and the viscous force. As the size of the bubble/droplet increases, the terminal velocity is increased. The terminal velocity is given by Hadamard [36] and Rybczynski [37] as:

$$u_t = \frac{g d^2 \Delta\rho (1 + K_1)}{6\mu_l (2 + 3K_1)} \tag{3.4}$$

Where d is the diameter of droplet or bubble, $\Delta\rho$ is the density difference between droplet/bubble and liquid medium, μ_l is the viscosity of the liquid medium and $K_1 = \frac{\mu_{bd}}{\mu_l}$. Here μ_{bd} represents the viscosity of droplets or bubbles. It should be noted that this correlation is valid for very low Reynolds number ($Re < 1$).

Ellipsoidal regime: The ellipsoidal regime is dominated by the surface tension and Bond number (Bo) lies between 0.25 and 40. The final shape is generally oblate with the convex interface, and terminal velocity in this regime is given by Mendelson [38] based on wave theory as:

$$u_t = \sqrt{\frac{2.14\sigma}{\rho_l d} + 0.505 g d} \tag{3.5}$$

Where σ is surface tension (to be more precise interfacial surface tension), ρ_l is the density of the liquid medium, d is the diameter of droplet or bubble, and g be the acceleration due to gravity.

Spherical cap regime: This regime is driven by inertial force. Bubble or droplet sizes are usually large, greater than 10 mm, and the Bond number (Bo) is greater than 40. Terminal velocity is proportional to the size of the droplet or of the bubble. High pressure is created on the front part and rear of the droplet/bubble because of the high inertia. Low pressure is created at the side of the walls, which leads to the greater deformation of the droplet/bubble. Terminal velocity in this regime can be given by the theory proposed by Davies et al. [39]:

$$u_t = \frac{2}{3}\sqrt{\frac{g d \Delta\rho}{2\rho_l}} \tag{3.6}$$

According to the size of the droplet or bubble, their respective terminal velocity in the liquid medium can be estimated from the formulas as mentioned above. The expected terminal velocity of calcium droplet and bubble in liquid steel can be seen in Figure 3-22.

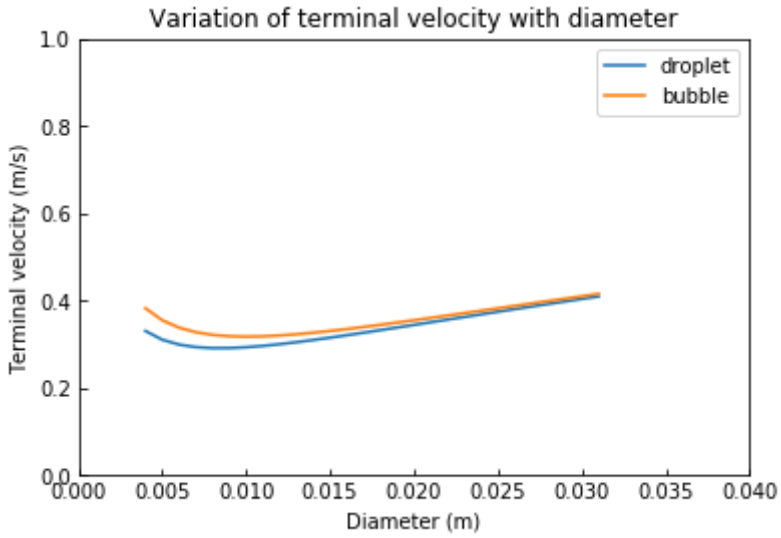

Figure 3-22 Expected terminal velocity of Ca droplet/bubble in liquid steel.

Remark: For a calcium droplet or bubble of size between 0.4 cm and 3 cm (diameter), Bond number (Bo) lies between 0.3 and 40. Therefore, Equation (3.5) is only used to calculate the terminal velocity for this specific range of sizes. Terminal velocity obtained using equation (3.5) is found to be in good agreement with the one obtained numerically (using ICI-tech). It was found difficult to determine terminal velocity experimentally.

3.8 Experimental observations

Experiments are performed below and above the boiling point of calcium (1480°C) and the yields (calcium recovery rates) are compared at different temperatures. Experiments provided information concerning the size of the calcium droplets and calcium bubbles, their number and total calcium absorbed in liquid steel. With all this information obtained from the experiments, the average mass transfer coefficient of calcium droplets or calcium bubbles in liquid steel can be obtained. Before going into the details of what has been observed experimentally, some precisions have to be underlined on what is calcium yield. Calcium yield is defined as the ratio between the total calcium detected inside the steel and the calcium that has been injected initially. Total calcium includes the calcium dissolved in the steel and the calcium trapped in the inclusions, e.g., calcium aluminate inclusions.

$$\%\, Yied = \frac{Total\ calcium\ detected\ inside\ the\ steel(g)}{calcium\ injected\ (g)}\ X100$$

3.8.1 Calcium injection below the boiling point of calcium

Some important experimental observations are explained in this section. One gram of calcium is injected at 1480°C (1 atmospheric pressure). This much quantity corresponds to 400 ppm of calcium in liquid steel of 2.6 kg quantity. Capsule shown in Figure 3-15 is used to inject 1 gram of calcium. Since the capsule is weighted with tungsten, we hoped that the capsule reached the bottom of the crucible. Later it was confirmed when the metal ingots were sliced, and the

capsule was found at the bottom of the crucible. The average time for the capsule to reach the bottom of the crucible can be known by calculating the terminal velocity of the falling capsule in liquid steel. The terminal velocity of the capsule can be calculated by balancing the downward gravitational force (F_g) with the buoyant force (F_B) and the drag force (F_d).

$$F_g = F_B + F_d \tag{3.7}$$

$$m_c\, g = \rho_{ls} V_{cap} g + \frac{1}{2}\rho_{ls} C_D A_c U_t^2 \tag{3.8}$$

m_c (mass of capsule)	0.042 kg
V_{cap} (volume of capsule)	2.7×10^{-6} m^3
C_D(drag coefficient)	0.7
A_c (cross-section area)	1.13×10^{-3} m^2

Table 3-3 Properties for calculating the terminal velocity of the capsule.

m_c corresponds to the total mass of the capsule with tungsten and calcium inside it. A_c is the total surface area of the capsule and V_{cap} is the volume of the capsule, which is calculated from Figure 3-15. C_D which is drag coefficient is taken as 0.7 (cylindrical body). Putting these values in equation (3.8), terminal velocity (U_t) is obtained as 0.28 m/s. For liquid steel of height around 7cm, the average falling time of capsule seems to be around 0.24s.

Once the capsule goes down at the bottom of the crucible, it melts, and the calcium is liberated in the form of droplets from the capsule. It should be noted that the inductors are turned off when the calcium is injected inside liquid steel to avoid the mixing caused by the inductors. During this very experiment (1g calcium injection at 1480°C) four droplets of calcium are observed at the surface of liquid steel, sizes varying from 0.2 cm to 0.8 cm of diameter (Figure 3-25). The size of the droplet is calculated with the help of the "ImageJ" software. Known distance (e.g., the diameter of crucible = 8 cm (centimeters) = 590 pixels) is calculated in pixels (Figure 3-23) and then the scale is set in cm. After that, the dimension of the droplet is calculated in cm.

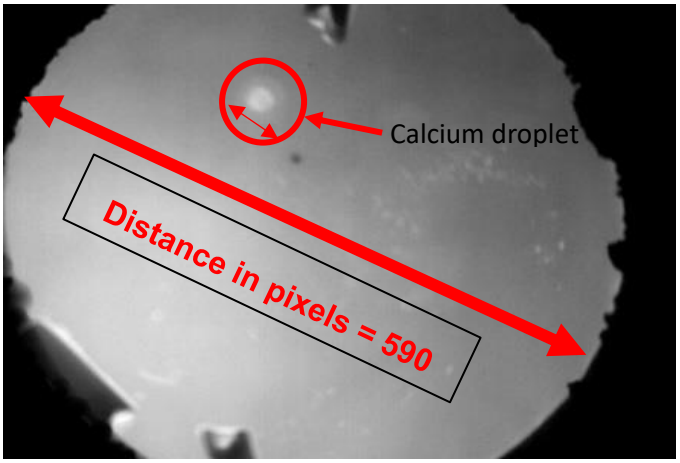

Figure 3-23 Image analysis of calcium droplet with ImageJ software.

Several droplets at the surface of liquid steel are formed. In this case, four droplets arrived at the surface bath (see figure3-25) even when the inductors are turned off. The possible reasons for the formation of many droplets instead of one single droplet can be numerous: the injection procedure, the way capsule melts, the calcium melting time, the capsule landing position, etc. However, it cannot be the result of the fragmentation of a rising calcium droplet in liquid steel. It is reported experimentally that the breakup of a droplet occurs when the Weber number exceeds a critical value [40]. T. Watanabe et al. [41] and F. Marcotte et al. [42] studied numerically the breakup phenomenon of droplet. T. Watanabe et al [41] found that the breakup of coalesced droplets occurs when the Weber number at coalescence exceeds a critical value. This breakup condition of the rising calcium droplet in liquid steel is discussed further below.

One gram of calcium corresponds to a single calcium droplet of diameter 1 cm. For calcium droplet of size 1 cm to fragment while rising in liquid steel, the Weber number (We), in equation (3.9), should be larger than critical Weber number ($We_{critical}$, equation (3.10)). However, it is not the case for a calcium droplet of size 1 cm. In equation (3.9), ρ_{ls} represents the density of liquid steel, v_t is the terminal velocity of calcium droplet, d_{cad} is the diameter of the calcium droplet, and $\sigma_{cad.ls}$ is the interfacial surface tension between calcium droplet and liquid steel. In equation (3.10), μ_{cad} represents the viscosity of the calcium droplet. Since, for the calcium droplet of 1 cm, Weber number (We) is smaller than the critical Weber number ($We_{critical}$) therefore, it supports the argument that not all the calcium melts at the same time to form one single droplet. For a calcium droplet to fragment while rising in liquid steel, the diameter of droplet should be larger than 1.8 cm (Figure 3-24). Terminal velocity (v_t) used for calculating Weber number is calculated from equation (3.5).

$$We = \frac{\rho_{ls} v_t^2 d_{cad}}{\sigma_{cad.ls}} \qquad (3.9)$$

$$\mathrm{We}_{\mathrm{critical}} = 12\left(1 + \frac{\mu_{cad}^2}{\rho_{cad} d_{cad} \sigma_{cad.ls}}\right) \quad (3.10)$$

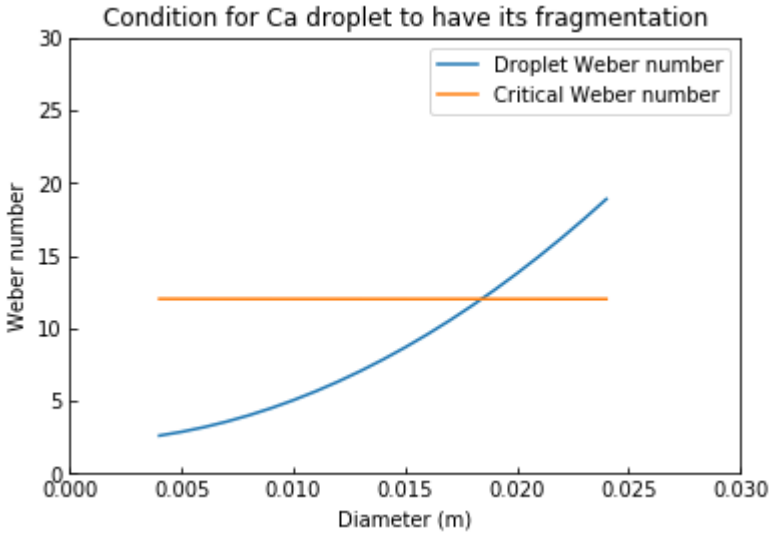

Figure 3-24 Variation of Weber number (calcium) with the diameter in liquid steel.

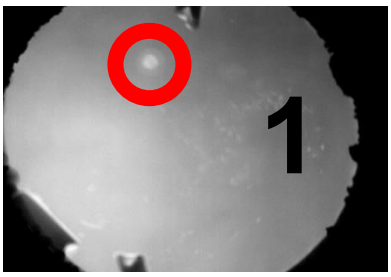

$d_{cad} = 0.3\ cm$ (at t_0 s)

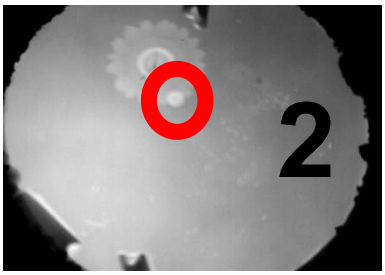

$d_{cad} = 0.35\ cm$ (at t_0 +0.0065 s)

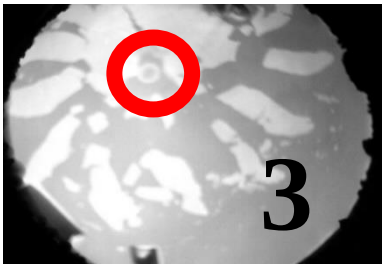

$d_{cad} = 0.35\ cm$ (at t_0 +0.1035 s)

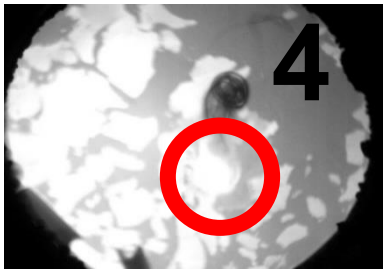

$d_{cad} = 0.75\ cm$ (at t_0 +0.3 s)

Figure 3-25 Calcium droplet arriving at the surface of liquid steel (1g calcium injected).

The four droplets which arrived at the surface of liquid steel can be seen in Figure 3-25. The first droplet of calcium arrived after 3 seconds (t_0 seconds) of the capsule being injected. The successive droplets arrival times are illustrated in Figure 3-25. The smaller droplets seemed to be perfectly spherical; therefore, we can conclude that the surface tension effects are dominant for the smaller droplet compared to the larger droplet, which led to the spherical shape of the smaller droplet. It is also observed that the smaller droplets arrived earlier as compared to the larger droplets. The possible reason for it can be: the smaller droplets melt earlier and henceforth, reached earlier at the surface of liquid steel. Once all the calcium reached the surface of liquid steel, steel samples are analyzed to determine the calcium content inside it.

There are two ways of calcium detection in liquid steel. In the first one, liquid samples are taken in quartz tubes (Figure 3-17) just after the calcium arrival at the surface of liquid steel, and then these samples are analyzed by spectrography. In the second method, liquid steel is cooled and allowed to get solidified. Then, the ingot is vertically sliced, and the vertically sliced ingots are then analyzed by spectrography to determine the total calcium content (Figure 3-18). When the experiments were performed below the boiling point of calcium, it was difficult to take the samples in the tube since liquid steel gets solidified quickly (melting point of liquid steel $\approx$ 1440°C). Therefore, the spectrographic analysis was done on the ingots to detect the total calcium absorbed in the steel. Table 3-4 shows the experimental observation concerning the total volume of calcium observed at the surface of liquid steel as well as the total calcium detected inside the steel.

Inductors turned off	Calcium injected (g)	No of calcium droplets at the surface of liquid steel	Total volume observed at the surface of liquid steel (cm3)	Theoretical volume expected (cm3)	Total Calcium (spectrographic analysis of the ingot) (ppm)
Yes	1	4	0.30	0.70	Non- detectable (less than 3 ppm)

Table 3-4 Experimental observations for the injection of 1 g of calcium below its boiling point.

Table 3-4 shows that 1g of calcium injected below the boiling point was not enough to detect the calcium in liquid steel. It can be attributed to the low diffusivity of calcium in liquid steel (4e-9 m^2/s). The error in the value of total calcium detected by spectrographic analysis is $\pm 20\%$.

The total volume observed at the surface (Table 3-4) is estimated from the observations of the calcium droplets arriving at the surface of liquid steel (via camera at the top). The theoretical volume specified in Table 3-4 is the volume of liquid calcium expected when all the solid calcium is converted into liquid calcium (density of calcium ρ_{ca}, at the melting point (840°C) is 1378 kg/m^3). Since the droplets seen at the surface of liquid steel are not circular

every time, some approximation has been taken in order to calculate their total volume, which is explained further below.

3.8.1.1 Calcium droplet size and volume calculation

Figure 3-26 General shapes of the calcium droplets at the surface of liquid steel bath. A) Circular B) Elliptical.

Our study in the previous section showed that the shape of the calcium droplet or bubble in liquid steel depends on the size of the droplet or bubble. For instance, if the size of droplets or bubbles is less than 0.2cm (high Bond number), it is expected to have a spherical shape while if the same is larger, it can have either ellipsoidal, wobbling or spherical cap shape as depicted in Figure 3-21. Different approximations are considered to calculate the size and volume of the calcium droplets or bubbles arriving at the surface of liquid steel. When the droplets observed at the surface seem to be circular as shown in Figure 3-26 (A), it is assumed that the droplets are spherical and their volume is calculated as $\frac{4}{3} * \mathbf{3.14} * \left(\frac{a}{2}\right)^3$. When the droplets seem to be elliptical in shape as shown in Figure 3-26 (B), their diameter is considered as $\frac{a+b}{2}$, and their volume is calculated as $\frac{4}{3} * \mathbf{3.14} * \left(\frac{a+b}{4}\right)^3$ respectively. Calculating the diameter and volume in this manner can lead to error in the total volume observed, therefore, some discrepancies have been observed between the theoretical volume expected and the total volume observed at the surface of liquid steel.

3.8.1.2 Calcium injection with inductors kept on

On the contrary of what has been observed when the inductors were turned off, a significant amount of calcium is detected in the steel when the inductors were mistakenly kept on during one of the experiments while injecting 0.93g (372 ppm) of calcium. The number of times calcium arrived at the surface increased from 4 to 8 (Figure 3-27). The first droplet of calcium arrived after 2.8 seconds (t_0 seconds) of the capsule being injected and the size of the calcium droplets varied between 0.15 cm to 0.7 cm. Experimental observations can be seen in Table 3-5. For some of the droplets formed at the surface, it was quite difficult to calculate their size because of their irregular shape as well as because of the formation of black fumes.

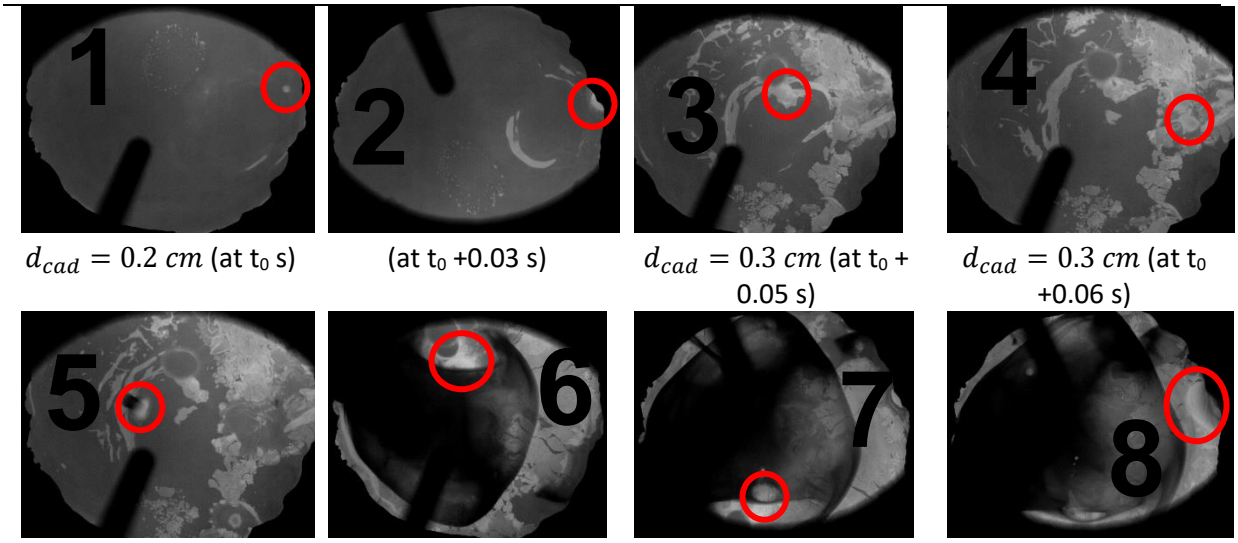

$d_{cad} = 0.2\ cm$ (at t_0 s) (at t_0 +0.03 s) $d_{cad} = 0.3\ cm$ (at t_0 + 0.05 s) $d_{cad} = 0.3\ cm$ (at t_0 +0.06 s)

$d_{cad} = 0.4\ cm$ (at t_0 +0.07s) $d_{cad} = 0.65\ cm$ (at t_0 +0.1 s) $d_{cad} = 0.65\ cm$ (at t_0 +0.18 s) $d_{cad} = 0.7\ cm$ (at t_0 + 0. 25 s)

Figure 3-27 Calcium droplet arriving at the surface of liquid steel (0.93g calcium injection).

Inductors turned off	Calcium injected (g)	No of calcium droplets at the surface of liquid steel	Total volume observed at the surface of liquid steel (cm3)	Theoretical volume expected (cm3)	Total Ca before injection (spectrographic analysis of the ingot) (ppm)	Total Ca after injection (spectrographic analysis of the ingot) (ppm)
No	0.93	8	0.60	0.70	3	20

Table 3-5 Experimental observation when inductors are kept ON during calcium injection

Table 3-5 shows the experimental observation for 0.93g of calcium injection. Keeping the inductors on increased the number of calcium droplets at the surface of liquid steel as well as the total calcium absorbed inside the steel. Hence, we can say that mixing can increase the dissolution of calcium in liquid steel even below the boiling point of calcium.

3.8.1.3 5g of calcium injection with inductors turned off

Injecting 1g of calcium with inductors off didn't lead us to detect the total calcium in the steel. Therefore, the quantity of calcium being injected is increased from 1g to 5g. In order to do so, we needed to modify the dimensions of our capsule too. The capsule of a larger dimension is used for injecting 5g of calcium at 1480°C as shown in Figure 3-16. 5g of calcium injection, which corresponds to 2400 ppm, led to a detectable amount of the total calcium inside the steel. In this configuration, at least nine droplets of calcium arrived at the surface of liquid steel with size varying from 0.2 cm to 0.9 cm along with the black fumes appearing in the end. The first calcium droplet arrived at 0.9 seconds (t_0 seconds) after the calcium has been injection. 9 Calcium droplets which arrived at the surface of liquid steel is shown in Figure 3-28, and the experimental observations are synthesized in Table 3-6 respectively.

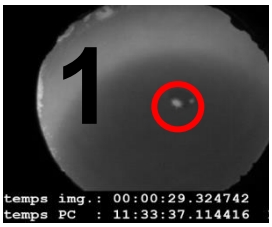

$d_{cad} = 0.30\ cm$ (at t_0 s)

$d_{cad} = 0.30\ cm$ (at t_0 + 0.0005 s)

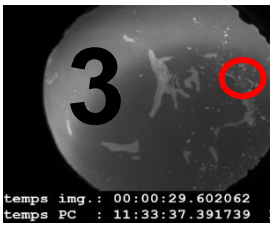

$d_{cad} = 0.35\ cm$ (at t_0 + 0.26 s)

$d_{cad} = 0.32\ cm$ (at t_0 + 0.28 s)

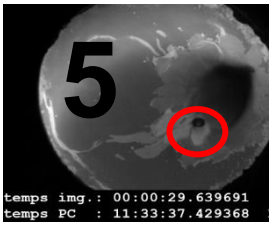

$d_{cad} = 0.6\ cm$ (at t_0 + 0.30 s)

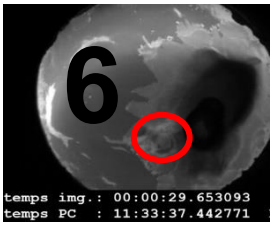

$d_{cad} = 0.5\ cm$ (at t_0 + 0.31 s)

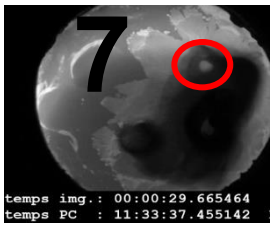

$d_{cad} = 0.4\ cm$ (at t_0 + 0.33 s)

$d_{cad} = 0.8\ cm$ (at t_0 + 0.335 s)

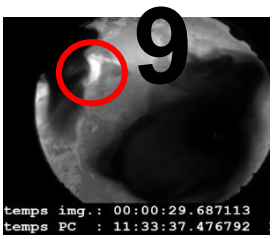

$d_{cad} = 0.85\ cm$ (at t_0 + 0.35 s)

Figure 3-28 Calcium droplet at the surface of liquid steel (5g calcium injection).

Inductors turned off	Calcium injected (g)	No of calcium droplets at the surface of liquid steel	Total volume observed at the surface of liquid steel (cm3)	Theoretical volume expected (cm3)	Total Ca detected before injection (spectrographic analysis of the ingot) (ppm)	Total Ca detection after injection (spectrographic analysis of the ingot) (ppm)
Yes	5	8	0.8	3.5	4	11

Table 3-6 Experimental observation when total calcium is detected below the boiling point.

It is observed that, even with 5g of calcium injection, we have the same order of magnitude for the total volume of calcium droplets observed at the surface of liquid steel and the theoretical volume expected. The slight difference observed in the volume can be explained by the shape of the droplet. As the droplet may not be perfectly spherical while reaching the bath surface so, there lies a possibility of error while measuring the droplet diameter. Another important thing observed is that the total calcium is detectable for this specific case (11 ppm).

Difference between the total calcium detected before, and after calcium injection, ΔC_{ca} is 7 ppm. A summary of the obtained yields for different experiments is presented in section 3.9. Total absorbed calcium is found to be completely uniform in the metal ingots. In order to verify the homogeneity of total calcium in liquid steel, spectrographic analysis is done on three different planes, as shown in Figure 3-29.

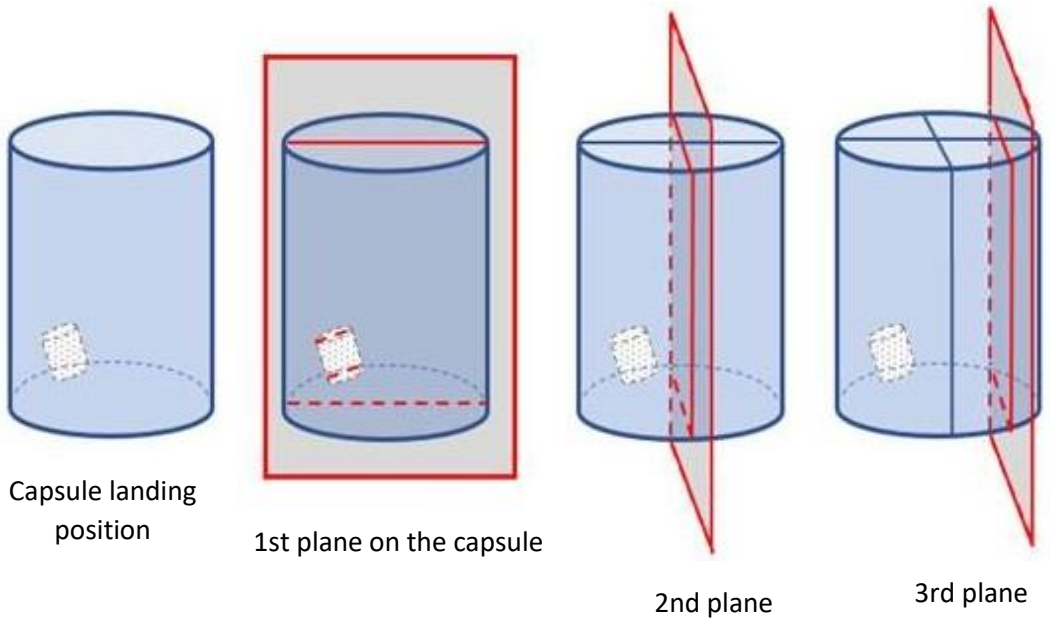

Figure 3-29 Different planes selected for spectrographic analysis.

The 1st plane is selected where capsule lands, the 2nd plane is a perpendicular plane selected closer to the capsule while the 3rd plane is selected little far from the capsule landing position. Spectrographic analysis results showed that the average value of total calcium detected in each plane is the same (11 ppm). This showed that the calcium is uniformly distributed in the metal ingot.

3.8.1.4 Sensibility test for calcium injection below the boiling point

Sensibility test for the calcium injection below the boiling is performed. 6g of calcium is injected at 1480°C, and the total calcium absorbed inside the steel is detected. Total calcium detected is then compared with the experimental observation of Table 3-6. For 6g of calcium injection, we used the same capsule that has been used for 5g of calcium injection (Figure 3-16).

Inductors turned off	Calcium injected (g)	Total Ca detected before injection (spectrographic analysis of the ingot) (ppm)	Total Ca detection after injection (spectrographic analysis of the ingot) (ppm)
Yes	6	4	12

Table 3-7 Reproducibility test below the boiling point of calcium.

It has been found that with 6 g of calcium being injected, we have more or less the same amount of total calcium detected inside the steel. The difference in the total calcium detected

before and after calcium injection (ΔCca) is 8 ppm. It confirms that the experiments performed are reproducible as far as the detection of total calcium inside liquid steel is concerned. With the experimental observations, the estimated value of the average mass transfer coefficient of calcium in liquid steel can be calculated. This is explained in the section below.

3.8.2 Mass transfer coefficient estimation

In order to understand the dissolution mechanism, the mass transfer coefficient between the calcium and liquid steel needs to be known. In this section, we are presenting the estimated value of the average mass transfer coefficient obtained from the experiments performed. Experiments gave us an idea about the number of droplets arriving at the surface of liquid steel, their size and the total calcium absorbed inside liquid steel. With all this information, we can get a fair idea about the average mass transfer coefficient of calcium droplets in liquid steel (K_{cadexp}). In section 3.8.1.3, it is observed that 5g of calcium led to the formation of 9 droplets (size varying from 0.2 cm to 0.9 cm) at the surface of liquid steel with black fumes arriving at the end. In this calculation, it is assumed that nine droplets of calcium are rising in liquid steel with each droplet having a size of 0.95 cm (diameter) which corresponds to the 5g of calcium release in liquid steel. We ignored the formation of black fumes in our calculation. K_{cadexp} is calculated from the equation (3.11) where $\emptyset$ is the mass flux (kg/s), S is the total surface area which is 2.55e-03 m^2 (for nine droplets), ρ_{ls} is the density of liquid steel (7200 kg/m^3), C_{ca} is the average concentration at the calcium droplet liquid steel interface (liquid steel side) at equilibrium (48 ppm [43]), and C_{ca}^{bath} (0 ppm) is the concentration in liquid steel initially.

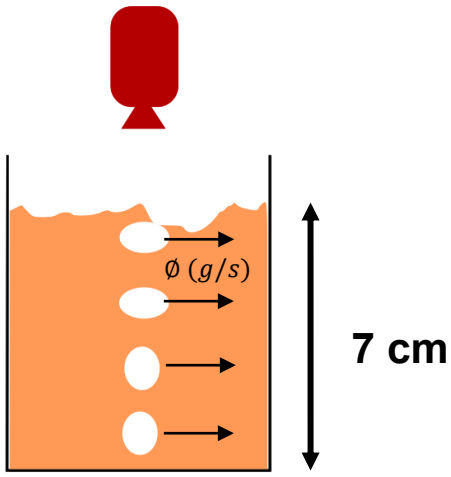

Figure 3-30 Calcium droplet rising in liquid steel with a camera at the top.

$$\emptyset = K_{cadexp}.S\rho_{ls}.(C_{ca} - C_{ca}^{bath}) \quad (3.11)$$

$\emptyset$ (kg/s) is calculated from the total calcium detected, and the residence time of the calcium droplets in liquid steel. Average rising velocity for a droplet of diameter 0.95 cm, is found to be around 0.26 m/s (obtained numerically) which leads to a residence time of around 0.27s in liquid steel of height 7 cm (Figure 3-30). Table 3-6 shows that ΔC_{ca} (difference in concentration

difference) is 7ppm, which is equivalent to 1.82e-05 kg of total calcium inside liquid steel for a crucible of capacity 2.6kg liquid steel. Mass flow rate (Ø) is then obtained as 6.74e-05 kg/s. Putting the value of Ø in equation (3.11), one gets a value of average mass transfer coefficient K_{cadexp} as **7.642e-02 m/s.**

Information obtained from experiments can be exploited further to obtain the estimated value of average mass transfer coefficient for different configuration like 5 g of calcium injection can also lead to 36 calcium droplets release each having size of 0.6 cm (diameter). With a size of 0.6 cm, average rising velocity is found to be around 0.25 m/s (calculated numerically) which can lead to a residence time of around 0.28 s in liquid steel of height 7cm. Assuming the total calcium inside steel (ΔC_{ca} =7 ppm) remains the same, K_{cadexp} is obtained as **4.5e-02 m/s**. Therefore, we can say that the experiments have given us pivotal information concerning the order of magnitude of the average mass transfer coefficient (K_{cadexp}) of calcium droplets in liquid steel.

Once sufficient knowledge concerning the calcium dissolution below the boiling point is obtained, we switched towards performing experiments above the boiling of calcium. Calcium injection above the boiling point of calcium is explained in the next section.

3.8.3 Calcium injection above the boiling point of calcium

During Industrial operation, calcium is injected above the boiling of calcium (~1560°C). Depending upon the depth at which the calcium is released, it can be either in the form of droplet or bubble. If released in the form of a droplet, during its rise in the ladle, phase change takes place, and the calcium droplet changes to calcium bubble (because of the decrease in Ferro-static pressure). Therefore, it is important to understand the calcium liquid-gas phase change mechanism as it can affect the dissolution of calcium in liquid steel. To achieve this objective, we injected calcium above the boiling point of calcium too. Injecting calcium at 1550°C (above the boiling point of calcium) allowed us to observe the calcium bubbles at the surface of liquid steel. The capsule used for these injections can be seen in Figure 3-15. A smaller amount of calcium is injected above the boiling point, for safety purposes because even a small amount of calcium can lead to significant gas formation. A 30 mg of calcium injection, which corresponds to 12 ppm of calcium being injected, led to the formation of at least 25 calcium bubbles. The size (d_{cab}) of the calcium bubble varied between 0.25 cm and 0.45 cm, respectively. We studied the condition for the rupture of the calcium bubble, and it was found that the minimum diameter of the calcium bubble to fragment while it is rising in liquid steel is around 2.1 cm (Figure 3-31). Experimental observations can be seen in Table 3-8.

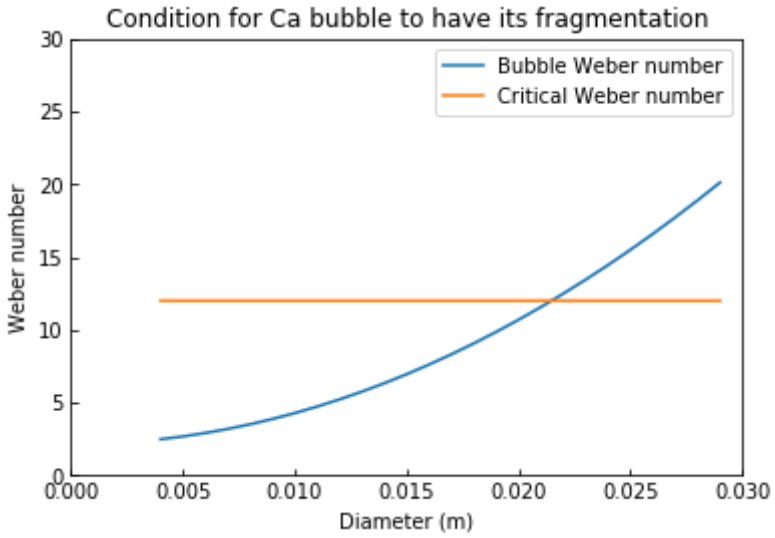

Figure 3-31 Variation of Calcium Weber number in liquid steel with the diameter.

Inductors turned off	Calcium injected (mg)	No of calcium bubbles at the surface of liquid steel	Total volume observed at the surface of liquid steel (cm3)	Theoretical volume expected (cm3)	Total Calcium (spectrographic analysis of the ingot) (ppm)
Yes	30	>25	~1	60	Non- detectable (less than 3 ppm)

Table 3-8 Experimental observation for calcium injection above the boiling point.

One observes that (Table 3-8), 30mg of calcium was not enough to detect the total calcium in liquid steel.

In order to detect the total calcium inside liquid steel, calcium injection is increased from 30 mg to 100mg during one of the experiments. For this specific configuration, a minimum of nine calcium bubbles is observed at the surface of liquid steel. The first calcium bubble arrived after 1.2 s (t_0) of calcium injection. The size of the calcium bubbles seemed to vary between 0.45 cm and 0.65 cm except for the one bubble which had a diameter of around 1.5 cm (Figure 3-32). It is observed that even a small amount of calcium injection (100 mg) above the boiling point, led to the significant black fumes formation. Once the calcium bubble reached the surface of liquid steel, spectrographic analysis is done on the samples taken in the tube as well as on the metal ingots. It is found that the total calcium detected is more or less the same in both the cases, 9 ppm for analysis done on the samples taken in the tube and 7 ppm for analysis done on the metal ingots.

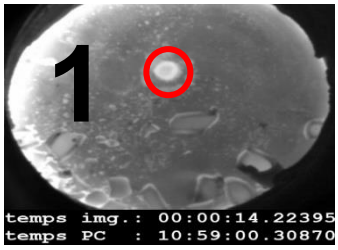

$d_{cab} = 0.60\ cm$ (at t_0 s)

$d_{cab} = 0.46\ cm$ (at t_0 + 0.37s)

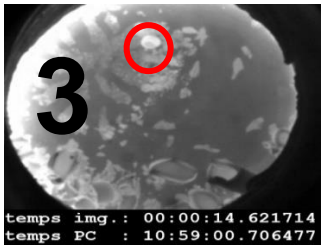

$d_{cab} = 0.60\ cm$ (at t_0 +0.4s)

$d_{cab} = 0.90\ cm$ (at t_0 +0.46s)

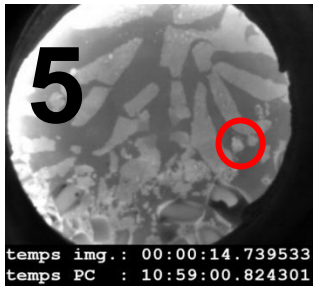

$d_{cab} = 0.25\ cm$ (at t_0 +0.52s)

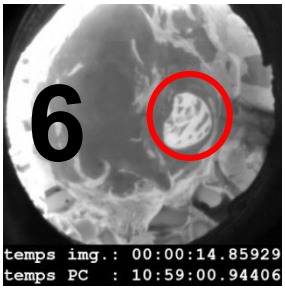

$d_{cab} = 1.5\ cm$ (at t_0 +0.65s)

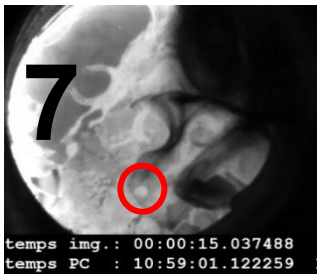

$d_{cab} = 0.35\ cm$ (at t_0 +0.83s)

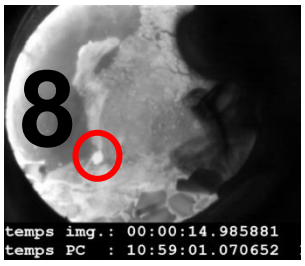

$d_{cab} = 0.40\ cm$ (at t_0 +0.85s)

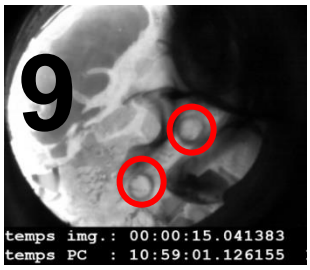

$d_{cab} = 0.60\ cm$ (at t_0 0.90 s)

Figure 3-32 Calcium bubble at the surface of liquid steel (100mg calcium injection).

Inductors turned off	Calcium injected (mg)	No of calcium bubbles at the surface of liquid steel	Total volume observed at the surface of liquid steel (cm3)	Theoretical volume expected (cm3)	Total Ca detected before injection (spectrographic analysis of the ingot) (ppm)	Total Ca detection after injection (spectrographic analysis of the ingot, samples in the tube) (ppm)
Yes	100	>12	~3	200	3	7 (ingot)
						9 (tube)

Table 3-9 Experimental observation with 100 mg of calcium injection (1550°C).

In order to investigate more into the dissolution phenomenon of calcium in liquid steel, calcium injection is increased from 100mg to 236mg at 1550°C in one of the experiments. With 236mg of calcium injection (94ppm), a minimum of 9 bubbles of calcium arrived at the surface of liquid steel (Figure 3-33). The first calcium bubble arrived after 1.2 s (t_0) of calcium injection.

Significant formation of black fumes at the surface of liquid steel has been observed too, similar to what has been observed with 100 mg of calcium injection. The size of the calcium bubbles varied between 0. 25 cm and 2.25 cm.

Increased calcium injection (from 100mg to 236 mg) led to an increase in calcium dissolution. Total calcium absorbed in the steel increased from 9 ppm to 17 ppm based on the spectrographic analysis of samples taken in a tube and from 9 ppm to 13 ppm based on the spectrographic analysis performed on the metal ingots.

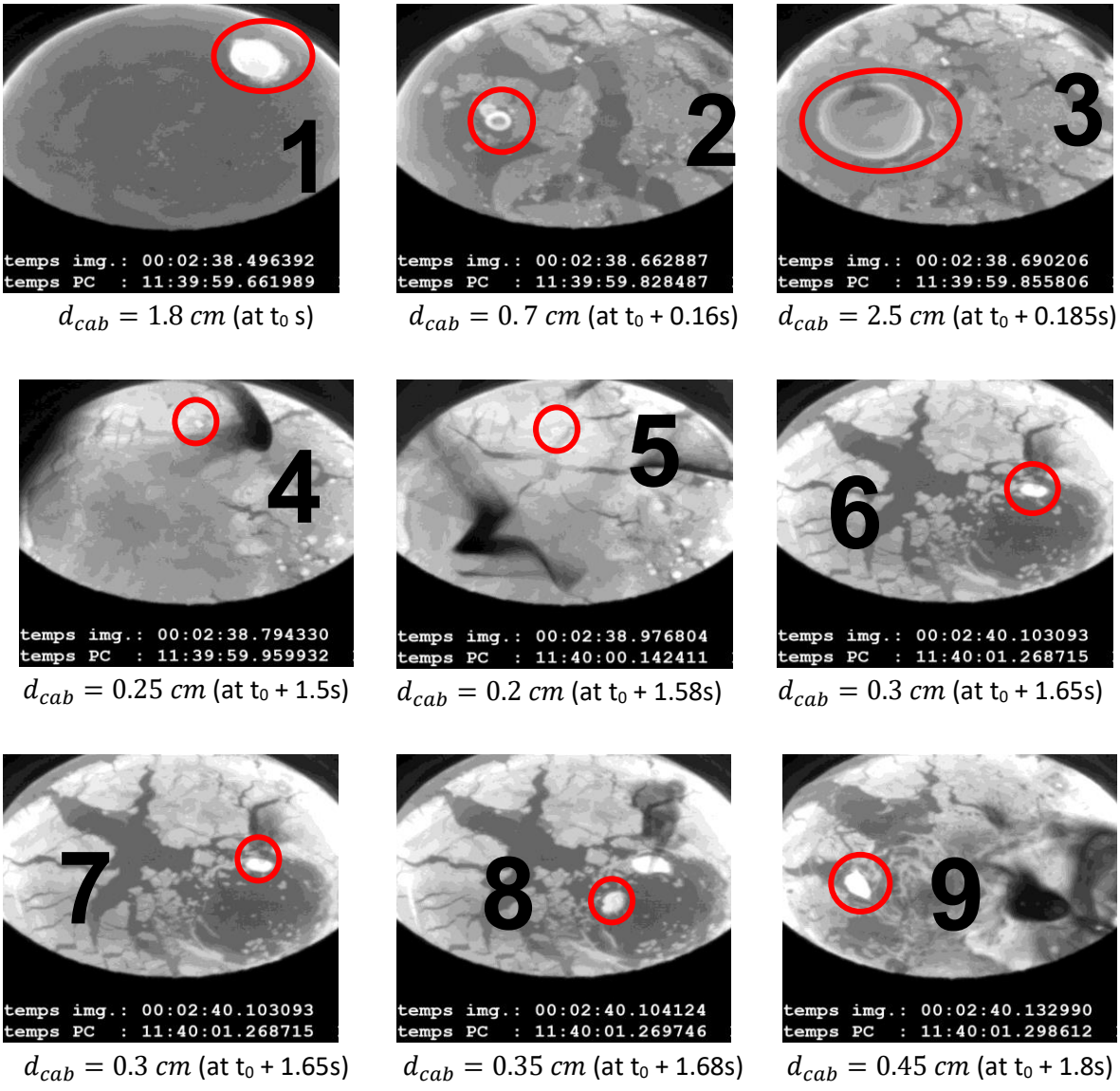

$d_{cab} = 1.8\ cm$ (at t_0 s) $d_{cab} = 0.7\ cm$ (at t_0 + 0.16s) $d_{cab} = 2.5\ cm$ (at t_0 + 0.185s)

$d_{cab} = 0.25\ cm$ (at t_0 + 1.5s) $d_{cab} = 0.2\ cm$ (at t_0 + 1.58s) $d_{cab} = 0.3\ cm$ (at t_0 + 1.65s)

$d_{cab} = 0.3\ cm$ (at t_0 + 1.65s) $d_{cab} = 0.35\ cm$ (at t_0 + 1.68s) $d_{cab} = 0.45\ cm$ (at t_0 + 1.8s)

Figure 3-33 Calcium bubble at the surface of liquid steel (236 mg calcium injection).

Inductors turned off	Calcium injected (mg)	No of calcium bubbles at the surface of liquid steel	Total volume observed at the surface of liquid steel (cm3)	Theoretical volume expected (cm3)	Total Ca detected before injection (spectrographic analysis of the ingot) (ppm)	Total Ca detection after injection (spectrographic analysis of the ingot, samples in the tube) (ppm)
Yes	236	>10	~13	472	3	13 (ingot)
						17 (tube)

Table 3-10 Experimental observation with 236 mg of calcium injection (1550°C).

3.8.3.1 Reproducibility test for calcium injection above the boiling point

The reproducibility of the experiments has been verified for the calcium injection above the boiling point too. For the reproducibility test, 236 mg of calcium is injected at 1550°C, and the experimental observations (Table 3-11) are compared with what has been observed in Table 3-10. Calcium at the surface can be seen in Figure 3-34 with t_0 = 1.3 s.

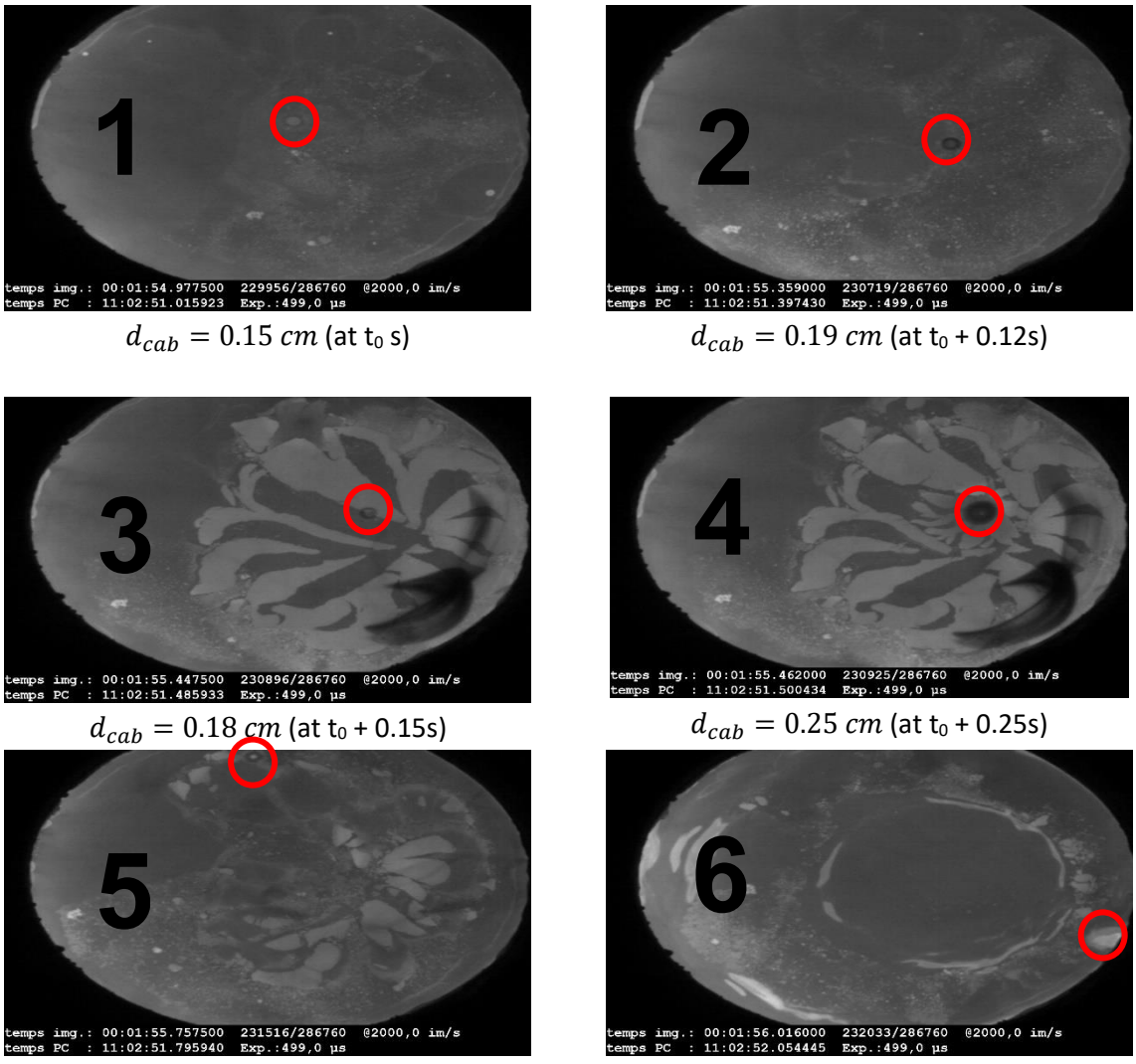

$d_{cab} = 0.15\ cm$ (at t_0 s)

$d_{cab} = 0.19\ cm$ (at t_0 + 0.12s)

$d_{cab} = 0.18\ cm$ (at t_0 + 0.15s)

$d_{cab} = 0.25\ cm$ (at t_0 + 0.25s)

$d_{cab} = 0.15\ cm$ (at t_0 + 0.30s)

(at t_0 + 0.32s)

Figure 3-34 Calcium bubble at the surface of liquid steel (236 mg calcium injection).

Significant black fume formation made it difficult to calculate the total volume of calcium at the surface of liquid steel. As far as the total calcium detected inside liquid steel is concerned, the same amount of total calcium (Table 3-11) has been detected, that has been detected for the previous calcium injection (Table 3-10). Thus, we can say that the experiments above the boiling point are reproducible as far as the total calcium absorbed in liquid steel is concerned.

Inductors turned off	Calcium injected (mg)	Total Ca detected before injection (spectrographic analysis of the ingot) (ppm)	Total Ca detection after injection (spectrographic analysis of the ingot) (ppm)
Yes	236	3	12.5

Table 3-11 Reproducibility test above the boiling point of calcium.

3.9 Discussion

During the experiments, calculating the exact volume of the calcium seemed to be a tedious task because of the irregular shapes (spherical, ellipsoidal or irregular) of the calcium droplets or bubbles at the surface of liquid steel bath. These variations in the shape can be partly explained by their position in the Grace diagram (Figure 3-21). When the experiments are performed below the boiling point of calcium, the same order of magnitude for the total volume of calcium droplet observed and the total volume expected is noticed, but the significant discrepancy has been noticed between the total volume observed and the total volume expected for the calcium injection above the boiling point. There can be different reasons to explain this discrepancy:

1) calcium injected above the boiling point rapidly leads to the formation of black fumes which prevent us from observing the bubbles reaching the bath surface;
2) some of the calcium arriving the surface might be the mixture of calcium liquid and calcium gas;
3) there is a significant amount of calcium that gets dissolved in liquid steel (~ 10 to 12%).

In the steel Industry, calcium dissolution is always discussed in terms of yield which is defined as the ratio between the total calcium detected in the steel and the calcium that has been initially injected (see section 3.8). The yield obtained at different temperatures (below and above the boiling point of calcium) is therefore calculated and is presented in the table below.

	Ca injected (g)	(°C)	Inductors Turned off	No. of droplets or bubbles observed	Total calcium detected (ppm)	Yield (%)
Droplet	1g (400 ppm)	1480	Yes	4	Non-detectable	NA
	0.93g (372 ppm)	1480	No	6	16	~4%
	5g (2000 ppm)	1480	Yes	8	7	~0.4%
	6g (2400 ppm)	1480	Yes	No info	8	~0.35%
Bubble	0.03g (12 ppm)	1550	Yes	>25	Non-detectable	NA
	0.1g (40 ppm)	1550	Yes	>13	4 (ingot)	~10%
					6 (tube)	~15%
	0.236g (94 ppm)	1550	Yes	>10	10 (ingot)	~11%
					14 (tube)	~15 %
	0.236g (94 ppm)	1550	Yes	~8	9.5 (ingot)	~10.8%

Table 3-12 Calcium yield obtained at different temperature.

It can be inferred from Table 3-12 that more calcium is absorbed by liquid steel when the temperature is above the boiling point. This result can be partially explained by the fact that the mass transfer area is much higher when calcium is released in the form of bubbles due to the volume involved, even when low calcium is injected. The other factor is that the rise of calcium bubbles are more violent as compared to the rise of calcium droplets because of the greater density difference between calcium bubbles and liquid steel. This increases the mixing inside liquid steel while the calcium bubbles are rising, and this can subsequently lead to the higher dissolution of calcium in liquid steel. In the case of calcium bubbles formation (1550°C), there can also be a possible impact of higher superheat (vs. droplet formation at 1480°C) on solidification time of liquid steel. This might also induce possible additional mixing after the inductors are turned off and can result in the increased calcium yield. It has also been observed

that the dissolution of calcium in liquid steel can increase even below the boiling point of calcium (Yield ~ 4%) when the inductors are kept ON. It confirms that mixing can have a significant effect on the dissolution of calcium in liquid steel.

3.10 Conclusion

In the context of this thesis, the dissolution of calcium in liquid steel is investigated via laboratory experiments. Calcium injection is performed at different operating temperatures, especially below and above the boiling point (1480°C) of calcium, and the respective yields are calculated. The experiments seemed to be reproducible as far as the total calcium in liquid steel is concerned. For all the experiments performed, special attention was given to turn off the inductors during the calcium rise. Inductors were mistakenly turned ON during one of the experiments performed below the boiling of calcium. The following conclusions are derived from the experiments performed:

1) The dissolution of calcium droplet is quite low in liquid steel with inductors being turned off (yield ~ 0.4%).
2) The shape of the calcium droplets reaching the surface can vary depending upon their respective sizes. In most of the cases, droplets smaller than 0.4 cm were found spherical at the surface of liquid steel, and the larger droplets were either elliptical or had an irregular shape.
3) Mixing (Inductors ON) can have a significant effect on the dissolution of calcium in liquid steel (yield ~ 4%) even at 1480°C (below the boiling point of calcium).
4) The average mass transfer coefficient of calcium droplets in liquid steel is calculated and is found to be in the order of ~ 7.642e-2 m/s.
5) Black fumes formation depends on the quantity of calcium being injected. Less than 900 mg of calcium injection did not lead to the black fume formation at the surface of liquid steel below the boiling point of calcium.
6) A significant discrepancy between the volume of calcium bubbles observed and the volume expected is found for calcium injection above the boiling point.
7) Above the boiling point, even a small amount of calcium injection (100 mg) led to a significant black fumes formation at the surface of liquid steel. It showed that the black fume formation not only depends on the amount of calcium being injected but also on the temperature at which it is injected. Further investigation needs to be done on the effect of melt composition and temperature on the black fume formation.
8) An increase in the calcium yield from 0.4% to 10% is obtained when calcium is injected at the temperature above the boiling point of calcium compared to calcium injection below the boiling point.

In conclusion, the experiments have helped us to understand the dissolution mechanism of calcium in liquid steel at different operating temperatures. Thus, experimental results could be utilized as a benchmark to validate the numerical model developed. In the future,

experiments need to be performed in order to verify the reproducibility as far as the number of bubbles arriving at the surface of liquid steel is concerned. It will further help us to understand the nucleation (calcium liquid-gas phase change) rate in a much better way. Hence, the next step was to proceed towards the numerical modeling part, which is being used to study the dissolution phenomenon of calcium in liquid steel. This has been covered in the next chapters.

3.11 Résumé Français

Les essais d'addition de calcium dans un acier liquide sont faits, certains à une température inférieure la température d'ébullition du calcium et d'autres à une température supérieure. La définition d'un nouveau protocole expérimental (nouvelle méthode d'injection de calcium dans l'acier) a permis de mieux comprendre et d'observer le comportement du calcium quand il atteint la surface libre. Les observations expérimentales ont éclairci certains points sur le comportement de la gouttelette ou de la bulle de calcium une fois qu'elle atteint la surface libre (l'interface acier/air). Le calcium total absorbé dans l'acier liquide et le nombre total de gouttelettes observées à la surface de l'acier liquide nous ont permis de calculer le coefficient de transfert de masse moyen entre les gouttelettes de calcium et l'acier liquide. Les expériences semblent reproductibles en ce qui concerne le calcium total absorbé dans l'acier liquide. Toutes les observations sont utilisées pour valider le modèle numérique.

Chapter 4:

Numerical Modeling

4 Numerical Modeling

In this chapter, we will present the numerical method which is being used to simulate our experiments. ICI tech code, which is based on the finite element method, is used in our study, and this section deals with the mathematical formulations involved and the overview of the usage of the ICI tech code.

To study our problem, dissolution of rising calcium droplet/bubble in liquid steel, the ICI-tech scientific computation library based on an adaptive finite element method is used. In this case, the governing partial differential equations are integrated over an element or volume after having been multiplied by a weight function [44]. The software library used in ICI-tech is developed at the High-Performance Computing Institute (HPC) of Ecole Centrale Nantes. In ICI tech code, a single mesh is used in the whole computation domain, and the different phases are determined by the level set functions. The Navier Stokes equation is solved by Variational Multiscale (VMS) method with mesh adaptation features controlled by a posteriori error estimation and a very good massively parallel performance. Adaptation of mesh plays an essential role in studying the dissolution phenomenon of calcium in liquid steel. All the features of the ICI tech code are explained in the sections below.

4.1 Introduction

Numerical simulation based on finite element methods depends strongly on the meshing capabilities of complex geometry and meshing becomes even more critical in multi-domain, multi-physics, fluid-structure interaction, and multiphase flow applications. One of the drawbacks of the common usage in multi-domain meshing is to keep the constraint of enforcement of the boundary or interface meshes in the volume mesh. These tasks become more and more difficult in computational mechanics when one wants to use a posteriori adaptive meshing and deal with boundary layers while using one mesh per involved phase.

In ICI-tech, an implicit representation of the boundary is used. It means that the boundary is not given by a surface mesh or an explicit representation, but implicitly by a scalar field whose value can be accessed anywhere in the domain of calculation. For instance, it can be the signed distance to the boundary, and therefore, the zero-value of this distance function defines the position of this same boundary. In our case, a filter of the signed distance with a hyperbolic tangent is used. A hyperbolic tangent enables to filter in a smooth way the signed distance function to a narrow band around the targeted boundary.

Another fundamental idea used is to interpolate the implicit function within meshes and to rely on an adaptive process based on a posteriori interpolation error framework to improve its representation. Anisotropic meshing is a powerful tool to do this task efficiently. With the anisotropic mesh, the result is an optimal capture of the interfaces within the meshes, whatever the complexity of the geometrical configuration is. The anisotropic techniques are based on a framework with a metric field constructed directly at the nodes of the mesh, without any direct information from the element, neither considering any underlying

interpolation. In the Eulerian grid-based method, the calculation domain is defined before carrying out the simulation.

4.2 Immersed volume method

In the Eulerian based method, the calculation domain is defined before carrying out the simulation. For this, we use an immersed volume method which is based on solving a single set of equations for the whole computational domain and on treating different subdomains as a single fluid with variable material properties, using an implicit boundary on a monolithic approach [45]. This section presents how the domain is divided into different phases and how the physical properties of the several phases are taken into account.

4.2.1 Level set methods

Boundary functions can be defined explicitly or implicitly. In an explicit boundary function, the solution is updated explicitly from a known value, but it has some drawbacks, e.g., sharp corners are handled incorrectly, special treatment is required for topology changes, node redistribution is required, etc. Therefore the first candidate for the implicit boundary function is the level set function [46], which enables to represent the interface between two phases as a zero level of a signed distance function. The value of the level set function is positive inside the domain and is negative outside the domain.

Since our study is focused on the study of calcium and liquid steel, let us consider $\boldsymbol{\Omega_l}$, $\boldsymbol{\Omega_c}$ and, Γi representing liquid steel domain, calcium domain, and the steel calcium interface. They verify:

$$\boldsymbol{\Omega_l} = \cup\ \boldsymbol{\Omega_c} = \boldsymbol{\Omega} \quad \text{and} \quad \boldsymbol{\Omega_l} \cap \boldsymbol{\Omega_c} = \Gamma\text{i} \tag{4.1}$$

For each node of the computational domain $\boldsymbol{\Omega}$, the level set function α, which is the signed distance from the interface reads the equation below and the physical properties in the domain are then calculated as a function of α.

$$\alpha(x) \begin{cases} > 0 & \text{If } x \in \boldsymbol{\Omega_l} \\ = 0 & \text{If } x \in \Gamma\text{i} \\ < 0 & \text{If } x \in \boldsymbol{\Omega_C} \end{cases} \tag{4.2}$$

The Interface is determined by the iso-value zero of the function $\alpha(x)$. The whole domain is decomposed into the subdomains of different fluids with the help of the distance function, $\alpha(x)$.

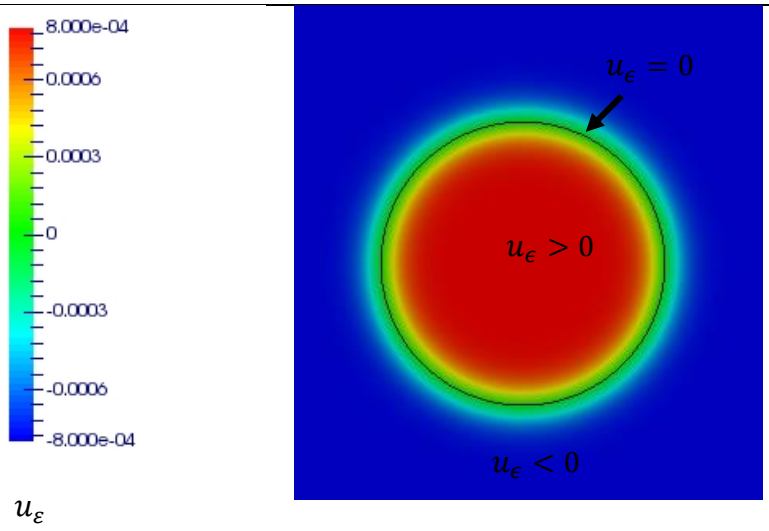

Figure 4-1 The smooth level set function of a circular domain with the interface highlighted in black.

From $\alpha(x)$, we can also calculate the Heaviside function $H(\alpha)$ as:

$$H(\alpha) = 1 \qquad if\ \alpha \geq 0$$
$$H(\alpha) = 0 \qquad if\ \alpha < 0 \tag{4.3}$$

The Heaviside function enables us to separate the domains strictly, but at the same time, it introduces discontinuity at the interface, which is incompatible with the resolution of the Navier-Stokes equation. Therefore, it is necessary to introduce a function to have continuity at the interface. To have continuity at the interface, one other implicit function u_ε is used, which can be seen in equation (4.4). It is a hyperbolic tangent function; its description is given in section (4.2.3).

$$u_\varepsilon(\alpha) = u(\alpha, \varepsilon) = \varepsilon \tanh\left(\frac{\alpha}{\varepsilon}\right) \tag{4.4}$$

The interface is completely defined by the zero value of this function, as shown in Figure 4-1. It introduces a thick interface, whose thickness is related to the parameter ε. u_ε gives a way to define a smooth truncation of the distance function allowing to introduce a narrow band of thickness ε and in which u_ε is approximating the distance function when $\alpha(x)$ is very large. The smooth Heaviside function is thus introduced by equation (4.5)

$$H_\varepsilon(\alpha) = \frac{1}{2}\left(1 + \frac{u_\varepsilon(\alpha)}{\varepsilon}\right) \tag{4.5}$$

The smoothed Heaviside function is used to deal with the multiphase modeling required by the implicit boundary approach. Suppose there is a material scalar field η, with the material

parameters η_1 and η_2 occupying two domains sharing an interface Γi implicitly defined by the signed distance function $\alpha(x)$, then we have:

$$\eta = \eta_1 H(\alpha) + \eta_2(1 - H(\alpha)) \tag{4.6}$$

Equation (4.6) represents a strict discontinuous variation of the global scalar field, and it is not tractable by standard numerical methods. However, if the regularized version of mixture law is considered, then there is a smooth transition which is controlled by the thickness parameter, for instance:

$$\eta_\varepsilon = \eta_1 H_\varepsilon(\alpha) + \eta_2(1 - H_\varepsilon(\alpha)) \tag{4.7}$$

Any kind of mixture is possible under the condition that limit ε tends to zero, then η_ε tends to η to converge the solution towards a sharp interface solution. $H_\varepsilon(\alpha)$ is known from the equation (4.5) where ε is the interface thickness. The regularization can be done for all material parameters replaced by material fields varying everywhere in the global domain. The regularized model gives solutions that are close approximations of the solution of the original discontinuous model.

Once material properties are defined everywhere, the velocity field (v) can be computed in all computational domain $\boldsymbol{\Omega}$, and then, the motion of an interface Γi is obtained by the advection equation which regularizes the $u_\varepsilon(\alpha)$:

$$\begin{gathered} \frac{\partial u_\varepsilon}{\partial t} + v.\nabla u_\varepsilon = 0 \\ u_\varepsilon(t=0,\alpha) = u_{\varepsilon 0}\,(\alpha) \end{gathered} \tag{4.8}$$

$u_{\varepsilon 0}\,(\alpha)$ is the initial value of the function $u_\varepsilon(\alpha)$. The above equation (4.8) does not preserve any geometrical property of level set function, and the solution of the above equation is not a distance function. When the interface is advected, the gradient $|\nabla u_\varepsilon|$ can change and provokes instability in the numerical scheme. In order to solve the problem, the function $u_\varepsilon(\alpha)$ is maintained as a smooth distance function which possesses two following properties:

$$\begin{gathered} \nabla u_\varepsilon = n \ \text{ on } \Gamma i \\ |\nabla u_\varepsilon| \cong 1 \ \text{ at the interface} \end{gathered} \tag{4.9}$$

n in the above equation is the unit normal vector at the interface pointing inward. The gradient of the level set function is the representation of each level (0 level in particular). The underlying idea is to retrieve the above-mentioned properties. For this, one standard technique is to use a supplementary re-initializing procedure. It means that when the condition $|\nabla u_\varepsilon| = 1$ is violated, a second equation of the Hamilton-Jacobi type [47] is solved to find $\beta(\tau,\alpha)$, such that:

$$\frac{\partial \beta}{\partial \tau} + S(u_\varepsilon).(|\nabla \beta| - 1) = 0 \qquad \beta(\tau = 0, \alpha) = u_\varepsilon(t, \alpha) \tag{4.10}$$

Where $s(u_\varepsilon)$ is a sign function:

$$S(u_\varepsilon) = \begin{cases} S = 1 & \text{If } u_\varepsilon > 0 \\ S = 0 & \text{If } u_\varepsilon = 0 \\ S = -1 & \text{If } u_\varepsilon < 0 \end{cases} \tag{4.11}$$

The solution $\beta(\infty, \alpha)$ of equation (4.10) is the reinitialized distance function, and it satisfies $|\nabla \beta| = 1$ while keeping the contour line zero coinciding with one of $u_\varepsilon(t, \alpha)$. The function $u_\varepsilon(t, \alpha)$ may then be corrected by $u_\varepsilon(\infty, \alpha)$.

4.2.2 Convective re-initialization

Usually, when the computed distance function $u_\varepsilon(t, \alpha)$ has a gradient that is too far from 1, the re-initialization procedure is activated. This procedure adds an additional step in the computation. T. Coupez et al. [48] proposed a convective reinitialization method in which the reinitialization procedure is directly integrated into the advection equation:

$$\frac{\partial u_\varepsilon}{\partial t} + v.\nabla u_\varepsilon + \lambda.S(u_\varepsilon).(|\nabla u_\varepsilon| - 1) = 0 \qquad u_\varepsilon(t = 0, \alpha) = u_{\varepsilon 0}(\alpha) \tag{4.12}$$

Where λ is a numerical coefficient which depends on the mesh size and on the time step. If we define an initialization velocity as:

$$U = S(u_\varepsilon)\frac{\nabla u_\varepsilon}{|\nabla u_\varepsilon|} \tag{4.13}$$

One may substitute equation (4.13) in equation (4.12) to obtain a purely hyperbolic equation:

$$\frac{\partial u_\varepsilon}{\partial t} + (v + \lambda U).\nabla u_\varepsilon = \lambda.S(u_\varepsilon) \qquad u_\varepsilon(t = 0, \alpha) = u_{\epsilon 0}(\alpha) \tag{4.14}$$

In the above equation, $v + \lambda U$ is the convective re-initialization velocity. In order to determine λ, the Courant-Friendriechs-Lewy condition (CFL condition) and $|U| \approx 1$ are taken into consideration.

$$\lambda \approx |\lambda U| \approx \frac{h(U)}{\Delta t} \tag{4.15}$$

$h(U)$ is the element size (Figure 4-2) according to the direction of the re-initialization velocity.

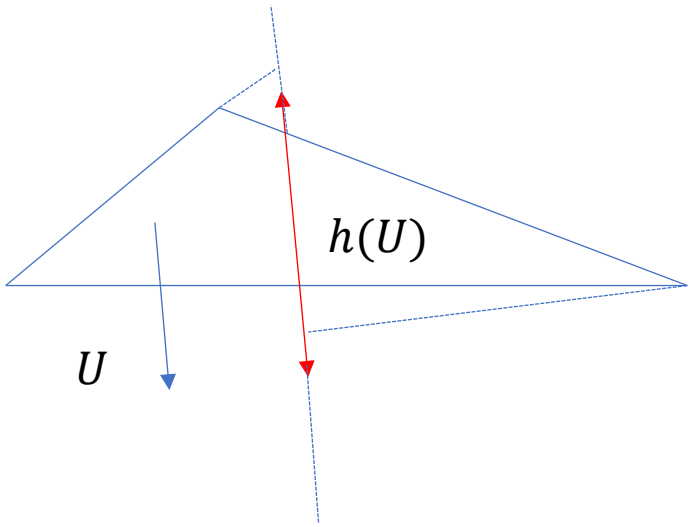

Figure 4-2 Measure on the element size according to the direction of the re-initialization velocity $U, h(u)$ [49].

4.2.3 Advecting a regularized function

As explained earlier, the decomposition of the computation domain in two phases is obtained by defining a distance function $u_\varepsilon(\alpha)$. The information we need is the exact position of the iso-value zero of this function representing the boundary. It shows that a complete solution of the distance function far from the iso-value zero is unnecessary. Singularity points on the boundary of the mesh, such as corners can cause numerical instabilities. Then these instabilities can propagate and create instabilities in the computation domain. In order to get rid of this problem, it is better to use another self-determinant function, which is regular near the interface and constant elsewhere. In order to respect this condition, a hyperbolic tangent function of the distance $u_\varepsilon(\alpha)$ has been chosen:

$$u_\varepsilon(\alpha) = u(\alpha, \varepsilon) = \varepsilon \tanh\left(\frac{\alpha}{\varepsilon}\right) \quad (4.16)$$

Where ε is once again the parameter that controls the thickness of the interface zone and $u_\varepsilon(\alpha, \Gamma i)$ is the distance function, which is positive if $\alpha \in \Omega$ and negative if $\alpha \notin \Omega$. Far from the region of the interface when $|\alpha| > 2\varepsilon$, the hyperbolic tangent function is nearly constant and equal to ε as $\varepsilon \geq |\alpha| > 0.964\varepsilon \approx \varepsilon$.

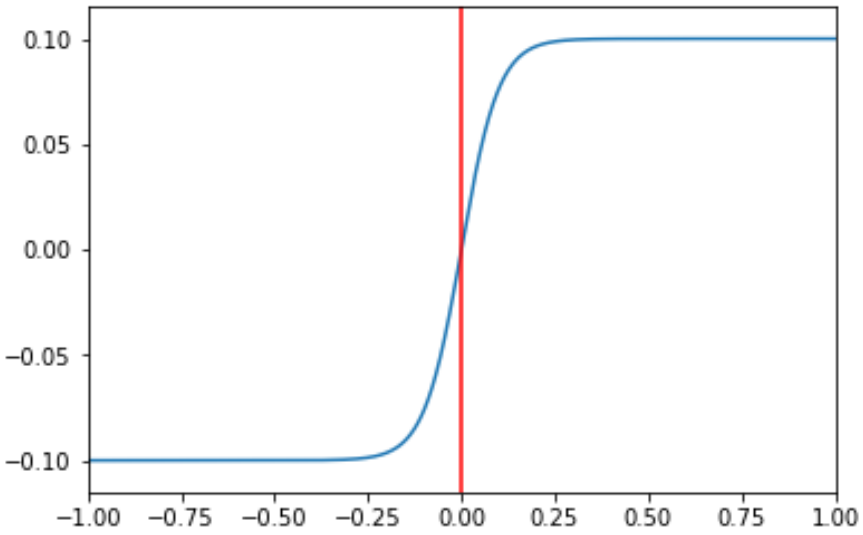

Figure 4-3 Analytical function, $y = 0.1 * \tanh\left(\frac{\alpha}{0.1}\right)$.

If we see the gradient of the hyperbolic tangent function, we have:

$$b = \varepsilon . tanh\left(\frac{\alpha}{\varepsilon}\right)$$

$$b' = 1 - \left(\frac{b}{\varepsilon}\right)^2 \quad (4.17)$$

In the above equation b is a arbitrary hyperbolic tangent function. The solution of the hyperbolic tangent function $u_\varepsilon(\alpha)$ satisfies:

$$|\nabla u_\varepsilon| = 1 - \left(\frac{u_\varepsilon}{\varepsilon}\right)^2 = g(u_\varepsilon)$$

$|\nabla u_\varepsilon|$ is not equal to one which is the case of standard distance function.

Using the property mentioned above in equation (4.12), one gets:

$$\frac{\partial u_\varepsilon}{\partial t} + v.\nabla u_\varepsilon + \lambda . S(u_\varepsilon).\left(|\nabla u_\varepsilon| - \left(1 - \left(\frac{u_\varepsilon}{\varepsilon}\right)^2\right)\right) = 0 \quad (4.18)$$

$$u_\varepsilon(t = 0, \alpha) = u_{\varepsilon 0}(\alpha)$$

If the convection re-initialization velocity $U = S(u_\varepsilon)\frac{\nabla u_\varepsilon}{|\nabla u_\varepsilon|}$ is put in the above equation, the final convection equation is obtained as:

$$\frac{\partial u_\varepsilon}{\partial t} + (v + \lambda U).\nabla u_\varepsilon = \lambda.S(u_\varepsilon).g(u_\varepsilon) \quad (4.19)$$

$$u_\varepsilon(t = 0, \alpha) = u_{\varepsilon 0}(\alpha)$$

4.2.4 Discretization and stabilization

The convective equation (4.19) presented above is solved using the Finite Element Method. Time discretization is done via the application of the Euler implicit scheme. A SUPG method is used to stabilize the convective term; otherwise, there can be numerical oscillation in the domain. If $\mathcal{T}_h$ is an unstructured triangular mesh of calculation domain $\boldsymbol{\Omega}_h$ in two dimensions which is tetrahedral mesh in three dimensions, then the functional space and weighting functional space are respectively defined by [50]:

$$V_h = \{u_h(x,t), u_h(x,t) \in C^0(\Omega_h), u_h|_k \in P^1(K) \quad \forall K \in \mathcal{T}_h \; \forall t\} \quad (4.20)$$

$$W_h = \{\widetilde{w_h}, \widetilde{w_h}|_k = u_h + \tau_{SUPG}.V.\nabla u_h \quad \forall K \in \mathcal{T}_h\}$$

In the above equation V_h is the functional space for velocity, W_h is the functional space for test function and u_h is the functional space for weight function. The SUPG stabilization parameter τ_{SUPG} is defined as:

$$\tau_{SUPG} \approx \left(\sum_{i=1}^{n} |V.\nabla N_i|\right)^{-1} \quad (4.21)$$

N_i is a polynomial of degree one which is equal to one at the node X_i and 0 at other nodes.

4.3 Stabilized finite element method for the resolution of the incompressible Navier-Stokes equations

The Navier-Stokes equations describe the motion of the different fluids. These equations arise from applying Newton's second law of the conservation of momentum. Let $\Omega \subset R^d$ be the spatial domain at time t ϵ [0, T], where d is the number of space dimension. The general form of the equations of fluid motion takes the form of:

$$\rho\left(\frac{dv}{dt} + v.\nabla v\right) - \nabla.\sigma = f \quad in\ \Omega \times [0,T] \quad (4.22)$$

Where v is the flow velocity, ρ is the fluid density, f is the body force vector (per unit volume), and σ is the total stress tensor.

If the fluid is incompressible and Newtonian:

$$\nabla . v = 0$$

$$\sigma = 2\mu\varepsilon(v) - pI_d \tag{4.23}$$

$$with\ \varepsilon(v) = \frac{1}{2}(\nabla v + \nabla v^t)$$

Replacing the expressions of equation (4.22) by the ones from equation (4.23), we obtain the Navier-Stokes equation for the Newtonian incompressible fluids as:

$$\rho\left(\frac{dv}{dt} + v.\nabla v\right) - \nabla.(2\mu\varepsilon v) + \nabla p = f \ \ in\ \Omega \ \times\ [0,T]$$

$$\nabla . v = 0 \ \ in\ \Omega \times [0,T] \tag{4.24}$$

The natural boundary conditions are,

$$v = k \ \ on\ \ \Gamma_g \times [0,T]$$

$$n.\sigma = h \ \ on\ \ \Gamma_h \times [0,T] \tag{4.25}$$

Where Γ_g and Γ_h are complementary subsets of the domain boundary Γ, n is the unit outward vector of Γ, and the initial condition is:

$$v(x,0) = v_0(x) \tag{4.26}$$

The initial condition should be inconsistent with the boundary condition. A weak formulation of the incompressible Navier Stokes equation is introduced, and the vectorial functional spaces for the velocity and the pressure are respectively defined by:

$$V = \{v(x,t) | v(x,t) \in H^1(\Omega)^d, \qquad v = k\ on\ \Gamma_g\ \}$$

$$Q = \{p(x,t) | p(x,t) \in L^2(\Omega)\ \} \tag{4.27}$$

Where H^1 represents the Sobolev space of functions which are square integrable as well as their derivatives. L^2 represents the space of functions whose square can be integrated. The functional space for the velocity is:

$$V_0 = \{v(x,t) | v(x,t) \in H^1(\Omega)^d, v = k\ on\ \Gamma_g\ \} \tag{4.28}$$

The weak formulation of the incompressible Navier Stokes equations consists in finding $(v, p) \in V \times Q$ such that:

$$\rho\left(\frac{dv}{dt},w\right)+\rho(v.\nabla u,w)_\Omega+\left(2\mu\varepsilon(v):\varepsilon(w)\right)_\Omega-(p,\nabla.w)_\Omega$$
$$=(f,w)_\Omega+(h,w)_{\Gamma_h}\ \forall w\ \in V_0 \qquad (4.29)$$
$$(\nabla.v,q)_\Omega=0\quad \forall q\ \in Q$$

Where $(\varphi,\psi)=\int_\Omega\ \psi\varphi d\Omega$, and $(\varphi,\psi)_{\partial\Omega}=\int_{\partial\Omega}\varphi\psi ds$.

In the above equation ρ is assumed to be constant. Assuming $\mathcal{T}_h$ to be an unstructured triangular mesh of the computational domain Ω_h in two dimensions (and a tetrahedral mesh in three dimensions). Using this partition $\mathcal{T}_h$, the functional spaces in equations (4.27) and (4.28) are approached by finite dimensional spaces spanned by continuous piecewise polynomials, such that

$$V_h=\{v_h(x,t)|v_h(x,t)\ \in\ C^0(\Omega_h)^d,v_h|_k\ \in P^1(k)^d,\quad \forall\ K\in\mathcal{T}_\mathrm{h}\}$$

$$Q_h=\left\{p_h(x,t)|p_h(x,t)\ \in\ C^0(\Omega_h)\ \ ,p_h|_k\ \in\ P^1(k),\quad \forall\ K\in\mathcal{T}_\mathrm{h}\right\} \qquad (4.30)$$

$$V_{0,h}=V_h\cap V_o$$

The Galerkin discrete problem consists of finding $(v_h,\ p_h)\ \in V_h\times Q_h$ for the following mixed problem:

$$\rho\left(\frac{\partial v_h}{\partial t},w_h\right)_\Omega+\rho(v_h.\nabla v_h,w_h)_\Omega+\left(2\mu\varepsilon(v_h):\varepsilon(w_h)\right)_\Omega-(p_h,\nabla.w_h)_\Omega$$
$$=(f,w_h)_\Omega+(h,w_h)\Gamma_\mathrm{h}\qquad \forall\ w_h\epsilon V_{o_h} \qquad (4.31)$$
$$(\nabla.v_h,q_h)=O\qquad \forall g_h\epsilon Q_h$$

The finite element discretization spaces for the velocity and pressure need to satisfy the "Ladyzhenskaya-Babuska-Brezzi (LBB) condition." If the interpolation functions are not used appropriately to represent velocity and pressure, then it can lead to unstable schemes in the computation domain [51] [52]. In our thesis, we are interested in studying the rise of calcium droplet or bubble in liquid steel, and since the rise of calcium droplet or bubble is a convection dominated problem, it can lead to numerical oscillation and pressure instability. The approximations presented above are not sufficient to prevent the solution oscillation. Therefore, the pressure and velocity fields need to be stabilized by the addition of stabilized terms, e.g., residual term weighted by tuned parameters.

4.3.1 Variational multiscale method

In order to stabilize the incompressible Navier-Stokes problem, the variational multiscale method is used, which has been developed by T. Coupez et al. [53]. The cause of the instabilities in the numerical computations are often due to the small-scale variations which cannot be taken into account by the generated mesh size [54]. These unresolved properties contaminate the computed quantities at the large scales. Although the objective is not to solve

the small-scale variations. The small scales have a significant effect on the resolvable scale, which is the one we wish to examine.

In the variational multiscale method, the physical quantities like functional spaces of the velocity and pressure are decomposed into the resolvable coarse scale and unresolved fine scale. The functional spaces are given as $V = V_h \otimes \mathrm{V}'$, $V_0 = V_{0,h} \otimes \mathrm{V}_0{}'$ and $Q = Q_h \otimes \mathrm{Q}'$. Decomposition of the velocity and the pressure is given by:

$$v = v_h + v\,', p = p_h + p' \tag{4.32}$$

Test functions are then decomposed as:

$$w = w_h + w\,', q = q_h + q' \tag{4.33}$$

The mixed finite element approximation in equation (4.29) is replaced by finding $(v,\ p) \in V \times Q$ such that: $\forall\ (w, q) \in V_0 \times Q$

$$\begin{aligned} \rho\left(\frac{\partial(v_h + v')}{\partial t},\ (w_h + w')\right) + \rho\big((v + v').\nabla(v_h + v'),\ (w_h + w')\big)_\Omega \\ + \big(2\mu\varepsilon(v_h + v'):\varepsilon(w_h + w')\big)_\Omega - \big(p_h + p',\ \nabla.(w_h + w')\big)_\Omega \\ = \big(f,\ (w_h + w')\big)_\Omega + \big(h,\ (w_h + w')\big)_{\mathcal{T}_h} \\ (\nabla.(v_h + v'),\ q_h + q')_\Omega = 0 \end{aligned} \tag{4.34}$$

The equation mentioned above is then split into two scales, one with having a coarse scale problem and another with the fine-scale problem. Coarse-scale resolution is defined as $\forall(w_h,\ q_h) \in V_{0,h} \times Q_h$.

$$\begin{aligned} &\rho\left(\frac{\partial(v_h+v')}{\partial t},\ (w_h)\right) + \rho\big((v_h + v').\nabla(v_h + v'),\ (w_h)\big)_\Omega + \big(2\mu\varepsilon(v_h + \\ &v'):\varepsilon(w_h)\big)_\Omega - \big(p_h + p',\ \nabla.(w_h)\big)_\Omega = \big(f,\ (w_h)\big)_\Omega + \big(h,\ (w_h)\big)_{\mathcal{T}_h} \quad \forall w_h \in V_{0,h} \\ &(\nabla.(v_h + v'),\ q_h + q')_\Omega = 0 \qquad\qquad \forall q_h \in Q_h \end{aligned} \tag{4.35}$$

The fine-scale one is written as: $\forall(w', q') \in V_0{}' \times Q'$

$$\begin{aligned} &\rho\left(\frac{\partial(v_h+v')}{\partial t},\ (w')\right) + \rho\big((v_h + v').\nabla(v_h + v'),\ (w')\big)_\Omega + \big(2\mu\varepsilon(v_h + \\ &v'):\varepsilon(w')\big)_\Omega - \big(p_h + p',\ \nabla.(w')\big)_\Omega = \big(f,\ (w')\big)_\Omega \quad \forall w_h \in V_{0,h} \\ &(\nabla.(v_h + v'),\ q')_\Omega = 0 \qquad\qquad \forall q' \in Q' \end{aligned} \tag{4.36}$$

The fine scale solution (v', p') is a function of coarse-scale solution. The resolution of equation (4.35) is complicated, and the following assumption is taken into consideration in order to simplify it:

- the fine-scale functional space is H^1-orthogonal to the coarse-scale space;
- the convective term is dominated by large-scale velocity and then is approximated using the coarse-scale velocity;
- the large-scale time-dependent residual effects the time dependence of fine-scale.

According to the assumptions as mentioned earlier, the fine-scale problem is reduced to:

$$\rho(v_h.\nabla v', w')_\Omega + \left(2\mu\varepsilon(v'):\varepsilon(w')\right)_\Omega - (\nabla p', w')_\Omega = (R_m w')_\Omega \quad \forall w' = V_0' \tag{4.37}$$

$$(\nabla.v', q')_\Omega = (R_c, q')_\Omega \quad \forall w' = V_0'$$

R_c and R_m are the moment residual and the continuity residual for the large resolved scales residual that are:

$$R_m = f - \rho\frac{\partial v_h}{\partial t} - \rho v_h.\nabla v_h - \nabla p_h \tag{4.38}$$

$$R_c = -\nabla.v_h$$

Even though taking these various assumptions, in the reduced fine-scale problem, the resolution of both velocity and pressure is complicated. Further suppositions have been taken, by only taking into consideration the effect of the fine-scale pressure on large scale pressure. T. Coupez et al. [53] proposed an approximate solution for the fine-scale pressure as defined below:

$$p' = \tau_c R_c \tag{4.39}$$

$$\tau_c = \left(\left(\frac{\mu}{\rho}\right) + \left(c\frac{\|v_h\|_k}{h}\right)^2\right)^{1/2}$$

In the above equation, h is the characteristic length of the element, whereas c is a constant independent of h. By assuming that the large-scale momentum residual R_m is constant for linear tetrahedral elements, the fine-scale velocity can be calculated as follows:

$$v'|_k = \tau_k R_m$$

$$\tau_k = \left(\left(\frac{2}{\Delta t}\right)^2 + \left(\frac{4\mu}{\rho h^2}\right)^2 + \left(\frac{2\|v_h\|_k}{h}\right)^2\right)^{-\frac{1}{2}} \tag{4.40}$$

When the final scale solutions are substituted in the coarse scale problem, the final equations obtained are:

$$\rho\left(\frac{\partial v_h}{\partial t},\ w_h\right)_\Omega + \rho(v_h.\nabla v_h,\ w_h)_\Omega + \left(2\mu\varepsilon(v_h):\varepsilon(w_h)\right)_\Omega - (p_h,\ \nabla.w_h)_\Omega - \sum_{k\varepsilon\mathcal{T}_h}(\tau_k R_m,\ \rho v_h\nabla w_h)_k + \sum_{k\varepsilon\mathcal{T}_h}(\tau_c R_c, \nabla.w_h)_k = (f,\ w_h)_\Omega + (h,\ w_h)_{\Gamma_h} \quad \forall w_h \in V_{0,h} \tag{4.41}$$

$$(\nabla.(v_h),\ q_h)_\Omega - \sum_{k\in\mathcal{T}_h}(\tau_k R_m,\ \nabla q_h)_k = 0 \qquad \forall q_h \in Q_h$$

The above equation can be decomposed into four main terms:

$$\underbrace{\rho\left(\frac{\partial v_h}{\partial t} + v_h.\nabla v_h,\ w_h\right)_\Omega + \left(2\mu\varepsilon(u_h):\varepsilon(w_h)\right)_\Omega - (p_h,\nabla.w_h)\Omega + (\nabla.(v_h),q_h)_\Omega - (f,w_h)_\Omega - (h,w)_{\Gamma_h}}_{Galerkin\ Terms}$$

$$\underbrace{+\sum_{k\in\mathcal{T}_h}\tau_k\left(\rho\frac{\partial v_h}{\partial t} + \rho v_h.\nabla v_h + \nabla p_h - f, \rho v_h\nabla w_h\right)_k}_{Upwind\ stabilization\ term}$$

$$\underbrace{+\sum_{k\in\mathcal{T}_h}\tau_k\left(\rho\frac{\partial v_h}{\partial t} + \rho v_h.\nabla v_h + \nabla p_h - f, \nabla q_h\right)_k}_{Pressure\ \ stabilization\ term}$$

$$\underbrace{+\sum_{k\in\mathcal{T}_h}(\tau_c - \nabla.v_h, \nabla.w_h)_k = 0 \quad \forall w_h \in V_{0,h}\,\forall q_h \in Q_h}_{Grad-div\ \ stabilization\ term}$$

In the final formulation, some additional integrals are obtained by replacing the approximated finite-scale solution to the large-scale solution. The stabilization term resolves the instability term associated with the convection term, and it overcomes the pressure instability too. Several other different approximations for stabilization can be found in different literature [55] [56].

In multiphase flow, the physical parameters like stress, strain across the interface also need to be calculated appropriately. Isotropic refinement of mesh at the interface can be used to reach the desired accuracy, but it can lead to an increase in computation cost. Therefore, it is preferred to use the adapted anisotropic meshes. The section below presents the anisotropic mesh adaptation method used in ICI tech.

4.4 Anisotropic mesh adaptation

In ICI-tech, an automatic anisotropic mesh adaptation technique is used. In numerical simulations, coupling the adaptive finite element analysis with error estimation has many

advantages. Simplified geometries can be constructed with a coarse isotropic mesh, but mesh refinement is critical at the interfaces for two reasons: firstly, because of the different physical and thermodynamic properties of the different phases; secondly, to pre-adapt complex three-dimensional geometries more precisely at the sharp corners [57]. As compared to an isotropic mesh, the generation of anisotropic meshing is more difficult and more complicated since the refinement is realized in a specific direction [58] and a posteriori estimator [59] [60] is used to compute the metric fields used in anisotropic adaptation. The use of anisotropic mesh offers the following advantages:

- capturing the interface between subdomains;
- comparing to an isotropic mesh a significant number of nodes is saved, which provides a lower, computational time and less memory capacity;
- construction of a metric field that fixes the mesh size in the Level set gradient direction.

Several adaptation methods exist, the most common are the following:

- h-adaptation, which changes the mesh size, generally the refinement is done in a specified region,
- p-adaptation, which increases the polynomial order of the shape function. It involves the enrichment of local element's degrees of interpolation,
- r-adaptation, which reposition the nodes especially near the interface without affecting its topology,
- hp-adaptation, it is a combination of h- adaptation and p- adaptation.

In order to solve our numerical problem in ICI tech, h-adaption is used [61]. The numerical solution is computed in the initial coarse mesh, and mesh refinement is obtained in certain regions where the solution errors are important.

For example, in two-phase flow, in order to adapt the mesh, error on the velocity field and on the advected phase function is taken into account. The main steps needed to adapt the mesh are explained in this section. Let Ω c R^d be a polynomial domain, and there is a discretization $\Omega = U_{k\varepsilon k}$ where k is simplex, such as a triangle (2D) or tetrahedron(3D). Let $\mathbb{Z}(i)$ be the "patch" associated with a vertex x^i of the mesh defined as the set of nodes which share one edge with x^i, and let us denote by x^{ij} the edge connecting x^i to x^j. The problem of finding a unitary metric M^i associated with the i^{th} node can be formulated as a least squares problem [62]. Let A be an analytic solution defined on the computational domain and let N denote the desired number of edges for the mesh. The aim is to create the "best" mesh H, i.e., the optimal metric M, to minimize the interpolation error $\|A - \pi_h A\|_1$ in L_1 norm. $\pi_h A$ is the linear interpolate of A on H. The local interpolation error distributed over the edges in the neighborhood of point a is written as:

$$e_M(a) = \frac{1}{2}\sum_{ij} S_{ij}^2 e_{ij} = \frac{1}{2}\sum_{ij} S_{ij}^2 \left| g^{ij}.X^{ij} \right| \qquad (4.42)$$

Where S_{ij} stands for mesh scaling factor, e_{ij} represents the error and g^{ij} represents the gradient along and in the direction of the edge x^{ij}. For a given number of edges N, the L_1 norm of error, the following problem is solved:

$$\min \epsilon\,(M) = \min \int_{\Omega} |e_M| d\Omega \tag{4.43}$$

Under the constraint:

$$C(M) = \left(\sum_{ij} n_{ij} \right) = N \tag{4.44}$$

Where n_{ij} is the evaluation of the number of created edges in relation to the scaling factor S_{ij}. The resulting optimal metric solution of the equation (4.43) for the L_1 norm in the three dimensions is expressed as:

$$M^i = \left(\frac{1}{d} \sum_{j \epsilon \Gamma(i)} \left(s_{ij}\right)^2 X^{ij} \otimes X^{ij} \right)^{-1} \tag{4.45}$$

Where,

$$S^{ij} = \left(\frac{\lambda}{e_{ij}} \right)^{1/P'} \tag{4.46}$$

$$\lambda = \left(\frac{\sum_i \sum_{j \in \Gamma(i)} e_{ij}^{\frac{p'}{p'+2}}}{N} \right)^{\frac{(p'+2)}{p'}} \tag{4.47}$$

p' is a penalty factor.

The recovered edge gradient g^{ij} is reconstructed from the numerical solution A_h by solving the following minimization problem:

$$g^{ij} = argmin \sum_{j\in\Gamma(i)} \left|(g - \nabla A_h).X^{ij}\right|^2 = argmin \sum_{j\in\Gamma(i)} \left|g.x^{ij} - (A_h(x^j) - A_h(x^i)\right|^2 \quad (4.48)$$

From equation (4.48) and equation (4.45), an approximation of the metric is derived. Then, an adapted mesh is generated with respect to the metric where the aim is to generate a mesh such that all edges have a length equal or close to unity in the prescribed metric and such that all elements are almost regular. The volume is adapted by local mesh modification of the previous mesh using local mesh operations: node insertion, edge and face swap, collapse, and node displacement. Finally, on the new mesh, the solutions (velocity, pressure, α) are linearly interpolated. In a static adaption, this procedure is repeated up to convergence. The process is considered converged when the difference between the two metrics is small.

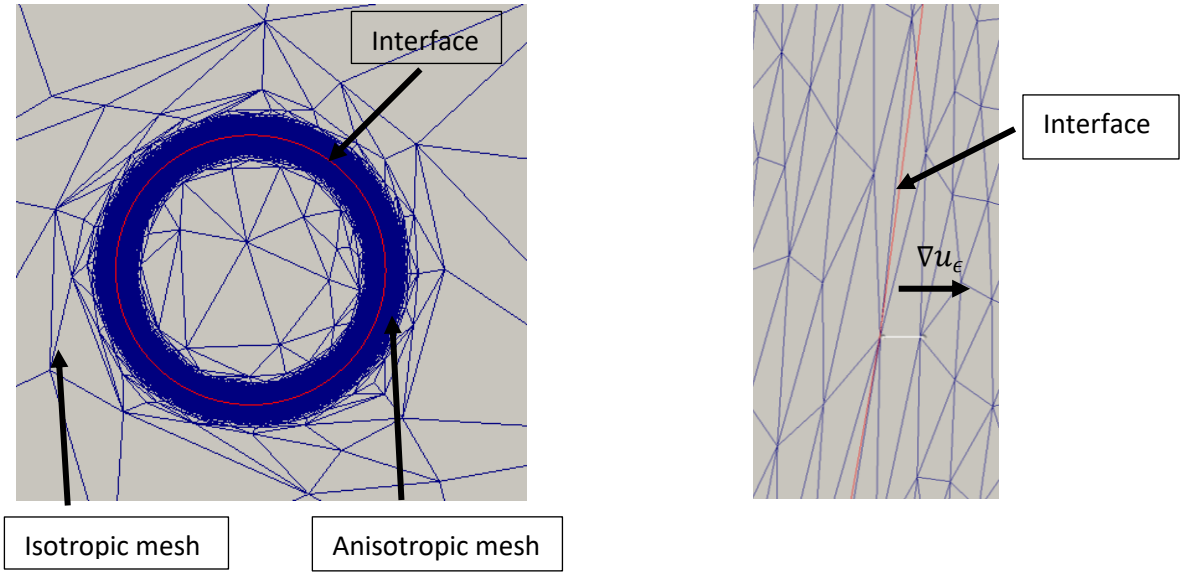

Figure 4-4 (a) Representation of a 2D interface with an anisotropic mesh technique (b) closer view of the interface.

4.5 Numerical test

In this section, a simple numerical test is performed, which demonstrates the capability of our code (ICI-tech) to predict the behavior of the rising bubble (air) at the surface of the water-air interface. In our experiments bursting of calcium droplet/bubble has been observed at the surface of liquid steel; therefore, in the beginning, we studied the bursting phenomenon of a bubble at the free surface. Different authors have studied the bursting phenomenon at the free surface, e.g. L. Duchemin et al. [63], B.Y. Ni et al. [64], C.H. Yu et al. [65]. In order to study this bursting phenomenon, we took B.Y. Ni et al. [64] as the reference. No slip boundary

condition is applied on the walls of the domain. The calculation domain used for the simulation can be seen in Figure 4-5.

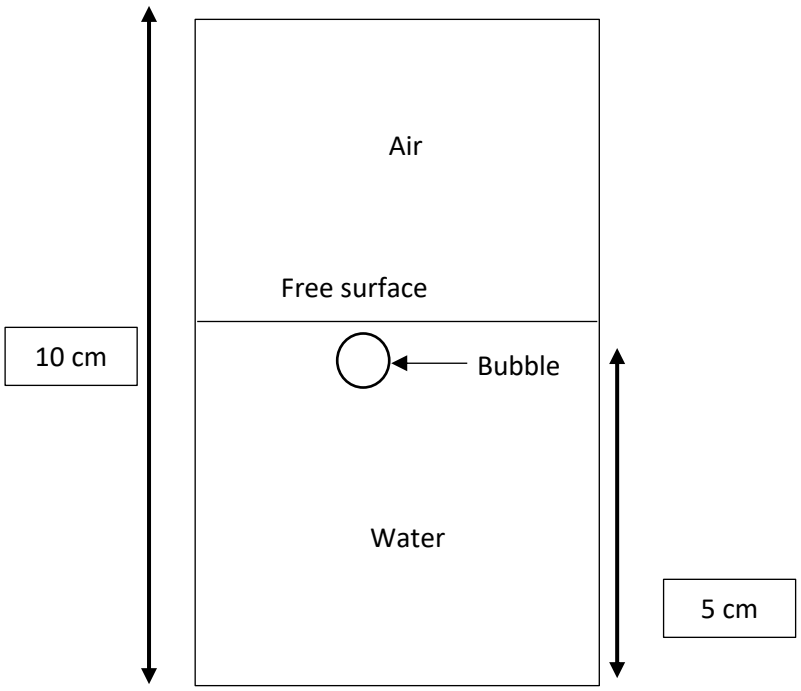

Figure 4-5 Calculation domain for simulation of bursting bubble at the free surface.

Radius (R_0) of the bubble is taken as 0.375 cm, and the bubble is kept just below the free surface (bubble is kept 0.4 cm below the free surface) to simplify the bubble rising process. Physical properties and numerical parameters that are taken for computing the rise of the bubble in water medium can be seen in Table 4-1 and Table 4-2, respectively. L_{max} and h_{min} in Table 4-2 represent the interface thickness (ε) and minimum cell size at the interface. Navier Stokes equation (4.24) with surface tension is solved. No slip boundary condition is taken at the wall of the domain. Initially, the bubble is kept at rest in the water medium, and because of the density difference between bubble and water, the bubble tends to rise. The evolution of the bubble rise with the time is computed that can be seen in Figure 4-6. Physical conditions are similar to what has been taken by B.Y. Ni et al. [64]. It has been illustrated by B.Y. Ni et al. [64] that, when the internal pressure of the bubble is high relative to the ambient pressure, and the submergence is relatively small, the bubble will burst through the free surface.

ρ_w	1000 (kg/m^3)
μ_w	0.001 (Pa.s)
ρ_b	1 (kg/m^3)

μ_b	0.00001 (Pa.s)
σ_{wb}	0.072 (N/m)
Bond number (Bo)	7.8
Morton number (Mo)	2.67e-11

Table 4-1 Physical properties for the bubble and water.

L_{max} (ε)	0.0001 (m)
h_{min}	0.00005 (m)
Δt	0.00001 (s)

Table 4-2 Numerical parameters for simulation.

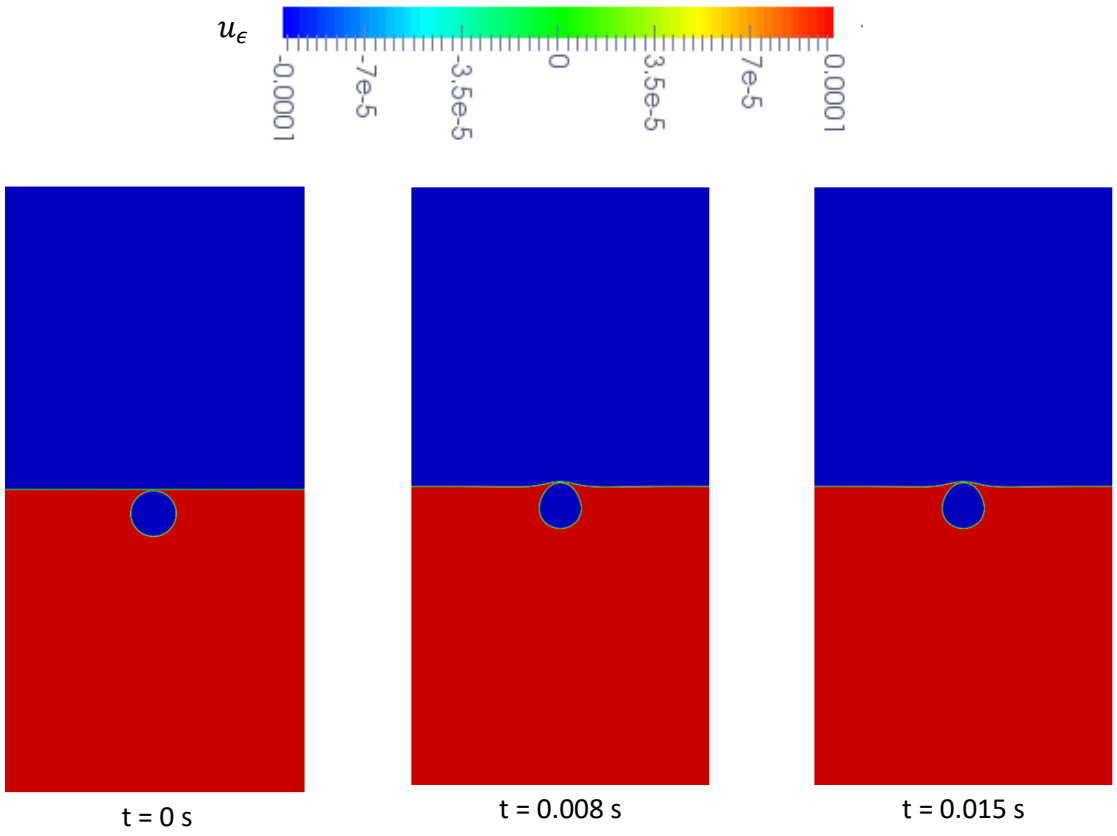

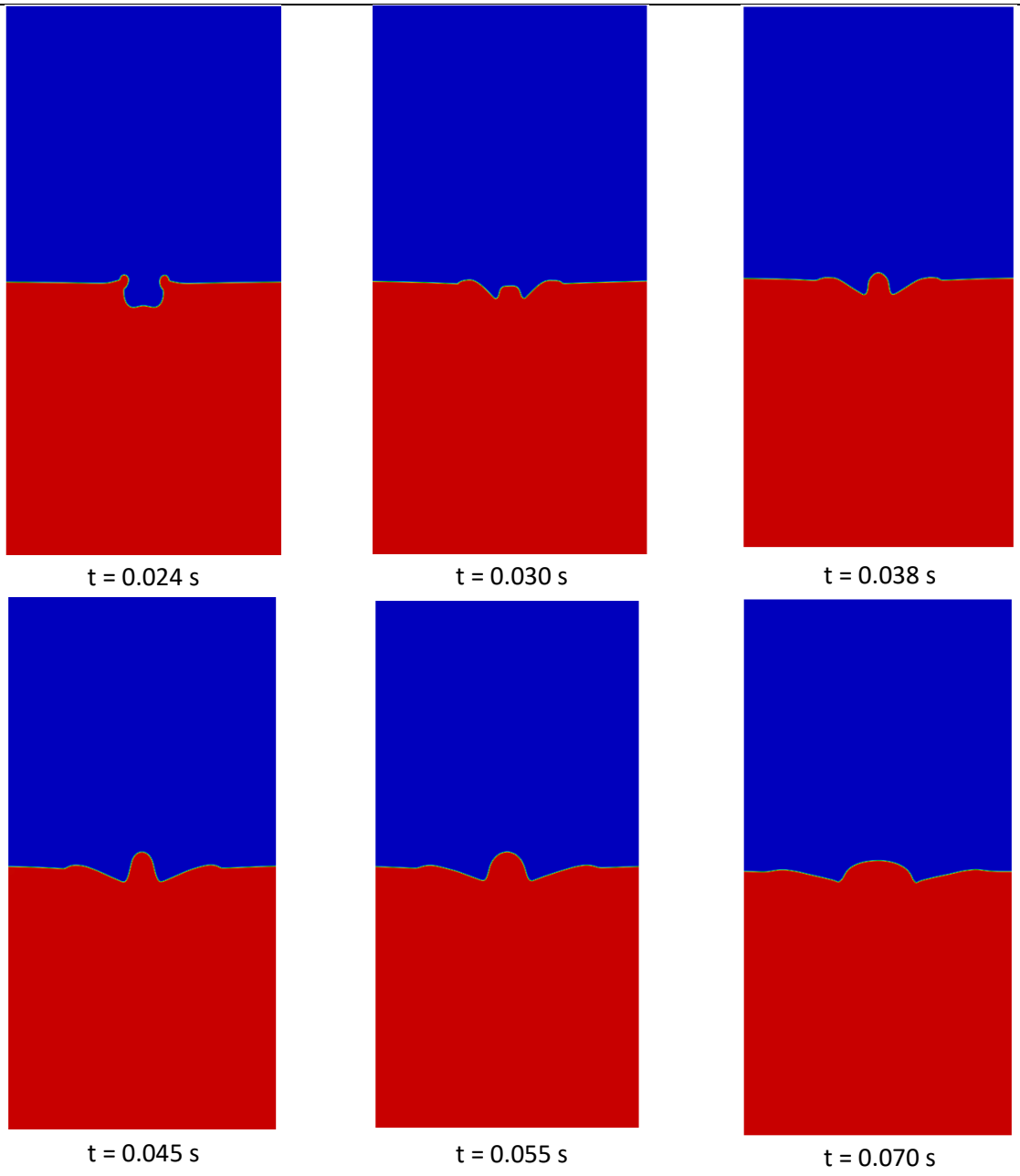

Figure 4-6 Simulation results of the bursting bubble at the free surface.

The numerical results (Figure 4-5) obtained showed that the ICI tech can simulate the progress successfully. The important steps which are being captured numerically are bubble rising, jet development (first peak formation), free surface rising and falling as well as the wave oscillation and propagation, which resembles the same as obtained by B.Y. Ni et al. [64] except the second peak formation. B.Y. Ni et al. [64] mentioned that the bubble bursting phenomenon and the different consequent steps depend on the Froude number (Fr), strength parameter (ζ) and distance parameter (λ).

$$Fr = \sqrt{\frac{P_\infty}{\rho_w g R_0}} \tag{4.49}$$

$$\zeta = \frac{P_0}{P_\infty} \tag{4.50}$$

$$\lambda = \frac{h}{R_0} \tag{4.51}$$

In the expression of Froude number (Fr), P_∞ is the ambient pressure, ρ_w is the density of the water, and R_0 represents the initial bubble radius. In equation (4.50) ζ is the strength parameter, P_0 represents the initial bubble pressure, and P_∞ represents the ambient pressure. In equation (4.51), λ is the distance parameter, h represents the distance between the center of the bubble and the free surface. B.Y. Ni et al. [64] explained that the bursting of the bubble occurs at large ζ (strength parameter) and small λ (distance parameter) whereas the peaks and troughs of the free surface, as well as its oscillation, depend on the Froude number.

We studied only the effect of the distance parameter (λ) on the jet development of the bubble rising in the liquid medium. Simulation has been performed for two different distance parameters (λ_0, λ_1) and corresponding jet height has been analyzed. It is observed that as the λ increases, the jet height becomes more advanced (Figure 4-7). The same behavior has been observed by B.Y. Ni et al. [64]. Thus, we can say that our code correctly predicts the effect of λ on jet height.

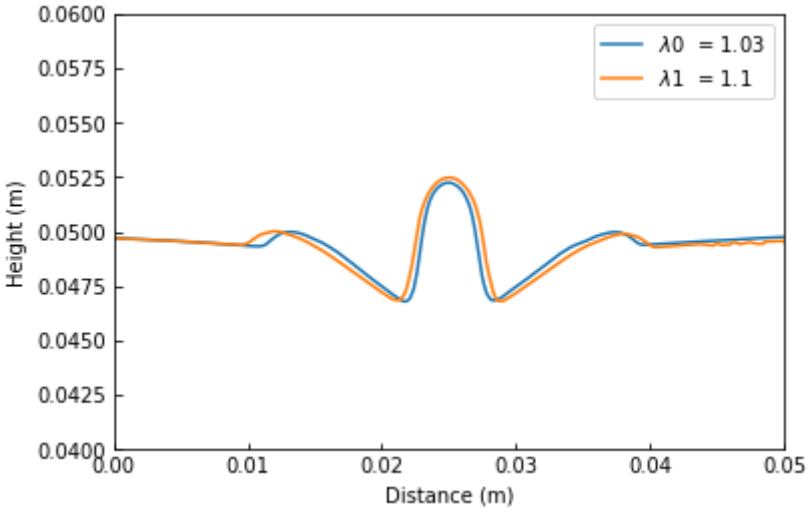

Figure 4-7 Position of the peak with different strength parameter

4.6 Conclusion

In this chapter, the numerical methods used in the ICI-tech library are presented. In the beginning, an implicit method that is used to capture the interface and the Immersed volume method is explained. It is shown that this method is based on the level set, mixing laws and mesh adaptation. The level set method is used to define the interface in the multiphase flows, and the mixing law is used to determine the physical properties inside the domain. Mixing law ensures the continuity of the physical properties at the interface.

Afterward, a convective derivative in the reinitialization of the level set is presented. This methodology allowed to retain the unitary gradient for the level set function at the interface. In this way, the basic properties of the level set are preserved when it is convected. Then the stabilized finite element method for the resolution of the incompressible Navier Stokes equation is presented, and the advantage of multiscale decomposition (VMS) applied to the weak form of the Navier Stokes equation is explained. In the end, to test our numerical software (ICI-Tech), a simple numerical simulation is presented where the rise of the bubble at the water-air free surface is studied.

4.7 Résumé Français

Dans ce chapitre, les méthodes numériques utilisées dans la bibliothèque ICI-tech ont été présentées. Au début, une méthode implicite pour capturer l'interface et la méthode volume immergé a été expliquée. Il a été démontré que cette méthode est basée sur un ensemble de niveaux, des lois de mélange et l'adaptation de maillage. La méthode de définition de niveau sert à définir l'interface dans les flux multiphases et la loi de mélange permet de déterminer les propriétés physiques à l'intérieur du domaine. Il assure la continuité des propriétés physiques à l'interface. Ensuite, une dérivée convective de la réinitialisation de l'ensemble de niveaux est présentée. Cette méthodologie a permis de conserver un gradient unitaire pour la fonction « level set » à l'interface. De cette manière, les propriétés de base du « level set » sont préservées lors de la convection. Ensuite, la méthode des éléments finis stabilisés pour la résolution de l'équation incompressible de Navier Stokes est présentée et l'avantage de la décomposition multi-échelle (SMV) appliquée à la forme faible de l'équation de Navier Stokes est expliquée. Enfin, afin de valider notre code, un calcul simple étudiant la montée de bulle à la surface libre eau-air est présenté.

Chapter 5:

Three Phase Flow and Dissolution Model

5 Three-phase flow and dissolution model

Three phase flows are quite common in industrial processes, e.g., in the steel industry, petroleum industry, nuclear industry, etc. The interaction of different phases is noticeable in these industries, and their interactions can lead to a complex chemical and physical phenomenon occurring between them. Either because of the calcium phase change taking place in the ladle or because of the liquid calcium droplets bursting at the air/steel surface, all these phenomena are three phase problems. Therefore, to understand the complex behavior of calcium in liquid steel, three-phase flow needs to be modeled. In pursuance of studying this complex problem, ICI-tech has been further developed to take into account such a three-phase flow. The development of three-phase flow in ICI-tech is explained in the section below.

5.1 Surface tension implementation

5.1.1 Circumventing the ternary point problem

One delicate point on a three-phase system is how surface tension forces (usually computed at each paired interface) can be computed. In the literature, authors N. Tofighi et al. [66], F. Boyer et al. [67], J. Kim [68], J. Bruchon et al. [69] have proposed different formulation for modeling incompressible, three-phase fluid flows, e.g., N. Tofighi et al. [64] used a continuum surface model to transform local surface tension force to a volumetric force using smooth color function.

In our case, the improvement of a previous version of ICI-tech (only being able to take into account surface tension on one interface) has been done to treat such a three-phase problem. The introduction of three-phase flows is delicate in terms of surface tension force calculation. Its implementation procedure is explained below.

Firstly, let us consider the two-phase flow case (Figure 5-1). Equations describing this immiscible flow are the Navier-Stokes equations, under the hypothesis of incompressibility. Contribution of surface tension forces, denoted by f_{st}, is obtained by adding a term (applied at the interface between the two phases) to the gravity forces. These equations can be thus written as, under appropriate boundary conditions:

$$\rho(\partial_t v + v.\nabla v) + \nabla p - \nabla.(\mu\big(\nabla v + (\nabla v^T)\big) = \rho g + f_{st} \;\; in\, \Omega \times [0,T] \tag{5.1}$$

$$\nabla.v = 0 \; in\, \Omega \; \times [0,T] \tag{5.2}$$

Where ρ and μ are the density and the dynamic viscosity, v and p denote the velocity field and the pressure field, g is the gravity force.

Variational form of this problem will introduce an integral over the interface, which has been treated in a volumetric way, using a localized surface tension force like the one given by [70]:

$$< f_{st}, w >_{\Gamma_{12}} = \int_{\Gamma_{12}} \sigma_{12}\kappa_{12}n_{12}.w = \int_{\Omega} \delta_{\Gamma 12}F_{12}.w \qquad (5.3)$$

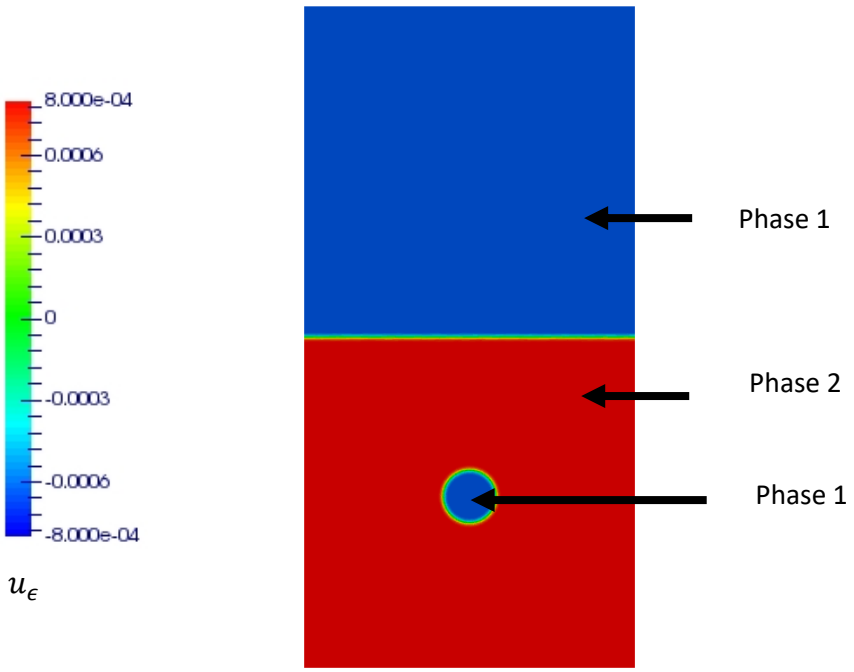

Figure 5-1 Two phase system with surface tension force calculation only at the one interface (two phases represented by one phase function)

In equation (5.3) F_{12} is the surface tension force, unique f_{st}, having one interface between phases 1 and 2. σ_{12} is the surface tension coefficient between the phases and the Dirac function, $\delta_{\Gamma 12}$ is the derivative of the Heaviside function that allows us to represent the phases. One Heaviside function is necessary to represent the whole problem, obtained from the advected modified level-set function. Supposing that we have defined one of the phases (phase 1), we recall the expressions for our phase function, the smoothed Heaviside and of the Dirac function:

$$u_{\varepsilon 1} = \frac{1}{\varepsilon}\tanh[\frac{d(x,\Gamma_{12})}{\varepsilon}] \text{ (advected function)}$$

$$H_{\varepsilon 1} = \frac{1}{2}[1 - \left(\frac{u_{\varepsilon 1}}{\varepsilon}\right)^2] \text{ (smooth Heaviside for phase 1)} \qquad (5.4)$$

$$\delta_{\Gamma 12} = \delta_{\varepsilon 1} = \frac{1}{2\varepsilon}[1 - \left(\frac{u_{\varepsilon 1}}{\varepsilon}\right)^2] \text{ (smooth Dirac of phase 1)}$$

The complementary of phase 1 (phase 2) has its Heaviside on each point of the domain equal to $H_{\varepsilon 2}(x) = 1 - H_{\varepsilon 1}(x)$. The normal to the interface (n_{12}) can be determined as the gradient of our level-set function:

$$n_{12} = n_{\varepsilon 1} = \frac{\nabla u_{\varepsilon 1}}{\|\nabla u_{\varepsilon 1}\|} \quad (5.5)$$

The curvature (K_{12}) is related to the divergence of the normal, as

$$\kappa_{12} = \kappa_1 = -\nabla . n_{12} \quad (5.6)$$

Thus, in the surface tension expression, the computation of the Dirac is needed ($\delta_{\varepsilon 1}$), but also the normal to the boundary (n_1, that is the normalized gradient of u_ε in the formulation) and the curvature which is the divergence of the normal, is needed. Since we have fields defined at nodes and gradient is computed at the element. Therefore a gradient recovery procedure is necessary at nodes; otherwise, it is not possible to have the curvature explicitly. For that, the nodal is obtained directly at the nodes, using the values of $u_{\varepsilon 1}$ along the edges, as detailed in T. Coupez et al [71]. It is first applied to equation (5.5) and then to equation (5.6), to get $G_1(x)$ recovered gradient and $K_1(x)$ curvatures respectively.

The second important point is that all this methodology is based on the fact that the interface has a certain thickness, ε (L_{max}). The convergence of the solution towards a sharp interface one is necessarily obtained by decreasing ε, but we have to ensure that, in this thickness, there are enough elements to represent u_ε (that is a hyperbolic tangent), the Heaviside or the Dirac function. This has been ensured by using our formerly described automatic anisotropic mesh adaptation procedure at the interface [71], building an error estimator that depends on several of these fields.

For three-phase flow, the above procedure has been adapted. In that case, one has to advect two phase functions that will allow us to determine all the Heavisides, normals and Diracs. In fact, a fluid particle may be affected by more than two interfaces simultaneously, which is the case near triple junctions where all the three phases meet. This is a problem that has been widely studied in the literature (in particular when one of the phases is a solid, less when the three are fluid). (R. Guillaument et al. [72], J. Bruchon et al. [69]).

In our case, the three level-sets being transported do not ensure ($\sum H_\varepsilon = 1$), or $H_{\varepsilon 2}(x) = 1 - H_{\varepsilon 1}(x) - H_{\varepsilon 3}(x)$. On the one hand, one needs to still keep this formulation for the level-sets. If one chooses to build other functions that separate advection and force at the same interface, undefined phases at some points may appear. Therefore, one needs Heaviside functions that respect the above condition (partition of unity), so that the ternary point (point of interaction of three phases) is well solved.

To circumvent this problem, we have chosen to build, once advection of the two level-set has been performed, color functions, $H^c_{\varepsilon i}$, represented schematically in Figure 5-3. These latter are computed as (one may also build "color level-set" ($u_{\varepsilon i}$)):

a) for phase 1 (the "background phase," in blue), the color function is the same as the Heaviside function,

$$H_{\varepsilon 1}^{c} = H_{\varepsilon 1}$$

$$u_{\varepsilon 1}^{c} = u_{\varepsilon 1} \quad (5.7)$$

b) for phase 2, in green, one may specify that it comes from the difference between the Heaviside and the formerly computed value for phase 1, restrained to positive values,

$$H_{\varepsilon 2}^{c} = H_{\varepsilon 2} - H_{\varepsilon 1}^{c} \quad \text{and} \quad H_{\varepsilon 2}^{c} \geq 0$$

$$u_{\varepsilon 2}^{C} = [2 \times H_{\varepsilon 2}^{c} - 1] \times \varepsilon \quad (5.8)$$

c) for phase 3, in red, one gets the default value that provides ($\sum H_{\varepsilon\alpha}^{c} = 1$),

$$H_{\varepsilon 2}^{c} = 1 - H_{\varepsilon 1}^{c} - H_{\varepsilon 3}^{c}$$

$$u_{\varepsilon 3}^{c} = [2 \times H_{\varepsilon 3}^{c} - 1] \times \varepsilon \quad (5.9)$$

By using the above equations (5.7, 5.8, 5.9), we have, $\sum_{\alpha=1}^{3} H_{\varepsilon\alpha}^{c} = 1$. Thus, the color functions ($H_{\varepsilon\alpha}^{c}$) have value one wherever phase α is present while the other color functions are zero in that phase. Introducing this new phase functions will give us a slightly different way of computing surface tension forces, as explained in the section below.

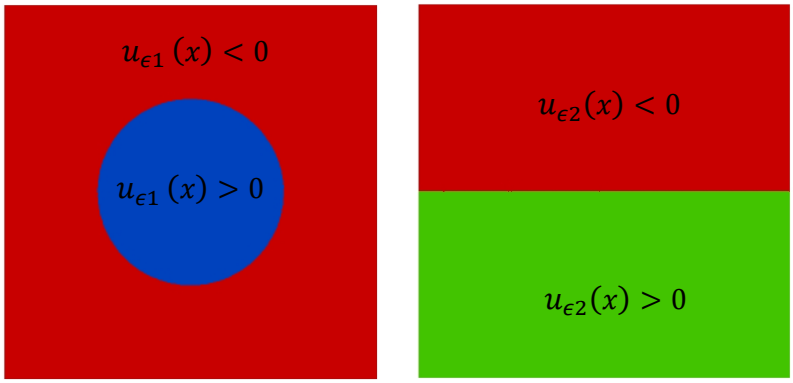

Figure 5-2 Two phase function used for advection in three phase problem

Remarks: The order is important; both to compute surface tension, but also to extend the formerly described mixture laws that provide property distribution in the whole domain. In our experimental case, for calcium droplet rising in liquid steel and bursting at the steel/air interface, one has: phase 1 is the calcium droplet; phase 2 is the steel, and phase 3 is the "background one," is the air. One other important point is that the two-phase flow is included in this case also.

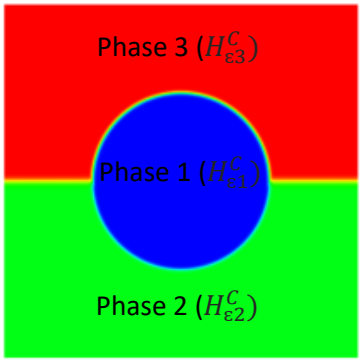

Figure 5-3 Color Heavyside function for each phase.

5.1.2 Computing the surface tension forces

In three-phase flow, we now compute the normal, the Dirac, and the curvatures using the color phase function of each phase separately. This means that the surface tension force is now calculated per phase ($\delta_{\Gamma\alpha}F_{\alpha}$), instead of at the interface. Then, the resultant volumetric surface tension force can be determined as the sum of surface tension force per phase ($f_{st} = \sum_{1}^{3}(\delta_{\Gamma\alpha}F_{\alpha})$), using equation (5.10):

$$f_{st} = \delta_{\Gamma 1}F_1 + \delta_{\Gamma 2}F_2 + \delta_{\Gamma 3}F_3 \tag{5.10}$$

Being:

$$F_{\alpha} = \sigma_{\alpha}\kappa_{\alpha}{}^{c}n_{\alpha}{}^{c} \tag{5.11}$$

The decomposition of the surface tension coefficient into phase-specific surface tension has been proposed by other authors [73], in which $\alpha^{\alpha\beta} = \sigma^{\alpha} + \sigma^{\beta}$. $\sigma^{\alpha\beta}$ is the physical surface tension between phase α and β, while σ^{α} and σ^{β} are the specific surface tension coefficients for αth and βth phases, respectively. The decomposition of the surface tension coefficient per phase can be expressed as (N. Tofighi et al. [66]):

$$\begin{aligned}\sigma^{1} &= 0.5(\sigma^{12} + \sigma^{13} - \sigma^{23})\\ \sigma^{2} &= 0.5(\sigma^{12} - \sigma^{13} + \sigma^{23})\\ \sigma^{3} &= 0.5(-\sigma^{12} + \sigma^{13} + \sigma^{23})\end{aligned} \tag{5.12}$$

Once the three-phase implementation was done, we studied its validation.

5.2 Validation of three-phase flow simulations

Validation of three-phase flow has been performed using the spreading of a liquid lens problem. Simulation results are presented, and the results are compared against the analytical equilibrium result. The typical configuration of this test is shown in Figure 5-4, where a three-interface contact angle is computed, resulting from the spreading of the lens on an interface [74]. The computation domain of $1m^2$ and $1m^3$ is taken, respectively, in 2D and 3D. The initial radius of the lens is taken as 0.25 m. All the fluid properties in each phase, such as density, viscosity, and surface tension for all the interfaces have the value 1 (in their respective units).

No slip condition is applied at all the boundaries in the Navier Stokes equations resolution. h_{min} (minimum cell size at the interface) is imposed as 0.01m at the interface. The timestep of 2e-04 seconds is taken for the simulation. These values verify the capillary time step restriction, which is given by [75]:

$$\Delta t^{cap} < \sqrt{\frac{\rho h_{min}^3}{\sigma}} \tag{5.13}$$

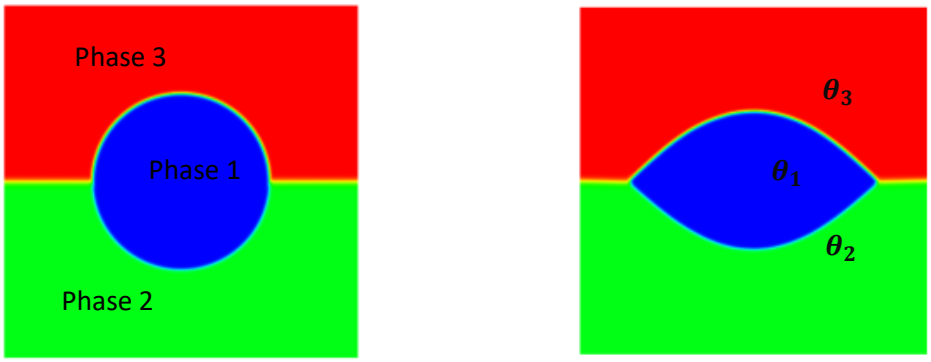

Figure 5-4 Lens benchmark for three-phase flows: (a) initial and (b) equilibrium phase profile (2D), when surface tensions are the same for all the phases.

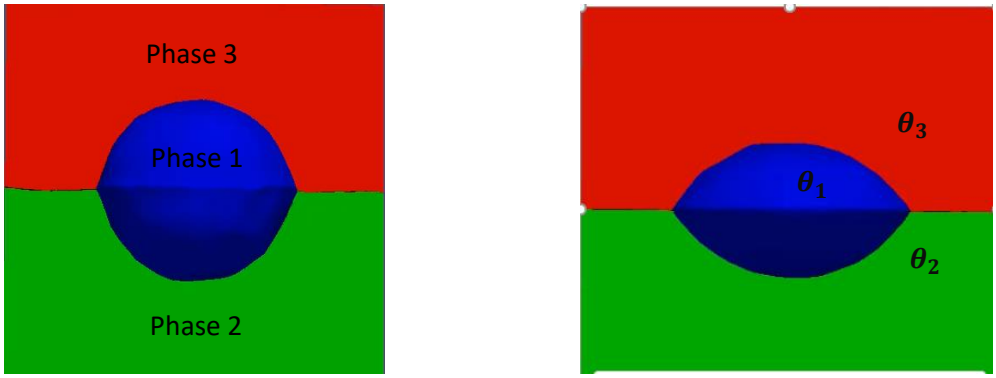

Figure 5-5 Lens benchmark for three-phase flows: (a) initial and (b) equilibrium phase profile (3D), when surface tensions are the same for all the phases.

The equilibrium contact angles are determined by

$$\frac{sin\theta_1}{\sigma_{23}} = \frac{sin\theta_2}{\sigma_{13}} = \frac{sin\theta_3}{\sigma_{12}} \tag{5.14}$$

where θ_1, θ_2, and θ_3 are the three-phase contact angles.

If the surface tension in all the three phases is the same ($\sigma_{23} = \sigma_{13} = \sigma_{12} = 0.5$) then the equilibrium contact angle according to the equation (5.14) is found to be 120°. In what concerns the numerical results, we have measured the equilibrium contact angle using the

ImageJ software. The equilibrium contact angle obtained numerically ($\theta_1 = \theta_2 = \theta_3 = 120°$) is found to be in good agreement with the analytical equilibrium contact angle.

5.2.1 Mesh sensitivity study

Mesh sensitivity study has been performed for the equilibrium contact angle obtained numerically. All the physical and numerical parameters are kept the same as the above problem except the minimum cell size (h_{min}) at the interface. Simulations are performed for three different values of h_{min} which are taken as 0.009 m, 0.008 m, and 0.007 m respectively.

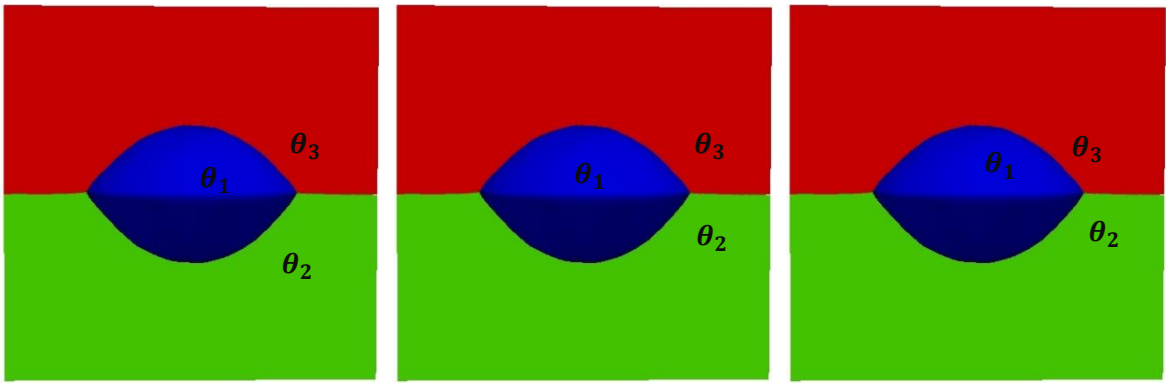

h_{min} = 0.009 m h_{min} = 0.008 m h_{min} = 0.007 m

Figure 5-6 Equilibrium phase profile for different mesh size at the interface.

It is found that, for different values of h_{min}, the equilibrium contact angle is identical, i.e. ($\theta_1 = \theta_2 = \theta_3 = 120°$). Thus, we can say that the equilibrium contact angle obtained numerically is mesh independent for h_{min} value smaller than 0.01m.

5.2.2 Equilibrium contact angle case study

Case studies (2D, 3D) have been done for the three phases where different values of surface tension are assigned to different phases, and the spreading of the lens at the interface has been studied. A time step of 2e-04 seconds is taken for computing the problem, and no-slip boundary condition is applied at the walls of the domain.

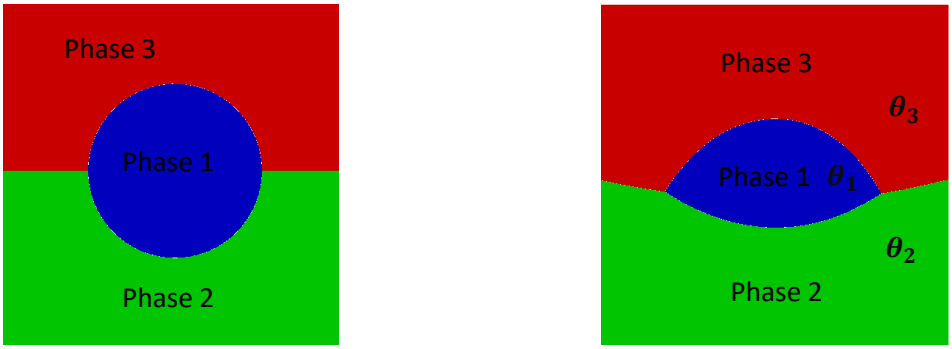

Figure 5-7 Lens benchmark for three-phase flows: (a) initial and (b) equilibrium phase profile, when surface tensions are different per phase (0.5 N/m, 1.5 N/m and 0.5 N/m, respectively, for phase 1, 2 and 3).

Figure 5-7 represents a case where the surface tension of Phase1 (σ_1), Phase2 (σ_2), and Phase3 (σ_3) are taken as O.5 N/m, 1.5 N/m and 0.5 N/m respectively. It can be seen that Phase 2 is pushing away from its phase because it has the highest individual surface tension (1.5 N/m) among all the three phases. As the decomposition of surface tension is expressed as $\alpha^{\alpha\beta} = \sigma^{\alpha} + \sigma^{\beta}$ in our code, σ_{23}, σ_{13} and σ_{12} are obtained as 2 N/m, 1 N/m and 2 N/m. The equilibrium contact angle (θ_1), (θ_2) and (θ_3) obtained numerically are 97°, 156°, and 107° respectively. Putting the value of (θ_1), (θ_2) and (θ_3) in equation (5.14), the value of $\frac{sin\theta_1}{\sigma_{23}}$, $\frac{sin\theta_2}{\sigma_{13}}$ and $\frac{sin\theta_3}{\sigma_{12}}$ is obtained as 0.49, 0.40 and 0.47. Ideally, the three values obtained should be identical, but the slight difference observed may be due to the error while measuring the contact angle with ImageJ software. Assuming 0.47 as the ideal expected value, the error obtained is 14% for 0.40 and 4% for 0.49 respectively.

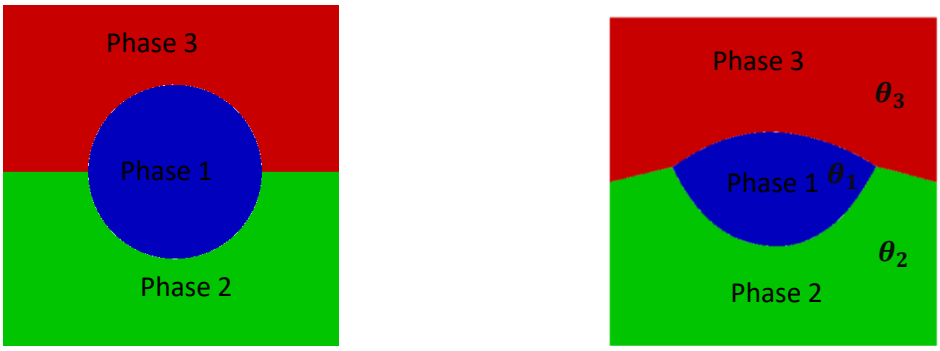

Figure 5-8 Lens benchmark for three-phase flow (a) Initial and (b) equilibrium phase profile, when surface tensions are different per phase (1.5 N/m, 0.5 N/m and 0.5 N/m, respectively, for phase 1, 2 and 3).

Figure 5-8 represents a case where the surface tension of Phase1 (σ_1), Phase2 (σ_2), and Phase3 (σ_3) are taken as 0.5 N/m, 0.5 N/m, and 1.5 N/m, respectively. In this case, it is Phase 3 that is pushing away from its phase, which is the highest individual surface tension (1.5 N/m) among all the three phases. σ_{23}, σ_{13}, and σ_{12} are 2 N/m, 2 N/m, and 1 N/m. The equilibrium contact angle (θ_1), (θ_2) and (θ_3) obtained are 96°, 108°, and 156°, which gives, for $\frac{sin\theta_1}{\sigma_{23}}$, $\frac{sin\theta_2}{\sigma_{13}}$ and $\frac{sin\theta_3}{\sigma_{12}}$, 0.49, 0.47 and 0.40 values respectively. Slight variation in the obtained values can be again attributed to the error while calculating the equilibrium contact angle. The error obtained is the same as the one obtained in the previous case (14% for 0.40 and 4% for 0.49).

The obtained numerical results showed that our code correctly predicts the spreading behavior of droplet at the three-phase interface but further tests need to be performed when one of the contact angles is zero.

5.3 Dissolution model

After validating the above three-phase flow, driven by surface tension forces, a dissolution model has been implemented in our code in order to study the dissolution of calcium in liquid steel. The implemented model is tested for the case where a stable droplet of calcium is

allowed to dissolve in liquid steel. The transport equation of the species concentrations in the respective phases are given by the equation:

$$\frac{\partial C_{lsca}}{\partial t} + v.\nabla C_{lsca} = \nabla.D_{lsca}\nabla C_{lsca} \quad (5.15)$$

Where C is the species molar concentration, D is the diffusion coefficient, v is the velocity field and the subscript ls and ca denote liquid steel phase and calcium phase, respectively.
In order to have the flux continuity at the interface (no mass accumulation), the flux at the interface is given by:

$$j.n_{interface} = -D_{ca}\frac{\partial C_{ca}}{\partial n} = -D_{ls}\frac{\partial C_{ls}}{\partial n} \quad (5.16)$$

In ICI-tech, the equation (5.16) is not imposed on the interface, but it is directly issued from the implicit boundary formulation. Diffusivity inside the interface is given by mixing law (see section 4.2.1):

$$D_{\varepsilon} = D_{ca}H_{\varepsilon}(\alpha) + D_{ls}(1 - H_{\varepsilon}(\alpha)) \quad (5.17)$$

Where $H_{\varepsilon}(\alpha)$ is given by:

$$H_{\varepsilon}(\alpha) = \frac{1}{2}\left(1 + \frac{u_{\epsilon}(\alpha)}{\varepsilon}\right) \quad (5.18)$$

In equation (5.18), $H_{\varepsilon}(\alpha)$ is the smoothed Heaviside function which is used to deal with the multiphase modeling required by the implicit boundary approach, $u_{\epsilon}(\alpha)$ is a smooth phase function, and ε represents the thickness of the interface. More details about this can be found in section (4.2.3).

5.3.1 Validation of the resolution of the diffusion problem

Mass transfer from a stationary spherical calcium drop is simulated, to validate the results on pure diffusion of Calcium.
Figure 5-9 shows the computational domain and the initial condition (at t = 0) where the concentration inside the calcium droplet (C_{ca}) and liquid steel is set to 1 ppm and 0 ppm respectively. The volume change due to mass transfer is neglected in our calculation.

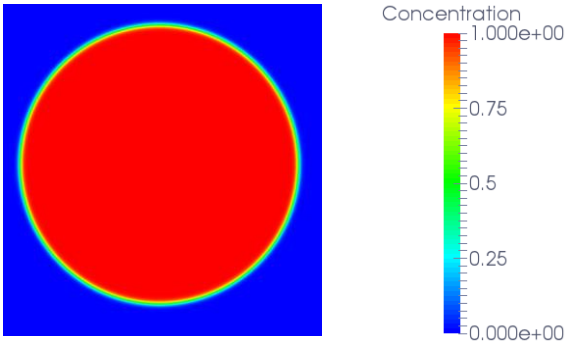

Figure 5-9 Stable calcium droplet in liquid steel.

Physical properties taken for this simulation are given in Table 5-1. Constant concentration of 1 ppm is imposed on the Ca droplet-liquid steel interface.

D_{ls}	4e-09 (m^2/s)
μ_{ls}	0.005 (Pa.s)
μ_{ca}	0.001 (Pa.s)
ρ_{ls}	7200 (Kg/m^3)
ρ_{ca}	1200 (Kg/m^3)

Table 5-1 Property of calcium droplet and liquid steel [31] [32] used to study liquid calcium diffusion in liquid steel

Analytical solution of equation (5.15) without convection is obtained and compared with the numerical solution. This Analytical solution of equation (5.15) along direction $\boldsymbol{x}$ in one dimension is given by:

$$C(x,t) = C_0\left(erfc\left(\frac{x}{\sqrt{4D_{ls}t}}\right)\right) \quad (5.19)$$

Where C_0 is the concentration imposed at the calcium-liquid steel interface, D_{ls} is the diffusivity of the calcium in liquid steel, x is the distance from interface and t is the time respectively. Since the diffusivity of calcium in liquid steel is quite low (4e-09 m^2/s), we need to take very small mesh size at the interface of the calcium-liquid steel, to capture the good diffusion layer. In our simulation, the minimum cell size at the interface (h_{min}) is 8 µm and a time step of 1e-03 seconds is taken. Predicted concentration fields at t= 1 seconds and at t= 2 seconds can be seen in Figure 5-10. The shown length corresponds to the distance from the interface. A good agreement between the analytical and numerical solutions was found.

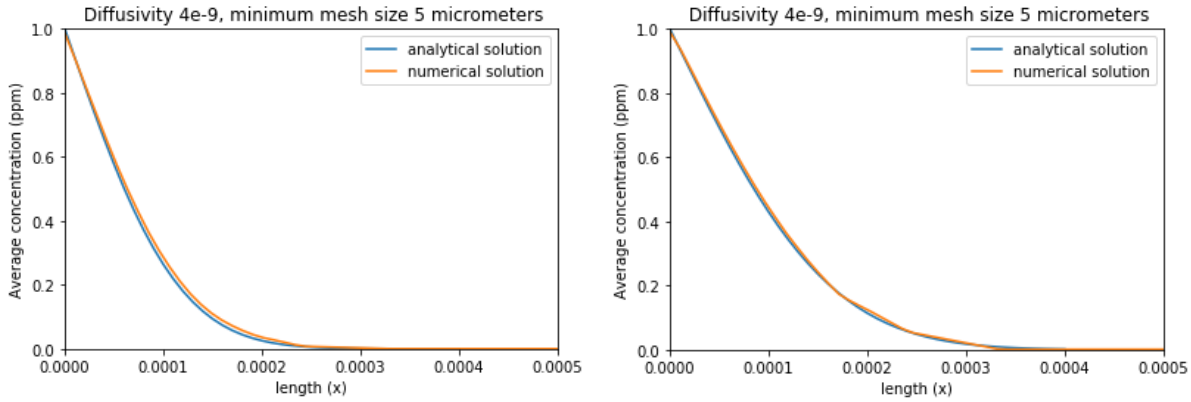

Figure 5-10 (a,b) Diffusion of liquid calcium in a liquid steel bath: comparison between numerical and analytical solution at a) t= 1 seconds and b) t = 2 seconds. Minimum mesh size (h_{min}) at the interface is 5 µm.

5.4 Mesh Sensitivity

Mesh sensitivity has also been studied, and it is found that the mesh size has a significant effect on the numerical solution of dissolution of a static calcium droplet in liquid steel. Numerical solutions with different mesh sizes can be seen in Figure 5-11. When we have minimum mesh size (h_{min}) of 7 µm or less at the calcium-liquid steel interface (Figure 5-11(b)), the numerical solution superimpose each other and are close to the analytical solution. As the minimum mesh size is increased (10 µm and 20 µm, Figure 5-11(a)), the numerical solution is far from the analytical solution. It shows that the minimum mesh size plays a vital role in determining the correct concentration gradient at the calcium droplet-liquid steel interface.

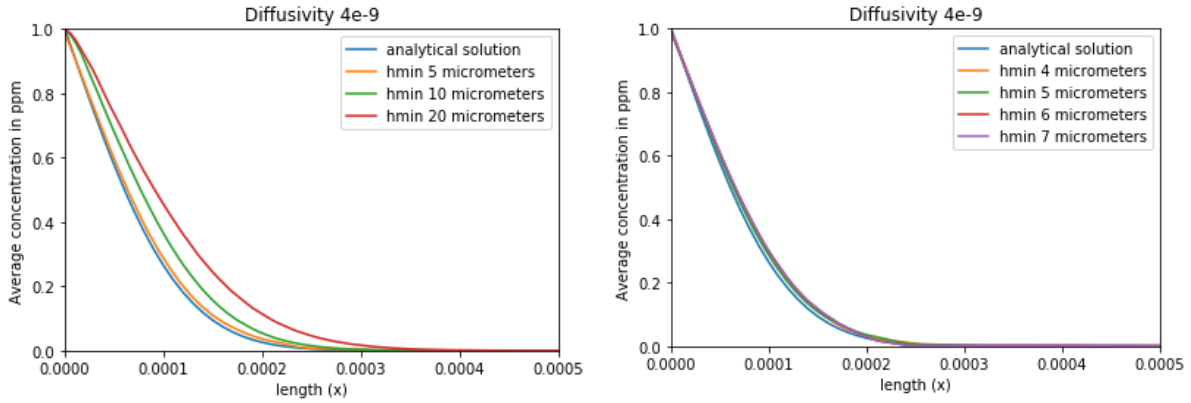

Figure 5-11 (a,b) Diffusion of liquid calcium in a liquid steel bath: mesh sensitivity study at t = 1 seconds.

5.5 Validation of the resolution of the convection-diffusion problem

This section presents the validation of the convection-diffusion model. The computation of the mass transfer coefficient for a droplet rising in the quiescent Newtonian fluid is presented here.

In order to compute the dissolution of the rising droplet in a stagnant liquid, dissolution equation (5.15) is coupled with the Navier Stokes equation (5.1). During the rise of the droplet in the liquid medium, the mass transfer occurs as a result of both convection and diffusion processes. In the main bulk of the liquid, the convective components of mass flow dominate while within the boundary layers, where the flow is weak, the diffusive transport assumes larger importance. The total flux across the interface is composed of diffusive flux as well as convective flux. Simulations are carried to predict the droplet shape, flow field, and transport of species from a droplet into the liquid phase.

The experimental data obtained by Grace [30] showed that the physical properties of the droplet or bubble liquid system determine the droplet or bubble shape and their rising velocity.

The rising velocity and their shape determine the flow field around the droplet/bubble. The flow field developed affects the mass transfer across the droplet/bubble and liquid phase interface. Therefore, it can be concluded that, in order to correctly predict the mass transfer coefficient, the model should correctly predict the pattern of the rising droplet or bubble (shape, velocity, etc.).

Dimensionless parameters used to analyze the results presented in this section are the Reynolds number (Re), the Bond number (Bo) and the Morton number (Mo). The Bond number with the Morton number is used to determine the regime of the rising droplet, providing the information on the Reynolds number (Re), which gives us the rising velocity. These dimensionless numbers can be computed as:

- Reynolds number

$$Re = \frac{\rho_l v_t d}{\mu_l} \tag{5.20}$$

- Bond number

$$Bo = \frac{(\rho_l - \rho_d) g d^2}{\sigma} \tag{5.21}$$

- Morton number

$$Mo = \frac{\mu_l^4 (\rho_l - \rho_d) g}{\rho_l^2 \sigma^3} \tag{5.22}$$

Two other dimensionless numbers, the Schmidt number (Sc) and the Sherwood number (Sh) are used to describe the mass transfer from the rising droplet in the liquid medium. The total flux across the interface is composed of the diffusive flux as well as the convective flux. In order to predict the total flux at the interface of a droplet in a liquid medium, the Sherwood number (Sh), given by the ratio of the convective mass transfer rate to the diffusive mass transfer rate, needs to be correctly determined.

These dimensionless numbers are expressed as:

- Schmidt number $$Sc = \frac{\mu_l}{\rho_l D_l} \quad (5.23)$$
- Sherwood number $$Sh = \frac{K_l d}{D_l} \quad (5.24)$$

In these expressions, K_l is the mass transfer coefficient at steady state, d is the initial diameter of the droplet, and D_l is the diffusivity of the droplet in the liquid medium. In the literature [76], it has been shown that the Sherwood number (Sh) depends on the Reynolds number (Re) and on the Schmidt number (Sc). Re is the ratio of the inertial force by the viscous force, and Sc is the ratio of the viscous diffusion rate by the molecular (mass) diffusion rate.

To couple this to our dissolution model and to validate it, three simulations in 3D were carried out, for three-different regimes of the Grace Diagram [30], and are illustrated in Figure 5-12. The domain of size 0.2m x 0.4m x 0.2m is taken for the simulations of all the three different cases. The size of the domain is taken such that the concentration far from the droplet liquid medium interface is zero, and the rising velocity is independent of the domain size. Respective Bond number (Bo) and the Morton number (Mo) used for the simulations can be seen in Table 5-2. It should be noted that the Schmidt number for all the different cases is taken as 1.

Case	Bo	Mo
1	1	1e-4
2	40	9e-3
3	3	5e-7

Table 5-2 Morton number, Bond number for three different cases of simulation with Schmidt number fixed 1.

No slip boundary conditions on the walls of the domain are applied as boundary conditions for the Navier-Stokes equation, and an average concentration of 0.14 ppm is imposed on the droplet liquid-medium interface (towards the liquid medium side). The average concentration imposed is just an arbitrary value.

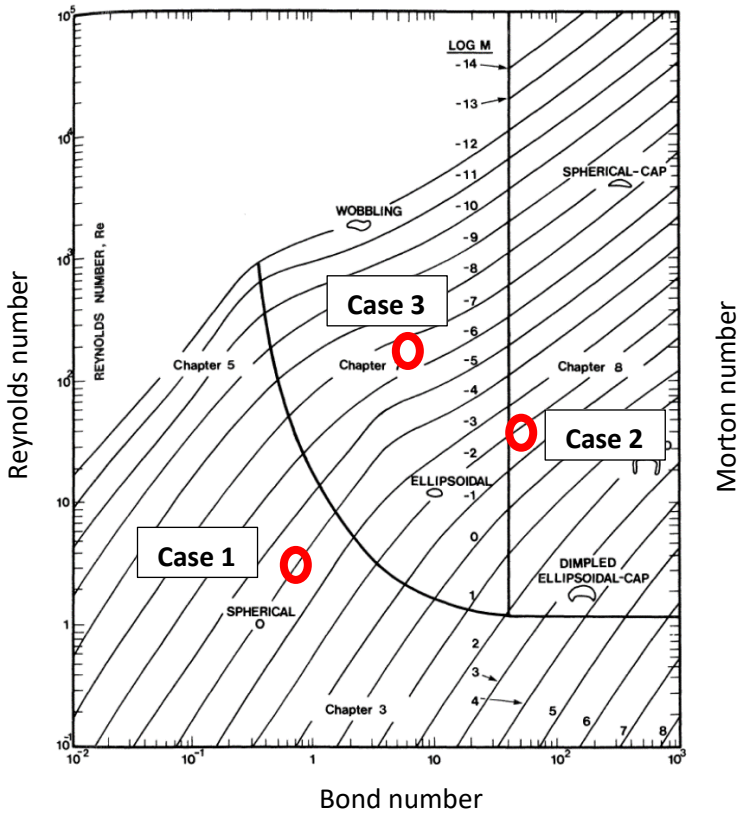

Figure 5-12 Grace diagram for the bubble/droplet shape and terminal rise velocity. [30]

In terms of computational resources, we have used one core for every 10000 nodes in the computational domain. For Case1, we had around 800000 nodes; therefore, 80 cores in total are used for the simulation. Interface thickness, minimum mesh size at the interface, and the time step taken for the different cases can be seen in Table 5-3.

	Interface thickness (L_{max}, ε, m)	Minimum mesh size at the interface, (h_{min} m)	Time step (s)
Case 1	6e-4	6e-5	2.5e -5
Case 2	5e-4	5e-5	1.5e-5
Case 3	4e-4	4e-5	1e-5

Table 5-3 Numerical parameters used for simulation dissolution simulations (rising droplet test case).

Figures below show the rising dissolving droplet for the three different cases with their respective velocity streamlines.

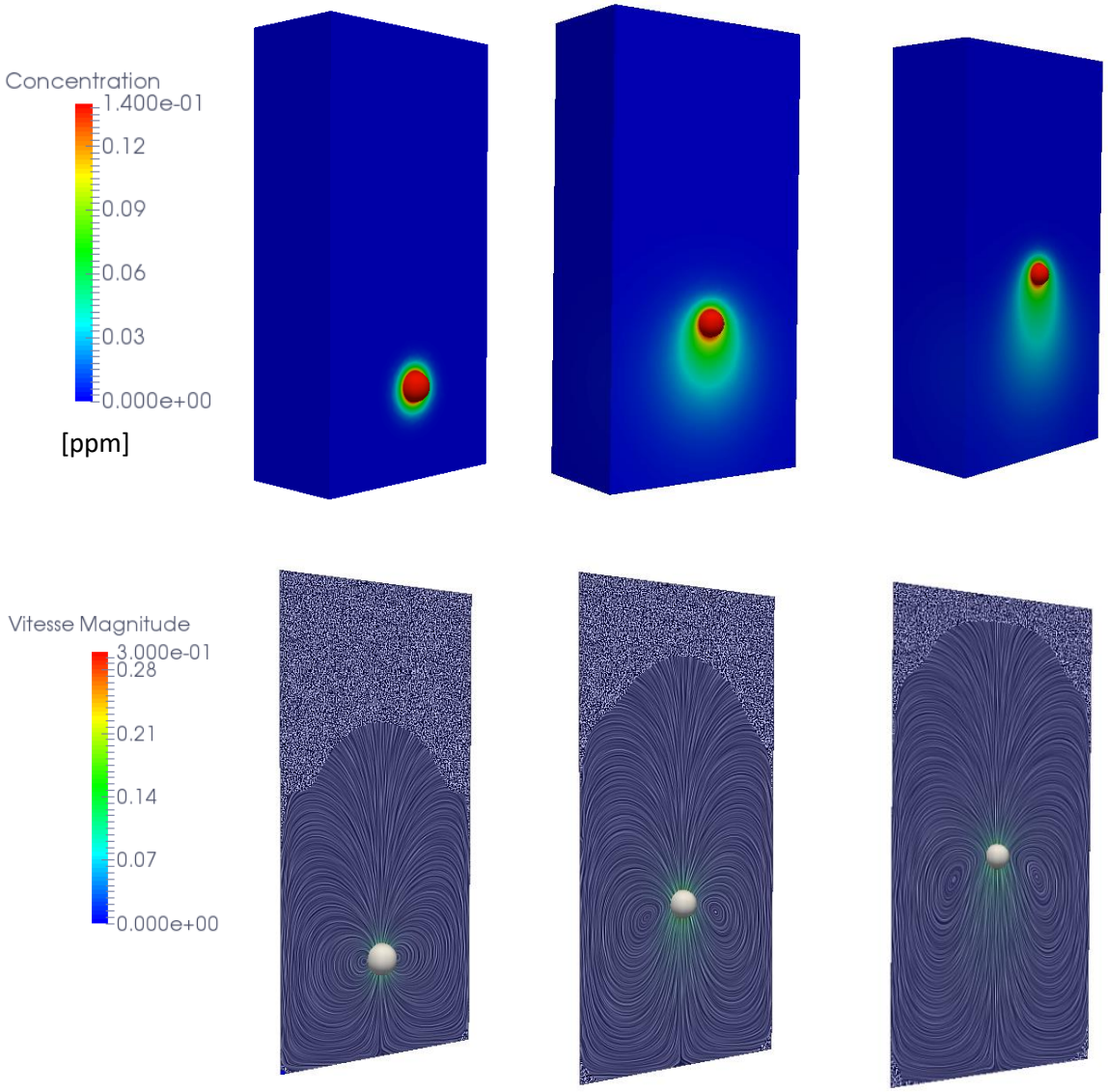

Figure 5-13 Case 1: Spherical droplet, Bo = 1, Mo = 1e-4, Sc = 1. Concentration profile and velocity streamlines.

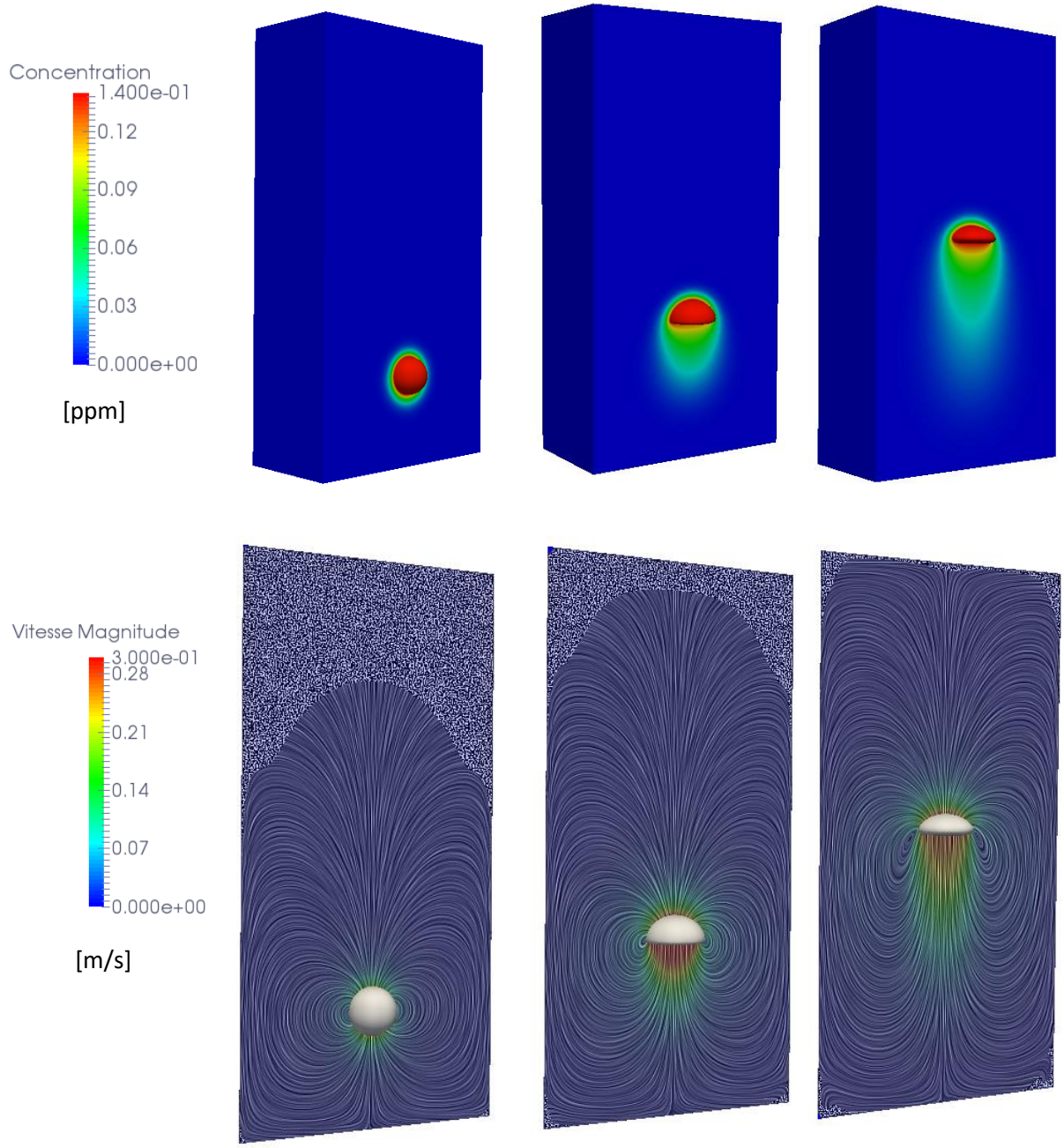

Figure 5-14 Case 2: Spherical cap droplet, Bo = 40, Mo = 9.2e-3, Sc = 1. Concentration profile and velocity streamlines.

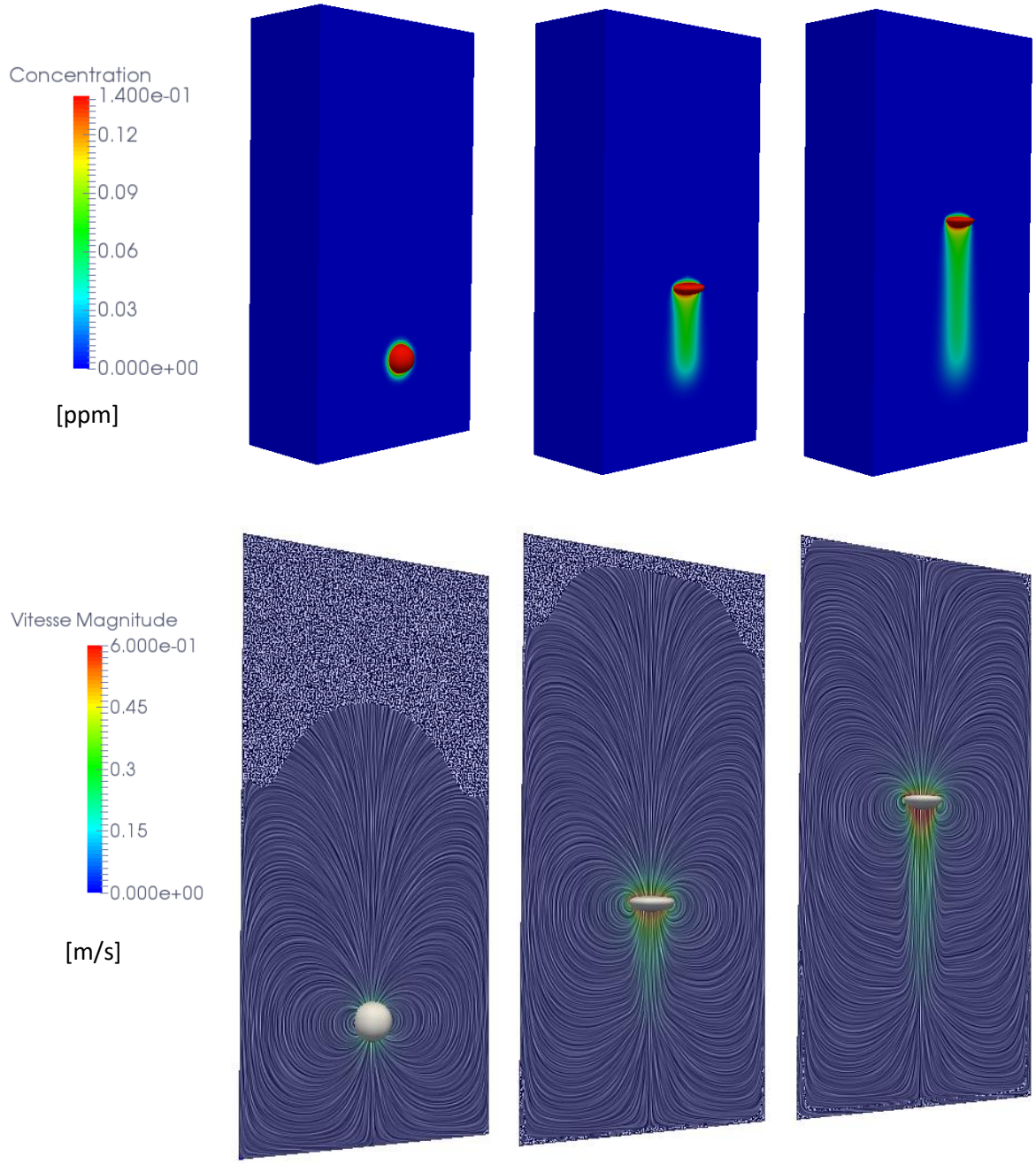

Figure 5-15 Case 3: Ellipsoidal droplet, Bo = 3, Mo = 5e-7, Sc = 1. Concentration profile and velocity streamlines.

5.5.1 Results and discussions

Figure 5-13, Figure 5-14, and Figure 5-15 show the shape of the droplet, velocity streamlines, and the dissolved species concentration at different time instants. Depending on the different physical parameters used in the three cases, the shapes of the droplet gradually evolve differently.

It can be noticed that the shape of the droplet remains the same during rising for case 1. It remains spherical with the course of time, because of the low Bond number, resulting from a dominant surface tension force. In case 2, the spherical cap is formed during the steady state rise of the droplet and, in case 3; the spherical droplet has transformed into an ellipsoidal

droplet. The shape of the droplets formed numerically at the steady state match exactly with what has been observed in Figure 5-12 of Grace diagram [30]. The comparison of the droplet regime and the Reynolds number (Re) can be seen in Table 5-4, and a good agreement has been found between the terminal Reynolds number found and the one obtained from Grace diagram.

	Droplet/Bubble regime	Grace [30]	Simulations
Case 1 (Re)	Spherical	5	4
Case 2 (Re)	Spherical cap	30	26
Case 3 (Re)	Ellipsoidal	100	103

Table 5-4 Comparison of the different regimes and Reynolds number obtained Grace diagram and Simulation results.

There is the development of the flow field near the droplet as the droplet tends to rise and the dissolved species are transported downstream. D. Darmana et al. [77] showed that the species transport near the droplet surface is divided into two regions, a roof, and a wake region. As far as the shape of the roof region is concerned, it is rather similar in all the three cases, except for a little difference in the radius of curvature. Since the shape formation determines the species distribution, there is similarity in the species distribution at the roof. As the Reynolds number increases from case 1 to case 3, the convective part of the species transfer becomes dominant, and the thickness of the concentration boundary layer becomes thin. The increase in the concentration gradient with the increase in Reynolds number (Re) is well captured in our model, which can be seen in Figure 5-13, Figure 5-14, and Figure 5-15.

In the wake region, the shapes of the droplet are entirely different in different cases. In case 1, the bubble has a closed wake at the bottom of the droplet, and since the Reynolds number is low in this case, there is a low transport of species in this region. In case 2, the recirculation wake is observed at the edge of the droplet, and the dissolved species gets trapped in this region. In case 3, the recirculation wake is also observed at the edge of the droplet but seems to be smaller than what has been observed in Case 2. As the Reynolds number increases, the size of the wake decreases, and fewer species are trapped in the wake region because of the reduced size.

In order to understand the effect of the Schmidt number and of the Reynolds number on the transport of species at the droplet liquid medium interface, mass transfer coefficient (K_l) is calculated numerically by solving the following equation:

$$K_l A \Delta C = D_l \oint (\nabla C . n) dA \tag{5.25}$$

A is the surface area of droplet, ΔC is the concentration difference between an interface and the bulk liquid medium, and $\nabla C . n$ is the concentration gradient normal to the surface of the droplet-liquid medium interface. Sh is calculated numerically by using K_l in equation (5.24) and is compared to the correlations given by K. Hayashi et al. [78] which is presented in

equation (5.26) and equation (5.26) respectively. The correlation given in equation (5.26) is valid for low Reynolds number (Re) (<100). We can use this correlation for the first two cases where Reynolds number is less than 100 (spherical and spherical cap regime). The correlation given in equation (5.27) is valid for high Reynolds number (Re > 100). We can use this correlation for Case 3 (ellipsoidal droplet regime).

$$Sh = 1 + \left(1 + 0.564 Re^{\frac{2}{3}} Sc^{\frac{2}{3}}\right)^{\frac{3}{4}} \quad \textbf{(5.26)}$$

$$Sh = \frac{2}{\sqrt{\pi}}\left[1 - \frac{2.89}{\sqrt{Re}}\right]^{\frac{1}{2}} Re^{\frac{1}{2}} Sc^{\frac{1}{2}} \quad \textbf{(5.27)}$$

Comparison of the Sh obtained from the correlation equation (5.26) and equation (5.27) with the one obtained numerically is presented in Table 5-5.

	Droplet/Bubble regime	Sh (Correlation)	Sh (Numerically)
Case 1	Spherical	2.94	2.70
Case 2	Spherical cap	4.80	3.90
Case 3	Ellipsoidal	9.68	8.35

Table 5-5 Comparison of Sh obtained by correlation and numerically, $Sc = 1$.

It can be seen that the mass transfer increases as the Reynolds number (Re) increases and a good agreement has been obtained between Sh obtained by the correlation and Sh obtained numerically for both low and high Re case. Different shapes of the droplet led to the different flow regime near the droplet, and it led to the different mass transfer across the droplet liquid medium interface.

The section below presents the dissolution of the rising calcium droplet in liquid steel.

5.6 Rise of calcium droplet in liquid steel

Once the convection-diffusion model is validated, the rise of calcium droplet in liquid steel is computed, and the average mass transfer coefficient of calcium droplet in liquid steel is calculated. The simulation consists of three phases: calcium droplet, liquid steel, and air at the top. The dimension of the domain is 7 cm x 12cm x 7cm, where the height of liquid steel is 7.5 cm. Calcium droplet of diameter 1cm is taken, which corresponds to 1 gram of calcium at 1480°C, and a constant concentration of 48 ppm is imposed on the surface of the calcium. An in-house code developed at ArcelorMittal R&D called CEQCSI [43] is used to calculate the equilibrium concentration (C_{ca}= 48 ppm) at the calcium droplet liquid steel interface. No slip boundary condition is applied on the walls of the domain. The physical property of the fluids used in the simulation can be seen in Table 5-6.

C_{ca}	48 (ppm)
D_{ls}	4e-09 (m^2/s)
μ_{air}	0.005 (Pa.s)
ρ_{air}	1 (Kg/m^3)
σ_{ls}	1.7 (N/m)
σ_{cad}	0.3 (N/m)
$\sigma_{cad.ls}$	1.4 (N/m)
μ_{ls}	0.005 (Pa.s)
μ_{cad}	0.001 (Pa.s)
ρ_{ls}	7200 (Kg/m^3)
ρ_{cad}	1200 (Kg/m^3)
Bo	4.28
Mo	2.63e-13

Table 5-6 Properties of fluid [31] [32].

Antonoff's [33] rule has been applied to calculate the surface tension between calcium droplet/liquid steel ($\sigma_{cad.ls} = \sigma_{ls} - \sigma_{cad}$) which predicts that the surface tension between two liquids is equal to the difference between the respective surface tension of the liquids. In our simulation, the interface thickness between calcium droplet/liquid steel is 8e-04m (L_{max}), minimum mesh (h_{min}) is 8e-05m (80 µm), and the time step is 1e-05 seconds, respectively. Schmidt number (Sc) for the rising calcium droplet in liquid steel is found to be 173. Figure 5-16 shows the rise of a dissolving calcium droplet in liquid steel with air at the top, and Figure 5-17 shows the velocity streamlines of the rising Calcium droplet. Small closed wakes can be seen clearly near the side of the calcium liquid steel interface.

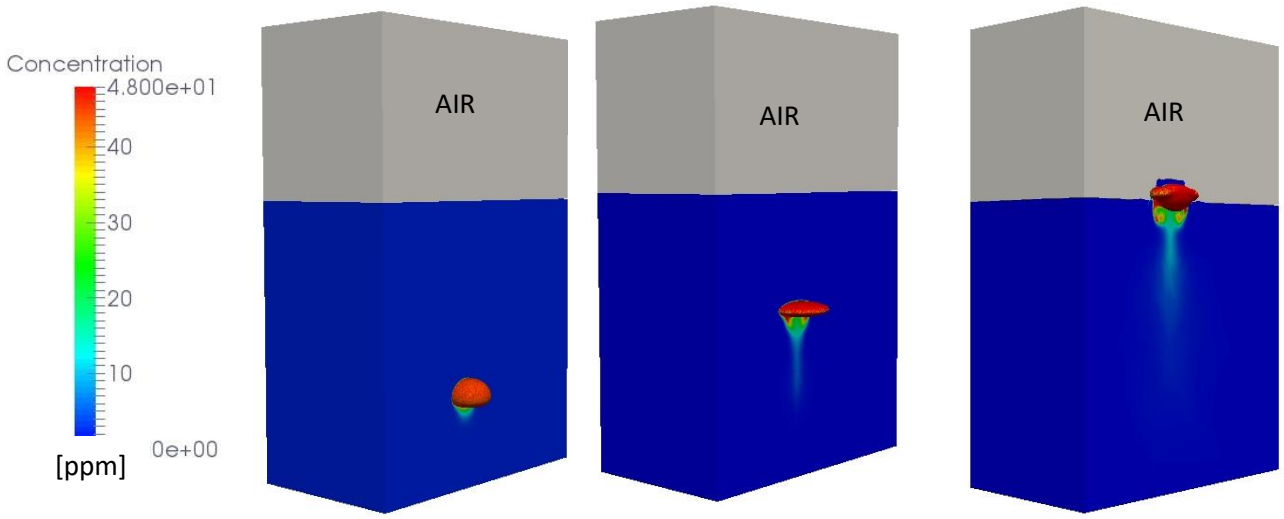

Figure 5-16 Calcium droplet rising and dissolving in liquid steel.

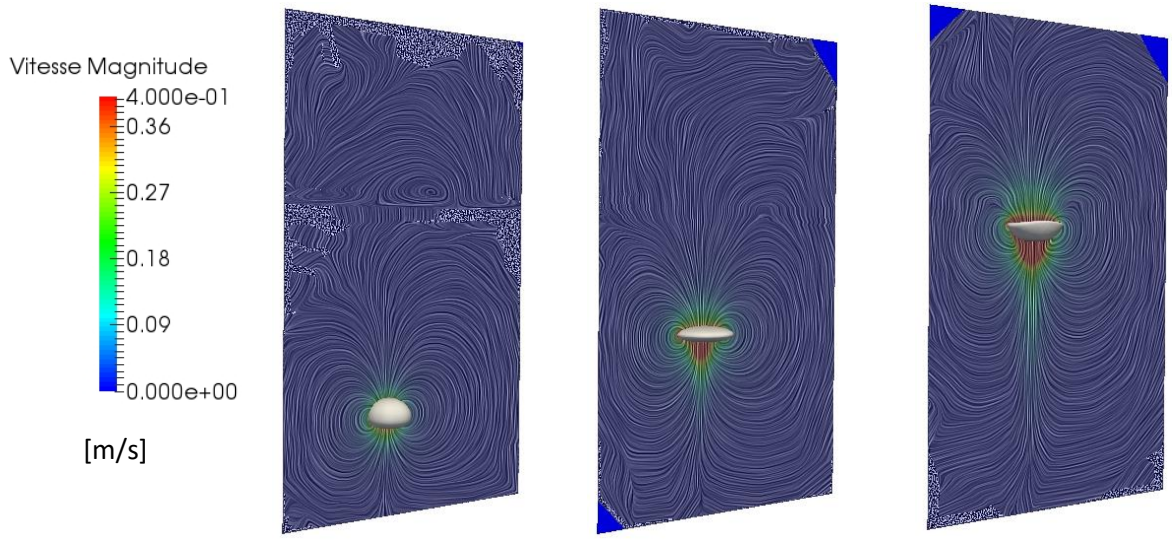

Figure 5-17 Velocity streamlines for the rising calcium droplet.

Total calcium dissolved in liquid steel is found to be around 0.085 ppm (volumetric average) when the calcium droplet reaches the surface of liquid steel. The total mass of the liquid steel domain is around 2.6 kg, and the average rising velocity of calcium droplet is found to be 0.285 m/s, which leads to a residence time of around 0.26 seconds. Flux (Ø) is found to be 8.5e-07 kg/s in liquid steel. In order to calculate the average mass transfer coefficient, we used the same formula which is being used for calculating the average mass transfer coefficient experimentally, which is:

$$\emptyset = K_{cadnum}.S\rho_{ls}.(C_{ca} - C_{ca}^{bath}) \quad (5.28)$$

For a droplet of diameter 1 cm (0.01 m), the surface area (S) is found to be 0.00031 m^2. C_{ca} (concentration imposed towards liquid steel side) is 48 ppm, $C_{ca}^{bath} \approx 0$ ppm and ρ_{ls} being 7200 kg/m^3, K_{cadnum} (average mass transfer coefficient obtained numerically) is found to be **7.93e-03 m/s.**

5.6.1 Continuity of shear stress across the interface

If two viscous fluids meet and a flow boundary is formed, then at this boundary (interface), the shear stress in one fluid should be equal to the shear stress in the other fluid. It means there should be continuity of shear stress across the interface. The fulfillment of these criteria is important for calculating the correct mass transfer and heat transfer across the interface. Therefore, we verified the continuity of shear stress across the calcium droplet liquid steel interface.

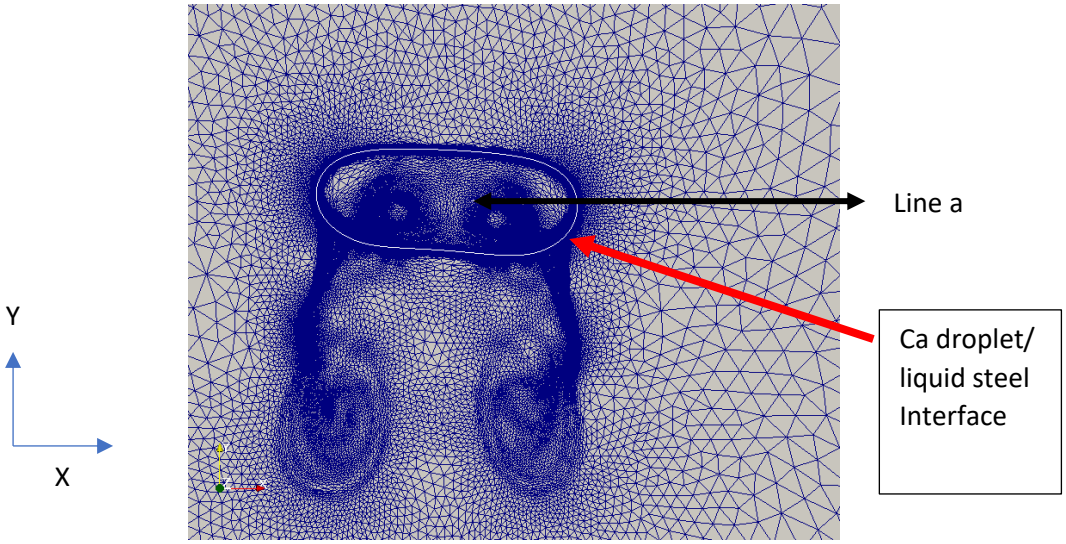

Figure 5-18 Rising calcium droplet with adaptive mesh.

Figure 5-18 shows the image of the calcium droplet at instant t. Velocity in the y-direction (V_y) is plotted across the **line a** as shown in Figure 5-18. X = 0.0004 m in the figure below represents the Ca droplet liquid steel interface. E_{mix} represents half of ε (L_{max}) which is the region within the interface where mixing law is applied, which is = 20 μm.

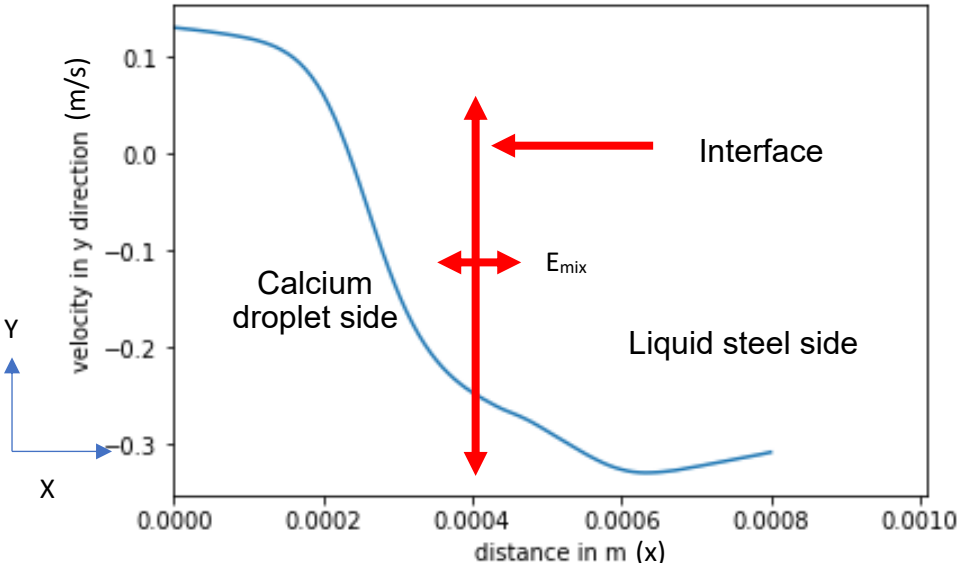

Figure 5-19 Velocity (V_y) across the line a (interface).

	Shear stress, liquid steel side = $\mu_{ls} \times \frac{\partial V_y}{\partial x}$ = 2 Pa	
	Shear stress, calcium droplet side = $\mu_{ca} \times \frac{\partial V_y}{\partial x}$ = 1.7 Pa	

Table 5-7 Shear stress across different phases: Calcium droplet side and liquid steel side.

$\frac{\partial V_y}{\partial x}$ across the calcium droplet and liquid steel has been found as 1700 s^{-1} and 400 s^{-1}, respectively. Shear stress obtained in the respective medium is shown in Table 5-7. Obtained values of shear stress confirms the continuity of the shear stress across the interface in our code.

5.7 Mesh sensitivity study for rising calcium droplet

As discussed in section (5.3), the size of the mesh at the interface can have a significant effect on the mass transfer from calcium droplet to liquid steel. Therefore, the effect of mesh size on the value of the average mass transfer coefficient has been studied in 2D as well as in 3D. Mesh sensitivity has been studied for the calcium droplet of size 1 cm diameter, and the minimum mesh size (h_{min}) has been varied from 120 μm to 20 μm in 3D and from 120 μm to 4 μm in 2D (Figure 5-20, log scale). We were not able to decrease the h_{min} below 20μm in 3D because of the high computation cost and time. The physical property of the fluids used in the simulation can be seen in Table 5-6 and the time step for the calculation has been chosen such that the CFL no [79] is less than one which is:

$$CFL = \frac{v\Delta t}{x_{hmin}} < 1 \qquad (5.29)$$

The obtained results showed the converging tendency of the average mass transfer coefficient value (K_{cadnum}) with the decrease in the mesh size at the interface. The results did not seem to be fully converged in 3D, but in 2D it seemed to converge better. One of the possible reason for not having the fully converged solution is the high Peclet number we are dealing with. Respective Reynolds, Schmidt number, and Peclet number (Pe) of our problem are presented in Table 5-8.

Remarks: Minimum mesh size (h_{min}) represents the short dimension of the tetrahedral mesh across the boundary layer. It should be noted that the simulation has not been performed for the complete rise of calcium droplet in liquid steel of height 7 cm but the final time for all the simulations is kept constant.

- Reynolds number	$Re = \frac{\rho_{ls} v_t d_{cad}}{\mu_l} \approx 4000$	(5.30)
- Schmidt number	$Sc = \frac{\mu_{ls}}{\rho_{ls} D_{ls}} = 173$	(5.31)
- Peclet number	$Pe = Re \times Sc \approx 700000$	(5.32)

Table 5-8 Reynolds no, Schmidt no and Peclet no for the Calcium droplet rise in liquid steel.

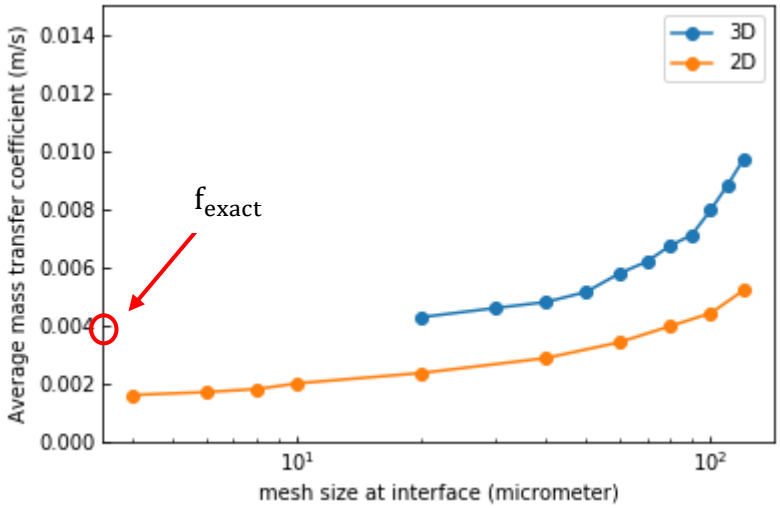

Figure 5-20 Mesh sensitivity study in 2D and 3D.

An approximation of the concentration boundary layer is given by Bird et al. [80] which is:

$$\delta_c \propto \delta_v Sc^{-1/2} \propto \frac{1}{Pe^{1/2}} \quad (5.33)$$

δ_c is the concentration boundary layer, and δ_v is the hydrodynamic boundary layer. Bird et al. [80] mentioned that the Peclet number of 10^4 to 10^7 could lead to a concentration boundary layer of a few micrometers or even less than that. For our problem too, we can expect the concentration boundary layer of a few micrometers.

5.7.1 Error analysis based on different mesh size

Mesh sensitivity study can lead to an estimation of error associated with discretization in space. Roache et al. [81] and Oberkampf et al. [82] discussed the error analysis based on Richardson Extrapolation. In order to do so, three mesh length h_1, h_2 and h_3 with a constant refinement ration (r) is taken.

$$r = \frac{h_3}{h_2} = \frac{h_2}{h_1} \quad (5.34)$$

If f_1, f_2 and f_3 are the computed result for the three corresponding values of h. Then based on truncation error analysis, expression of f as a function of h takes the following form:

$$f_1 = f_{exact} + ah_1^p \quad (5.35)$$

$$f_2 = f_{exact} + ah_2^p \quad (5.36)$$

$$f_3 = f_{exact} + ah_3^p \quad (5.37)$$

$$p = \ln\left(\frac{f_3 - f_2}{f_2 - f_1}\right)/\ln(r) \quad (5.38)$$

$$f_{exact} = f_1 - \frac{f_2 - f_1}{r^p - 1} \quad (5.39)$$

In the above equations f_{exact} represents the exact solution with zero mesh refinement. f_{exact} has been calculated based on the mesh sensitivity study performed. h_1, h_2 and h_3 are taken as 30 μm, 60 μm and 120 μm respectively. Corresponding values of f_1, f_2 and f_3 are 0.00457 m/s, 0.00576 m/s and 0.00969 m/s respectively. Putting the respective values in the above equation, p is obtained as 1.72 and f_{exact} is obtained as 0.004 m/s. It should be noted that the f_{exact} is not obtained for the complete rise of calcium droplet in liquid steel of height 7 cm.

In order to investigate more, we studied the concentration profile at the calcium droplet-liquid steel interface. The obtained result is then compared with the reference issued in the literature. It is presented in the section below.

5.8 Prediction of correct mass flux at the interface

As mentioned above, the concentration boundary layer can be in the order of micrometers for Peclet number of around 700000. Therefore, it is crucial to determine whether the mass flux across the interface has been properly calculated or not. A qualitative comparision of the numerical solution with some reference values obtained from literature has been performed which is discussed further below.

I. Calmet et al. [83] studied the mass transfer through the flat shear-free surface of a turbulent open-channel flow. The turbulent Reynolds number ($Re = 360$) in their study is high enough for the turbulence region to be close to isotropy and independent of the flow structure. They plotted the dimensionless the mean concentration profile near the free surface for four Schmidt number ($Sc = 1, 10, 100, 200$) varying from 1 to 200, and all the four-profile collapsed into a single curve which is presented in Figure 5-21 (x-axis log scale). In Figure 5-21, Sc is the Schmidt number and $Y^+ = \frac{U^*}{\nu_{ls}} \times (\delta - y)$. $U^* = \sqrt{\frac{\tau_{ls}}{\rho_{ls}}}$, ν_{ls} is the kinematic viscosity of liquid medium (in our case it is liquid steel), $(\delta - y)$ is the distance from the interface, τ_{ls} being the tangential shear stress towards the liquid medium side and ρ_{ls} is the density of the liquid medium (in our case it is liquid steel).

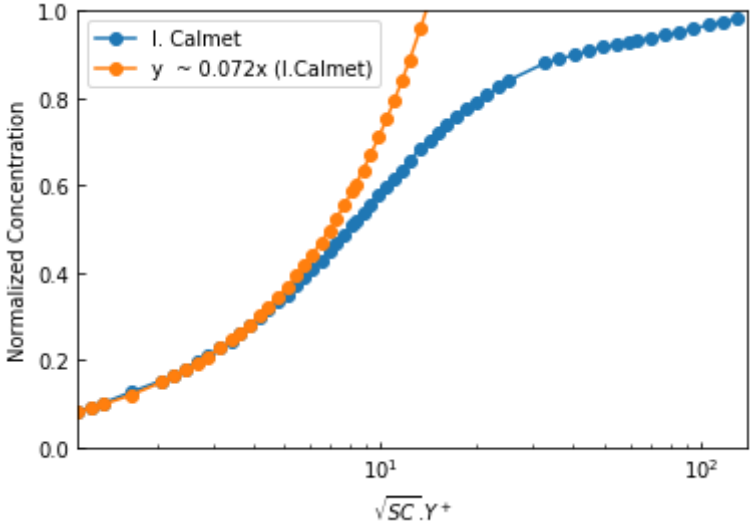

Figure 5-21 Mean concentration profile in the near surface region.

It can be seen in the above figure that until $Sc^{\frac{1}{2}}Y^+ \approx 5$, the concentration is linear, which corresponds to the diffusive sublayer. In this layer, the normalized concentration ≈ 0.072 $Sc^{1/2}Y^+$. They mentioned that this factor is Re dependent. Even for $Sc = 1$, they observed that the viscous sublayer at the surface is thicker than the diffusive sublayer. The reason explained was having different boundary condition, one is Dirichlet type (concentration), and other is Neuman boundary condition (velocity gradient is zero at the interface). The Kolmogorov sublayer where the normal velocity grows linearly with Y extends up to 8.5 in their case. Hence, they concluded that the diffusive sublayer is almost half that of the Kolmogorov sublayer for the Reynolds number (Re = 360) they had. The diffusive layer is followed by the buffer layer, where the mean concentration varies rapidly. After the buffer region, the mean concentration profile obeys logarithmic law which has been detected for the $Sc^{1/2}Y^+$ greater than 40. It can be said that far from the surface, molecular diffusivity does not play an important role in the mass transfer mechanism. It is mainly guided by the convective term.

In our case, for the rise of calcium droplet in liquid steel, Sc = 170, therefore, we are in the range of case study of I. Calmet et al. [83], but our Reynolds number is not the same. The mean concentration profile at the calcium droplet liquid steel interface has been plotted (Figure 5-22), and it has been compared with the one obtained by I. Calmet et al. [83].

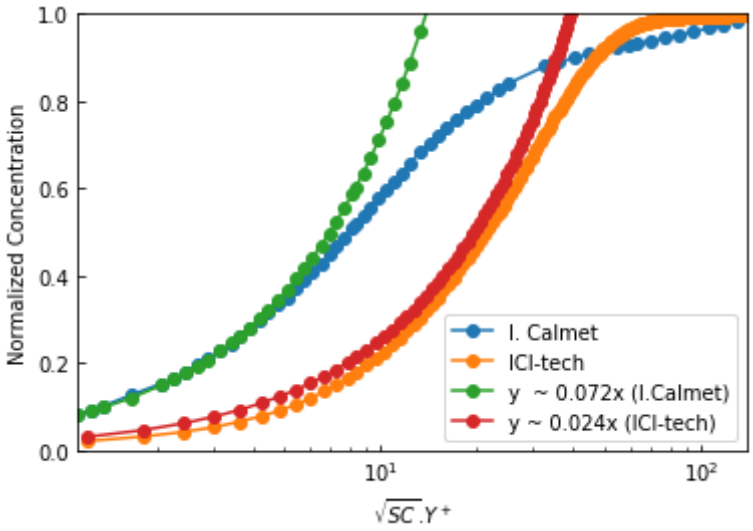

Figure 5-22 Comparison of the mean concentration profile in the near surface region.

The graph shown in Figure 5-22 corresponds to the mesh size of 6 µm at the calcium droplet liquid steel interface (2D). The profile obtained by our code (ICI-tech) does not match exactly with what has been obtained by I. Calmet et al. [83], but, the nature of the profile is the same. The important point concerning the profile obtained at the calcium droplet liquid steel interface is the linear evolution of the concentration profile (x-axis log scale). In order to calculate the mass flux correctly at the interface, the diffusive sublayer (which is linear) should be captured properly, and it has been done so in our numerical calculation, but we have to accept the fact that we have less number of mesh points close to the interface compared to I. Calmet et al. [83]. In the diffusive sublayer layer, we found, the normalized concentration ≈ 0.024 $Sc^{1/2}Y^+$ contrary to normalized concentration ≈ O.072 $Sc^{1/2}Y^+$ obtained by I. Calmet et al. [83]. This difference can be explained because of the two reasons: first, the insufficient mesh points close to the interface, and the second; we are not simulating the same regime. In our case, it is the mass transfer through the rising calcium droplet in liquid steel whereas, in the case of I. Calmet et al. [83], it is the mass transfer through the flat shear-free surface. The local flow near to the calcium droplet liquid steel interface might not be the same as that of flow near a flat shear-free surface in an open channel.

The section below demonstrates the rise of multiple calcium droplets in liquid steel, where the average mass transfer coefficient obtained numerically is compared with the average mass transfer coefficient obtained experimentally.

5.9 Multiples calcium droplet rise in liquid steel

During our experiments, multiple calcium droplets were observed at the surface of liquid metal. In order to validate our numerical results, the rise of multiple calcium droplets in liquid steel (3-phase flow, 3D) has been computed, and the results obtained numerically have been compared with one obtained experimentally. For computing, this, eight calcium droplets of 1

cm diameter (0.01 m) each are taken. Height of liquid steel is taken as 7cm, length 7 cm and breadth 7 cm respectively. The total volume of the liquid steel (3.43 cm^3) corresponds to 2.46 kg of liquid steel. The minimum mesh size (h_{min}) at the interface is 80 µm, and a time step of 1e-05 second is taken respectively.

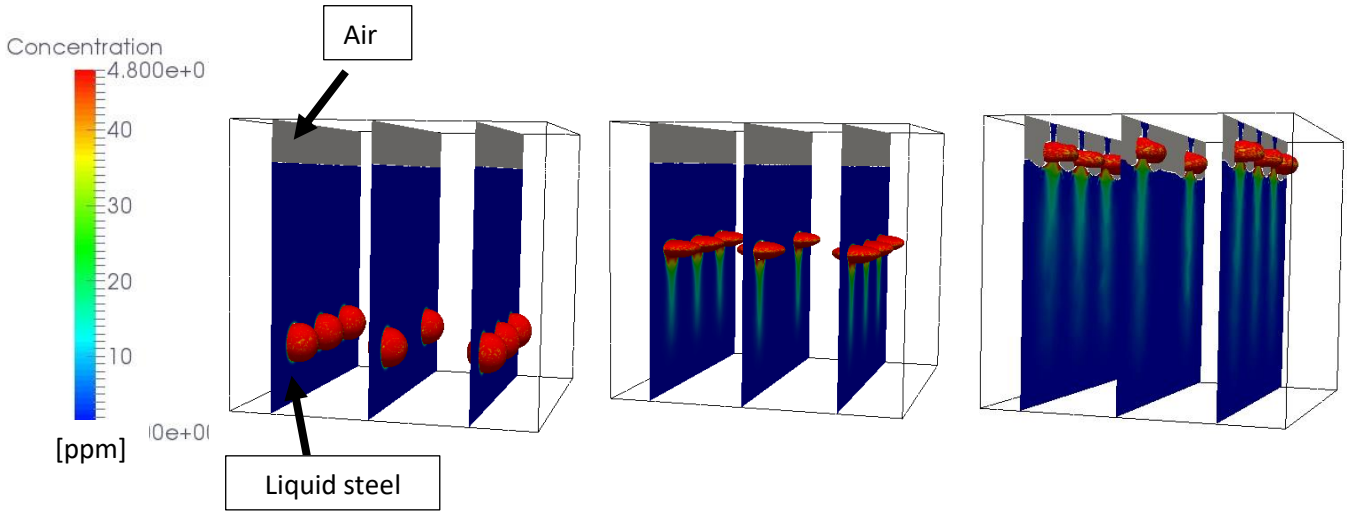

Figure 5-23 Multiple calcium droplets rising in liquid steel.

Once all the calcium droplet reaches the surface of liquid steel, total calcium in liquid steel is found to be 1.02 ppm (volumetric average) numerically. In the plane where three droplets of calcium are rising, average calcium in liquid steel is found to be 3.2 ppm, and in the plane where two droplets are rising, total calcium in liquid steel is found to be 2.2 ppm. The average residence time of calcium droplets in liquid steel is found to be 0.26 seconds. Once, the total calcium inside liquid steel is known, the average mass transfer coefficient (K_{cadnum}) is calculated numerically using equation (5.40).

$$\emptyset = K_{cadnum}.S\rho_{ls}.(C_{ca} - C_{ca}^{bath}) \quad (5.40)$$

1.02 ppm of total calcium in liquid steel corresponds to 2.509e-06 kg of total calcium in liquid steel of 2.46kg. In order to calculate ∅ (Kg/s), total calcium dissolved in liquid steel is divided by the residence time of droplets in liquid steel. So, ∅ (Kg/s) is obtained as 9.65e-06 Kg/s. C_{ca} is taken as 48 ppm, and C_{ca}^{bath} is total calcium in liquid steel, which is ≈ 0 ppm. S corresponds to the total surface area of calcium droplets which is 2.512e-03 m^2 and ρ_{ls} corresponds to 7200 Kg/m^3 respectively. Putting these values in equation (5.40), K_{cadnum} is obtained as **1.08e-02 m/s.** The average mass transfer coefficient obtained numerically for the rise of eight Ca droplets in liquid steel (**1.08e-02 m/s**) is slightly more than the one obtained numerically for the rise of single Ca droplet in liquid steel (**7.93e-03 m/s**).The possible reason could be the increase in the shear stress across the calcium droplet-liquid steel interface when eight Ca droplets are rising in liquid steel. The increased shear stress could increase the calcium mass transfer rate in the liquid steel.

5.9.1 Discussion

If we compare the average value of the mass transfer coefficient obtained numerically, K_{cadnum} (**1.08e-02 m/s)** with the one obtained experimentally K_{cadexp} (**7.642e-02 m/s**), a factor of 7.07 is found between them. One point should be noted that the K_{cadnum} is not obtained with the finest mesh in 3D (for multiple droplets rising in liquid steel). If the mesh size would be reduced further, we could expect the factor of 7.07 to increase further, since the average mass transfer coefficient decreases with the reduction in mesh size at the interface (Figure 5-20).

Various reasons could explain the difference in the average value of the mass transfer coefficient obtained numerically and experimentally:

1) It is shown in chapter 2, (Section 2.2.1) that, the calcium pick-up rate in liquid steel depends not only on the interfacial area but also on the sum of oxygen and sulfur content in liquid steel. De-sulfurization and de-oxidation reactions in the liquid film elevate the concentration profile slope, which finally leads to an increase in the mass transfer rate of calcium in liquid steel. In our numerical model developed, the effect of chemical composition (mainly oxygen and Sulfur content) on the mass transfer rate is not taken into account. It could be one of the reasons for the underprediction of the mass transfer coefficient obtained numerically.
2) In our experiments, during the calcium injection, inductors were turned off just at the time of calcium injection. It does not ensure that there is no mixing at all by the inductors. There can have some end effect of inductors on the mixing inside liquid steel, which can increase the dissolution of calcium in liquid steel.
3) When the calcium is injected in the form of a capsule with tungsten inside it, the bouncing dynamics of the capsule at the bottom of the crucible could have a significant effect on the fluid flow regime. It can generate the vorticity near the surface wall, which can consequently affect the dissolution of calcium in liquid steel. E. Izard et al. [84] studied the bouncing dynamics of the sphere in a viscous fluid on a flat surface, and they found that, for a sphere to bounce back in the viscous fluid, the Stokes number should be greater than 1000. Stokes number is given by the equation below:

$$St = \frac{(\rho_p + 0.5\rho_f)v_t D}{9\mu_f} \quad (5.41)$$

Where ρ_p is the density of particle (sphere), ρ_f is the density of the fluid, v_t is the terminal velocity of the sphere, D being the diameter of sphere and μ_f is the viscosity of the fluid. Stokes number for the falling capsule in liquid steel is calculated, and its value is obtained as 2430. In order to calculate the Stokes number, ρ_p is taken as 19188 kg/m^3 (density of capsule with tungsten and calcium in it), $\rho_f = \rho_{ls}$ = 7200 kg/m^3, v_t = 0.4 m/s (terminal velocity of the capsule, calculated in section 3.8), D is taken as 0.012 m (width of capsule) and $\mu_f = \mu_{ls}$ = 0.005 Pa.s. Stokes number obtained (≈2400) suggested that there is a high probability of capsule to bounce back at the bottom

surface of the crucible, which can lead to the vorticity near the bottom of the crucible. This could finally affect the dissolution of calcium in liquid steel.

Remark: If the melting time of the capsule is considerably higher than the descending time of the capsule, then the bouncing effect of the capsule would have a negligible effect on the dissolution of calcium in liquid steel.

5.10 Rise of calcium droplet with different sizes

Rise of calcium droplet having different sizes have been computed, and total calcium inside liquid steel is calculated numerically (with h_{min} = 80 μm) for the configuration mentioned above. Observed values can be seen in the table below.

Size of calcium droplet (cm)	Number of calcium droplet	Total calcium (ppm)
1.5	1	0.23
1.0	1	0.088
0.5	1	0.02

Table 5-9 Total calcium in liquid steel corresponding to different calcium droplet size.

According to the observed values in Table 5-9, total calcium in liquid steel can be calculated numerically depending on the total number of calcium droplets formation. Five grams of calcium injection can lead to the formation of 3 droplets of diameter 1.5 cm, eight droplets of diameter 1 cm and 64 droplets of diameter 0.5 cm respectively. Assuming that the rise of the calcium droplet is independent of each other, total calcium in liquid steel can be determined numerically as 0.69 ppm for 3 Ca droplets of 1.5 cm diameter, 0.71 ppm for 8 Ca droplets of 1 cm diameter and 1.28 ppm for 64 Ca droplets of 0.5 cm diameter respectively. As far as the calcium yield is concerned, it will be around 0.03% (3 calcium droplets of 1.5 cm diameter), 0.036% (8 calcium droplets of 1 cm) and 0.06 % (64 calcium droplets of 0.5 cm diameter). Numerical results showed the low dissolution of calcium droplets in liquid steel.

The section below shows the rise of a calcium bubble in liquid steel (without phase change and growth).

5.11 Rise of calcium bubble in liquid steel

Rise of calcium bubble in liquid steel is simulated too, and the average mass transfer coefficient of calcium bubble in liquid steel is calculated. The simulation consists of three phases, a calcium bubble, liquid steel, and air at the top. The dimension of the domain is 7 cm x 12cm x 7cm, where the height of liquid steel is 7.5 cm. The calcium bubble of diameter 1 cm is taken, and a constant concentration of 48 ppm is imposed on the surface of the calcium. The physical property of the fluids used in the simulation can be seen in Table 5-10.

C_{ca}	48 (ppm)
D_{ls}	4e-09 (m^2/s)
μ_{air}	0.005 (Pa.s)
ρ_{air}	1 (Kg/m^3)

σ_{ls}	1.7 (N/m)
σ_{cab}	≈ 0 (N/m)
$\sigma_{cab.ls}$	1.7 (N/m)
μ_{ls}	0.005 (Pa.s)
μ_{cab}	0.0001 (Pa.s)
ρ_{ls}	7200 (Kg/m^3)
ρ_{cab}	0.5 (Kg/m^3)
Bo	4.23
Mo	1.76e-13

Table 5-10 Properties of fluid [31] [32].

Antonoff's [33] rule has been applied to calculate the surface tension between calcium bubble/liquid steel ($\sigma_{cab.ls} = \sigma_{ls} - \sigma_{cab}$). In our simulation, the interface thickness between calcium bubble/liquid steel is 8e-04m (L_{max}), minimum mesh (h_{min}) at the interface is 8e-05m (80 µm), and the time step is 1e-05 seconds respectively. Schmidt number (Sc) for the rising calcium bubble in liquid steel is of the same order as that of the calcium bubble, which is 173. Figure 5-24 shows the rise of a dissolving calcium bubble in liquid steel with air at the top, and Figure 5-25 shows the velocity streamlines of the rising Calcium bubble. Even for the rising Ca bubble, small wakes are observed at the side of the calcium bubble/liquid steel interface.

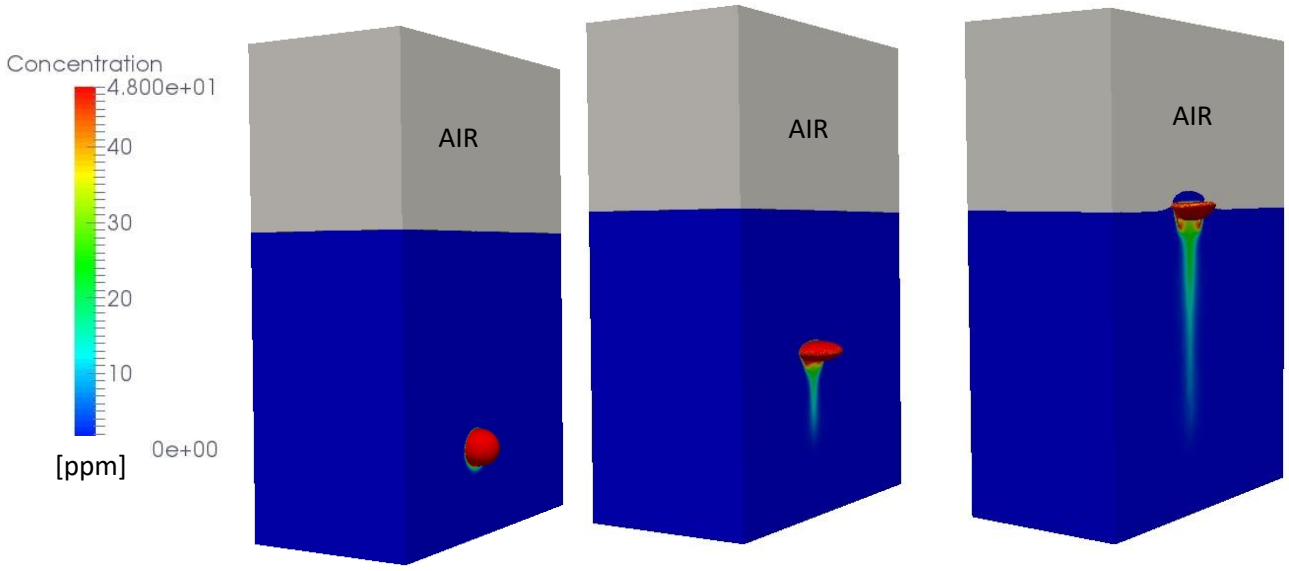

Figure 5-24 Calcium bubble rising and dissolving in liquid steel.

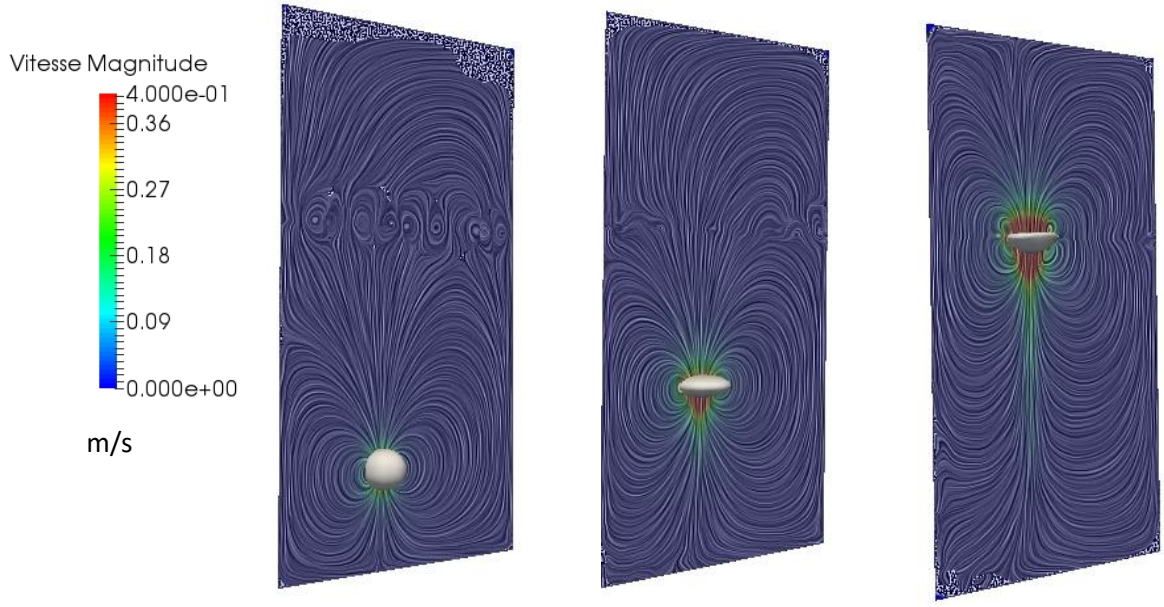

Figure 5-25 Velocity streamlines for the rising calcium bubble.

Total calcium dissolved in liquid steel is found to be around 0.09 ppm (average volumetric) when the calcium bubble reaches the surface of liquid steel. The total mass of liquid steel domain is around 2.6 kg, and the average rising velocity of calcium droplet is found to be 0.30 m/s, which leads to a residence time of around 0.25 seconds. Total calcium in liquid steel is found to be 2.34e-07 kg (with 0.09 ppm Ca dissolved) which leads to the flux (Ø) of around 9.36e-07 kg/s in liquid steel. In order to calculate the average mass transfer coefficient, we used the same formula which is being used for calculating the average mass transfer coefficient experimentally, which is:

$$\emptyset = K_{cadnum}.S\rho_{ls}.(C_{ca} - C_{ca}^{bath}).(10^{-6}) \quad (5.42)$$

For a bubble of diameter 1 cm (0.01 m), the surface area (S) is found to be 0.00031 m^2. C_{ca} (concentration imposed) is 48 ppm, $C_{ca}^{bath} \approx 0$ ppm and ρ_{ls} being 7200 kg/m^3, K_{cabnum} (average mass transfer coefficient of calcium bubble in liquid steel) is found to be **8.73e-03 m/s.**

It is observed that the average mass transfer coefficient of Calcium droplet (K_{cadnum} = **7.93e-03 m/s**) and the calcium bubble (K_{cabnum}= **8.73e-03 m/s**) is more or less of the same order of magnitude for the minimum mesh (h_{min}) of 80 µm. It can be explained by the fact that the calcium bubble lies just above the calcium droplet in the Grace diagram (Figure 3-21). Therefore, we can expect the same order of magnitude of terminal velocity for calcium droplet and calcium bubble (though calcium bubble having little higher terminal velocity than calcium droplet). Since the normalized concentration at the interface $\propto Sc^{1/2}Y^+ \left(Y^+ = \frac{U^*}{\nu_{ls}} \times (\delta -$

$y)\ and\ U^* = \sqrt{\frac{\tau_{ls}}{\rho_{ls}}}$). Having almost the same order of magnitude of terminal velocity can lead to the same order of magnitude of velocity gradient and subsequently to the same tangential shear stress (τ_{ls}) towards liquid steel side. Since the Schmidt number (Sc) is the same for both the cases (calcium bubble and calcium droplet), we could expect more or less the same concentration profile at the calcium droplet-liquid steel interface and at the calcium bubble-liquid steel interface. Later it was verified in 2D simulation. τ_{ls} (tangential stress) at instant t (time) across calcium bubble-liquid steel interface was found to be 1.31 Pa, and for calcium droplet-liquid steel, it was found 1.05 Pa.

5.12 Conclusion

In this chapter, we presented the development of a numerical model realized to compute the dissolution of rising calcium droplets or bubbles in liquid steel. In the beginning, we presented the method used for implementing three phases in our ICI-tech code. Implementation of three-phase flow was necessary to compute the rise of calcium droplet or calcium bubble in liquid steel with air at the top. Validation of three-phase flow is performed using classical benchmarks issued from the literature. After that, a case study is performed where the spreading of the lens is studied with different values of surface tension assigned at the interface.

Once the three-phase flow is validated, we implemented the dissolution model in the ICI -tech code, and the model is validated for a static droplet of calcium (Diffusivity of Ca =4e-09 m^2/s in liquid steel) dissolving in still liquid iron. We also validated the dissolution model (diffusion and convection) for the case where droplets are rising in the liquid medium. Simulations of three different physical properties have been conducted to demonstrate the capabilities of the model to predict the shapes and their rising velocity. Mass transfer coefficient obtained for these three different cases corresponded well with the one obtained from the correlations given in the literature.

Continuity of shear stress at the interface has been verified, which is an important criterion for determining the mass transfer and heat transfer across the interface correctly. After that, the rise of calcium droplet is computed in both 2D, 3D, and mesh sensitivity study is performed to evaluate the value of the average mass transfer coefficient of calcium droplet in liquid steel. In 3D, we obtained a converging tendency of mass transfer coefficient with the decrease in mesh size still; the results were not fully converged. The possible reason for not having a fully converged solution is the high Peclet number (~700000) we are dealing with, but in 2D, the results seemed to converge better.

Simulation has been performed for the rise of multiple calcium droplets in liquid steel, and the average mass transfer coefficient obtained numerically is compared with the one obtained experimentally. The average mass transfer coefficient obtained numerically is qualitatively in good agreement with experimental measurements.

In the end, simulation has been performed for the rise of calcium bubble in liquid steel (without phase change and nucleation) and the average mass transfer coefficient of calcium bubble in liquid steel has been reported. It is found that the average mass transfer coefficient of calcium bubble and calcium droplet in liquid steel are of the same order of magnitude.

The next chapter deals with the preliminary numerical results of the calcium liquid-gas phase change.

5.13 Résumé Français

Dans ce chapitre, nous avons présenté le développement du modèle numérique réalisé afin de calculer la dissolution de gouttelettes ou de bulles de calcium montantes dans l'acier liquide. Au début, nous avons présenté la méthode utilisée pour mettre en œuvre les trois phases de notre code ICI-Tech. La mise en œuvre d'un écoulement triphasique était nécessaire pour simuler la remontée de gouttelettes ou de bulles de calcium dans l'acier liquide avec de l'air au sommet. La validation de l'écoulement triphasique a été réalisée à l'aide de points de références classiques issus de la littérature. Ensuite, une étude de cas a été réalisée dans laquelle les angles de contact au point triple ont été reproduits pour différentes valeurs de tension superficielle à l'interface.

Une fois les écoulements triphasiques validés, nous avons implémenté le modèle de dissolution dans le code ICI-tech et le modèle a été validé pour une gouttelette statique de calcium (Coefficient de diffusion du Ca (calcium) = 1e-09 m^2/s dans du fer pur) se dissolvant dans du fer liquide. Nous avons également validé le modèle de dissolution (diffusion + convection) pour le cas où des gouttelettes montent dans le milieu liquide. Une simulation avec trois propriétés physiques différentes a été réalisée pour démontrer les capacités du modèle à prédire la forme et la vitesse ascendante des gouttelettes générées. Le coefficient de transfert de masse obtenu pour ces trois cas correspond bien à celui obtenu à partir des corrélations de la littérature.

La continuité de la contrainte de cisaillement à l'interface a été vérifiée, ce qui est un critère important pour déterminer correctement le transfert de masse et le transfert de chaleur à travers l'interface. Ensuite, l'élévation des gouttelettes de calcium est simulée en 2D, 3D et la sensibilité des résultats au maillage a été étudiée pour évaluer le coefficient de transfert de masse moyen. En 3D, nous avons obtenu une tendance convergente du coefficient de transfert de masse avec la taille du maillage, mais les résultats n'ont pas été totalement convergents. La raison possible de ne pas avoir une solution entièrement convergée est le nombre élevé de Peclet (~ 700000) auquel nous faisons face, mais en 2D, les résultats semblaient mieux converger.

Une simulation a été réalisée pour le cas de l'ascension simultanée de plusieurs gouttelettes de calcium dans de l'acier liquide. Le coefficient de transfert de masse moyen obtenu numériquement est comparé à celui obtenu expérimentalement. Plusieurs hypothèses ont été émises pour expliquer la différence entre les résultats expérimentaux et numériques.

Enfin, une simulation a été réalisée pour l'ascension de la bulle de calcium dans l'acier liquide (sans changement de phase) et un coefficient de transfert de masse moyen pour la bulle de calcium dans l'acier liquide a été déterminé.

Chapter 6:

Nucleation

6 Nucleation

As explained in chapter 2, calcium addition through the cored wire is the most commonly used method in the steel plants. Calcium is injected at a certain depth to avoid the phase change at the location where the wire dissolves into the steel melt. Thus, the calcium is released in the form of droplets due to the Ferro-static pressure of liquid steel. During the ascension of calcium droplets in liquid steel bath, Ferro-static pressure reduces, and the phase change of liquid calcium towards gaseous calcium takes place. It is essential to understand the exact mechanism of calcium liquid-gas phase change. Since the phase change mechanism can induce mixing inside the steel bath, which can subsequently affect the dissolution of calcium in liquid steel.

In this chapter, we present the literature survey on the possible nucleation (liquid-gas phase change) mechanisms and the possible nucleation rate. Then, the growth of a bubble in a superheated liquid medium is studied, and a simple growth model has been implemented in our ICI-tech code. Preliminary numerical results for phase-change are then presented. These implementations provide a first set-up for future studies in order to understand the calcium liquid-gas phase change and understand the dissolution mechanism of calcium gas in liquid steel.

6.1 Nucleation theories

Nucleation is the localized formation of a distinct thermodynamic phase. It is the process where droplets of liquid can condense from a vapor, or bubbles of gas can form in a boiling liquid. The physical concept of bubble nucleation can be understood by considering a volatile fluid in contact with the other condensed phase. The type of nucleation depends on the contact angle of the fluid with the enclosing phases. If the fluid has surface and interfacial tensions such that it has zero contact angles with all enclosing phases, then bubbles nucleated entirely within the liquid are thermodynamically more stable and this type of nucleation is defined as **homogeneous nucleation**. Another type of nucleation is Heterogenous nucleation.

Heterogeneous nucleation of bubbles is the nucleation at an interface between a volatile liquid and surrounding condensed phase when the contact angle of the volatile fluid is greater than zero. To create a bubble in a liquid requires the creation of a new interface as well as the transfer of molecules from the liquid into the bubble. When a small bubble of vapor is formed in the liquid, there are two contributions to the change in the energy of the system. The energy decreases because the energy per unit volume of vapor is lower than the energy of the liquid but increases because an interface between the liquid and vapor is created. Since the number of atoms that have changed from liquid to vapor varies as the cube of the radius (r) of the bubble, whereas the area of the interface varies as r^2, the total energy at first increases with increasing radius before reaching a maximum value at a critical radius ($r^* = r_c$), and then decreases, as shown in Figure 6-1.

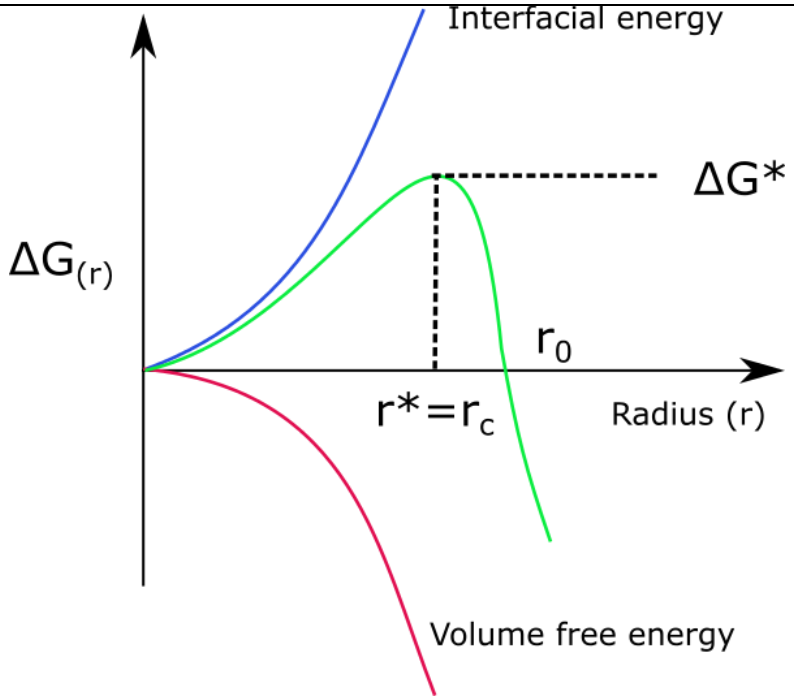

Figure 6-1 Free energy change during phase change [85].

In Figure 6-1, maximum (ΔG^*) is the barrier which prevents the nucleation of the bubbles and which must be surpassed before a measurable rate of boiling is observed. The higher the temperature is, the smaller is the surface tension of the liquid, which leads to a smaller maxima (ΔG^*) and to a greater rate at which bubble grows.

The steady-state rate of formation of bubbles per unit volume per unit time (J_s) is calculated from classical nucleation theory [86] [87]. In the nucleation theory, it is mentioned that the probability of heterogeneous nucleation is higher as compared to homogeneous nucleation if the wetting angle of the volatile fluid on the enclosing phase is significantly above zero. The theory also states that a liquid held at atmospheric pressure will not nucleate homogeneously until it has been superheated to the temperature, which is 89% of its critical temperature. Different possible nucleation mechanisms are explained in the following subsections.

6.1.1 Homogeneous nucleation theory: The classical approach

Many authors have studied the classical theory of kinetics of nucleation like Volmer et al. [88], Farkas [89], Becker et al. [90], and Zeldovich [91]. In the classical theory of nucleation, the rate of nucleation is governed by the rate at which bubbles of size less than the critical volume grow larger than the critical volume. The bubble grows with the vaporization of molecules from the liquid at the interface into the bubble. The rate of vaporization of molecules is a major factor governing the nucleation rate.

In order to study nucleation, the first thing which should be understood is the minimum work required to form a bubble of gas of volume V_G from the homogenous liquid phase at a constant temperature. Work equal to $\sigma.A$ is done to create the new surface where σ is the surface tension between the liquid-gas phase and A is the surface area of the bubble. However, in creating a cavity containing x gas molecule, part of this surface work is done by the gas

entering the cavity. The maximum possible work that the x gas molecules vaporizing into the cavity can provide, would be that obtained along a reversible path. If the vaporization of x molecules at a constant pressure P_v into a semipermeable membrane of constant area submerged in a medium at a pressure P_l and kept under an external counterforce per unit area $(P_v - P_l)$, then the work done W_1, by the gas on the environment providing that the counterforce is $(P_v - P_l)V_G'$. Here V_G' is the volume inside the membrane having x molecules at the pressure P_v. The maximum work done on the environment W_2 [85] is given by equation (6.1) if the volume is changed from V_G' to V_G keeping the number of molecules inside the membrane constant.

$$W_2 = \int_{VG'}^{V_G} (P - P_l)dv = P_G V_G - P_v V_G' - P_l(V_G - V_G') - \int_{P_v}^{P_G} v dp$$
$$= P_G V_G - P_v V_G' - P_l(V_G - V_G') - x(\mu_G - \mu_L) \quad (6.1)$$

In the above equation (6.1), P is the pressure inside the membrane during the change in volume from V_G' to V_G. μ_G and μ_l are the chemical potential of the gas phase and liquid phase, respectively. The maximum work obtained from vaporizing the gas to a volume V_G at a pressure P_G is therefore $W_1 + W_2$. The minimum work needed to form a bubble is, therefore [92]:

$$W = \sigma A - W_1 - W_2 = \sigma A - (P_G - P_l)V_G + x(\mu_G - \mu_l) \quad (6.2)$$

The work in order to create a bubble first increases to a maximum and then decreases as the volume increases. The bubble formed is called a critical bubble, and the radius is called critical radius (r_c) when P_G is equal to P_v and when the volume of the bubble is such that the radius r is given by:

$$P_v = P_l + \frac{2\sigma}{r_c} \quad (6.3)$$

Bubble smaller than the critical size tends to collapse and bubble larger than the critical size tends to continue to grow spontaneously. If other factors do not govern the rate of vaporization (e.g., inertial or viscous forces, diffusion of molecules, heat transfer), then the bubble will be in chemical equilibrium with the liquid such that, $P_G = P_v$ and $\mu_G = \mu_l$. If the hydrodynamic constraints are not taken into account, then one can write:

$$P_G \approx P_l + \frac{2\sigma}{r} \quad (6.4)$$

The above equation presumes that the bubble is close to mechanical equilibrium. In such a case, one can show (Katz and Blander [93]) that,

$$W \approx \frac{4}{3}\pi r_c^2 - 4\pi\sigma(r - r_c)^2 . B \quad (6.5)$$

Case corresponding to mechanical equilibrium, $B \approx 1 - \frac{1}{3}(1 - \frac{P_l}{P_v})$. Usually $P_l \ll P_v$, then the factor $B = \frac{2}{3}$. On the other hand, if it is assumed that the bubble is in chemical equilibrium that is $P_G = P_v$ and $\mu_G = \mu_l$, then the value of B becomes equal to 1. For the cavitation also, the value of B is equal to 1. Bubbles are formed as a density fluctuation in the liquid. A region where the bubble is formed is a localized region that has a lower average density, and it is described as a region of the bubble of radius r containing a x number of molecules. The number n of bubbles per unit volume containing x molecules is related exponentially to the minimum work w required to form the bubble as given in equation (6.2) is:

$$n = Nexp(-\frac{W}{kT}) \tag{6.6}$$

Where it is considered that the pre-factor N is the number density of the liquid, k is the Boltzmann's constant and T is the temperature respectively. At the gas-liquid interface, the growth and decay of bubbles take place by the evaporation or condensation of molecules. The net rate of transformation of molecules x to $x + 1$ is governed by vaporization as well as the condensation. At a steady state, this rate is independent of x, and the rate of formation of bubbles per unit time per unit volume J is then found to be an integral of n [92].

$$J = {\beta}\Big/{\int [nA]^{-1} dx} \tag{6.7}$$

Where β is the rate per unit area at which a bubble surface gains or loses molecules. It is approximated as $\beta = \frac{P}{(2\pi mkT)^{1/2}}$ .The integral in equation (6.7) is obtained as:

$$J = \beta A(r_c) n(r_c) Z \tag{6.8}$$

Where $A(r_c)$, $n(r_c)$ are the surface area, and the number density of critical bubbles. Z is known as the Zeldovich factor which is given by:

$$Z = (\frac{\sigma KT}{B})^{1/2} [P_v A(r_c)]^{-1} \tag{6.9}$$

Where P_v, the vapor pressure is equal to the pressure inside the critical bubble. The largest contribution to J from the integral occurs at radii close enough to the critical radius so that the work to make a bubble is adequately represented by the quadratic function of $(r - r_c)$ given by equation (6.5). Most of the obstruction concerning the steady-state J occurs near the critical size. The Zeldovich factor Z is a correction to the rate which arises from the fact that the steady state concentration of the critical size bubble is less than the equilibrium number given by equation (6.5). Combining equation (6.5) and (6.9) one obtains:

$$J = N[2\sigma/\pi mB]^{\frac{1}{2}} exp[-16\pi\sigma^3/3KT[P_v - P_l]^2] \tag{6.10}$$

In the above equation, m represents the mass of the bubble, T represents the temperature, and K represents the Boltzmann constant. If $P_v - P_l$ needs to be presented in terms of equilibrium pressure (P_e), there needs to be a correction factor which is expressed as:

$$P_v - P_l \approx (P_e - P_l)\delta \tag{6.11}$$

the correction factor for the effect of pressure on the vapor pressure δ is given by the equation:

$$\delta = 1 - \left(\frac{\rho_g}{\rho_l}\right) + \frac{1}{2}\left(\frac{\rho_g}{\rho_l}\right)^2 \tag{6.12}$$

Where ρ_l is the density of the liquid, and ρ_g is the density of the gas. Combining equation (6.10) and (6.11) for nucleation rate, one obtains:

$$J \approx 3.73(10^{35})\left[\frac{\rho_l \sigma}{m^3 B}\right]^{1/2} exp\left[\frac{(-1.182(10^5)\sigma^3)}{(T(P_e - P_l)^2\delta^2)}\right] \tag{6.13}$$

Where B depends on the process, it is 2/3 except for cavitation in which $B = 1$. Thus, from equation (6.13), it can be seen that any temperature change will have a very strong effect on the rate of nucleation. It was observed experimentally, that nucleation occurs at about $0.89T_c$ (T_c is the critical temperature) and the predicted rate of nucleation is about 10^4-10^6 bubbles $cm^{-3}s^{-1}$. Its value changes about three to four orders of magnitude per degree Celsius (data are for boiling of n-pentane in sulfuric acid, (Katz and Blander [93])).

Nucleation theory can be extended for cases where hydrodynamic and transport constraints influence the rate of nucleation. The nucleation rate is given by Kagan et al. [94] :

$$J_\lambda = J/(1 + \delta_\lambda) \tag{6.14}$$

Where J is given by equation (6.13) and J_λ includes the influence of heat transfer on the bubble nucleation rate. δ_λ is the correction term for heat flux.

Nucleation theory can also be extended for cases where diffusion phenomenon influences the rate of nucleation, and the rate of nucleation is lowered from J to J' (Kagan et al. [94]) :

$$J' = J/(1 + \delta_D) \tag{6.15}$$

δ_D is the correction term for diffusion control.

Experimental observation: n-pentane has a boiling point of 36°C, and it nucleates at a temperature of 147.8°C [95]. When hexadecane is added in the sulfuric acid, the nucleation temperature is increased to 197°C, and the rate of nucleation is minimized because of the diffusion controlled nucleation. The dilution of n-pentane by hexadecane raises the surface

tension and lowers the vapor pressure. This requires heating to a higher temperature to overcome nucleation barriers.

6.2 Heterogeneous nucleation

In heterogeneous nucleation, the bubble is not formed in the middle of the liquid medium but on the pre-existing surface. The heterogeneous rate is higher than the homogenous nucleation rate in the same conditions: the existing surface reduces the cost of surface formation, and the nucleation barrier is low. Under most conditions in which boiling occurs, bubbles are nucleated heterogeneously at the interface between a boiling liquid and the contacting surface. Different types of heterogeneous mechanisms are further discussed below.

6.2.1 Nucleation on a smooth rigid surface

Crystalline solid generally contain numerous cracks, cavities, and imperfections and cannot be considered as smooth plane surfaces. Unscratched glasses may have smooth rigid surfaces. This case concerns the glassy material. The minimum work [96] needed to form such a bubble is given by equation (6.16).

$$W = \sigma_{LG}A_{LG} + (\sigma_{SG} - \sigma_{SL})A_{SG} - (P_G - P_l)V_G + x(\mu_G - \mu_L) \qquad (6.16)$$

Where surface free energy of the solid interface gas is denoted by SG, LG is for liquid gas, and SL is for the liquid-solid interface. σ_{LG} and σ_{SL} is the surface tension between liquid gas and solid glass liquid. μ_G and μ_l are the chemical potential of the gas phase and liquid phase, respectively. The volume of the bubble (V_G) and the interfacial areas can be calculated in terms of its radius of curvature R and the contact angle θ. Defining m = Z/R in Figure 6-2.

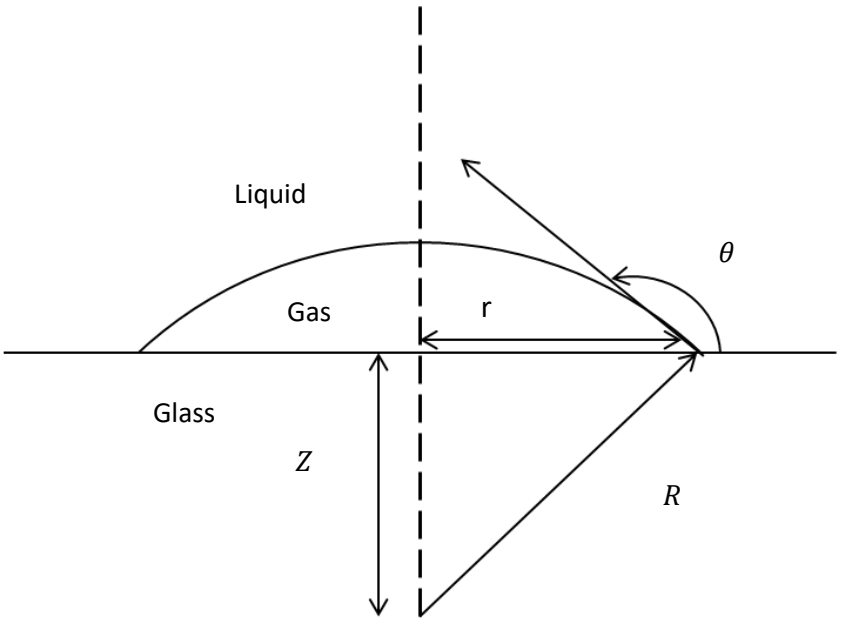

Figure 6-2 Gas bubble at the glass-liquid interface [96].

$$m = \cos(\pi - \theta) = -cos\theta \quad (6.17)$$

$$V_G = \frac{1}{3}\pi(R - Z)^2(2R + Z) = \frac{1}{3}\pi R^3(2 - 3m + m^3) \quad (6.18)$$

$$A_{LG} = 2\pi r(R - Z) = 2\pi R^2(1 - m^2) \quad (6.19)$$

$$A_{SG} = \pi R^2(1 - m^2) \quad (6.20)$$

Since by the force balance at the edge of the bubble (young's Laplace equation):

$$\sigma_{SL} = \sigma_{SG} + \sigma_{LG}Cos(\pi - \theta) = \sigma_{SG} + m\sigma_{LG} \quad (6.21)$$

Then,

$$m = \frac{\sigma_{SL} - \sigma_{SG}}{\sigma_{LG}} \quad (6.22)$$

A force balance at the edge of the bubble implies that mechanical equilibrium holds and Laplace equation is given by:

$$P_G - P_l = \frac{2\sigma}{R} \quad (6.23)$$

The chemical potential is expressed in terms of the radius R as:

$$\mu_G - \mu_L = KTln\left(\frac{P_G}{P_v}\right) = KTln\frac{P_l + 2\sigma/R}{P_l + 2\sigma/r_c} \quad (6.24)$$

Where r_c is the radius of the critical-sized bubble and P_v is the gas pressure inside critical size bubble. The number of molecules x in the bubble is related to the radius R via the equation of state:

$$x = \frac{P_G V_G}{KT} = \frac{\left(P_l + \frac{2\sigma}{R}\right)4}{3}\frac{\pi R^3 F}{KT} \quad (6.25)$$

Where $F \equiv (2 - 3m + m^3)/4$ and then the minimum work required to form a bubble is given by:

$$W = \frac{4}{3}\pi R^2\sigma F + \frac{4}{3}R^3 F\left(P_l + \frac{2\sigma}{r}\right)ln\frac{P_l + 2\sigma/R}{P_l + 2\sigma/r_c} \quad (6.26)$$

For the rate of nucleation N number density of the liquid changes to $N^{2/3}$. Since one view each molecule at the surface instead of each molecule in the droplet as a potential bubble. The rate of nucleation (J) obtained is:

$$J = N^{\frac{2}{3}}S\left[\frac{2\,\sigma}{\pi mBF}\right]^{1/2} exp\left[\frac{-16\pi\sigma^3 F}{3KT[(P_v - P_l)^2]}\right] \quad (6.27)$$

Where S = (1-m)/2. Equation (6.27) for heterogeneous nucleation can be compared with equation (6.10) for a homogenous equation. The pre-exponential term in equation (6.27) is smaller than the corresponding term in equation (6.10) by a factor of $N^{\frac{1}{3}}$. However, the exponential term of equation (6.27) is larger than those in equation (6.10) when the factor F is less than unity. A value of F less than 0.77 leads to a higher probability for heterogeneous nucleation than that of homogeneous nucleation.

6.2.2 Nucleation at liquid-liquid interface

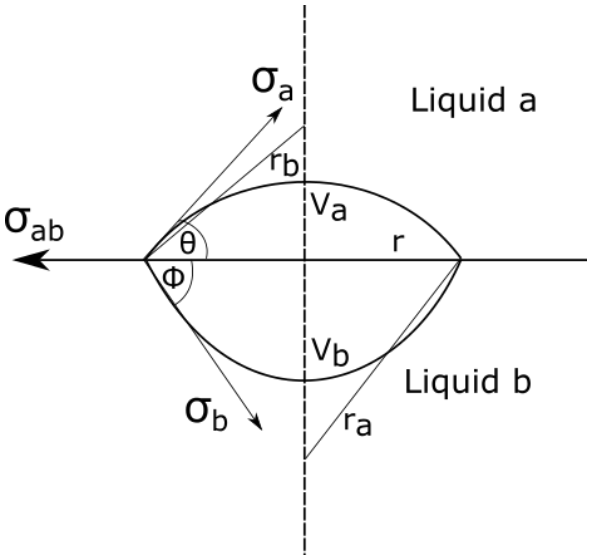

Figure 6-3 Vapor bubble at a liquid-liquid interface [97].

In this section, the mechanism of nucleating a vapor bubble at a liquid-liquid interface is explained. The minimum work required to create a vapor bubble of "radius" r with an internal pressure P, at a liquid-liquid interface is given by [97]:

$$W(r,P) = \sigma_a A_a + \sigma_b A_b - \sigma_{ab} A_{ab} + (V_a + V_b)\left[\left[-P_G + P_l + P_G . ln\left(\frac{P_G}{P_L}\right)\right]\right] \quad (6.28)$$

Where A_a and A_b are the areas of the liquid interfaces, A_{ab} is the interfacial area destroyed in creating the vapor bubble, V_a, and V_b are the respective volumes of the lenticular parts. σ_a, σ_b, and σ_{ab} are the respective surface tension and interfacial tensions. r_a and r_b are the respective radii of curvature of each surface. A force balance on the bubble yields:

$$\sigma_{ab} = \sigma_a cos\theta + \sigma_b cos\emptyset \quad (6.29)$$

$$\sigma_a sin\theta = \sigma_b sin\emptyset \quad (6.30)$$

$$M_a = cos\theta = \frac{\sigma_a^2 + \sigma_{ab}^2 - \sigma_b^2}{2\sigma_a\sigma_{ab}} \quad (6.31)$$

$$r = r_a sin\theta = r_b sin\emptyset \tag{6.32}$$

Combining equation

(6.32) and equation (6.30) leads to:

$$\frac{\sigma_a}{r_a} = \frac{\sigma_b}{r_b} \tag{6.33}$$

Minimum work required for forming a bubble of radius r in terms of surface tension and interfacial tension is found as:

$$W(r) = 4\pi\left(\frac{r}{\gamma}\right)^2 + \frac{4}{3}\pi\left(\frac{r}{\gamma}\right)^3 \sigma_a^3 F \times \left\{-2\left(\frac{\gamma}{r}\right) + (P_l + 2\gamma/r \times ln\left(\frac{P_l + 2\gamma/r}{P_l + 2\gamma/r_c}\right)\right\} \tag{6.34}$$

Where $\gamma = \sigma_a sin\theta = \sigma_b sin\emptyset$

And $\sigma_a^3 = \frac{1}{4}[\sigma_a^3(2 - 3M_a + M_a^3) + \sigma_b^3(2 - 3M_b + M_b^3)]$

The critical radius r_c is obtained by setting $\frac{\partial W}{\partial r} = 0$; the condition required that the bubble is in both mechanical and chemical equilibrium. Thus r_c is obtained as:

$$r_c^2 = \frac{4\gamma^2}{(P_v - P_l)^2} = \frac{\sigma_{ab}^2}{(P_v - P_l)^2} \times \left[\left(\frac{\sigma_a + \sigma_b}{\sigma_{ab}}\right)^2 - 1\right]\left[1 - \left(\frac{\sigma_a - \sigma_b}{\sigma_{ab}}\right)^2\right] \tag{6.35}$$

It can be seen that r_c will be zero or imaginary when any of the inequalities are satisfied.

$$\sigma_{ab} \geq \sigma_a + \sigma_b \tag{6.36}$$

$$\sigma_b \geq \sigma_a + \sigma_{ab} \tag{6.37}$$

$$\sigma_a \geq \sigma_b + \sigma_{ab} \tag{6.38}$$

In equation (6.36), the interfacial tension is equal to or greater than the sum of the two surface tensions, is physically unrealizable and therefore of no importance. Equation (6.37) and equation (6.38) are the spreading conditions when satisfied liquid a spread on liquid b or liquid b spreads on liquid a. When r_c is equal to zero, the vapor bubble will exist totally in one or the other of the bulk liquids depending on which liquid spreads on the other. If liquid a spread on liquid b, it takes less work to create a vapor bubble totally in liquid a than at the liquid-liquid interface. Similarly, if liquid b spreads on liquid a, it takes less work to create a vapor bubble totally in liquid b than the interface. r_c is real and positive only if neither liquid spreads on the other liquid. In terms of the surface and interfacial tensions, the requirement for a critical size, mechanically stable bubble at a liquid-liquid interface is both $(\boldsymbol{\sigma}_{ab} > \boldsymbol{\sigma}_b - \boldsymbol{\sigma}_a)$ and $(\boldsymbol{\sigma}_{ab} > \boldsymbol{\sigma}_a - \boldsymbol{\sigma}_b)$. In this situation, it takes less work to create a vapor bubble at the liquid-liquid interface than in the bulk liquid.

Observation:

Hydrocarbons, water, and surfactants were mixed, and the superheat limits of these emulsions are lower than those of either pure liquid, and it was found that a high interfacial tension is required for nucleation to occur at the liquid-liquid interface [97].

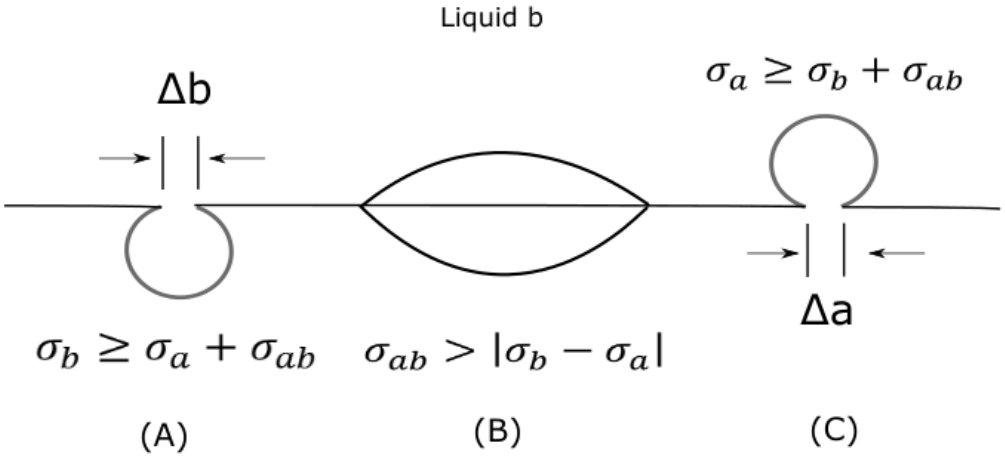

Figure 6-4 Shape of the bubble formed depending on the interfacial surface tension [97].

Nucleation at the liquid-liquid interface in an emulsion always results in the lowest work of formation. Both the liquids can contribute to the vapor pressure in the bubble, and the nucleus position can be predicted by the criteria given in Figure 6-4. To make this prediction, the interfacial tension between the two liquids as well as their individual surface tension must be known.

In this section, we saw the description for the nucleation rate for the heterogeneous nucleation, which includes nucleation at the smooth surface and nucleation at the liquid-liquid interface. The section below deals with the nucleation at a liquid non-smooth solid interface, which is the most common type of nucleation in the engineering processes.

6.2.3 Nucleation at a liquid non- smooth solid interface

In this type of nucleation, bubbles nucleate at the imperfections on the surface submerged in the liquid. This case has been discussed in detail by Cole [98]. These imperfections can be scratches, pits, and grooves commonly called cavities, which form on the surface during its preparation. It is explained by Cole [98] that the superheats associated with heterogeneous nucleation are much lower. The reason for the lower inception superheat can be easily rationalized if it is considered that the cavities generally trap air or other non-condensable substance. The amount of air trapped in the cavity depends on the surface tension, the contact angle, and the shape of the cavity. With heating, the gas expands and pushes the interface outwards. The liquid superheat required for thermal equilibrium increases with a reduction in the radius of the bubble; the highest superheat is needed when the bubble radius is equal to

the cavity radius. Thus, the bubble inception is controlled by the size of the cavity. As the cavities become fewer and fewer, their size decreases, and the observed nucleation temperature approaches the homogeneous nucleation temperature. The trapped gas not only promotes nucleation, but it also reduces the vapor pressure in the bubble. Using Dalton's law of partial pressure, the pressure (P_b) in the bubble nucleus can be written as:

$$P_b = P_v + P_g \tag{6.39}$$

P_g is the pressure inside the bubble due to the trapped gas. Since the vapor pressure difference across the interface is reduced by P_g, the liquid superheats for thermal equilibrium is also reduced accordingly such that:

$$T_l - T_{sat} = \frac{\left(\frac{2\sigma}{r} - P_g\right)}{\rho_v H_v} T_{sat} \tag{6.40}$$

The above equation is derived from the Clausius-Claperyon equation, which is:

$$\frac{\Delta P}{\Delta T} = \frac{H_v}{V_{fg}\left(T_{sat} + \frac{\Delta T}{2}\right)} \tag{6.41}$$

V_{fg} is the difference in specific volumes of vapor and liquid at the system pressure, H_v is the specific enthalpy change of evaporation. For homogeneous nucleation and for $\Delta T \ll T_{sat}$, taking ΔP from Clausius-Clapeyron equation and combining with mechanical equilibrium [99], degree of superheat for homogeneous nucleation is given by:

$$T_l - T_{sat} = \frac{2\sigma V_{fg} T_{sat}}{r H_v} \tag{6.42}$$

If we compare equation (6.42) with equation (6.40), we can find that the degree of superheat in heterogeneous nucleation is much lower than that of in homogeneous nucleation.

Nucleation at non- smooth solid interface can be categorized into pool boiling and flow boiling. In pool boiling, the boiling takes place on the external surface when the object is submerged in a large bulk of fluid which is generally motionless, e.g., boiling of water in the hot pan or large chunk of hot metal immersed in the liquid for quenching. In general, the fluid is motionless, but the rising bubbles induce the motion inside the liquid locally. On the other hand, flow boiling occurs when all the phases are in bulk flow. It is always accompanied by the convection effects. Conditions strongly depend on the geometry, which involves external flow over heated plates. In a nuclear reactor, most boiling regimes are forced convection boiling. The section below explains the different regimes in pool boiling.

Pool boiling is conventionally discussed with the boiling curve (Figure 6-5) [100]. Imagine the bulk of liquid on the surface with a temperature T_w and saturation temperature of the liquid being T_{sat}. Heat flux is denoted by q'_w and the variation of heat flux with temperature $T_w - T_{sat}$ is presented in the pool boiling curve. A to B (Regime I) in Figure 6-5 is a natural convection

zone. In this region, the temperature of the bulk fluid is below the saturation temperature. The fluid gets heated, and temperature tends to increase. Regime II is the region of the isolated bubble. Solid surface temperature is more than saturation temperature, which leads to the formation of bubbles. In the IIIrd regime, the number of isolated bubbles increases, the distance between the bubbles decreases, and the frequency of bubble generation increases. This region comprises of vapor columns and jets. In Regime IV, the vapor columns and jets try to merge. This region is also called developed nucleate boiling. In the Vth regime, the surface is partially blocked by vapor patches and partially contacting the liquid. It is called transition boiling. Ultimately in the VIth regime, the entire surface is covered by a thin vapor film, and it is denoted by film boiling.

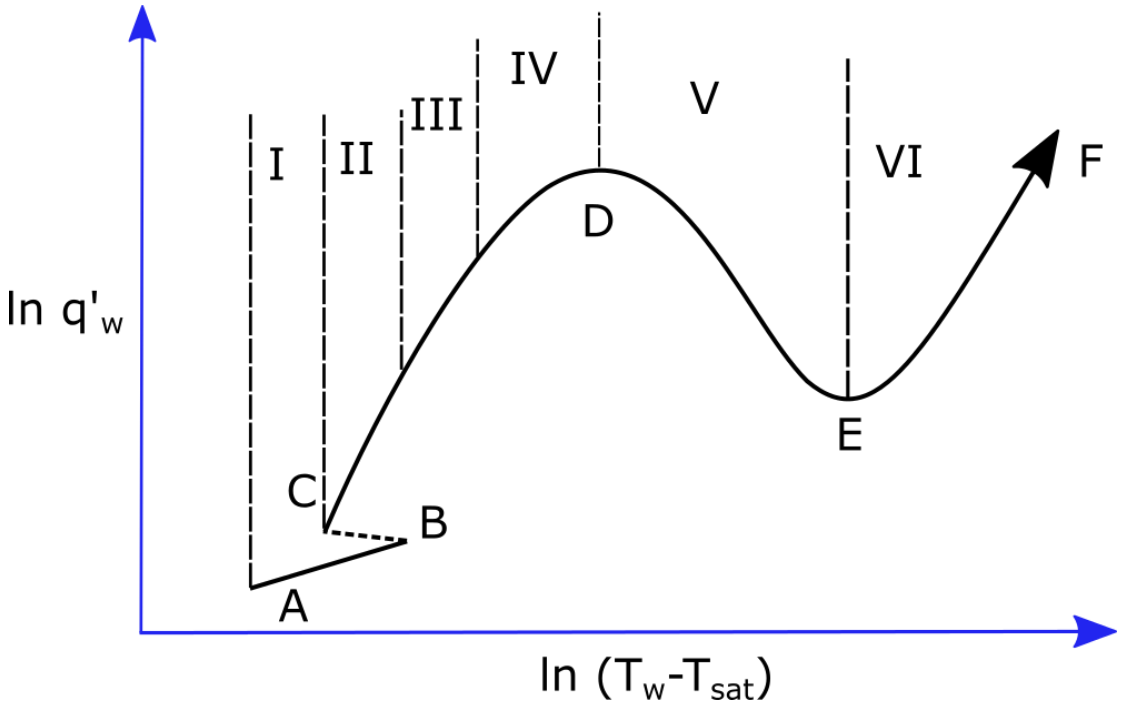

Figure 6-5 Pool boiling curve [98].

D in Figure 6-5 is called the critical heat flux point. At this very point, vapor patches are formed, and an increase in the temperature leads to a decrease in the heat flux. From D to E, the entire surface is covered by a thin film of vapor and vapor film has low heat transfer capability, which leads to the reduction in heat flux. Out of the different regimes in the boiling process, the depart of the boiling process starts from the isolated bubble formation. Slugs and columns in the boiling curve are ultimately coming from the isolated bubbles. In order to understand the nucleation phenomenon properly, the bubble formation and its growth need to be understood properly. Since at this stage of our research, implementing the nucleation rate (bubble formation) in our code (ICI-tech) seemed to be a toilsome task; therefore, we studied the growth of an already formed nucleus (bubble) in a super-heated liquid. The section below explains the growth of an isolated bubble in an extensive liquid pool and its implementation in our code ICI-tech.

6.2.4 Bubble growth in an extensive liquid pool

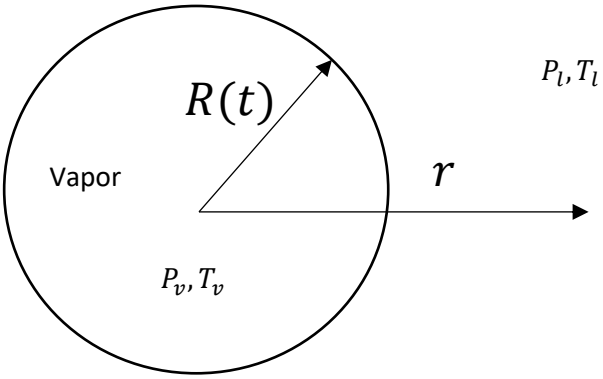

Figure 6-6 Bubble growing in a superheated liquid.

Many complex bubble growth mechanisms exist for the bubble growth near the heated surface, but the simplified version of bubble growth is presented here which deals with the growth of spherical bubbles [100] in a uniformly superheated heated liquid.

Let us suppose, a bubble of radius R at instant t. The bubble is in a bulk of liquid which has pressure P_l, temperature T_l. The pressure and temperature inside the bubble are P_v and T_v, respectively. When the bubble is first formed, the interface temperature is equal to the superheated liquid temperature and has a maximum pressure inside the bubble equal to $P_{sat}(T_l)$. As the liquid superheats, the interface is consumed to provide the latent heat of vaporization, the temperature at the interface drop towards $T_{sat}(P_l)$. As the bubble's size increase during its growth, the pressure difference across the interface reduces (Laplace law), and the pressure inside the bubble reduces toward P_l. The pressure and the temperature lie in the range of:

$$P_l \leq P_v \leq P_{sat}(T_l) \tag{6.43}$$

$$T_{sat}(P_l) \leq T_v \leq T_l \tag{6.44}$$

Rate of the bubble growth is dictated by:

1) Fluid momentum and pressure difference
2) Rate of vaporization which depends on the rate of heat transfer
3) The local thermodynamic equilibrium which is assumed to exist at the interface, i.e., $P_v = P_{sat}(T_v)$

There are two limiting cases of bubble growth:

1) Inertia controlled: It is an initial stage of growth and pressure has the maximum value, $P_{sat}(T_l)$, and the temperature inside the bubble is close to liquid temperature ($T_v \approx T_l$). The growth in the inertia controlled regime is dictated by momentum transfer, not

by the rate of heat transfer. Rayleigh [101] predicted the growth of the bubble in the liquid medium by using the conservation of momentum equation, which is obtained as:

$$R(t) = \left\{\frac{2}{3}\frac{(T_l - T_{sat}(P_l))}{T_{sat}(P_l)}\frac{H_v\rho_v}{\rho_l}\right\}^{\frac{1}{2}} t \tag{6.45}$$

It is shown that the radius increases linearly with time (t) during the initial inertial-controlled stage of the growth of the bubble.

2) Heat transfer controlled growth: It is a later stage of bubble growth. In this regime, T_v approaches the minimum value $T_{sat}(P_l)$ and $P_v \approx P_l$. The slower transport of heat to the interface lowers the interface motion. In this regime, the bubble is generally large, and the interface temperature has been decreased significantly. By the energy balance equation, the bubble growth in this regime is given by:

$$R(t) = 2C_R\sqrt{\alpha_l t} \tag{6.46}$$

Where,

$$C_R = \sqrt{\frac{3}{\pi}}Ja \text{ and } Ja = \frac{\rho_l C_{pl}(T_l - T_{sat})}{\rho_v H_v} \tag{6.47}$$

α_l denotes the thermal diffusivity of liquid and Ja is the Jacob number. The above equations are only valid for the isotropic bubble growth.

In order to have a complete bubble growth process, Mikic et al. [102] proposed a mathematical formulation that can take into account inertial as well as heat controlled bubble growth. They compared the derived relation with the existing experimental results for bubble growth in a uniformly superheated liquid (water) with very good agreement. The proposed bubble growth equation is:

$$R^+ = \frac{2}{3}\left[(t^+ + 1)^{3/2} - (t^+)^{\frac{3}{2}} - 1\right] \tag{6.48}$$

Where,

$$R^+ = \frac{RA}{B^2} \text{ and } t^+ = tA^2/B^2 \tag{6.49}$$

$$A = \left(\frac{b\Delta T H_v\rho_v}{T_{sat}\rho_l}\right)^{1/2} \tag{6.50}$$

$$B = \left(\frac{12\alpha_l}{\pi}\right)^{1/2} Ja \tag{6.51}$$

In equation (6.48), R^+ denotes the non-dimensional bubble radius, and t^+ denotes the non-dimensional time defined by equation (6.49); therefore, it represents the variation of the bubble radius with time. A and B in equation (6.49) is defined by equation (6.50) and (6.51), respectively. b = 2/3 for bubble growth in an infinite medium and b = $\pi/7$ for bubble growth on a surface. When $t^+ < 1$, equation (6.48) behaves as an inertial controlled regime and when $t^+ > 1$, the equation (6.48) behaves as a heat controlled regime. In order to exist in thermodynamic equilibrium with the surrounding liquid, the radii of the bubble should be higher than the critical radius (r_c) given by equation (6.52).

$$r_c = \frac{2\sigma(T_{sat})}{H_v \rho_v \Delta T} \tag{6.52}$$

σ in the above equation represents the surface tension between the bubble and liquid medium, T_{sat} is the liquid saturation temperature, H_v is the latent heat of vaporization, ρ_v is the density of the vapor and ΔT is the liquid superheat ($T_l - T_{sat}$). The magnitude of R^+ relative to one indicates the regime of bubble growth. R^+ much lesser than one shows the inertia controlled growth and the R^+ relatively larger than one shows heat transfer controlled growth. The bubble growth proposed by this correlation is less accurate for the higher superheat values as the formulation uses a linearized formula of the Clapeyron equation to relate $P_v - P_l$ to $T_v - T_{sat}$. Studies by Thefanous et al. [103] and Plesset et al. [104] focused mainly on the bubble growth for higher superheat. In order to study the growth of the bubble in the liquid medium, we implemented the basic model (growth model) proposed by, Mikic et al. [102] in our ICI-tech code.

6.3 Implementation of growth model in ICI-tech

Bubble growth rate equation (6.48) is implemented in the ICI-tech in order to simulate the calcium liquid-vapor phase change. A compressible solver for multiphase flow is used for computing the growth of a bubble in the liquid medium. The momentum equation for the compressible flow is given by:

$$\rho(\partial_t v + v.\nabla v) + \nabla p - \nabla.\left(\mu\left(\nabla v + (\nabla v^T)\right)\right) = \rho g + f_{st} + \frac{1}{3}\mu\nabla(\nabla.v) \tag{6.53}$$

Where ρ and μ are the density and the dynamic viscosity, v and p denote the velocity field and the pressure field, g is the gravity force. If we compare equation (6.53) with equation (5.1) which is the Navier-Stokes equation for the incompressible solver, the difference is the $\frac{1}{3}\mu\nabla(\nabla.v)$ in the equation (6.53). $\nabla.v$ represents the divergence of velocity, which is not zero in case of compressible Navier-Stokes equation. In order to advect the interface, the level set equation (4.8) is modified, and the resultant equation for the advection of interface is in the form of equation (6.54).

$$\frac{\partial u_\varepsilon}{\partial t} + (v + v_c).\nabla u_\varepsilon \quad = 0$$
$$u_\varepsilon(t = 0, x) = \ u_{\varepsilon 0}(x) \tag{6.54}$$

v_c which is the growth velocity of the interface, is implemented in the ICI-tech code whose value ($\frac{dR}{dt}$) is obtained from equation (6.48). The growth velocity (v_c) is then represented as:

$$v_c(t) = \frac{dR(t)}{dt} = A\left(\left(t\frac{A^2}{B^2} + 1\right)^{1/2} - \left(t\frac{A^2}{B^2}\right)^{\frac{1}{2}}\right) \tag{6.55}$$

In 2D, the variation of the area (dA) of the growing bubble is given by:

$$\frac{dA(t)}{dt} = v_c \times 2\pi R(t) \tag{6.56}$$

In the case where there is flow deformation, the variation of bubble area can be expressed as equation (6.57) where $perimeter(t)$ is the perimeter of the growing bubble at instant t.

$$\frac{dA(t)}{dt} = v_c \times perimeter(t) \tag{6.57}$$

If the bubble is not perfectly spherical, then the $perimeter(t)$ is expected to be larger than the perimeter of the perfectly spherical bubble (Mikic et al. [102] growth model is valid for perfectly spherical bubble only). In order to conserve the sphericity approximation of the model, modified growth velocity (v_{c-mod}) is used, which is given by the equation below:

$$v_{c-mod} = v_c \times \frac{2\pi R(t)}{perimeter\ (t)} \tag{6.58}$$

In equation (6.58), $2\pi R(t)$ is the perimeter given by Mikic et al. [102] growth model and $perimeter(t)$ is the perimeter of the elongated bubble obtained numerically. Another critical point for multiphase flow is that the bubble will not grow if it is outside the liquid which is vaporizing; therefore, the modified growth velocity (v_{c-mod}) is multiplied by the Heaviside of the liquid which is vaporizing to obtain $v_{c-effec}$.

$$v_{c-effec} = v_{c-mod} \times H_l(\alpha) \tag{6.59}$$

Apart from the implementation of corrected growth velocity ($v_{c-effec}$), as mentioned, compressible solver equation (6.53) is used, and in the compressible solver, $\nabla.v$ is obtained from the formulation given by son et al. [105] which is:

$$\nabla.v = \left(\frac{(\rho_v - \rho_l).\overrightarrow{v_{c-effec}}}{\rho_l}\right).\nabla H_\varepsilon(\alpha) \tag{6.60}$$

In the above equation, ρ_v denotes the density of vapor, ρ_l is the density of the liquid, $H_\varepsilon(\alpha)$ represents the smooth Heaviside function and $\overrightarrow{v_{c-effec}} = \ v_{c-effec}.\vec{n}$. Here $\vec{n}$ is normal to the interface and $v_{c-effec}$ is scalar quantity in our calculation. The final equation for advection of interface thus becomes:

$$\frac{\partial u_\varepsilon}{\partial t} + (v + \overrightarrow{v_{c-effec}}).\nabla u_\varepsilon = 0 \quad (6.61)$$

Once the growth velocity ($v_{c-effec}$) and the divergence of velocity ($\nabla.v$) is implemented in ICI-tech code. We computed the growth of a bubble in a uniformly superheated heated stable liquid. It is explained in the section below.

6.4 Validation of growth model implemented in ICI tech code

Mikic et al. [102] compared their results obtained by the analytical correlation (equation (6.48)) with the experimental results of Lien et al. [106] for bubble growth rates (water vapor) in a uniformly superheated liquid (water). A good agreement was found between the bubble growth predicted by the analytical solution of Mikic et al. [102] and the experimental results. In order to validate our growth model, we studied the growth of a bubble in a uniformly superheated stable liquid (water) and compared our results with the mathematical formulation proposed by Mikic et al. [102]. For computing, the growth of the bubble (water vapor) in a uniformly superheated liquid, domain of length 0.3 cm and height 1 cm is taken (Figure 6-7).

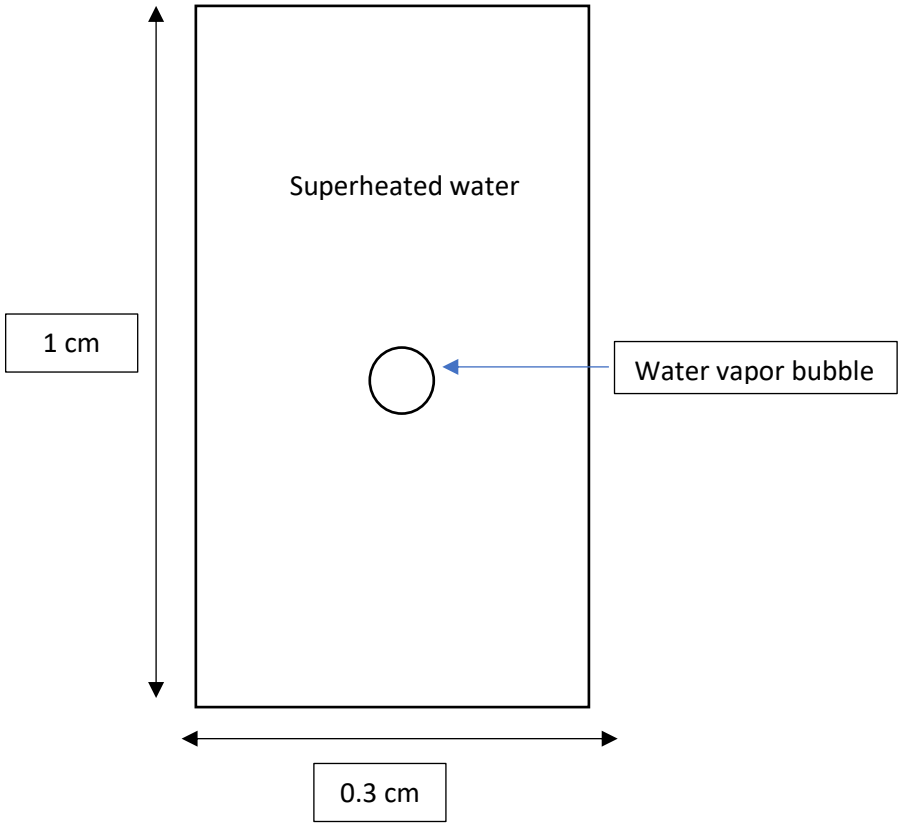

Figure 6-7 Calculation domain for computing the bubble growth in superheated water.

A water vapor bubble of diameter 0.03 cm is taken initially, which is allowed to grow due to the evaporation of the vapor-liquid interface. Physical properties and numerical parameters

for computing the growth of the bubble in water medium can be seen in Table 6-1 and Table 6-2, respectively. No boundary condition is applied on the walls of the domain.

H_{vw}	2250000 (J/kg)
μ_w	0.001 (Pa.s)
ρ_b	1 (kg/m^3)
μ_b	0.00001 (Pa.s)
σ_{wb}	0.072 (N/m)
α_w	1.67e-07 (m^2/s)
C_{pw}	4185 (J/kg.K)
$\Delta T = T_\infty - \mathrm{T_{sat}}$	6.2 (°C)

Table 6-1 Physical properties for the bubble and water [31] [32]

L_{max}	0.000015 (m)
h_{min}	0.0000015 (m)
Δt	0.0000003 (s)

Table 6-2 Numerical parameters for simulation

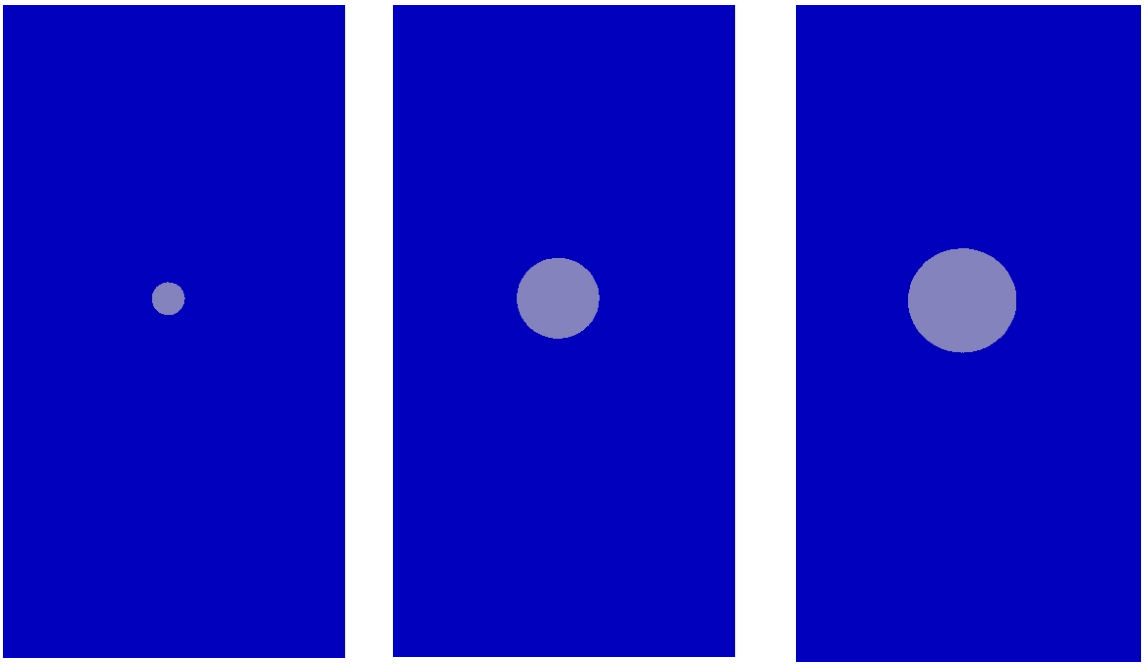

t = 0 (s) t = 0.00011 (s) t = 0.00022 (s)

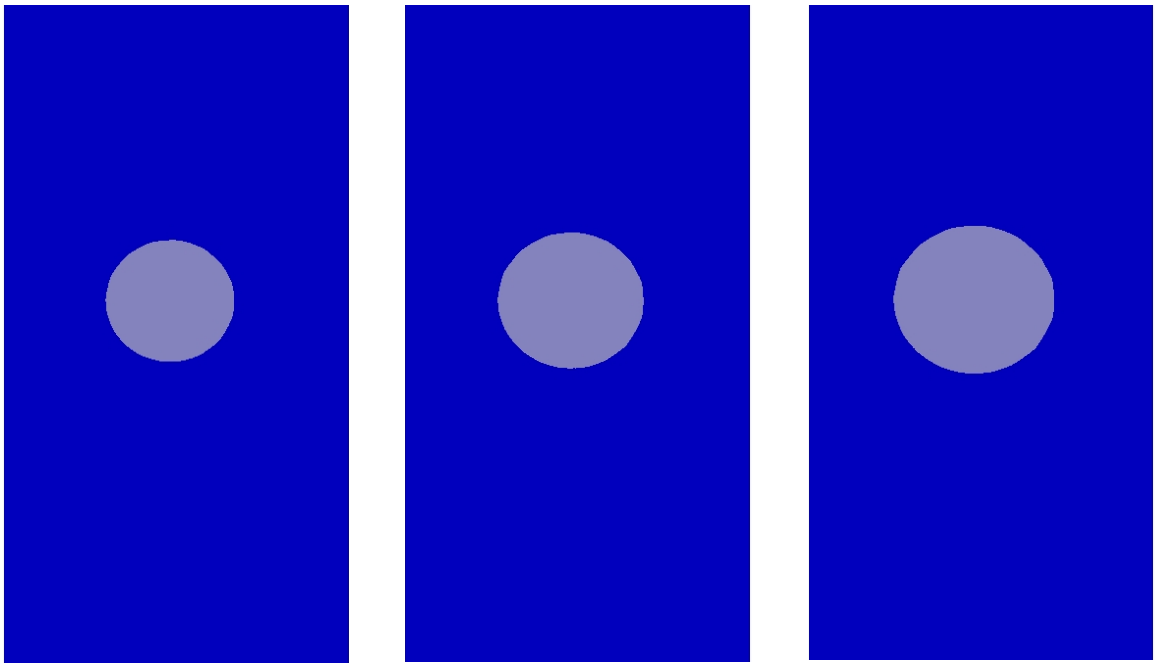

Figure 6-8 Growth of a water vapor bubble in superheated liquid (water).

Figure 6-8 shows the growth of a water vapor bubble in superheated water. When the vapor density is small ($\rho_b = 1$), the small evaporation of water leads to substantial bubble growth. Variation of the water vapor bubble radius with time is plotted in Figure 6-9, and the numerical solution is then compared with the analytical solution given by Mikic et al. [102]. A good agreement has been found between the numerical solution and the analytical solution. Thus, we can say that our model correctly predicted the bubble growth in a stable liquid (water).

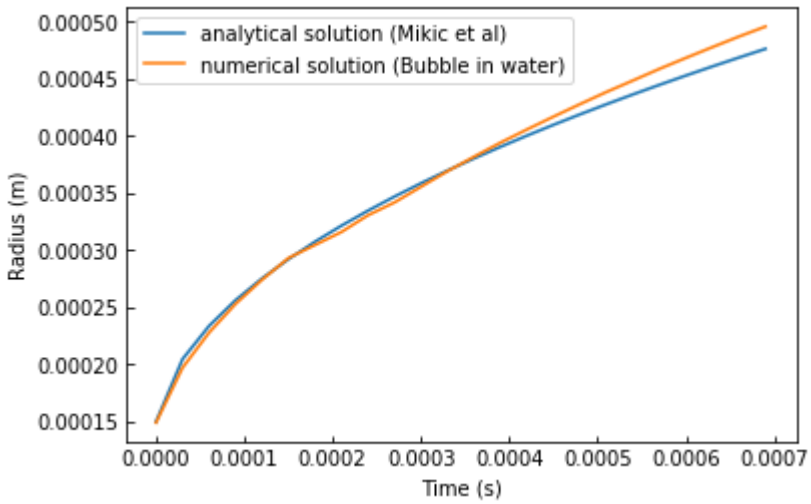

Figure 6-9 Comparison of the numerical solution with an analytical solution (growth of water vapor bubble in superheated water).

Once the growth of the water vapor bubble is computed, then we computed the growth of a calcium bubble in the stable calcium liquid. The growth rate obtained numerically is then compared with the analytical solution. The domain of the same size (0.3cm X 1 cm) is taken for computing the growth of the calcium bubble in calcium liquid. The physical and the numerical parameters which are taken for the simulation can be seen in Table 6-3 and Table 6-4, respectively.

H_{vca}	3855000 (J/kg)
μ_{cad}	0.001 (Pa.s)
ρ_{cab}	0.5 (kg/m^3)
μ_{cab}	0.00001 (Pa.s)
$\sigma_{cad.ls}$	1.4 (N/m)
$\sigma_{cad.cab}$	0.3 (N/m)
α_{Cad}	6.14e-05 (m^2/s)
C_{pcad}	950 (J/kg.K)
$\Delta T = T_{\infty} - \mathrm{T_{sat}}$	5.5 (°C)

Table 6-3 Physical properties for the Ca bubble and Ca liquid [31] [32].

L_{max}	0.000015 (m)
h_{min}	0.0000015 (m)
Δt	0.0000003 (s)

Table 6-4 Numerical parameters for simulation.

Figure 6-10 shows the growth of a calcium bubble in a uniformly superheated liquid calcium with time. Variation of the calcium bubble radius with time is plotted in Figure 6-11, and then the numerical solution is compared with the analytical solution. A good agreement between the numerical solution and the analytical solution has been found.

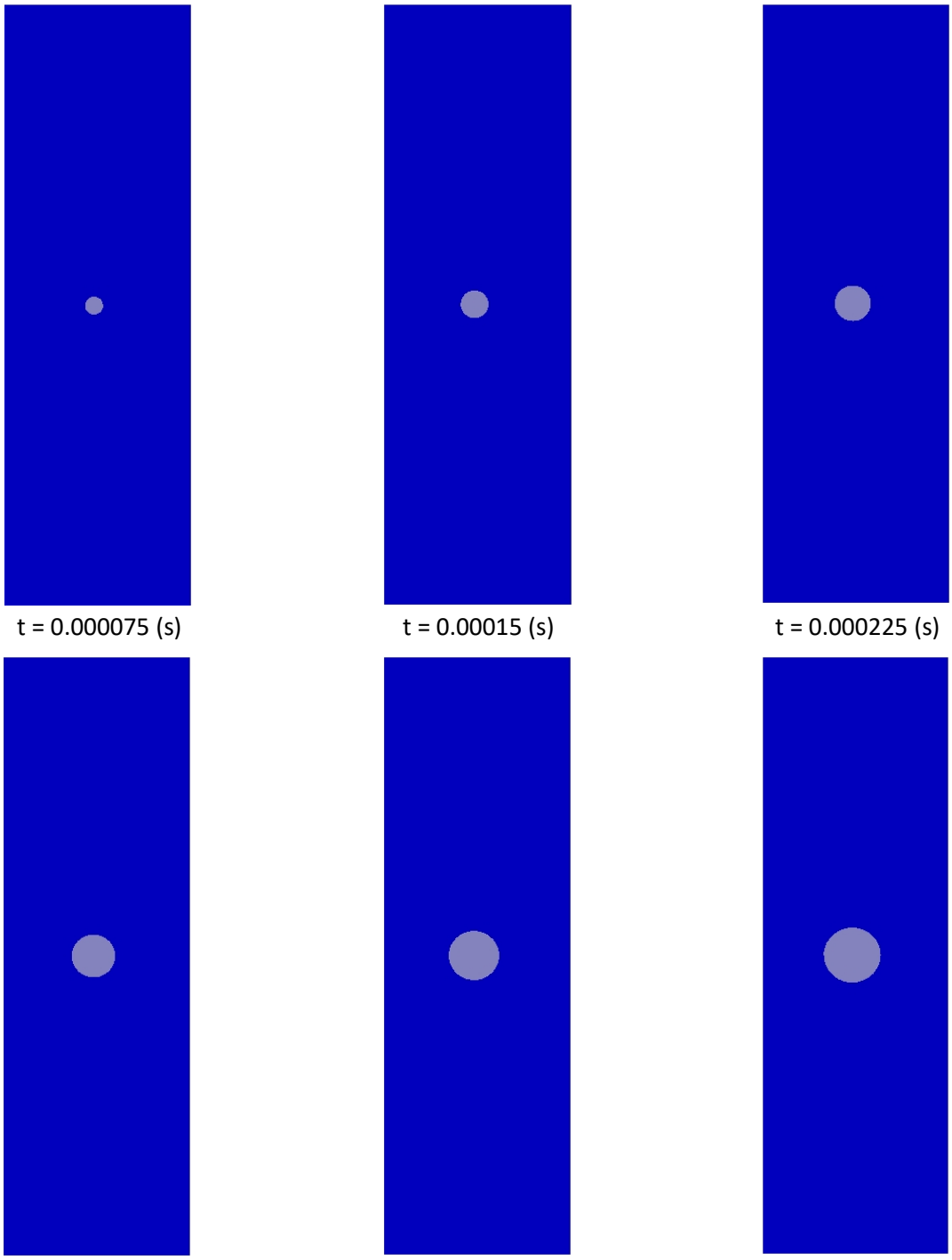

Figure 6-10 Growth of Ca bubble in a super-heated Ca liquid.

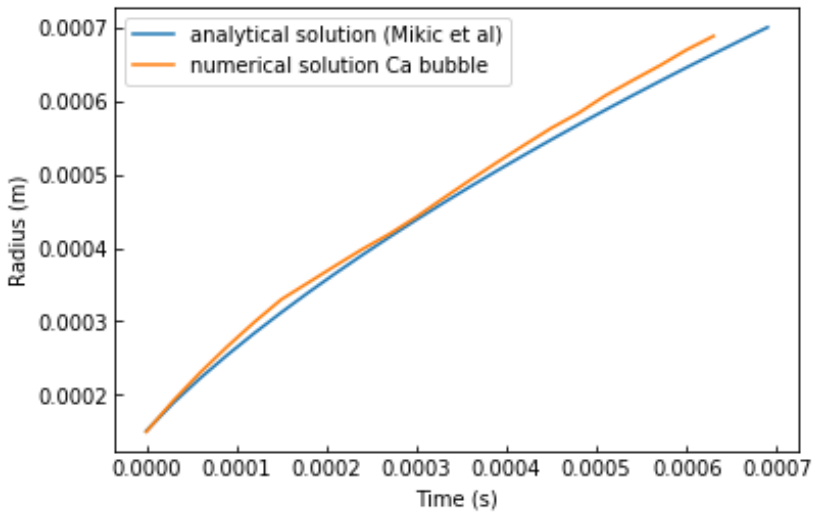

Figure 6-11 Comparison of the numerical solution with an analytical solution for the growth of Ca bubble in uniformly superheated stable liquid calcium.

6.5 Calcium liquid-gas phase change

Once the growth model has been validated, the calcium liquid-gas phase change has been computed. We studied the phase change of rising calcium droplet in liquid steel. Initially, a calcium bubble nucleus is placed inside the calcium droplet. The computational domain can be seen in Figure 6-12. Dimension of the computational domain, calcium droplet, and calcium bubble is presented in Table 6-5. Slip boundary condition is applied on the side walls of the domain and at the top of the domain free surface boundary condition is applied.

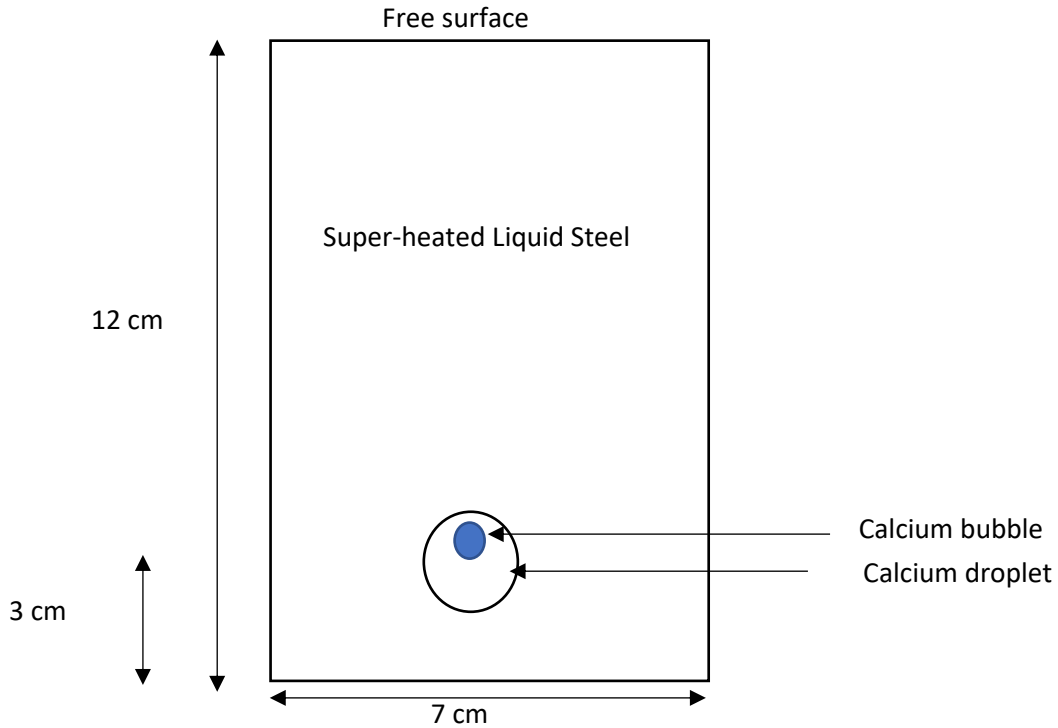

Figure 6-12 Schematic domain for computing Ca liquid-gas phase change.

Domain	12 cm X 7 cm
Calcium droplet diameter	1.4 (cm)
Calcium bubble diameter	0.16 (cm)

Table 6-5 Dimension for computing Ca liquid-gas phase change.

L_{max}	0.0004 (m)
h_{min}	0.00004 (m)
Δt	4e-06 (s)

Table 6-6 Numerical parameters for Ca liquid-gas phase change simulation.

In order to compute the calcium liquid-gas phase change, the radius of the calcium bubble is chosen such that it is greater than the critical radius (80 µm) given by equation (6.52). The physical properties of calcium bubble, calcium droplet, and liquid steel can be seen in Table 5-6 and Table 6-3, respectively. It should be noted that in order to simplify our calculation, the surface tension between the calcium droplet-calcium bubble and calcium droplet-liquid steel is neglected. In the figure below, the dark blue color represents the calcium bubble, light blue is the calcium droplet, and the red color represents liquid steel, respectively.

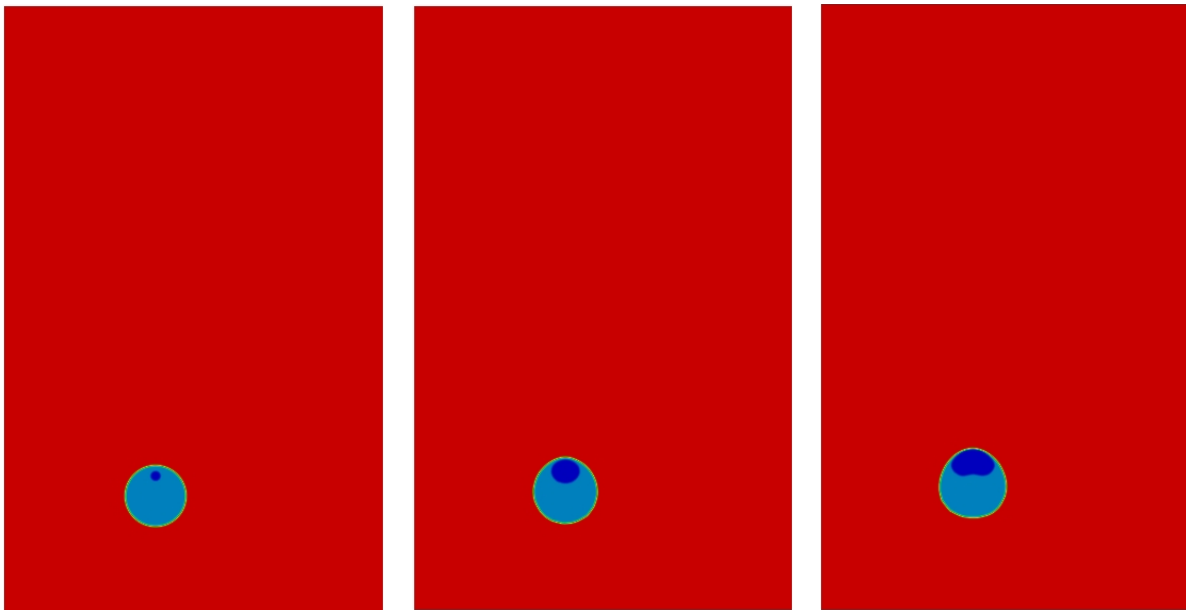

t = 0.0 (s) t = 0.000075 (s) t = 0.000225 (s)

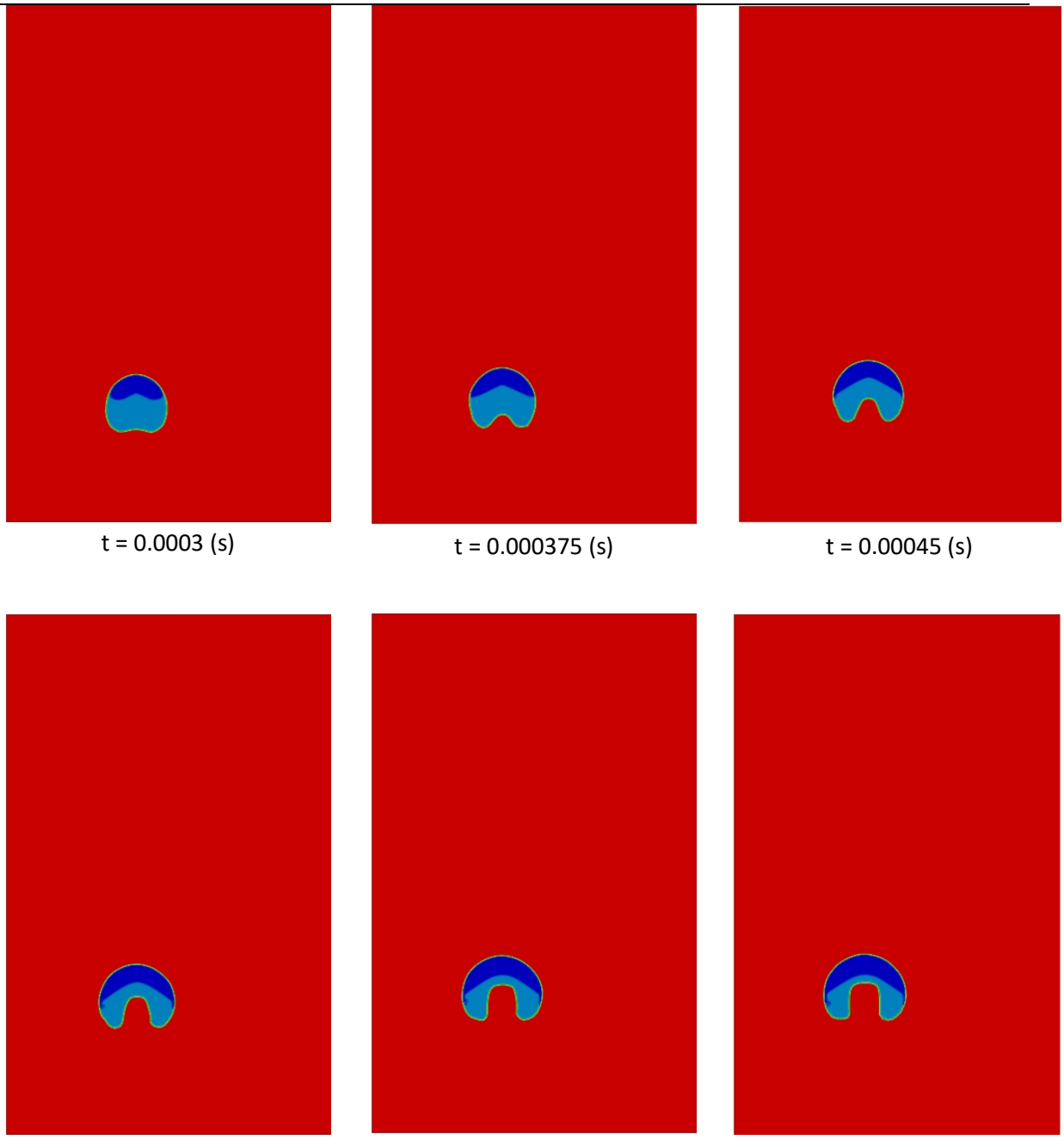

Figure 6-13 Ca liquid-gas phase while rising in liquid steel (without surface tension).

Figure 6-13 shows the growth of a calcium bubble inside the calcium droplet as well as the rise of both calcium droplet and calcium bubble in liquid steel (2D simulation). The growth of calcium bubble is directly related to the equivalent consumption of the mass of the calcium droplet. It can be seen that both calcium droplet and calcium bubble are elongated since the surface tension forces are neglected for this specific simulation. It should also be noted that the calcium bubble remains inside the calcium droplet during its course of ascension. It does not cross the calcium droplet interface.

The section below shows the computation of calcium liquid-gas phase change without neglecting the surface tension forces.

6.5.1 Calcium liquid-gas phase change with surface tension

Simulation has also been performed for the calcium liquid-gas phase, taking into account the surface tension force between calcium droplet - calcium bubble ($\sigma_{cad.cab}$) and Ca droplet-liquid steel ($\sigma_{cad.ls}$). The computational domain can be seen in Figure 6-14. Table 6-5 shows the dimension of the computational domain, calcium droplet, and calcium bubble, respectively. The numerical parameters used for the computation are presented in Table 6-7.

L_{max}	0.00008 (m)
h_{min}	0.000008 (m)
Δt	1e-07 (s)

Table 6-7 Numerical parameters for Ca liquid-gas phase change simulation

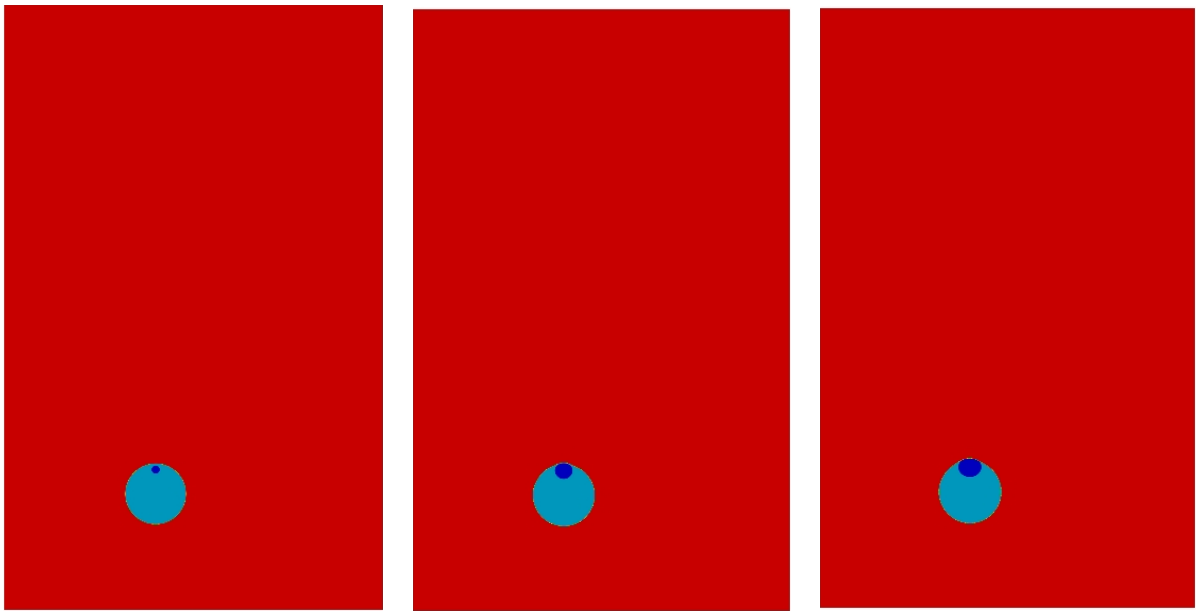

t = 0 (s) t = 0.0000025 (s) t = 0.0000050 (s)

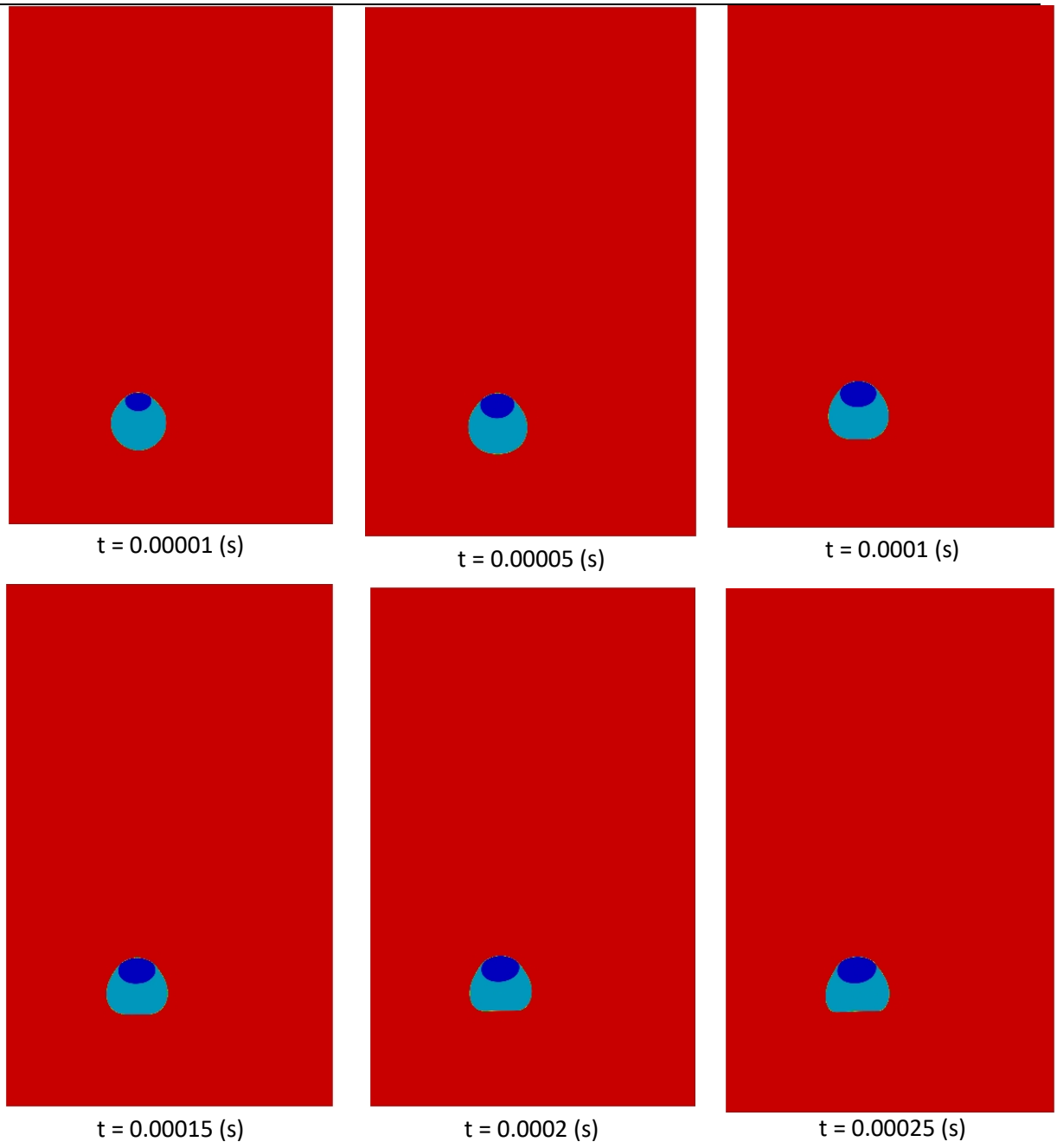

Figure 6-14 Ca liquid-gas phase while rising in liquid steel (with surface tension).

With the surface tension force being activated, the droplets and bubbles are no more elongated. They try to retain their spherical shape during their ascension. Another important point that should be noted is that; the calcium bubble remained inside the calcium droplet even when the surface tension forces are activated. Since the time step for the simulation was too small (1e-07s), the computational time was too long to compute the complete calcium liquid-gas phase change. We need to optimize the implemented phase change model in order to compute the whole phase change transformation, which is the main perspective of this research work.

6.6 Conclusion

At the beginning of this chapter, a short bibliography concerning the different nucleation mechanisms (homogeneous and heterogeneous) is presented. It is found that the homogenous or heterogeneous nucleation depends mainly on the contact angle of the fluid enclosing the phases. If the contact angle between the fluid is greater than zero, then there is a high probability of heterogeneous nucleation; otherwise, it is homogenous nucleation. Another important parameter to judge the nucleation mechanism is the temperature at which the nucleation takes place. If the bath temperature is closer to the boiling point when the phase change occurs, then there are high chances of heterogeneous nucleation. The presence of cavities or scratches lead to the heterogenous nucleation, and the degree of superheat in the case of heterogeneous nucleation is much lower than for the homogenous nucleation. Due to the inclusions present during the calcium treatment of steel, calcium liquid-gas phase change is expected to be heterogeneous.

In order to study the calcium liquid-gas phase change, a simplified nucleation model has been implemented in the ICI-tech code. For this, compressible Navier Stokes solver is being used for the conservation of momentum and mass. Validation of the implemented model has been performed, using classical benchmarks issued from literature (growth of a bubble in a uniformly superheated liquid). A typical test is performed, where the growth of a bubble (water vapor) in uniformly superheated water and growth of a calcium bubble in a uniformly superheated calcium liquid is computed. A good agreement has been predicted between the analytical solution and the numerical solution. The growth approach presented in this model offers a simple way to model the phase mechanism without solving the thermal equation.

Preliminary numerical simulation of the calcium liquid-gas phase for a calcium droplet rising in liquid steel is presented too. The implemented phase change model needs to be optimized in order to have the complete Ca liquid-gas phase change transformation.

6.7 Résumé Français

Au début de ce chapitre, une brève bibliographie concernant les différents types de mécanismes de nucléation (homogène et hétérogène) est présentée. On constate que la nucléation homogène ou hétérogène dépend principalement de l'angle de contact du fluide englobant les phases. Si l'angle de contact entre le fluide est supérieur à zéro, il y a une forte probabilité de nucléation hétérogène, sinon il s'agit d'une nucléation homogène. Un autre paramètre important pour juger du mécanisme de nucléation est la température à laquelle la nucléation a lieu. Si le changement de phase a lieu à une température proche du point d'ébullition, il y a de fortes chances que la nucléation soit hétérogène. La présence de cavités ou de rayures conduit à la nucléation hétérogène et le degré de surchauffe en cas de nucléation hétérogène est beaucoup plus faible que la nucléation homogène. En raison des inclusions présentes lors du traitement de l'acier au calcium, le changement de phase du Ca (Calcium) liquide en phase gazeuse devrait être hétérogène.

Afin d'étudier le changement de phase du calcium de l'état liquide à l'état gazeux, un modèle de nucléation simplifié (ébullition nucléée) a été mis en œuvre dans le code ICITech. Pour cela, le solveur de Navier Stokes compressible est utilisé pour la conservation de la quantité de mouvement et de la masse. La validation du modèle mis en œuvre a été effectuée en utilisant des points de repère classiques issus de la littérature (croissance d'une bulle dans un liquide uniformément surchauffé). Un test typique a effectué où la croissance d'une bulle (vapeur d'eau) dans une eau uniformément surchauffée et la croissance d'une bulle de Ca (calcium) dans un liquide de Ca (calcium) uniformément surchauffé sont calculées. Un bon accord a été prédit entre la solution analytique et la solution numérique. L'approche de croissance présentée dans ce modèle offre un moyen simple de modéliser le mécanisme de changement de phase sans résoudre l'équation de bilan thermique.

Une simulation numérique préliminaire du changement de phase liquide/gaz de calcium dans de l'acier liquide est également présentée. Le modèle de changement de phase mis en œuvre doit être optimisé pour obtenir la transformation complète du changement de phase liquide-gaz calcium.

Chapter 7:

Conclusions and Perspectives

7 Conclusions and Perspectives

The main objective of the thesis was to study the dissolution of calcium in liquid steel. The dissolution of calcium (experimentally and numerically) in liquid steel was never studied in the past in such details. Having a macro perspective of the objective helped us to get acquainted with the possibility of the technical glitches and subsequently, the ameliorations helped us to achieve our desired objectives.

We divided our thesis into two parts. First, the experimental study of calcium treatment, under simplified conditions, has been led. Then, a numerical analysis of the same problem has been conducted.

Dedicated experiments were performed at the temperature below and above the boiling point of calcium. The objective was to predict the average mass transfer coefficient between the calcium and liquid steel based on the knowledge of the total calcium absorbed in liquid steel.

As far as the experiments are concerned, a new method of calcium injection was used in which calcium was placed inside the capsule of stainless steel weighted with tungsten. This specific method of calcium injection allowed the experiments to be more reproducible. The experiments below the boiling point showed calcium droplets arriving at the surface of liquid steel. The total volume of calcium droplets observed at the surface of liquid steel was found to be of the same order of magnitude of the total volume of calcium droplets expected. Concerning the calcium dissolution below the boiling point (1480°C), it was found that calcium retention was quite low for calcium droplets. At the same time, it was also observed that the mixing caused by the inductors could have significant effects on the dissolution of calcium droplets in liquid steel. Experiments seemed to be reproducible below the boiling point, as far as the total calcium absorbed in liquid steel is concerned. Experimental results concerning the total calcium absorbed in liquid steel, allowed us to calculate the average mass transfer coefficient of calcium droplets in liquid steel. The value of the average mass transfer coefficient obtained experimentally was then compared with the one obtained numerically.

Experiments above the boiling point gave information concerning the number of calcium bubbles arriving at the surface, their size as well as the calcium retention in liquid steel. Significant discrepancies have been observed in the total volume of calcium bubbles observed and the total volume expected at that specific temperature (1550°C). Various reasons were reported for this discrepancy, e.g., significant formation of black fumes at the surface of liquid steel which prevented from observing the bath surface when bubbles reached there, and the very likely the partial phase change of calcium from droplets to bubbles. The better yield was obtained for calcium bubbles as compared to the calcium droplets. Experiments were reproducible even at the temperature above the boiling of calcium as far as the total calcium in liquid steel is concerned. Observation of the total number of calcium bubbles at the liquid metal surface during the experiments did provide a strong base for modeling the nucleation rate of calcium in liquid steel.

Regarding the development of the numerical model, we used ICI-tech software, which is based on finite element and dynamic remeshing methods. Since the rise of calcium cavities (droplet/bubble) in liquid steel is a three-phase problem (calcium/liquid steel/free surface), ICI-tech was further developed to take into account such a three-phase flow and validation was performed, using classical benchmarks issued from the literature. After that, the dissolution model was implemented in ICI-tech and was validated for the case of stable calcium droplet dissolving in liquid steel. Consequently, the validation of the convection-dissolution model was done for low Schmidt numbers. Simulations with three different physical properties were performed to demonstrate the capability of the model. The computed Reynolds number and the shapes of the rising droplet in the stable liquid were compared with the one obtained from the Grace diagram. It was observed that the shapes of the rising droplet and their respective Reynolds number agreed well with the data obtained from this diagram. It was also found that the Sherwood number obtained numerically agreed well with the analytical formulation obtained in the literature.

Once the dissolution-convection model was validated, we studied the rise of the dissolving calcium droplet in liquid steel. Mesh convergence study was performed in both 2D and 3D to evaluate the average mass transfer coefficient of the calcium droplet in liquid steel.

Continuity of shear stress across the interface is an important parameter to predict the mass transfer coefficient in a multiphase flow correctly. Therefore, we verified the continuity of the shear stress across the calcium droplet-liquid steel interface. Simulations were performed for the rise of multiple calcium droplets dissolving in liquid steel. The total calcium absorbed in liquid steel given by the model was compared with the one obtained experimentally. The numerical model also confirmed the low dissolution of calcium droplets in liquid steel. Rise of the calcium bubble (without phase change and growth) in liquid steel has been studied too, and the average mass transfer coefficient of the calcium bubble in liquid steel was reported.

Identifying the correct mechanism for calcium liquid-gas phase change is essential to understand the dissolution of rising calcium droplets or bubbles in liquid steel. We presented a preliminary model to study the phase change mechanism. Nucleation (growth) model was implemented in the ICI-tech code, and a typical test was performed, where the growth of a bubble (water vapor) in uniformly superheated water and growth of a calcium bubble in a uniformly superheated Ca liquid was computed. A good agreement has been predicted between the analytical solution and the numerical solution. In the end, we studied the calcium liquid-gas phase change in 2D, but the model implemented showed some limitations. The time step in our simulation was too small, which led to high computational time. Further investigation needs to be done in order to improve the model efficiency concerning the phase change mechanism.

7.1 Perspective

The current work can be extended in the following directions:

- As far as the experiments are concerned, the biggest challenge we faced while observing the calcium droplets or calcium bubbles at the surface of liquid steel was the formation of black fumes. Black fumes formation was found to be directly associated with the amount of calcium to be injected as well as the temperature at which it was injected. Even a small amount of calcium injection (100 mg) above the boiling point led to the significant formation of black fumes, which clearly showed the effect of temperature on the black fumes formation. The possible reason for the black fumes formation needs to be figured out (like melt composition), and then the experimental trials need to be performed in order to clearly observe the calcium droplets or bubbles at the surface of liquid steel.
- Having a camera at the top of the furnace allowed us to observe only the surface phenomenon. Other 3D imaging techniques could be used which can give crucial information concerning what is happening inside liquid steel, e.g., the shape of the rising calcium droplet or calcium bubble, calcium release mechanism from the capsule, calcium liquid-gas phase mechanism, etc. This information would help us to understand and model the dissolution mechanism of calcium in a much better way.
- As far as numerical modeling is concerned, the three-phase model implemented needs further testing. The sensitivity of different numerical and physical parameters needs to be performed. The model implemented could be easily extended to different multiphase systems like two fluids-one solid (e.g., spreading of liquid at the solid surface) and validation needs to be performed. It would be interesting to study the bursting phenomenon of calcium droplets and calcium bubbles at the surface of liquid steel in more detail.
- While simulating high Reynolds and high Schmidt number problems, which are the cases for rising calcium droplets or calcium bubbles in liquid steel, the concentration boundary layer needs to be adequately resolved, and it seemed to be a quite difficult task in 3D. Therefore, further studies with improved mesh refinement in the interface should be performed to verify the average mass transfer coefficient of calcium in liquid steel.
- The growth model implemented should be exploited further in order to understand the calcium liquid-gas phase transformation better. The implemented model needs to be coupled with the dissolution model in order to study the effect of nucleation-growth (calcium liquid-gas phase change) mechanism on the dissolution.
- In our nucleation model, we only took into account the temperature, which might not be true in the ladle furnace where pressure is the main driving force for the calcium liquid-gas phase change. Therefore, the implemented model should be extended further so that it can model the phase change mechanism in the industrial ladle.

- Further study needs to be done, to implement the phase change model, which can also take into account the nucleation rate (rate of formation of bubbles).

8 References

[1] Y. Lee, "A model study of CaSi Cored Wire Injection, Proceedings of the International Symposium on Developments in Ladle Steelmaking and Continuous Casting," pp. 154-166, 1990.

[2] S. Sanyal, S. Chandra, S. kumar and G. Roy, "An improved model of cored wire injection in steel melts," *ISIJ International,* vol. 44, no. 7, pp. 1157-1166, 2004.

[3] A. Carre and S. Gerardin, "Recent developments in Calcium treatment in steelmaking: a source of technical efficiency and cost savings," in *Clean Steel Conference* , Budapest, 2015.

[4] D. Lu, "Kinetics, Mechanisms and Modelling of Calcium treatment of Steel, McMaster University, PhD Thesis," McMaster University, 1992.

[5] D. Lu, G. Iron and W. Lu, "Modeling of Calcium treatment," *76 Steelmaking Conference Proceedings,* vol. 76, pp. 449-456, 1993.

[6] E. Turkdogan, "International Calcium treatment symposium, University of Strathclyde, Glasgow," no. 2, 1988.

[7] H. Suito and R. Inoue, "Thermodynamics on Inclusions composition in ultra clean steels," *ISIJ International,* vol. 36, no. 5, pp. 528-536, 1996.

[8] G. Ye, P. Jonsson and T. Lund, "Thermodynamics and Kinetics of the Modification of Al2O3 Inclusions," *ISIJ International,* vol. 36, pp. 105-108, 1996.

[9] N. Bannenberg, K. Harste et O. Bode, «Melting Behaviour of Cored wire during Injection,» *In Scaninject VI, 6th International Conference on refining processes ,* pp. 247-265, 1992.

[10] W. Tiekink, "The behaviour of case in steelmaking and casting of calcium treated aluminium killed steel," *Aachener Stahlkolloquium,* 2015.

[11] D. Mazumdar, A First Course in Iron and Steelmaking, Kanpur: Universities Press India, 2015.

[12] D. LU and B. Eng, "Kinetics Mechanism and Modelling of calcium treatment of steel (Thesis)".

[13] F. Mucciardi, "Master's thesis Dept. of Mining and Metallurgical Eng, McGill University," 1997.

[14] C. Cicutti, J. Madias, C.E and J. Gonzalez, "Control of microinclusions in calcium treated aluminium killed steels," 1997.

[15] L. Holappa, M. Hamalainen, M. Liukkonen and M. Lind, "Thermodynamic examination on inclusion modification and precipitation from calcium treatment to solidified steel,," *Iron and Steelmaking,* vol. 30, no. 2, pp. 111-115, 2003.

[16] R. Tuttle, J. Smith et K. Peaslee, *Metall. Mater. Trans. B,* vol. 36, pp. 885-892, 2005.

[17] L. B. E. Dennis, "Kinetics mechanisms and modelling of calcium treatment of steel (Thesis)," 1992.

[18] R.Higbie, "AIChE," vol. 31, p. 365, 1935.

[19] A. Lochiel and P. Caldebanki, *Chemical Eng Soc,* vol. 19, pp. 471-484, 1964.

[20] Davidson, M. Baird and J.F., "Chem. Eng. Soc," vol. 17, pp. 87-93, 1962.

[21] M. Weber, *Chem. Eng. Soc,* vol. 30, pp. 1507-1510.

[22] Richardson, A. Bradshaw et D. F, «Chemical engineering in Iron and steel industry,» 1970.

[23] D.-Z. Lu, G. Irons and W.-K. Lu, "Modeling of calcium treatment of steel," in *SteelMaking Conference Proceedings* , Canada, 1993.

[24] Y. Higuchi, M. Numata, S. Fukagawa and K. Shinme, "Inclusion modification by calcium treatment," *ISIJ International ,* vol. 36, pp. 151-154, 1996.

[25] D.-Z. Lu, G. Irons and W.-K. Lu, "Proc. conf. scaninject VI," 1992.

[26] G. Irons, *Metall Trans,* no. 151-154, 1978.

[27] Kkmurray, «Spectrometer schematic.gif,» *https://commons.wikimedia.org/wiki/Files:Spectrometer_schematic.gif.*

[28] Scanning Electron Microscopy, ETH Zurich, Switzerland.

[29] Atomic Emission spectroscopy, Wikipedia.

[30] J. R. Grace, «Trans. Inst. chem. Eng,» vol. 116, p. 51, 1973.

[31] T. Ototani, "Calcium Clean Steel," *Springer-Verlag,* pp. 4-7, 1986.

[32] M. Joyant and C. Gatellier, "IRSID Report, PCM-RE, 1108," Mai, 1984.

[33] A. Yoffe and E. Heymann, Note on Antonoff's rule, Chemistry department, University of Melbourne, Australia, 1945.

[34] Surface Tension, Appendix 9, Knovel: Engineering Technical reference information, Lamar University, Beaumont, Texas, 2011.

[35] L. A. Bower et T. Lee, «Single bubble rising dynamics for moderate Reynolds number using Lattice Boltzman Method,» *Computers and Fluids,* vol. 39, pp. 1191-1207, 2010.

[36] J. Hadamard, "Mouvement permanent lent d'une sphere liquide et visqueuse dans une liquide visqueuse," *CR Academic Science,* vol. 152, pp. 8-1735, 1911.

[37] W. Rybczynski, "On the translatory motion of a fluid sphere in a viscous medium," *Bull Int Acad Pol Sci Lett,* pp. 6-40, 1911.

[38] H. Mendelson, "The prediction of bubble terminal velocities from the wave theory," *AIChE,* vol. 13, pp. 2-250, 1967.

[39] R. Davies and G. Taylor, "The mechanics of large bubbles rising through extended liquids in tube," *Proc R Soc Ser A ,* vol. 200, pp. 90-375, 1950.

[40] G. Wallis, "One dimensional two-phase flow," McGraw-Hill, New York, 1969.

[41] T. Watanabe and K. Ebihara, "Numerical simulation of coalescence and break up of rising droplets," *Computers and Fluids,* vol. 32, no. 6, pp. 823-834, 2003.

[42] S. Z. F. Marcotte, "Density contrast matters for drop fragmentation thresholds at low Ohnesorge number," *Physics.flu-dyn,* 2019.

[43] J. Lehmann, "Application of ArcelorMittal Maizières thermodynamic models to liquid steel elaboration," *Revue de Metallurgie,* vol. 105 (11), pp. 539-550, 2008.

[44] J. N. reddy, An Introduction to the Finite Element Method, Singapore: McGraw Hill International edition , 1984.

[45] L. Ville, L. Silva and T. Coupez, "Convected level set method for the numerical simulation of luid buckling," *International journal for numerical methods in fluids,* vol. 66, no. 3, pp. 324-344, 2011.

[46] S. Oshe and J. Sethian, "Fronts propogating with curvature dependent speed: algorithms based on Hamilton-Jacobi Formulations," *Journal of Computaional Physics ,* vol. 79, no. 1, pp. 12-49, 1988.

[47] E. Pichelin and T. Coupez, "Finite element solution of the 3d mold filing problem for viscous incompressible fluid," *Comput. Methods Appl. Mech Eng,* vol. 163, pp. 359-371, 1998.

[48] T. Coupez, L. Silva and L. Ville, "Convected level set method for the numerical simulation of fluid buckling," *International Journal for Numerical Methhods in Fluids,* vol. 66, no. 3, pp. 324-344, 2011.

[49] H. C. Nguyen, “Thesis Report, Anisotropic space-time adaptation for multi-fluid simulation,” 2015.

[50] T. Coupez, "Reinitialisation convective et locale des fonctions level set pour le mouvement de surafces et d'interafces," in *Activités universitatire de Mécanique* , La Rochelle , 2006.

[51] A. Brooks and T. Hughes, "Streamline upwind/petrov-galerkin formulations for convection dminated flows with particular emphasis on the incompressible navier-stokes equations," *Applied mechanics and engineering ,* vol. 32, pp. 199-259, 1982.

[52] C. Baiocchi, F. Brezzi and L. P. Franca, "Virtual bubbles and the Galerkin least squares method," *Computer methods in Applied Mechanics and engineering,* vol. 32, pp. 199-259, 1982.

[53] E. Hachem, T. Kloczko, H. Digonnet and T. Coupez, "Stablized finite element solution to handle complex heat and fluid flows in industrial furnaces using the immersed volume method," *International Journal for Numerical Methods in Fluids ,* vol. 68, no. 1, pp. 99-121, 2012.

[54] G. Scovazzi, "A Discourse on Galilean Invariance, Supg Stabilization and the variational multiscale framework," *Computer methods in applied mechanics and engineering ,* vol. 196, pp. 1108-1132, 2007.

[55] T. E. Tezduyar and Y. Osawa, "Finite element stabilization parameters computed from element Matrices and vectors," *Computed methods in applied mechanics and engineering,* vol. 190, pp. 411-430, 2000.

[56] R. Codina, "Stabilized Finite element approximation of transient incompressible flows using orthgonal subscales," *Computer methods in applied mechanics and engineering,* vol. 191, pp. 4295-4321, 2002.

[57] Z. Sun, R. Logé and M. Bernacki, "3d finite element model of semi solid permeability in an equiaxed granular structure," *Computational Mateial Science,* vol. 49, pp. 158-170, 2010.

[58] T. Coupez., " Grand transformations et Remaillage Automatique, PhD thesis, Ecole Nationale Supérieure des Mines de Paris," 1991.

[59] F. Alauzet, P. Frey et B. Mohammadi, «Adaptation de mailage non structurés pour les problèmes instationnaires en trois dimensions,» *Congrés National d'Analyse Numérique, La grande Motte,* 2003.

[60] C. Dobrzynski, O. Pironneau et P. Frey, «Numerical coupling for air flow computations in complex architecures,» Jyvaskyla, 2004.

[61] F. Alauzet and P. J. Frey, "Estimateur d'erreur géométrique et métriques anisotropes pour l'adaptation de maillage," RR-4789, 2003.

[62] T. Coupez, «Metric construction by length distribution tensor and edge based for anisotropic adative meshing,» *J. Comput Phys,* vol. 7, pp. 2391-2405, 2011.

[63] L. Duchemin, S. Popinet, C. Josserand and S. Zaleski, "Jet formation in bubbles bursting at the free surface," *Physics of Fluids,* vol. 14, no. 9, 2002.

[64] B. Y. Ni, A. M. zhang and G. X. Wu, "Simulation of a fully submerged bubble bursting through a free surface," *European journal of mechanics,* vol. 55, pp. 1-14, 2016.

[65] C. H. Yu, Z. ye and Y. T. L. X. Z. Z. Tony W.H. Sheu, "An improved interface preseving level set method for simulating three dimensional rising bubble," *International Journal of Heat and Mass transfer,* vol. 103, pp. 753-772, 2016.

[66] N. Tofighi and M. Yildiz, "Numerical simulation of single droplet dynamics in three phase flow using ISPH," *Computers and Mathematics with Applications,* vol. 66, pp. 525-536, 2013.

[67] F. Boyer, C. Lapuerta, S. Minjeaud, B. Piar and M. Quintard, "Cahn-Hilliard/Navier-stokes Model for Simulation of Three-Phase Flows," *Transport in Porous Media,* vol. 82, pp. 463-483, 2010.

[68] J. Kim, "Phase field computations for ternary fluid flows," *Computer methods in applied mechanics and engineering ,* vol. 196, pp. 4779-4788, 2007.

[69] J. bruchon, Y. Liu and N. Moulin, "Fnite element setting for fluid flow simulations with natural enforcement of the triple junction equilibrium," *Computers and Fluids ,* vol. 171, pp. 103-121, 2018.

[70] J. Brackbill, D. Kothe and C. Zemach, "A continum method for modeling surafce tension," *computational physics,* vol. 100, pp. 335-354, 1992.

[71] T. Coupez, "Metric construction by length distribution tensor and edge based erroe for anisotropic adaptive meshing," *Journal of Computation Physics,* vol. 230, pp. 2391-2405, 2011.

[72] R. Guillaument, S. Vincent, J. Caltagirone, J. Duclos, M. Laugier and P. Gardin, "A new volume of fluid model for handling wetting effects. Application to the impact of emulsion o/w droplets on a moving plate," in *7th International conference on Multiphase flow*, 2010.

[73] K. A. Smith, F. J. Solis and D. L. Chopp, "A projection method for motion of triple junctions by level sets," *Interface Free Bound,* vol. 4, pp. 263-276, 2002.

[74] J. Kim, "Phase field computations for ternary fluid flows," *Comput. Methods Applied mechanics and engineering,* vol. 196, pp. 4779-4788, 2007.

[75] N. E. Kosseifi, Numerical simulation of boiling for industrial quenching processes (PhD Thesis report), Ecole National Supérieure des Mines de Paris, 2012.

[76] J. R. Grace and M. E. Weber, "Bubbles, Drops and Particles," Academic Press 1978.

[77] D. Darmana, N. G. Deen and J. A. M. Kuipers, "Detailed 3D Modeling of Mass transfer Processes in Two phase flows with Dynamic Interfaces," *Chem. Eng. Technology,* vol. 29, no. 9, pp. 1027-1033, 2006.

[78] K. Hayashi and A. Toiyama, "Interface tracking simulation of mass transfer from a dissolving bubble," Graduate school of engineerin, Kobe University , Japan, 2011.

[79] R. Courant, K. Friedrichs and H. Lewy, On the partial difference equations of mathematical physics, Courant Institute of Mathematical Sciences , Germany, 1928.

[80] Bird, S. R. Byron, Warren, E. Lightfoot and Edwin, "Transport Phenomenon," John wiley and sons, 2007.

[81] P. J. Roache, "Verification and validation in computational science and engineering," Hermosa Publishers, 1998, pp. 403-412.

[82] W. L. Oberkampf and T. G. Trucano, "Verification and validation in Computational Fluid Dynamics," in *Sandia National Laboratory Report SAND2002-059*, 2002.

[83] I. Calment and J. Magnaudet, "Turbulent mass transfer through a flat shear free surface," *Journal of Fluid Mechanics,* vol. 5553, pp. 155-185, 2006.

[84] E. Izard, L. Lacaze and T. Bonometti, "Modelling the normal bouncing dynamics of spheres in a viscous fluid," in *Powder and Grains 2017*, 2017.

[85] J. Gibbs, "the collected works," vol. 2, 1928.

[86] P. G. Debenedetti, "Metastable liquids : Concepts and Principles," Princeton University Press, 1997.

[87] H. R. Pruppacher et J. D. Klett, «Microphysics of clouds and priciples,» Princeton university press , 1997.

[88] Weber and M. Volmer, *Physical chemistry,* vol. 119, pp. 277-301, 1926.

[89] L. Farkas, *Physical chemistry,* vol. 236, no. 125, 1927.

[90] R. Becker and W. Doring, "The kinetic treatment of nuclear formation in supersaturated vapors," *Ann. Physics,* pp. 719-752, 1935.

[91] "On the Theory of New Phase Formation:caviation," *Acta Physicochim,* p. 18, 1943.

[92] M. Blander and J. L. Katz, "Bubble Nucleation in Liquids," *AICHE Journal ,* vol. 21, no. 5 , pp. 833-847, 1975.

[93] Blander, Milton, Joseph and L. Katz, "The role of bubble nucleation in explosive boiling," Atlanta, 1973.

[94] K. Yu and K. Zh Fiz, Russ, 1960.

[95] M. Blander and D. Hengstenberg, "Bubble nucleation in n-pentane, n-hexane, n-pentane + hexadecane Mixtures and water," vol. 75, no. 23, 1971.

[96] Katz, B. Milton and L. Joseph, "Bubble Nucleation in liquids," vol. 21, no. 5, 1975.

[97] J. T. Jarvis, Donohue, D. Marc, L. Katz and Joseph, "Bubble Nucleation Mechanism of liquid droplets superheated in other liquids," vol. 50, no. 2, 1974.

[98] R. Cole, Boiling Nucleation, 1974.

[99] M. Ellion, "Study of Mechanism of Boiling heat transfer," no. 20-88, March 1954.

[100] V. P. Carey, Liquid Vapour Phase Change Phenomenon, Mechanical Engineering Department, University of California at Berkeley, 1980.

[101] L. Rayleigh, «On the pressure developped in a liquid during the collapse of a spherical cavity,» *Philos Mag,* vol. 34, pp. 94-98, 1917.

[102] Mikic, B. B. Rohsenow et Griffith, «On bubble growth rates,» *Heat and Mass transfer ,* vol. 13, pp. 657-666, 1970.

[103] Theofanous, T. G and P. D. patel, "Universal relations for the bubble growth," *Heat and Mass Transfer,* vol. 2, pp. 83-98, 1976.

[104] A. Prosperetti and M. S. Plesset, "Vapour bubble growth in a superheated liquid," *Fluid Mechanics ,* vol. 85, pp. 349-368, 1978.

[105] G. Son and V. K. Dhir, "Three dimensional simulation of saturated film boiling on a horizontal cylinder," *Heat and Mass Transfer ,* Vols. 51.5-6, pp. 1156-1167, 2008.

[106] Y. L. a. P. Griffith, The bubble growth at resuced pressure, Mechanical Eng Dept, Jan 1969.

Titre : Etude expérimentale et numérique du traitement inclusionnaire de l'acier par injection de calcium

Mots clés : Traitement calcium, Transfert de masse, CFD, Ecoulements triphasiques, Nucléation

Résumé : Afin de réduire les effets nocifs des inclusions d'alumine et d'améliorer la coulabilité de l'acier en fusion, le traitement au calcium est largement utilisé pour transformer les inclusions solides en inclusions liquides. Cependant, le traitement au calcium donne des résultats très irréguliers, difficilement explicables. Même si de nombreux efforts ont été déployés pour comprendre le comportement du calcium dans l'acier liquide, il n'a pas encore été prédit avec précision. Par conséquent, le mécanisme par lequel le calcium se dissout dans la masse fondue et transforme les inclusions solides doit être compris pour optimiser les conditions de traitement tels que la vitesse d'injection, la profondeur d'injection, le diamètre du fil d'injection, le temps d'agitation, etc. Afin de comprendre le mécanisme par lequel le calcium se dissout dans l'acier liquide, des expériences en laboratoire ont été effectuées dans un petit four à induction d'une capacité de 2,5 kg de métal. L'objectif est de confronter les résultats expérimentaux avec les résultats du modèle numérique développé.

La remontée des gouttelettes de calcium ou des bulles dans l'acier liquide est un problème à trois phases (gouttelettes ou bulles de calcium/acier liquide/air au sommet). Par conséquent, une plate-forme de calcul scientifique interne (ICI-tech) basée sur des méthodes par éléments finis est adaptée pour permettre la modélisation de telles solutions. Les écoulements triphasiques sont validés à l'aide de références classiques issues de la littérature. Le modèle de dissolution a été mis en œuvre dans notre logiciel et la validation du modèle de dissolution a été réalisée. Les gouttelettes et les bulles de calcium sont étudiées dans l'acier liquide et leur coefficient de transfert de masse moyen est indiqué.

Afin d'étudier le changement de phase calcium liquide/gaz, un modèle de nucléation a été implémenté dans le code ICI-tech. Un test typique est effectué où la croissance d'une bulle (vapeur d'eau) dans une eau uniformément surchauffée et la croissance d'une bulle de calcium dans du calcium liquide uniformément surchauffé sont calculées.

Title: Experimental and numerical study of calcium treatment of steel

Keywords: Calcium treatment, Mass transfer, CFD, Three phase flow, Nucleation

Abstract: In order to diminish the harmful effects of aluminate inclusions and improve the castability of molten steel, calcium treatment is widely used in Aluminum killed steels. However, calcium treatment gives irregular results. Even with many efforts done to understand the behavior of calcium in liquid steel, it is not yet accurately predicted. Therefore, the mechanism by which the calcium dissolves into the liquid steel and transforms the solid inclusions must be understood to optimize the process conditions such as injection speed, injection depth, injection wire diameter, stirring time, etc. In order to understand the mechanism by which the calcium dissolves into the liquid steel, laboratory scale experiments have been performed in a small induction furnace of 2.5 kg metal capacity.

The calcium injections are performed at the temperature below and above the boiling point of calcium. Then, the corresponding yields (calcium recovery) are compared.

Rise of calcium droplet or bubble in liquid steel is a three-phase problem (calcium droplet or calcium bubble/liquid steel/air at the top). Therefore, an in-house scientific computational platform (ICI-tech) based on finite element methods is adapted to allow the modeling of such three-phase flows, which is validated using the classical benchmark issued from the literature. The dissolution model has been implemented in our software, and their validation has been performed. Thereafter, the rise of Calcium droplets and bubbles are studied in the liquid steel, and their respective average mass transfer coefficient in the liquid steel is reported.

In order to study the calcium liquid/gas phase change, the nucleation model has been implemented in the code (ICI-tech). A typical test is performed where the growth of a bubble (water vapor) in uniformly superheated water and growth of a calcium bubble in uniformly superheated Ca liquid is computed.